

2012

## Developing an Unstructured Grid, Coupled Storm Surge, Wind Wave and Inundation Model for Super-regional Applications

Yi-Cheng Teng

*College of William and Mary - Virginia Institute of Marine Science*

Follow this and additional works at: <https://scholarworks.wm.edu/etd>



Part of the [Meteorology Commons](#), and the [Oceanography Commons](#)

---

### Recommended Citation

Teng, Yi-Cheng, "Developing an Unstructured Grid, Coupled Storm Surge, Wind Wave and Inundation Model for Super-regional Applications" (2012). *Dissertations, Theses, and Masters Projects*. Paper 1539616874.

<https://dx.doi.org/doi:10.25773/v5-2jj9-2t97>

This Dissertation is brought to you for free and open access by the Theses, Dissertations, & Master Projects at W&M ScholarWorks. It has been accepted for inclusion in Dissertations, Theses, and Masters Projects by an authorized administrator of W&M ScholarWorks. For more information, please contact [scholarworks@wm.edu](mailto:scholarworks@wm.edu).

**Developing an Unstructured Grid, Coupled Storm Surge, Wind Wave and Inundation  
Model for Super-regional Applications**

---

**A Dissertation**

**Presented to**

**The Faculty of the School of Marine Science**

**The College of William and Mary in Virginia**

**In Partial Fulfillment**

**Of the Requirements for the Degree of**

**Doctor of Philosophy**

---

**by**

**Yi-Cheng Teng**


**2012**

APPROVAL SHEET

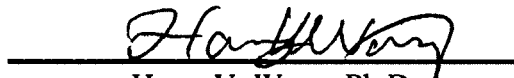
This dissertation is submitted in partial fulfillment of

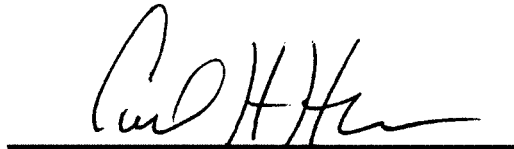
the requirements for the degree of

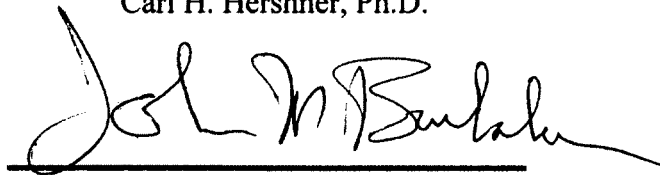
Doctor of Philosophy

  
Yi Cheng Teng

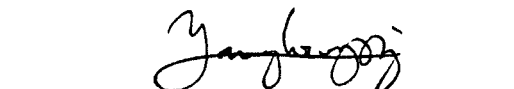
Approved, by the Committee, 2012

  
Harry V. Wang, Ph.D.  
Committee Chairman/Advisor

  
Carl H. Hershner, Ph.D.

  
John M Brubaker, Ph.D.

  
Jian Shen, Ph.D.

  
Yinglong Joseph Zhang, Ph.D.

Oregon Health & Science University, Beaverton, Oregon

## TABLE OF CONTENTS

TABLE OF CONTENTS .....	iii
ACKNOWLEDGMENTS.....	vi
LIST OF TABLES .....	vii
LIST OF FIGURES.....	ix
ABSTRACT .....	XX
CHAPTER I. Introduction.....	2
1.1 Background and significance .....	2
1.2 Objectives.....	10
CHAPTER II. Development of fully coupled 3D wave-current interaction model on unstructured grid.....	14
2.1 Introduction .....	14
2.2 Hydrodynamic (current) model .....	19
2.2.1 Basic equations.....	19
2.2.2 Initial and boundary conditions .....	22
2.2.3 Turbulence closure model .....	24
2.2.4 Wetting and drying algorithm.....	26
2.2.5 Coriolis force and tidal potential .....	27
2.2.6 Numerical algorithm and new features of SELFE.....	28
2.3 Spectral wave model (WWM II).....	33
2.3.1 Governing equations and numerical approach .....	33
2.3.2 Physical formulation.....	37
2.4 Modeling wave-current interaction .....	39
2.4.1 Wave-induced radiation stress.....	39
2.4.2 Wave-enhanced surface stress .....	42
2.4.3 Wave-enhanced bottom stress .....	43
2.5 Model coupling procedure.....	46
2.6 Conclusions .....	46

CHAPTER III. Model calibration .....	53
3.1 Introduction .....	53
3.2 Model verification – analytical solutions and laboratory experiments.....	54
3.2.1 Current induced shoaling and refraction on wave .....	54
3.2.2 Analytical solution for the wave set-up.....	55
3.2.3 Wave set-up and wave-breaking of Boers (1996) .....	58
3.2.4 HISWA experiment of Dingemans (L51 test, 1987).....	60
3.2.5 The wave blocking experiment of Lai et al. (1989).....	62
3.3 Model verification – field events.....	64
3.3.1 Hurricane Isabel (2003) in the Chesapeake Bay .....	64
3.3.2 Hurricane Ivan (2004) in the Gulf of Mexico.....	71
3.4 Efficiency of the coupled model.....	74
3.5 Conclusions .....	76
CHAPTER IV. The effect of bottom boundary layer dynamics on the forerunner simulation during 2008 Hurricane Ike in the Gulf of Mexico.....	122
4.1 Introduction .....	122
4.2 Model description.....	130
4.2.1 Sediment transport model.....	130
4.2.2 Bottom stress calculations for sediment transport .....	132
4.2.3 Modified bottom boundary conditions for sediment stratification .....	135
4.2.4 Modified surface boundary conditions for wave-enhanced wind stress.....	137
4.3 Validation and setup of coupled wave, current, and sediment-transport-BBL model.....	138
4.3.1 Model domain and grid .....	138
4.3.2 Circulation model validation – 3D Ekman motion.....	139
4.3.3 Tidal validation during Hurricane Ike in the Gulf of Mexico .....	144
4.3.4 Atmospheric and wave forcing.....	147
4.3.5 Wave model validation.....	148
4.3.6 Sediment-transport model validation –steady uniform open-channel flow.....	148
4.3.7 Sediment model parameters used for the Hurricane Ike case.....	149
4.3.8 Experimental setup .....	150
4.4 Results and discussion.....	152

4.4.1 Experiment 1: storm tide simulation (base case).....	152
4.4.2 Experiment 2: effects of wave-current interaction on storm surge simulation.....	154
4.4.3 Experiments 3 and 4: effects of sediment-induced stratification on the forerunner.....	156
4.5 Practical approach .....	164
4.6 Conclusions .....	168
CHAPTER V. The effects of wave-current interactions on coastal flooding in Scituate Harbor during the April 2007 Nor'easter .....	221
5.1 Introduction .....	221
5.2 Extratropical storm in the Gulf of Maine-April 2007 Nor'easter.....	222
5.3 Model setup and experiments.....	223
5.3.1 Model setup .....	223
5.3.2 Numerical experiments.....	225
5.4 Validations and results of experiments.....	225
5.4.1 Tidal validation in Scituate domain.....	225
5.4.2 Wave model validation in the Gulf of Maine .....	226
5.5 The wave-current interaction and its effect on inundation .....	227
5.5.1 The wind wave effect on coastal currents .....	228
5.5.2 The wind wave effect on transport through the Harbor mouth .....	229
5.5.3 The wind wave effect on coastal inundation .....	229
5.5.4 Mechanism analysis.....	230
5.6 Conclusions .....	232
CHAPTER VI. Summary and Conclusion .....	261
APPENDICES.....	266
Appendix A Definition of statistical measures for error analysis.....	266
Appendix B Definition of wave characteristics used for model-data comparison .....	267
LITERATURE CITED.....	269
VITA .....	300

## ACKNOWLEDGMENTS

I would like to thank to all those who helped me in the completion of my PhD work. I shall especially express my sincere gratitude to my advisor, Dr. Harry V. Wang, for his continuous support for my dissertation project. He is always strict, but patient; precise, but amiable; enthusiastic, and wise. He guided me into the area of physical oceanography, and taught and showed me how to do sound science. I could not have imagined having a better mentor at the starting point of my career.

Besides my advisor, I would like to thank the rest of my committee members: Dr. Carl H. Hershner, Dr. John M. Brubaker, Dr. Jian Shen, and Dr. Yinglong Zhang, for their encouragement, insightful and instructive comments, and most importantly, their patience to a student who is always catching up with the deadlines. Moreover, I would like to thank Dr. A. Roland, Dr. Yanqui Meng, and Mr. Mac Sisson for their tremendous help during this study. I also would like to thank Dr. Jim Perry, the official moderator for both my qualification exam as well as the final defense.

I also could not finish my dissertation without the kind help from each member in the Three-Dimensional Numerical Modeling Group.

I shall thank to all my friends at VIMS, especially Amy, Daniel and all of my fellow Chinese friends. I felt extremely lucky be around such a group of kind-hearted people my first stop to US.

Finally I should thank to my parents for their tolerance and forever supporting, to my wife, Xiao, for her understanding and encouragement.

## LIST OF TABLES

Table 3-1 Station information and availability of observations during Hurricane Isabel used in this study. ....	77
Table 3-2 Principal tidal constituents with periods (hours), tidal potential constants (m), and associated effective earth elasticity factors. ....	78
Table 3-3 Comparison of observed and predicted mean tidal amplitudes at 11 selected tidal gauge stations. ....	79
Table 3-4 Comparison of observed and predicted mean tidal phases at 11 tidal gauge stations. ....	80
Table 3-5 Locations of NOAA stations around Gulf of Mexico used in the Hurricane Ivan case and the statistical analysis for the comparisons between modeled and NOAA predicted tide. ....	81
Table 3-6 Locations of NOAA stations along East Coast used in the Hurricane Ivan case and the statistical analysis for the comparisons between modeled and NOAA predicted tide. ....	82
Table 3-7 Results of Timing tests for the model efficiency of three models: ADCIRC, FVCOM, and SELFE. ....	83
Table 4-1 Statistic Comparisons of tidal amplitudes (in meters) and phases (in degrees) derived from harmonic analysis of simulated and NOAA predicted tidal levels (groups of stations based on different States). ....	171
Table 4-2 Model parameters for sediment transport model validation – open channel flow case. ....	172
Table 4-3 Model parameters for sediment transport model for storm surge cases. ...	173



Table 4-4 Setup of numerical experiments. ....	174
Table 4-5 Mean of depth-averaged velocity in the inner-LATEX shelf and results of ideal Ekman set-up based on Eq. (4.1) from each numerical experiment. ....	175
Table 5-1 Scituate tide amplitude comparison (5/1/2010 to 5/31/2010). ....	233
Table 5-2 The comparison of flooding areas inside Scituate at 04:00 UTC 4/18/2007. ....	234

## LIST OF FIGURES

- Figure 2-1 The wetting and drying scheme in SELFE. (a) Initial wet/dry interface at step  $n$ ; (b) evaluate wet/dry status for interfacial nodes based on new elevation at step  $n + 1$ ; (c) update the wet/dry interface, and iterate between (b) and (c); (d) final extrapolation of elevations along the final interface (or “coastline”). Note that this figure is re-plotted from Zhang and Baptista (2008b). ..... 48
- Figure 2-2 Example of horizontal triangular grid used in SELFE model. Note that this figure is re-generated from Cho (2009). ..... 49
- Figure 2-3 A vertical grid of hybrid coordinate system used in SELFE. (a) a schematic view; (b) vertical view; (c) a unit of computational triangular prism with uneven bottom and top surfaces. Note that this figure is re-plotted from Zhang and Baptista (2008a). ..... 51
- Figure 2-4 A schematic view of domain decomposition used in SELFE. Each color (number) presents each sub-domain on different computing node. Each sub-domain is augmented with 1 layer of ghost elements (gray regions) where exchange the information between different sub-domains. .... 52
- Figure 3-1 Schematic of the surface wave propagation in a domain with ambient water current. (a) Following current case; (b) opposing current case; and (c) slanting current case. .... 85
- Figure 3-2 Comparisons of SELFE-WWM II with the analytical results for (a) following current field; (b) opposing current field; (c) slanting current field (significant wave height); and (d) slanting current field (wave direction). ..... 87

Figure 3-3 Sketch of sloping beach used in the Longuet-Higgins and Stewart wave set-up test. ....	87
Figure 3-4 Top view of the grid domain used in the Longuet-Higgins and Stewart wave set-up test. ....	88
Figure 3-5 Convergence to steady state for elevation at $x=0.38\text{m}$ ( $h=0.038\text{m}$ ).....	89
Figure 3-6 Comparison of analytical (dotted line) and numerical solutions (red solid line) for (a) wave-induced set-up and (b) significant wave height. ....	90
Figure 3-7 Sketch of Boers (1996) laboratory set-up. ....	91
Figure 3-8 Wave boundary conditions for Boers (1996) laboratory set-up. ....	92
Figure 3-9 Convergence to a steady state for elevation for the test of Boers (1996) laboratory set-up: Case A at $x=28.6\text{ m}$ . ....	93
Figure 3-10 Comparison of wave heights, zero down crossing periods (average period), and wave-induced set-up for the three investigated cases between lab data (dots) and model results (dashed lines) under steady state conditions. ....	94
Figure 3-11 (a) Topography of HISWA Experiment of Dingemans (L51 test); (b) Top view of the grid domain used in L51 test. ....	96
Figure 3-12 Comparison of wave-induced surface currents from (a) laboratory data; (b) model results; (c) absolute errors ((b)-(a)). ....	99
Figure 3-13 (a) Comparison of $H_s$ at 26 stations between the laboratory data (red dot) and model results (blue circles); the scale is shown at the upper right corner, and the dotted line is 0.4 m isobaths; (b) absolute errors (model-data). ....	100
Figure 3-14 Along-channel profiles of the Lai et al. (1989) experiment (a) current velocity, (b) water level, and (c) bathymetry. The station locations P-1 to P-6 are marked with a star from left to right increasing station number. ....	101
Figure 3-15 Convergence history of elevation along the 5 measurement locations (see Fig. 3-14). ....	102

Figure 3-16 Measured (dashed) and computed wave spectra (solid) at the given locations (see Fig. 3-14) in a logarithmic scale. ....	103
Figure 3-17 Track of Hurricane Isabel (from <a href="http://www.erh.noaa.gov">www.erh.noaa.gov</a> ). ....	104
Figure 3-18 (a) Bathymetry in the whole computational domain, and (b) zoom-in of the Chesapeake Bay area with the computational mesh. ....	106
Figure 3-19 (a) Locations of the wave buoys, and (b) tidal gauges inside the Chesapeake Bay area. ....	107
Figure 3-20 Comparison between modeled and measured wind at Chesapeake Bay Light buoy (CHLV2, Fig. 3-19). ....	108
Figure 3-21 Comparison of (a) Hs; (b) Tp; and (c) Tm02, between modeled results (solid lines) and buoy observation (circles). ....	110
Figure 3-22 Comparison of elevations predicted from 2D mode with/without waves. Close-ups near the surge peaks can also be seen in Fig. 3-23. Note that the observation has a gap near the maximum surge peak at Station Windmill Pt...	111
Figure 3-23 Comparison of elevations predicted from 2D and 3D modes with/without waves effects. ....	112
Figure 3-24 Best track for Hurricane Ivan, 2-24 September 2004 (from Stewart, 2005, Tropical Cyclone Report Hurricane Ivan, NHC). ....	113
Figure 3-25 Model domain and grid for Hurricane Ivan ....	114
Figure 3-26 (a) Model domain with bathymetry (m) and locations of 22 NOAA tidal gauge stations around Gulf of Mexico and (b) 10 NOAA tidal gauge stations (red under line) along East Coast we use to compare with model results. ....	116
Figure 3-27 Location of NDBC buoys in Gulf of Mexico used in the comparison..	117
Figure 3-28 Comparison of significant wave height between model (solid lines) and buoy observation (circles) for the Hurricane Ivan case. ....	118

- Figure 3-29 Comparison of peak period between model (solid lines) and buoy observation (circles) for the Hurricane Ivan case..... 119
- Figure 3-30 Comparison of storm surge between modeled results and observations at Dauphin Island during the Hurricane Ivan. .... 120
- Figure 3-31 Overview of the speed up of the coupled mode, SELFE and WWM II on the C1A/C1B high performance computer at ECMWF. .... 121
- Figure 4-1 (a) Model domain used in this study with bathymetry (m), and (b) Bathymetry of LATEX shelf, with tracks of Hurricane Ike (black curve). Black squares represent the locations of NOAA tidal stations used for the model validation. Green dot is 30 km from Station 8771510 and is used for the description of model vertical profile. .... 177
- Figure 4-2 (a) Time series of water level anomaly during Hurricane Ike at ten NOAA stations (observed water surface minus predicted tide). The black dashed line represents the date of landfall and the red dashed line represents 24 hours before landfall, and (b) Water level anomaly during Hurricane Ike along the LATEX Coast (observed water surface minus predicted tide). The black dashed line represents the date of landfall and the red dashed line represents 24 hours before landfall. .... 179
- Figure 4-3 Data assimilated wind field (a) at 12 hours before Hurricane Ike's landfall; (b) at time that Ike made landfall. The 50-m depth contour is given by the white line. .... 181
- Figure 4-4 Time series of measured (red dots) and computed water level with (black) and without (blue) Coriolis forcing at Station Galveston Pleasure Pier (8771510). .... 181

- Figure 4-5 Time series of measured (black) and computed water level with (red), without (blue) Coriolis forcing, and increased bottom friction (green) at Lawma, Gauge Y (High Island), Manchester Houston, and Gauge S (Locations are shown in map). Note that these results are presented by Kennedy et al. (2011). ..... 182
- Figure 4-6 Location map and wind and water-column conditions during the passage of a cold front along the Louisiana Coast, March 7-10, 2001. (a) Wind velocity vectors represent a 10-min average of continuous shipboard meteorological data and are plotted in the meteorological convention with vectors pointing in the direction wind is coming from; (b) SSC; (c) salinity; (d) temperature. Note that these results are presented by Kineke et al. (2006). ..... 183
- Figure 4-7 Schematics of the azimuthal wind drag, showing (left) extents of sectors in relation to direction of storm movement, and (right) wind drag coefficient variability by storm sector. (This figure was re-plotted from Dietrich et al., 2011b). ..... 184
- Figure 4-8 Ekman motion test case – Magnitude (a) and direction (b) of velocity in the first 3m. The analytical solution is shown with red line, while the model results are shown with blue lines. .... 185
- Figure 4-9 Ekman motion test case – The velocity spiral in the surface Ekman layer. The analytical solution is shown with a red line, while the model results are shown with a blue line. .... 186
- Figure 4-10 Comparison of amplitudes as measured by NOAA and predicted by SELFE. Each figure represents each tidal constituent. The over- or under-predicted results are shown by color. .... 187
- Figure 4-11 Comparison of phases as measured by NOAA and predicted by SELFE. Each figure represents each tidal constituent. The over- or under-predicted results are shown by color. .... 188

- Figure 4-12 Inter-model tidal comparison between four different unstructured-grid models with same tidal forcing and model setup. .... 189
- Figure 4-13 Locations of the NDBC buoys used for the validations of predicted wind and waves in the Gulf of Mexico during Hurricane Ike. .... 190
- Figure 4-14 Wind components (a) u directions; and (b) v directions during Hurricane Ike at 10 NDBC buoys. The measured data are shown with red lines, while the predicted results are shown with blue lines. .... 192
- Figure 4-15 Modeled wave characteristics during Hurricane Ike at 10 NDBC buoys. (a) Significant wave height (m); (b) peak wave period (sec); (c) mean wave period (sec); (d) peak wave direction (degrees). The measured data are shown with red dots, while the predicted results are shown with blue lines. .... 196
- Figure 4-16 Open channel test case -Vertical profiles of velocity, eddy diffusivity, and sediment concentration for two of turbulence closure options of analytical parabolic expression and  $k-\epsilon$ . Simulations used 21 vertical stretched levels.... 197
- Figure 4-17 Time series of modeled (Exp. 1, base case, blue line) and observed (red dots) storm tides for 10 stations in the LATEX shelf. The black dashed line represents the date of landfall and the red dashed line represents 24 hours before landfall. The unit of storm tide is in meters..... 199
- Figure 4-18 Comparisons between Exp. 2a (blue line), Exp. 2b (green line), Exp. 1 (black line) and observed (red dots) storm tides for 10 stations in the LATEX shelf. The black dashed line represents the date of landfall and the red dashed line represents 24 hours before landfall. The unit of storm tide is in meters. ... 201
- Figure 4-19 Effect of wave set-up through radiation stress on the maximum water levels (m) during Hurricane Ike. The white line indicates the 50-m isobath line. .... 202

- Figure 4-20 Effect of wave set-up through radiation stress + wave-enhanced bottom stress on the maximum water levels (m) during Hurricane Ike. The white line indicates the 50-m isobath line. .... 203
- Figure 4-21 Comparisons between Exp. 2a (blue line), Exp. 3 (green line), Exp. 1 (black line) and observed (red dots) storm tides for 10 stations in the LATEX shelf. The unit of storm tide is in meters. The black dashed line represents the date of landfall and the red dashed line represents 24 hours before landfall..... 205
- Figure 4-22 Difference between the maximum envelope of water during Ike obtained by Exp. 3 (considering the effect of sediment stratification on bottom friction) and Exp. 1 (base case) simulations..... 206
- Figure 4-23 Comparisons between Exp. 3 (blue line), Exp. 4 (green line), Exp. 1 (black line) and observed (red dots) storm tides for 10 stations in the LATEX shelf. The unit of storm tide is in meters. The black dashed line represents the date of landfall and the red dashed line represents 24 hours before landfall..... 208
- Figure 4-24 Difference between the maximum envelope of water during Ike obtained by Exp. 4 (considering the full wave-current interaction and effect of sediment stratification on bottom friction) and Exp. 1 (base case) simulations. .... 209
- Figure 4-25 Sediment vertical distribution (location is shown in Fig. 4-1b, green dot) in the water column for the period from 0000 UTC 9/12/2008 to 0000 UTC 9/14/2008 (including forerunner, primary surge, and post-runner). The sediment concentration was predicted by Exp. 3 (red dot) and Exp. 4 (blue cross), respectively. Notice that the concentration predicted by Exp. 3 is multiplied by 10 for visualization. .... 211
- Figure 4-26 (a) Time series of the flux Richardson number  $R_f$  in the water column (Eq. (4.11)), at the location 30 km from Station 8771510 (see Fig. 4-1b, green dot) during the period from 0000 UTC 9/11/2008 to 1200 UTC 9/14/2008..... 212



- Figure 4-27 (a) Time series of bottom stress due to current alone (red line) without stability function (Eq. (4.13)), combined bottom stress due to waves and current (blue line), and bottom stress due to current alone (green line) with stability function. Note that the green and red lines represent the stresses that were used in current model and the blue line represents the combined stress used in the sediment transport model; (b) Time series of wave orbital velocity at the location 30 km from Station 8771510 (see Fig. 4-1b, green dot) during the period from 0000 UTC 9/12/2008 to 0000 UTC 9/14/2008..... 213
- Figure 4-28 Profiles of eddy diffusivity for the suspended-sediment-stratified BBL (Exp. 4, red line) and for the neutrally stratified BBL (Exp. 1, black line) at the location 10 km from Station 8771510 (see Fig. 4-1b, green dot) during Ike forerunner stage (Note that this plot represents a snap-shot at 12:00 UTC, 9/12/2008)..... 214
- Figure 4-29 Time series of horizontal velocity in the water column at the location 30 km from Station 8771510 (see Fig. 4-1b, green dot) during the Ike forerunner period from 1800 UTC 9/11/2008 to 1200 UTC 9/13/2008..... 215
- Figure 4-30 Mean of depth-averaged horizontal velocity in the LATEX inner shelf during Ike forerunner period from each case..... 216
- Figure 4-31 Plots of the sediment-induced stratification (Exp. 4, during the period from 0000 UTC 9/12/2008 to 0000 UTC 9/14/2008) as represented by flux Richardson number  $R_f$  as a function of normalized orbital velocity. Black line is the best fit of the data. .... 217
- Figure 4-32 Comparisons between Exp. 4 (blue line), practical approach (green line), Exp. 1 (black line) and observed (red dots) storm tides for 5 stations along the LATEX shelf. The unit of storm tide is in meters. The black dashed line indicates the date of landfall and the red dashed line indicates 24 hours before landfall. 218

- Figure 4-33 Schematic of the two stages of the storm surge induced by Ike: (a) in the first stage, the forerunner surge was generated by the combination of Ekman set-up and BBL dynamics; (b) at the primary surge stage, the surge was mainly driven by the onshore directed winds (local wind effects)..... 219
- Figure 4-34 Sea surface temperature (SST) during Hurricane Ike: (a) 7 hours before landfall; (b) 17 hours after landfall; (c) 41 hours after landfall. These plots were generated by Bhagat (2009) using GOES-SST data..... 220
- Figure 5-1 (a) Locations of GoMOOS buoys (red point) in Gulf of Maine. (b) Observed wave heights from GoMOOS buoys at the (1) GoMOOS A01 - Massachusetts Bay and (2) GoMOOS B01 - Western Maine Shelf, for the period of the 2007 Patriot's Day Nor'easter. .... 235
- Figure 5-2 The test site for this study: Scituate, Massachusetts. .... 236
- Figure 5-3 Schematic diagram showing the components for Northeast Coastal Ocean Forecast System (NECOFS). More details can be found in [http://fvcom.smast.umassd.edu/research\\_projects/NECOFS/index.html](http://fvcom.smast.umassd.edu/research_projects/NECOFS/index.html). This figure was provided by UMass Dartmouth/WHOI group in SURA testbed (group members include R. Beardsley in WHOI, and C. Chen, Q. Xu, J. Qi, and H. Lin in UMass-Dartmouth)..... 237
- Figure 5-4 (a) Nested, Scituate inundation grid (left) and the GoM regional FVCOM grid (right). The larger area model is used to drive the high-resolution Scituate inundation model in SURA test bed project (Figures are from SURA Semi-Annual Progress report of Super-Regional Modeling testbed); (b) zoom in to the high-resolution Scituate inundation grid. .... 238
- Figure 5-5 Time series of wind speed (WS), wind direction (WD), wave height (WH), dominant wave period (WP), surface, surface air pressure (BP, and air (blue) and

water (red) temperature for the period April 10-21, 2007 (data are recorded on the NDBC buoy 44013, location can be found in Fig. 5-7).....	239
Figure 5-6 Locations chosen for model data comparison (Station F) and inter-model comparison (Station A, B, C, D, E, G, H, and I) inside Scituate Harbor during April Nor'easter 2007. Time sequence of volumetric transport ( $m^3 s^{-1}$ ) at three transects (red solid line) is calculated to study the effects of wave-current interaction on inundation. ....	240
Figure 5-7 Locations of the NDBC buoys used for the validations of predicted wave in the Gulf of Maine during April Nor'easter 2007.....	241
Figure 5-8 Modeled wave characteristics during April Nor'easter at 22 NDBC buoys. (a) Significant wave height (m); (b) peak wave period (sec); (c) mean wave period (sec); (d) peak wave direction. ....	245
Figure 5-9 Time series of surface water level and depth-averaged velocity at nine locations inside Scituate Harbor (Fig. 5-6). Red color and blue color represent simulated results without wind wave effect from SELFE and FVCOM, respectively.....	250
Figure 5-10 Time series of surface water level and depth-averaged velocity at nine locations inside Scituate Harbor (Fig. 5-6). Red color and blue color represent simulated results with wind wave effect from SELFE and FVCOM, respectively. ....	255
Figure 5-11 Computed water level and depth-averaged current field (left: without wave effect; right: with wave effect) at 04:00 UTC 4/18/2007.....	256
Figure 5-12 Time series of water transport at transect A, B, and C (Fig. 5-6). Red line and blue line represent calculated results without and with the wind wave effect, respectively.....	257

- Figure 5-13 Computed water level (a) without wave effect, and (b) with wave effect on 04:00 UTC 4/18/2007. Black and blue circles represent the inundated areas that are influenced by wave-current interaction. .... 258
- Figure 5-14 Simulated flooding areas inside Scituate Harbor (with and without the wind wave effect) on 04:00 UTC 4/18/2007. The blue shade represents the flooding areas and the red shade represents the drying areas..... 259
- Figure 5-15 The difference of flooding areas between with wave and without wave effects on 04:00 UTC 4/18/2007. The blue shade represents the areas that are flooded in both cases; the red shade represents the drying areas in both cases; the black shade represents increased flooding and gray shade represents reduced flooding due to the wave effects..... 260

## ABSTRACT

During extreme weather conditions such as hurricanes and nor'easters, both the currents and wind waves generated by the atmospheric forces are important. Although they may act and dominate on different temporal and spatial scales, their interactions and combined effects are without doubt significant. In this dissertation, a major effort has been made to couple an unstructured grid circulation model SELFE (semi-implicit, Eulerian-Lagrangian finite element model) and the WWM II (Wind Wave model II). Moreover, this new coupled model system can be executed in a parallel computational environment. After the coupled model was successfully built, the model was verified with ideal test cases, either through comparisons with analytic solutions or with laboratory experiments. It was further validated by field-measured data during two hurricane events.

The SELFE-WWM II model framework described above was used to participate in a SURA testbed project that was recently funded by the NOAA IOOS program. The purpose was to improve the storm surge and inundation modeling skill throughout the Gulf of Mexico as well as along the U.S. East Coast. The coupled tide, surge, and wind wave models in two and three dimensions were tested and compared systematically. Two well-known cases were investigated in detail. One was the event of Hurricane Ike of 2008 in the Gulf of Mexico and the other was the April Nor'easter of 2007 in the Gulf of Maine.

For the Gulf of Mexico study, the key scientific issue is the origin of the forerunner. It has long been recognized that the forerunner plays an important role in generating large hurricane-induced storm surge in the Gulf of Mexico. The forerunner is a phenomenon whereby water level throughout the vast coastal region was elevated days before the hurricane makes landfall. The forerunner can contribute significantly to the total water level that results subsequently during the primary surge when the hurricane makes landfall. The 2008 Hurricane Ike, which devastated the Galveston Bay along the Texas Coast, is a good example: 1.4 m out of 4.5 m maximum surge was contributed by the forerunner in the Gulf of Mexico. The consensus from initial results of multiple models indicates that the forerunner occurred as a result of Ekman set-up along the broad Louisiana-Texas (LATEX) shelf by the shore-parallel wind field. By contrast, the primary surge was dominated by the low pressure and the maximum wind along a path perpendicular to the shore as the

hurricane made landfall. It was found that the cross-shore Ekman set-up is highly sensitive to the bottom boundary layer (BBL) dynamics, especially to the drag coefficient. Given the fact that the Gulf of Mexico is known to be rich in fluid mud, and near-bed flows generally are very weak under fair-weather conditions, one plausible hypothesis is that, during the stormy condition, the suspended sediment-induced density stratification is likely to be ubiquitously present at the bottom boundary layer. A sediment-transport model and wave-current bottom boundary layer sub-model including the sediment-induced stratification effect were coupled to the unstructured grid circulation and wind wave model (SELFE-WWM II) for simulating the forerunner during Hurricane Ike. The model results demonstrate that the bottom boundary layer dynamics have a significant effect on the velocity veering as well as the Ekman set-up across the shelf.

In the Gulf of Maine study, the high-resolution coupled SELFE-WWM II model was applied in the Scituate Harbor, a small, shallow coastal embayment, south of Boston. The key issue for the study was the recurring inundation related to the role played by wind waves during nor'easter events. With limited observation data in the Scituate, the model result from SELFE was compared with that from FVCOM. The major findings are summarized as follows: (1) wind waves generated by the nor'easter can profoundly affect the coastal current by increasing the magnitude and altering its direction, (2) while the mean water level inside the Harbor stays the same, the total transport across the harbor mouth increases when wind waves are included, and (3) the total inundation area, primarily in the northern and southern basins within the Harbor, does increase when wind waves are included. There is a question as to why the inclusion of the wind waves did not cause the mean water level to change inside the Harbor while the inundation area was increased. The plausible explanation is that this lack of impact could be that the Stokes transport was small and the increase of water level by the wave set-up was compensated by the expansion of the inundation area in the shallow region.

**Keywords:** Gulf of Mexico, Bottom boundary layer, Forerunner, Sediment-induced stratification, Geostrophic-controlled surge, Wave-current interaction, Unstructured grids, SELFE, WWM II

**Developing an Unstructured Grid, Coupled Storm Surge, Wind Wave and Inundation  
Model for Super-regional Applications**

## CHAPTER I. Introduction

### 1.1 Background and significance

Storm surge is defined as an abnormal rise of sea level accompanying tropical or extratropical storms, and whose height is the difference between observed sea level and the level that would have occurred in the absence of the storms (National Hurricane Center, NWS, 2009). The five distinct processes that can alter the water level in tidal water regions are: (a) the pressure effect, (b) the wind effect, (c) the Coriolis force effect, (d) the effect from waves, and (e) the effect by rainfall (Harris, 1963).

An extratropical storm (mid-latitude storm) such as a nor'easter is a type of macro-scale storm that moves along the East Coast of the United States and the Atlantic Canada. It differs from a tropical cyclone in that a nor'easter is a cold-core low-pressure system that forms in the middle latitudes and thrives on cold air, while a tropical storm is a warm-core low pressure system developed in the tropics. Nor'easters may occur at any time of the year but are mostly known for their formations in the spring and winter seasons. These extratropical storms usually develop between Georgia and New Jersey within 100 miles of the coastline, and are drawn across to the northeast by the jet stream. They usually strengthen while moving to the north, and reach peak intensities while off the Canadian Coast, with the



strength sometimes equaling that of tropical storms. During a typical nor'easter, the temperature usually falls significantly, indicating the presence of cold air. High wind gusts and heavy precipitation are also associated with a nor'easter, which can cause severe floods to the coastal areas (Gao, 2011). The 2007 Patriot's Day Nor'easter and 2009 Mid-Atlantic Nor'easter are good examples of extratropical storms that caused dramatic storm surge and coastal inundation to the Gulf of Maine areas and the Chesapeake Bay coastal areas, respectively.

In contrast, tropical storms (hurricanes or typhoons) are smaller and more intense than extratropical storms (mid-latitude storms) and more difficult to predict in atmospheric models since they require very high resolution (Emanuel et al., 2008). Their impact within coastal regions can be more devastating, especially if they make landfall in areas with high population density. High tides, coastal surges driven by atmospheric pressures and winds, and wave set-up induced by wave-breaking can all contribute to their destructive power and cause severe coastal flooding.

The coastal inundation caused by storm surge along the U.S. Atlantic and Gulf Coasts has been a great threat to residents' properties, communities' infrastructures, and human life, as well as to the coastal ecosystem. For example, in the States, the City of New Orleans is still recovering from Hurricane Katrina that occurred in 2005. It was the sixth strongest Atlantic hurricane in history and the third strongest on record to make landfall in the States. The most severe loss of life and damage of properties occurred in New Orleans, Louisiana, which was flooded as the levee system catastrophically failed several hours after the storm had moved inland (United

States Congress, 2006). Another example was during the 2008 Atlantic hurricane season, when a hundred people were killed by four consecutive tropical cyclones (Fay, Gustav, Hanna, and Ike) in August and September. The 2008 season was very destructive, with over 50 billion U.S. dollars in damage, mostly during Hurricane Ike, which was the most destructive storm in 2008. This hurricane made landfall near Galveston, Texas, at a Category 2 intensity and caused a particularly devastating storm surge due to its size and path.

In order to reduce the loss of human life and the damage to properties caused by storm surge associated with coastal inundation in the near-shore area, many numerical models have been developed to give an early warning of storm surge and inundation in different areas (Blumberg and Mellor, 1987; Flather et al., 1991; Luettich et al., 2002; Jelesnianski et al., 1992; Westerink et al., 1994; Zhang et al., 2008a). For example, the Sea, Lake, and Overland Surge from Hurricane (SLOSH) model developed by the National Oceanic and Atmospheric Administration (NOAA) (Jelesnianski et al., 1992) partitions the U.S. East Coast and Gulf Coast into more than 30 overlapping basins (Glahn et al., 2009). Additionally, in order for a structured grid model such as SLOSH to cover a large area and maintain the fine resolution near the coast without losing computational efficiency, a polar, elliptical, or hyperbolic grid with gradually varying cell size is usually chosen to represent the model domain. This allows the model grid to cover a basin extending from the inland areas possibly flooded by storm surge to the deep water 200 km to 250 km offshore. Due to the shape of the grid cell, the structured grid model is often inadequate to represent

complex shoreline geometry and the ship channel in the waterway. Moreover, the inflexibility of the grid size further limits its capability to cover a sufficiently large domain to account for the remote effect (Blain et al., 1994; Shen and Gong, 2009).

To properly resolve the complex geometry that results from artificial structures along the shorelines, ADCIRC, the second - generation storm surge model, was built by using a continuous Galerkin finite element numerical scheme and a generalized wave continuity equation (GWCE) to render a smooth, noise-free, dampened solution. It uses the unstructured grid to resolve the complex coastline and the bathymetry of shallow water, and employs a large domain with an offshore boundary 1800 km in length and extending to longitude 60 degrees W, covering the entire U.S. East Coast and the Gulf of Mexico. Overcoming some of the shortcomings of SLOSH, ADCIRC was able to attain some success on large scale tide, storm surge, and inundation simulation (Blain et al., 1994; Westerink et al., 1994).

Another considerable issue of storm surge simulation is the uncertainty in forecasting wind and pressure fields driving storm surge models (Zhong et al., 2010). On the temporal scale, the longer the forecast period is, the larger the uncertainty for the predicted wind. On the spatial scale, all coastal areas that are influenced by the storm need to be covered in the surge model grid. A fine-resolution atmospheric model grid covering the entire East Coast and Gulf Coast is ideal. However, it is not feasible to run the model over a large domain with a fine-resolution grid covering the entire U.S. East Coast and Gulf Coast due to the limitation of computation power required to solve the numerical algorithms. Thus, an ensemble approach using

products from several different atmospheric models and mixed spatial resolutions (i.e. a coarse grid in the open ocean and fine resolution along the coast) is optimal (Xu et al., 2010).

In recent years, due partly to Hurricane Katrina's damage in New Orleans, and partly to the potential increase in the strength and frequency of hurricane and sea level rise associated with climate change, there has been a renewed interest for further improving accuracy, robustness, and reliability of the storm surge and inundation models. This interest will need to be accompanied with a better understanding of the physical processes and advances in operational capability for real-time prediction (Valle-Levinson et al., 2002; Wang et al., 2005; Bernier and Thompson, 2006; Li et al., 2006; Kohut et al., 2006; Weisberg and Zheng, 2006, 2008; Shen et al., 2006a, 2006b, 2009; Gong et al., 2007, 2009; Xie et al., 2008; Shen, 2009; Shen and Gong, 2009; Dietrich et al., 2010; Rego and Li, 2010a, 2010b; Xu et al., 2010; Bertin et al., 2012; Kennedy et al., 2011).

In terms of the total water level, a broad energy spectrum exists in oceans, with wave periods ranging from seconds to months. Short waves, such as wind-driven waves and swell, have periods that range from 0.5-25s. Longer waves, such as seiches, tsunamis, storm surges, and tides, have periods that range from minutes to months. These short and long waves are well-separated in the energy spectrum and have well-defined spatial scales. These separations lead to distinct modeling approaches, depending on whether the associated scales can be resolved. For the oceanic scale, short wave models cannot resolve spatially or temporally the individual

wind-driven waves, and thus they treat the wave field as an energy spectrum and apply the conservation of wave action density to account for wave-current interactions. Although wind-driven waves and circulation are separated in the spectrum, they can interact (Peregrine and Jonsson, 1983). For example, waves may affect the generation of surges by affecting sea surface roughness. Janssen (1989, 1991) introduced the concept of wave stress in which wave age affects the sea surface roughness and implemented it in the WAM model (The Wamdi Group, 1988). It should be pointed out here that, although the wind stress can be modeled empirically very successfully through wind speed and wave age, the actual process of transfer of momentum and energy from the atmosphere to the sea via wind waves is still not fully understood (Janssen, 2004). Wave action can also enhance the bottom friction experienced by currents in shallow water regions as discussed, e.g. Grant and Madsen (1979). Water level (including tide and surge) and currents affect the propagation of waves and the location of wave-breaking zones. Conversely, the effect of rapidly oscillating surface wind waves on currents is manifested through the provision of additional momentum and mass flux to the mean flows. It is usually accommodated by averaging the rapid oscillations over longer time scales and provides a mechanism for the inclusion of the so-called wave effect on current (WEC). The terms corresponding to WEC in the mean flow equations can be represented as the gradient of radiation stress (Longuet-Higgins and Stewart, 1964) or as vortex force (VF, Craik and Leibovich, 1976). The radiation stress is defined as the flux of momentum due to surface gravity waves. Wave transformation generates radiation stress gradients that

drive set-up and currents. However, the VF representation splits the wave-averaged effects into gradients of a Bernoulli head and a vortex force. The Bernoulli head is an adjustment of pressure in accommodating incompressibility (Lane et al., 2007), while, after wave averaging, the vortex force is a function of wave-induced Stokes drift and flow vorticity. Wind-driven waves affect the vertical mixing and bottom friction that, in turn, affect the circulation. Also high-wave events have combined with massive flooding (e.g., New Orleans during Hurricane Katrina in 2005) and have warranted attention in recent years. Thus, in many coastal applications, waves and circulation processes should be coupled (Funakoshi et al., 2008; Bunya et al., 2010; Dietrich et al., 2010).

The coupling of wave and circulation models has been implemented typically with heterogeneous meshes (Bunya et al., 2010). A coupling application may have one unstructured circulation grid and several structured wave meshes, and the models may pass information via external files. This so-called “loose” coupling is disadvantageous because it requires intra-model interpolation at the boundaries of the nested, structured wave grids and inter-model interpolation between the wave and circulation grids. Recently, a new generation of wind wave model (WWM) was developed, which solves the Wave Action Equation on spatially unstructured grids (Hsu et al., 2005; Roland, 2009). This unstructured wind-wave model allows direct coupling with the circulation model. The original version of the WWM (Hsu et al., 2005) utilizes the Crank-Nicolson scheme, and for the solution of the WAE (wave action equation) in geographical space, the CNTG (Crank-Nicolson Taylor-Galerkin)

FEM (Finite Element Method) has been implemented into the WWM. The above-mentioned schemes are non-monotone and result in oscillations when strong gradients in the solution are present. In order to remedy this behavior, alternative numerical schemes have been implemented into the WWM II. Since the WWM II employs a Residual Distribution method for the discretization of the model area (unstructured mesh), resolution can be enhanced near-shore and relaxed in deep water, allowing the model to simulate the wave evolution efficiently (Roland et al., 2012).

Given that the U.S. East Coast and Gulf Coast are regions that are constantly under threat by tropical and extratropical storms, it is highly desirable to develop a super-regional storm surge and wind wave model that is robust, reliable, and accurate and that can be coupled operationally with ensemble atmospheric forcing for coastal inundation prediction. There are several models, such as ADCIRC+SWAN or FVCOM+SWAVE, that are being developed to reach these goals. However, the operability and scalability are still the key issues. My dissertation will be focusing on cooperating with faculty members between VIMS and the Center for Coastal Margin Observational and Prediction, Oregon Health and Science University, in developing a computationally efficient numerical model named Eulerian-Lagrangian Circulation (ELCIRC, Zhang et al., 2004) and semi-implicit, Eulerian-Lagrangian finite element model (SELFIE, Zhang et al., 2008). ELCIRC and SELFIE have had some successes recently in casting the model domain in spherical coordinates and implementing on an MPI parallel computational platform, features that are extremely important for a large-scale super-regional model. A major effort of my dissertation will be to jointly

develop an unstructured grid storm surge model coupled with wind waves and inland inundation, and apply tests in three different regions under realistic tropical and extratropical storms. These four tests include (1) Chesapeake Bay under 2003 Hurricane Isabel, (2) Hurricane Ivan (2004) in the Gulf of Mexico, (3) Louisiana and northern Texas (LATEX) coasts under 2008 Hurricane Ike, and (4) New England under the 2007 Patriot's Day Nor'easter. Important processes of current-wave interactions such as (1) wave-induced radiation stress, (2) wave-enhanced surface stress, and (3) wave-enhanced bottom stress will also be investigated and elucidated in detail in this dissertation.

## 1.2 Objectives

The overall objective of this study is to develop an efficient, reliable, and accurate storm surge model coupled with wind waves and inland inundation, and is capable of being applied in multiple regions for tropical and extratropical storms. Tropical storm surge will be validated by the 2003 Hurricane Isabel in Chesapeake Bay and the 2004 Hurricane Ivan and the 2008 Hurricane Ike in the Gulf of Mexico; extratropical storms will be validated for the 2007 Patriot's Day Nor'easter in the Gulf of Maine. In this study, a state-of-the-art, unstructured grid, semi-implicit, Eulerian-Lagrangian, finite element model with parallel computing capability (SELFIE) will be jointly developed and applied for modeling tides, storm surge, wind wave, and the resulting inundation along the U.S. East and Gulf Coasts and for tropical and extratropical storms. The specific objectives of this study are:



1. To develop a super-regional model covering the entire U.S. East Coast and Gulf of Mexico with the computationally efficient model SELFE capable of predicting storm surge and inundation.
2. To employ wind data and simulate four cases of storm surge, including (1) the 2003 Hurricane Isabel in Chesapeake Bay, (2) the 2004 Hurricane Ivan in the Gulf of Mexico, (3) the 2008 Hurricane Ike in the Gulf of Mexico, and (4) the 2007 Patriot's Day Nor'easter in the Gulf of Maine. The model results will be compared with observation data to examine the prediction capability of our super-regional model.
3. To demonstrate the importance of the inclusion of the wave-circulation interaction by employing the integrated SELFE+WWM II model.
4. To identify the wave effects (wave-induced radiation stress, wave-enhanced surface stress, and wave-enhanced bottom stress) on storm surge by using the fully coupled mode compared with the decoupled mode.
5. To identify the influence of wave-current interaction on inland inundation.

The outline of this dissertation is as follows:

In Chapter 2, details of the coupled hydrodynamic model SELFE and the Wind Wave Model WWM II are described, including the governing equations, treatment of surface and bottom boundary conditions, parameterization of turbulence vertical mixing, wet and dry scheme, Coriolis force, tidal potential, and total source term in the wave action equation. The physical mechanics of their coupling, such as

wave-induced radiation stress, wave-enhanced surface stress, and wave-enhanced bottom stress, are also introduced.

In Chapter 3, the coupled model is then validated using two analytical and several laboratory tests, followed by two field tests of Hurricanes Isabel (2003) and Ivan (2004). In all cases, the coupled model is shown to be able to qualitatively and quantitatively capture the important physical processes for wave-current interaction at a modest cost. The parallel performance of our coupled model is also evaluated in this chapter.

The storm surge simulations of 2008 Hurricane Ike are described in Chapter 4, and results are presented and analyzed here. Before that, the coupled model is calibrated using a harmonic tide at its open boundary. Then atmospheric forces such as air pressure and winds are included for the storm surge and inundation simulations. Model surge results are compared to NOAA water level observations for storm surge evaluation, and model wave characteristics are compared with NDBC buoy records. Additionally, more effort is made to investigate the effect of sediment stratification on the bottom boundary layer as well as the forerunner surge, which caused severe coastal inundation 24 hours before landfall during Hurricane Ike in the northern Gulf of Mexico.

The modeled surge and inundation results of the 2007 Patriot's Day Nor'easter in the Gulf of Maine are presented in Chapter 5 to investigate the effects of wave-current interactions on the storm surge and coastal inundation. Specifically, we are interested in the contribution of waves to the peak storm surge as well as the

changes in the inundations and drying areas in Scituate Harbor during the 2007 Patriot's Day Nor'easter.

Chapter 6 summarizes the work being done in this study, and gives a final conclusion and discussion.

## CHAPTER II. Development of fully coupled 3D wave-current interaction model on unstructured grid

### 2.1 Introduction

The interaction of ocean waves and currents is a rapidly evolving research topic and is shown to be of importance for various applications. Examples of this are SST predictions (e.g. Janssen, 2010), suspended sediment transport in the coastal regions, where surface currents are strongly influenced by Stokes' drifts due to wave motion, and storm surge and inundation simulations, where waves can have a significant contribution to the total water levels (Warner et al., 2008; Bennis and Arduin, 2011).

The nonlinear interaction between long-period "currents" (e.g. tidal circulation) and short-period (<30 sec) "waves" plays an important role in the near-shore region (so-called surf zone), through at least the following mechanisms: (1) the wave-induced momentum flux via radiation stress, which was originally derived by Longuet-Higgins and Stewart (1962, 1964) and later expanded for 3D flows by Mellor (2003, 2005, 2008, 2011a, b) and Xia et al. (2004); the more sophisticated "vortex-force" formalism was discussed by McWilliams et al. (2004); Arduin et al. (2008); and Uchiyama et al. (2010); (2) wave-induced surface roughness, stress, and surface mixing (e.g., Janssen, 1989, 1991, 2001; Craig and Banner, 1994); (3) wave-induced bottom stress in shallow waters (Grant and Madsen, 1979, hereafter GM79;

Xie et al., 2001, Zhang et al., 2004). Other important mechanisms include the Stokes' drifts generated by the wave (Ardhuin et al., 2009; Bennis and Ardhuin, 2011). However, the interaction of wind-generated waves with the ocean currents is still a very active research area since some of the underlying processes are still not fully understood. For example, there is no consistent derivation of the wave action equation (WAE) on vertical shear currents available so far (although traces can be found in Lavrenov (2004); a full elaboration of wave growth on vertically sheared currents needs a careful derivation starting from basic principles).

The new advancements in the theoretical framework notwithstanding, the ultimate validation of the new wave-current interaction formulations needs to be carried out with a realistic and consistent numerical model at contrasting scales ranging from  $O(1\text{m})$  to  $O(1000\text{km})$  and beyond (e.g., global wave climate). Several fully coupled wave-current models have been proposed in the past decade (Xia et al., 2004; Xie et al., 2001; Warner et al., 2008; Uchiyama et al., 2010), most of which are based on structured-grid formulation due to its inherent simplicity. However, in the nearshore zone, the geometry and bathymetry are so complex and the unstructured-grid technique (Dietrich et al., 2011a) is needed to present the critical features such as levee systems along the coastal regions. The advantages of using unstructured-grid coupled models as well as the relative merit of each unstructured-grid model (ADCIRC+SWAN, FVCOM+SWAVE, and the present SELFE+WWM II, which is used in this study) are being carefully investigated in a NOAA/IOOS-sponsored

project for the U.S. East Coast and Gulf of Mexico regions (SURA/inundation project, 2011).

In this chapter we introduce a new community-driven, parallel, and innovative numerical framework that can be utilized to study the wave-current interaction processes based on unstructured meshes in geographical space. We shall only introduce the basic numerical building blocks that pave the way for future development in this field. In particular, we have coupled the wind wave model (WWM II, Roland, 2009) to the ocean circulation model SELFE (Zhang and Baptista, 2008a), accounting for the wave-induced momentum flux from waves to currents, based on the radiation stress formulations according to Longuet-Higgins and Stewart, 1964, Xia et al., 2004, and Mellor, 2003 (currently we are also working on the vortex force formalism based on Ardhuin et al., 2011), the wave boundary layer (WBL) according to Grant and Madsen, 1979, surface mixing following Craig and Banner, 1994, and the current-induced Doppler shift for waves (Komen et al., 1994).

The new model is suitable for the study of the combined wave-current action in super-regional scale applications. The current model is based on SELFE, originally proposed by Zhang and Baptista (2008a) and applied by many others (Burla et al., 2010; Bertin et al., 2009; Brovchenko et al., 2011; Bruneau et al., 2011). As a 3D hydrodynamic model with unstructured triangular grid cells in the horizontal and hybrid terrain-following S-Z coordinates in the vertical, SELFE uses an efficient semi-implicit time stepping in conjunction with an Eulerian-Lagrangian method (ELM) to treat the advection. As a result, numerical stability is strongly enhanced and

the errors from the “mode splitting” method are avoided; in fact, the only stability constraints are related to the explicit treatments of the horizontal viscosity and baroclinic pressure gradient, which are much milder than the stringent CFL condition. The default numerical scheme is 2<sup>nd</sup>-order accurate in space and time, but optional higher-order schemes have been developed as well (e.g., the dual Kriging ELM proposed by LeRoux et al., 1997). The model also has the capacity to calculate wetting and drying in a natural way, and has been rigorously benchmarked for inundation problems (Zhang and Baptista, 2008b; Zhang et al., 2011; NTHMP, 2011). As an open-source community-supported model, SELFE has been well-demonstrated to be accurate, efficient, robust, and flexible, with a wide range of applications from general circulation (Brovchenko et al., 2011), tsunami inundation (Zhang et al., 2011), storm surge (Bertin et al., 2012), ecology (Rodrigues et al., 2009), oil spill (Azevedo et al., 2009), and water quality studies (Teng et al., in prep.).

For realistic applications, phase-averaged wave models (so-called spectral wave models) have the advantage of simulating sea state in an efficient way (Komen et al., 1994). The wave model we adopt in this study is the Wind Wave Model II (WWM II), which is based on the source code by Hsu et al. (2005) but has been overhauled by Roland (2009) in nearly all aspects of numerical schemes, physics, robustness, and the efficiency to its present version. The WWM II incorporates the framework of residual distribution schemes (Abgrall, 2006) within a hybrid fractional splitting method utilizing third-order Ultimate Quickset schemes in spectral space, as also used by Tolman (1992) in the Wave Watch III (WWIII) model, and robust and

accurate integration of the source terms based on a multiple splitting technique using TVD Runge-Kutta schemes for shallow water wave-breaking and bottom friction, dynamic integration of the triad interaction source term, and semi-implicit integration of the deep water physics.

The WWM II model has previously been coupled to the SHYFEM (Shallow Water Finite Element Model, Umgiesser et al., 2004) and shown to be efficient in a variety of applications ranging from the Lagoon of Venice (Ferrarin et al., 2008), the Adriatic Sea, and the Gulf of Mexico (Roland et al., 2009). Moreover, it was successfully applied by Babanin (2011) in a multi-scale application in the South China Sea in order to investigate typhoon-induced waves in the vicinity of Taiwan.

The numerical schemes for the advection of wave action in geographic space in WWM II have also been successfully exported to the WWIII model and demonstrated to be accurate and efficient in several studies (Ardhuin et al., 2009, 2010; Ardhuin and Roland, 2012).

The work described in this chapter is a logical continuation from previous efforts, and further integrates WWM II into a current model such as SELFIE that is fully parallelized with a domain decomposition method. The wave and current models have been tightly coupled, with WWM II written as a routine inside SELFIE. In addition, the whole system has been parallelized via domain decomposition and Message Passing Interface (MPI); the two models share the same sub-domains but may use different time steps and a different integration strategy such as quasi-steady integration in the WAE in order to maximize efficiency.



At this stage of the development, the physical model for wave-current interaction is based on some relatively simple formulations of the underlying processes mentioned above. We show the capabilities as well as the limitations of this approach in different validated cases and indicate in this way the clear necessity for the implementation of a consistent theoretical framework developed in this field (Bennis and Ardhuin, 2011).

In this chapter, we present the details of each model and the coupling strategy. In Section 2.2, the descriptions of formulations for the current model, including governing equations, treatment of bottom and surface boundary conditions, turbulence closure model, wetting and drying scheme, Coriolis force, and tidal potential are presented. In Section 2.3, the details of the wind wave model, such as the governing equations and the physical formulations for source terms, are described. The details of coupling strategy are presented in Section 2.4.

## 2.2 Hydrodynamic (current) model

### 2.2.1 Basic equations

The SELFE (Semi-implicit Eulerian-Lagrangian Finite Element) model developed by Zhang and Baptista (2008a) is used to simulate the storm surge and inundation caused by hurricanes and nor'easters in this study. The model is governed by the three-dimensional shallow-water equations with the Boussinesq approximation, and transport equations for salt, heat, and tracers. The equations are

solved for free surface elevation, water velocities, salinity, and temperature of the water in a Cartesian coordinate system that has an eastward x-axis, a northward y-axis, and an upward z-axis, written as follows (Zhang and Baptista, 2008a):

$$\nabla \cdot \vec{u} + \frac{\partial w}{\partial z} = 0 \quad (2.1)$$

$$\frac{\partial \eta}{\partial t} + \nabla \cdot \int_{-h}^{\eta} \vec{u} dz = 0 \quad (2.2)$$

$$\frac{D\vec{u}}{Dt} = \vec{f} - g\nabla\eta + \alpha g\nabla\hat{\phi} - \frac{1}{\rho_0}\nabla P_A + \frac{\partial}{\partial z}\left(v\frac{\partial\vec{u}}{\partial z}\right) - \frac{g}{\rho_0}\int_z^{\eta}\nabla\rho d\zeta + \nabla \cdot (\mu\nabla\vec{u}) \quad (2.3)$$

$$\frac{DS}{Dt} = \frac{\partial}{\partial z}\left(K_h\frac{\partial S}{\partial z}\right) + precip. - eva. \quad (2.4)$$

$$\frac{DT}{Dt} = \frac{\partial}{\partial z}\left(K_h\frac{\partial T}{\partial z}\right) + \frac{\dot{Q}}{\rho_0 C_p} \quad (2.5)$$

$$\frac{\partial p}{\partial z} = -\rho_0 g \quad (2.6)$$

where

t : time [s];

x, y, z : Cartesian coordinates [m];

$\eta(x, y, t)$  : free surface elevation [m];

$\nabla$  : horizontal gradient  $\left(\frac{\partial}{\partial x}, \frac{\partial}{\partial y}\right)$  [ $m^{-1}$ ];

$\vec{u}$  : Cartesian horizontal water velocity components (u, v) [ $m s^{-1}$ ];

$w$  : vertical velocity [ $\text{m s}^{-1}$ ];

$h(x, y)$  : bathymetric depth [m];

$\mathbf{f}$  : Coriolis parameter [ $\text{s}^{-1}$ ];  $\mathbf{f} = -f\mathbf{k} \times \mathbf{u}$ ;

$g$  : acceleration of gravity [ $\text{m s}^{-2}$ ];

$\hat{\phi}$  : tidal potential [m];

$\alpha$  : effective Earth elasticity factor (0.69);

$\rho(x, y, t)$  : water density [ $\text{kg m}^{-3}$ ];

$\rho_0$  : reference water density [ $\text{kg m}^{-3}$ ];

$P_A(x, y, t)$  : atmospheric pressure at the free surface [ $\text{N m}^{-2}$ ];

$S, T$  : salinity and temperature of the water (psu, °C);

$\nu, K_h$  : vertical eddy viscosity and horizontal eddy viscosity [ $\text{m}^2 \text{s}^{-1}$ ];

$\kappa$  : vertical eddy diffusivity, for salt and heat [ $\text{m}^2 \text{s}^{-1}$ ];

$\dot{Q}$  : rate of absorption of solar radiation [ $\text{W m}^{-1}$ ];

$C_p$  : specific heat of water [ $\text{J kg}^{-1} \text{K}^{-1}$ ]

The differential equation system for Equations (2.1) to (2.5) is closed with the hydrostatic approximation (Equation (2.6)), equation of state, parameterizations for

horizontal and vertical mixing via turbulence closure equations, and appropriate initial and boundary conditions.

### 2.2.2 Initial and boundary conditions

#### Initial conditions

The governing equations presented in Section 2.2.1 require, in general, the initial condition (for elevation, velocities, salinity, and temperature) to start the model. Since only the barotropic mode is invoked for storm surge and inundation simulation, the initial condition applied is the “no motion” condition and the model is “spun up” by the tidal elevation specified at the open boundary using a ramp-up function. The ramp-up function being used is a hyperbolic tangent function and the duration is 1 day. For a super-regional scale domain, the tidal potential forcing also needs to be turned on.

#### Vertical boundary conditions

Vertical boundary conditions for the original horizontal momentum equations without wind wave effects are described in this section. At the sea surface, the internal Reynolds stress is balanced by the applied shear stress. A bulk aerodynamic algorithm developed by Zeng et al. (1998) is used to account for ocean surface fluxes under various conditions of stability of the atmosphere. The balance between the internal Reynolds stress and the parameterized surface shear stress is shown as follows:

$$\rho_0 \nu \left( \frac{\partial u}{\partial z}, \frac{\partial v}{\partial z} \right) = (\tau_{Wx}, \tau_{Wy}) = \rho_a C_{DS} |\bar{W}| (W_x, W_y) \quad \text{at } z = \eta \quad (2.7)$$

where  $\rho_a$  is the air density [ $\text{kg m}^{-3}$ ],  $|\bar{W}| = (W_x^2 + W_y^2)^{\frac{1}{2}}$ ,  $W_x$  and  $W_y$  are the horizontal components of wind velocity at 10 m above the sea surface [ $\text{m s}^{-1}$ ], and  $C_{DS}$  is the wind drag coefficient (without wind wave effects) based on the following equation (Smith, 1980; Pond and Pickard, 1998):

$$C_{DS} = 10^{-3}(0.61 + 0.063|\bar{W}|) \quad \text{if } 6 \leq |\bar{W}| \leq 50 \text{ [m s}^{-1}\text{]} \quad (2.8)$$

Eq. (2.8) shows that  $C_{DS}$  is in the form of a linear function with constant values outside the range.

Because the bottom boundary layer is usually not well-resolved in ocean models, the no-slip boundary condition at the sea bottom ( $u = v = 0$ ) is replaced by a balance between the internal Reynolds stress and the bottom frictional stress,

$$\rho_0 v \left( \frac{\partial u}{\partial z}, \frac{\partial v}{\partial z} \right)_b = (\tau_{bx}, \tau_{by}) = \rho_0 C_{Db} \sqrt{u_b^2 + v_b^2} (u_b, v_b) \quad \text{at } z = -h \quad (2.9)$$

where  $C_{Db}$  is the bottom drag coefficient without the wave effect. Typically the bottom drag coefficient varies in space and also temporal scales and, thus, site-specific calibration is often required. Instead of using a constant drag coefficient  $C_{Db}$  for the entire domain, a logarithmic law is often applied to calculate the spatially varied  $C_{Db}$  by specifying the local bottom roughness (in meters) at each node. The latter requires a rather finer discretization of the bottom in the model vertical grid to get good estimations of  $C_{Db}$ . The coefficient estimated by the logarithmic law is given as follows:

$$C_D = \left[ \frac{1}{\kappa} \ln \left( \frac{z_b}{z_0} \right) \right]^{-2} \quad (2.10)$$

where  $\kappa = 0.4$  is the von Karman constant,  $Z_b$  is the height from the bottom to the top of the bottom computational cell, and  $Z_0$  is the local bottom roughness.

### 2.2.3 Turbulence closure model

SELFE uses the Generic Length Scale (GLS) turbulence closure through the General Ocean Turbulence Model (GOTM) suggested by Umlauf and Burchard (2003; 2005), which encompasses most of the 2.5 closure schemes [ $k$ - $\epsilon$  (Rodi, 1984);  $k$ - $\omega$  (Wilcox, 1998); Mellor and Yamada, 1982]. Under this framework, the transport, production, and dissipation of the turbulence kinetic energy ( $k$ ) and of a generic length-scale variable ( $\psi$ ) are expressed by:

$$\frac{DK}{Dt} = \frac{\partial}{\partial z} \left( v_k^\psi \frac{\partial K}{\partial z} \right) + \nu M^2 + \mu N^2 - \epsilon \quad (2.11)$$

$$\frac{D\psi}{Dt} = \frac{\partial}{\partial z} \left( v_\psi \frac{\partial \psi}{\partial z} \right) + \frac{\psi}{K} (c_{\psi 1} \nu M^2 + c_{\psi 3} \mu N^2 - c_{\psi 2} F_w \epsilon) \quad (2.12)$$

where

$v_k^\psi, v_\psi$ : vertical turbulent diffusivities;

$c_{\psi 1}, c_{\psi 2}, c_{\psi 3}$ : model-specific constants (Umlauf and Burchard, 2003; Zhang et al., 2004);

$F_w$ : wall proximity function;

$M, N$ : shear and buoyancy frequencies;

$\epsilon$ : dissipation rate;

The generic length-scale is defined as:

$$\psi = (c_\mu^0)^p K^m l^n \quad (2.13)$$

where  $c_\mu^0 = \sqrt{0.3}$ ,  $l$  is the turbulence mixing length,  $p$ ,  $m$ , and  $n$  are constants and lead to the different closure models mentioned above. Therefore, vertical viscosities and diffusivities that appear in Equations (2.3) to (2.5) are related to  $K$ ,  $l$ , and stability functions and can be defined as follows:

$$\nu = \sqrt{2} s_m K^{1/2} l \quad (2.14)$$

$$k_h = \sqrt{2} s_h K^{1/2} l \quad (2.15)$$

$$\nu_k^\psi = \frac{\nu}{\sigma_k} \quad (2.16)$$

$$\nu_\psi = \frac{\nu}{\sigma_\psi} \quad (2.17)$$

where  $\sigma_k^\psi$  and  $\sigma_\psi$  are the Schmidt numbers, and stability functions,  $s_m$  and  $s_h$ , are given by an Algebraic Stress Model (Kantha and Clayson, 1994; Canuto et al., 2001; Galperin et al., 1988). At the free surface and at the bottom of oceans, the turbulent kinetic energy and the mixing length are specified as Dirichlet boundary conditions:

$$K = \frac{1}{2} B_1^{2/3} |\tau_b|^2 \quad (2.18)$$

$$l = \kappa_0 d_b \text{ or } \kappa_0 d_s \quad (2.19)$$

where  $\tau_b$  is a bottom frictional stress,  $\kappa_0$  is the von Karman constant (0.4),  $B_1$  is a constant, and  $d_b$  and  $d_s$  are the distances to the bottom and free surface, respectively.

The more detailed descriptions of the turbulence model in SELFE can be found in Zhang and Baptista (2008a).

#### 2.2.4 Wetting and drying algorithm

The inundation scheme used in SELFE is natural and relatively straightforward. At the beginning of each computing time step, the interfaces between wet and dry regions are computed. Then, at the end of this time step, each node on the interfaces is examined in order to determine if the “shorelines” need to be advanced or retreated. The interfaces are then updated and the process is repeated until new interfaces are found. The procedure for the wetting and drying scheme used in SELFE can be simplified as follows:

1. Compute wet and dry interfaces ( $\Gamma^n$ ) at time step  $n$  (Fig. 2-1a);
2. At the end of time step  $n + 1$ , go through and examine all interfacial nodes on  $\Gamma^n$ . If a node (e.g. node A) is surrounded by wet elements (with all nodes being wet-based on the newly computed elevation ( $h + \eta > h_0$ , where  $h_0$  is a small positive number used in the code in lieu of zero in order to avoid underflow)), the local interface line (or “coastline”) is advanced into the dry region, and the velocity at the center of the dry side is calculated as the average of the adjacent sides (Fig. 2-1b);
3. Update interfacial lines based on the computing results from step 2, and iterate until the final “coastlines” at the step  $n + 1$  ( $\Gamma^{n+1}$ ) are found (Fig. 2-1c);



4. Go through all nodes on  $\Gamma^{n+1}$ , and constant extrapolation of the elevations is calculated into the dry region (e.g.,  $\text{elevation}(A'') = \text{elevation}(A')$ ) if the total volume flux from the adjacent sides on the interface is into the dry region (Fig. 2-1d).

Note that step 4 is similar to the extrapolation strategy in Titov and Synolakis (1995), and is an efficient way to smooth numerical instabilities commonly found near the interfaces; otherwise the large elevation gradients near the interface would lead to unrealistically large velocity.

#### 2.2.5 Coriolis force and tidal potential

The earth rotation is represented through the Coriolis acceleration in the momentum equations. The Coriolis parameter,  $f$ , is a sine function of latitude,  $\varphi$ :

$$f(\varphi) = 2\Omega \sin\varphi \quad (2.20)$$

where  $\Omega = 7.29 \times 10^{-5} \text{ rad s}^{-1}$  is the angular velocity of the earth rotation. The  $\beta$ -plane approximation is used to minimize coordinate inconsistencies that are produced by Cartesian coordinates in a super-regional domain. Hence,

$$f = f_c + \beta(y - y_c) \quad (2.21)$$

where subscript C denotes the mid-latitude of the domain and  $\beta$  is the local derivative of the Coriolis factor  $f$ .

In order to simulate the super-regional scale tide, the tidal potential, caused by the marine tides and small periodic deformations of the entire solid body of the planet, is defined following Reid (1990):

$$\hat{\varphi}(\varphi, \lambda, t) = \sum_{n,j} C_{jn} f_{jn}(t_0) L_j(\varphi) \cos \left[ \frac{2\pi(t-t_0)}{T_{jn}} + j\lambda + v_{jn}(t_0) \right] \quad (2.22)$$

where

$C_{jn}$  : constant characterizing the amplitude of tidal constituent n of species j

(j=0, declinational; j=1, diurnal; j=2, semi-diurnal);

$t_0$  : reference time;

$f_{jn}(t_0)$  : time-dependent nodal factor;

$v_{jn}(t_0)$  : time-dependent astronomical argument

$L_j(\varphi)$  : species-specific coefficients

( $L_0 = 3\sin^2\varphi$ ;  $L_1 = \sin(2\varphi)$ ,  $L_2 = \cos^2\varphi$ );

$T_{jn}$  : period of constituent n of species j.

## 2.2.6 Numerical algorithm and new features of SELFE

### Numerical algorithm

A detailed numerical algorithm of SELFE is well-described in Zhang and Baptista (2008a). The key features of SELFE are presented as follows:

1. SELFE solves the differential equation system with finite-element and finite volume schemes by using a semi-implicit method (Casulli and Walters, 2000).
2. The advection is solved with the Eulerian-Lagrangian method (ELM) in the momentum equations.

3. SELFЕ treats the advection terms in the transport equations either with the ELM, the finite-volume upwind (FVUM), or the high-order Total Variation Diminishing (TVD) scheme.
4. Horizontally, unstructured triangular grid cells are used in SELFЕ (Fig. 2-2), the orthogonality of the horizontal grid is not necessary since finite element discretization is used. In the vertical grid, SELFЕ uses hybrid-vertical coordinates, which means partly terrain-following S-coordinates and partly Z-coordinates (Fig. 2-3a and 2-3b).

SELFЕ solves Eqs. (2.2) and (2.3) simultaneously using a semi-implicit scheme with ELM treatment of advection in Eq. (2.3). A Galerkin finite-element scheme is applied to Eqs. (2.2) and (2.3), resulting in a positive-definite, symmetric, and sparse matrix that can be solved with an efficient iterative solver such as the Jacobi Conjugate Gradient Method (Zhang and Baptista, 2008a). In SELFЕ, linear shape functions are used as weighted functions. Since SELFЕ uses linear shape functions for the elevations, the two components of the horizontal velocity are solved from the momentum equation independently from each other after the elevations are found. After the elevations are found at all nodes, SELFЕ solves the momentum Eq. (2.3) along each vertical column at side centers. The pressure gradient and the vertical viscosity terms are treated implicitly, and other terms treated explicitly. After the velocities at all sides are determined, the velocity at each node is computed by a weighted average of all surrounding sides in its ball, and evaluated by proper interpolation in the vertical. Alternatively, the velocity at a node can also be

computed within each element from the three sides using the linear shape function and is kept discontinuous between elements. Since this approach leads to parasitic oscillations, a Shapiro filter (Shapiro, 1970) needs to be used to suppress the noise. To solve the vertical velocity, a finite-volume method is applied to a typical prism, as depicted in Fig. 2-3c, because it serves as a diagnostic variable for local volume conservation especially when a steep slope is present (Zhang et al., 2004). The vertical velocity is then solved from the bottom to the surface, in conjunction with the bottom boundary condition  $(u, v, w) \cdot n = 0$ . The closure error between the calculated  $w$  at the free surface and the surface kinematic boundary condition is an indication of the local volume conservation error (Luettich et al., 2002). Because the primitive form of the continuity equation is solved in the model, this closure error is generally negligible.

### Parallelization

The efficiency of SELFE is boosted with parallelization using the MPI (Message Passing Interface) and domain decomposition (schematic picture is shown in Fig. 2-4) with the ParMETIS graph partitioning library. The detailed scalability analysis of the MPI SELFE is presented in the next chapter.

### 2D mode

The original 3D SELFE utilizes the bottom boundary layer formulation (logarithmic profile) to decouple Eqs. (2.2) and (2.3), and therefore the 3D formulation in SELFE cannot be simplified to 2D. However, decoupling is readily done in 2D using the assumption that the velocity is uniform in the vertical with only

1 layer. The discretized Eq. (2.3) with the Manning formulation for the bottom drag ( $C_d = \frac{gn_0^2}{h^{1/3}}$ , where  $n_0$  is Manning coefficient) represents a simple relation between the unknown velocity and the elevation gradient, which can be directly substituted into Eq. (2.2). The detailed formulations of the 2D model can be found in Zhang et al. (2011).

### Spherical coordinates

For super-regional scale applications, map projection will lead to unacceptable errors and spherical coordinates are ultimately required. Most of the ocean models achieve this by transforming the governing equations into the spherical coordinates (i.e., latitude and longitude). In SELFE, an alternative and more elegant approach was adapted. This kind of approach was proposed by Comblen et al. (2009), where a series of local frames are utilized at various locations of the unstructured grid (nodes/sides/elements); inside these local frames the original form of Eqs. (2.1) - (2.3) can be used without any modification, and the problem essentially boils down to a series of coordinate transformations. The advantages of such an approach include: (1) polar singularity is fully circumvented; (2) only small modifications are needed for the existing codes, and in the case of SELFE, all the useful properties of the matrix are preserved. Note that, since all distances are measured in physical space instead of the transformed latitude/longitude space, very fine-scale inundation can be conducted within this kind of framework. The spherical-coordinate configuration of SELFE has been verified by the 1964 Prince William Sound Tsunami simulations (Zhang et al., 2011). Note that, in this study, simulations for our wave-current

coupled model were conducted using spherical coordinates for most of the cases, except the small Scituate domain described in Chapter 5.

#### Non-hydrostatic mode

The default SELFE model uses the hydrostatic assumption so the flow is assumed to be essentially horizontal and vertical acceleration is small. In some applications (e.g. internal waves, short waves, and landslide tsunamis), this assumption is no longer valid.

The hydrostatic assumption can be relaxed through the so-called second-order pressure correction method (Fringer et al., 2006). The key is the decomposition of total pressure  $P$  into hydrostatic and non-hydrostatic components:

$$\frac{P}{\rho_0} = \frac{g}{\rho_0} \int_z^\eta \rho d\zeta + q \quad (2.23)$$

Where  $\rho$  is density of the water with a reference value  $\rho_0$  and  $q$  is the normalized non-hydrostatic pressure. The vertical momentum equation then becomes:

$$\frac{Dw}{Dt} = \frac{\partial}{\partial z} \left( v \frac{\partial w}{\partial z} \right) - \frac{\partial q}{\partial z} \quad (2.24)$$

where we have neglected the horizontal viscosity and other terms that are generally small.

A predictor-corrector method is used to solve the equations in hydrostatic and non-hydrostatic steps. The hydrostatic step follows a similar technique as described in Zhang and Baptista (2008a). The correction step leads to a classical Pressure Poisson Equation (PPE) to  $q$ , which is then solved with a 3D Galerkin finite-element method. Since the Laplacian operator is positive and symmetric, the resulting matrix can also

be solved efficiently using the same solver. Since we do not use the non-hydrostatic mode in this study, details for the non-hydrostatic SELFE can be found at <http://www.stccmop.org/CORIE/modeling/selfe/>.

## 2.3 Spectral wave model (WWM II)

### 2.3.1 Governing equations and numerical approach

The Wave Action Equation (hereafter WAE), describing growth, decay, advection and refraction of wind waves due to depths and currents (computed by the hydrodynamic model), can be written for Cartesian coordinates as follows (e.g. Komen et al., 1994):

$$\underbrace{\frac{\partial}{\partial t} N}_{\text{Change in Time}} + \underbrace{\nabla_{\mathbf{x}} (\dot{\mathbf{X}} N)}_{\text{Advection in horizontal space}} + \underbrace{\frac{\partial}{\partial \sigma} (\dot{\theta} N) + \frac{\partial}{\partial \theta} (\dot{\sigma} N)}_{\text{Advection in spectral space}} = \underbrace{S_{tot}}_{\text{Total Source Term}} \quad (2.25)$$

where  $N$  is the wave action density spectrum that is invariant in slowly varying media (Bretherton and Garrett, 1969), and is expressed as:

$$N_{(t, \mathbf{x}, \sigma, \theta)} = \frac{E_{(t, \mathbf{x}, \sigma, \theta)}}{\sigma} \quad (2.26)$$

with  $E$  being the variance density of the sea level elevations. The advection velocities in the different phase spaces (Eqs. (2.27) - (2.29)) are given following the Geometric Optics Approximation (e.g., Keller, 1958).

$$\dot{\mathbf{X}} = c_{\mathbf{x}} = \frac{d\mathbf{X}}{dt} = \frac{d\omega}{dk} = c_g + U_A \quad (2.27)$$

$$\dot{\theta} = c_{\theta} = \frac{1}{k} \frac{\partial \sigma}{\partial d} \frac{\partial d}{\partial m} + \mathbf{k} \cdot \frac{\partial \mathbf{U}_A}{\partial s} \quad (2.28)$$

$$\dot{\sigma} = c_{\sigma} = \frac{\partial \sigma}{\partial d} \left( \frac{\partial d}{\partial t} + \mathbf{U}_A \cdot \nabla_x d \right) - c_g \mathbf{k} \frac{\partial \mathbf{U}_A}{\partial s} \quad (2.29)$$

Here  $s$  represents the coordinate along the wave propagation direction and  $m$  represents that perpendicular to it.  $\mathbf{X}$  is the Cartesian coordinate vector ( $x, y$ ) in the geographical space,  $d$  is the water depth obtained from SELFE,  $\mathbf{k}$  is the wave number vector,  $c_g$  the group velocity and  $\nabla_x$  is the gradient operator in the geographical space. The group velocity is calculated from the linear dispersion relation. The effective advection velocity  $\mathbf{U}_{A(k)}$  depends in general on the wave number vector of each wave component (Andrews and McIntyre, 1978a, b). In the presented applications, this was approximated by the surface current. In Eq. (2.25), the terms on the left-hand side represent, respectively, the change of wave action in time, the propagation of wave action in geographical space, depth-, and current-induced refraction (with propagation velocity or turning rate  $c_{\theta}$ ), and the shifting of  $\sigma$  due to variations in mean current and depth (with propagation velocity or shifting rate  $c_{\sigma}$ ). The wave diffraction effect is introduced into the WAE through the correction of wavenumber and propagation velocities using a diffraction-corrected parameter (see Holthuijsen et al., 2003 or Liao et al., 2011). This approximation is based on the mild-slope equation or the extended mild-slope equation for the wave-refraction-diffraction. The source term  $S_{tot}$  at the right-hand side describes the net source terms defined by the energy input due to wind, the nonlinear interaction in deep and shallow



water, the energy dissipation due to whitecapping, and depth-induced wave-breaking and the energy dissipation due to bottom friction.

$S_{tot}$  is the source term including the energy input due to wind ( $S_{in}$ ), the nonlinear interaction in deep and shallow water ( $S_{nl4}$  and  $S_{nl3}$ ), the energy dissipation in deep and shallow water due to whitecapping and wave-breaking ( $S_{ds}$  and  $S_{br}$ ), and the energy dissipation due to bottom friction ( $S_{bf}$ ); the source term can be presented as:

$$\frac{DN}{Dt} = S_{total} = S_{in} + S_{nl4} + S_{ds} + S_{nl3} + S_{br} + S_{bf} \quad (2.30)$$

WWM II solves the WAE using the fractional step method as described by Yanenko (1971). The fractional step method allows the splitting of the time-dependent four-dimensional problems in well-defined parts Eqs. (2.31-2.34) for which dedicated numerical methods can be used in order to have a well-defined consistent and convergent numerical method (e.g. Tolman, 1992):

$$\frac{\partial N^*}{\partial t} + \frac{\partial}{\partial \theta}(c_\theta N^*) = 0; [N^*_{(t=0)} = N_0] \text{ on } [0, \Delta t] \quad (2.31)$$

$$\frac{\partial N^{**}}{\partial t} + \frac{\partial}{\partial \sigma}(c_\sigma N^*) = 0; [N^{**}_{(t=0)} = N^*_{(t=\Delta t)}] \text{ on } [0, \Delta t] \quad (2.32)$$

$$\frac{\partial N^{***}}{\partial t} + \frac{\partial}{\partial x}(c_x N^{**}) + \frac{\partial}{\partial y}(c_y N^{**}) = 0; [N^{***}_{(t=0)} = N^{**}_{(t=\Delta t)}] \text{ on } [0, \Delta t] \quad (2.33)$$

$$\frac{\partial N^{****}}{\partial t} = S_{(N^{**}),tot}; [N^{****}_{(t=0)} = N^{***}_{(t=\Delta t)}] \text{ on } [0, \Delta t] \quad (2.34)$$

WWM II first solves the geographical part (Eq. 2.33). As an alternative and innovative method to the well-known family of finite volume schemes or finite

element schemes, the family of Residual Distribution Schemes (RD schemes, also known as “fluctuation splitting schemes”, (e.g. Abgrall, 2006)) has been implemented in the present WWM II model.

The RD schemes are a new family of numerical schemes that borrow ideas from the finite element (FE) and the finite volume (FV) framework. As a result, compact schemes and accurate solutions that are carefully designed in order to obey most important constraints, such as the conservation property, positivity, and linear preservation (2<sup>nd</sup>-order in smooth flow) and that can be well parallelized, can be achieved. Abgrall (2006) gives a recent review on the history and future trends of fluctuation splitting schemes. The residual distribution technique was first introduced by Roe (1982) and further developed and improved by other scientists (e.g. Abgrall, Deconinck, Roe and others). In the 2<sup>nd</sup> step, the spectral advection is treated by using Ultimate Quickest scheme (Leonard, 1991) in theta- and sigma-space following the approach in WWIII (Tolman, 1992). The source terms are integrated in three separate fraction steps according to their time scales or nonlinearity. In the 1<sup>st</sup> step we integrate the dissipative terms in shallow water such as wave-breaking and bottom friction and this is done without the necessity of an action limiter using a TVD Runge-Kutta scheme of 3<sup>rd</sup> order (Gottlieb and Shu, 1998). Following this we integrate the triad interaction source terms using a dynamic approach as suggested by Tolman (1992). The reason for this procedure is that the strong influence of the limiter on the integration of the triad interaction term has been found whereas, in the dynamic approach, the limiter is applied only in the last iteration step. In the last step

we integrate the deep water source terms using the well-known semi-implicit approach by Hersbach and Janssen (1999). This approach ensures good convergence and reduces the influence of the limiter only to the deep water physics with a small influence in the integration of the triad interactions, thus increasing the consistency of the entire numerical solution. There is absolutely no limiter acting on the left-hand side of the WAE.

The implemented schemes in the wave model are accurate (e.g., less than 6% SCI in the application of WWIII; Ardhuin et al., 2012) and very efficient over global and local scales. However, for an unstructured grid, the spatial resolution near the coastlines (shallow water regions) is usually very high (e.g.  $\sim 1\text{m}$ ), an implicit scheme is more efficient, and we are in the process of parallelizing it using the domain decomposition method.

### 2.3.2 Physical formulation

Most of the source terms are formulated as semi-empirical relations, except for the Boltzmann integral, describing the nonlinear energy transfer in deep water ( $S_{nl4}$ ), which can be calculated exactly using e.g. EXACT-NL (Van Vledder, 2006) for arbitrary wave spectra. An exact calculation of the nonlinear energy transfer is for practical applications not feasible because the solution procedures are too complex. The efficient calculation of the Boltzmann integral has fascinated scientists since the derivation of the formula by Klaus Hasselmann in 1962. In 1985, Klaus Hasselmann and Susanne Hasselmann found a good approximation for the quadruplet interactions,

which is called DIA (Discrete Interaction Approximation). This approximation made it possible to introduce a nonlinear physical process into spectral wave models. The introductions of the DIA spurred the development of the so-called 3<sup>rd</sup> generation spectral wave models.

In WWM II, the wind input term,  $S_{in}$ , (see e.g. Janssen (2001) for a review) and the dissipation term, ( $S_{ds}$ ), (see e.g. Babanin (2011) for a review) in the total source term of WAE are undergoing continuous improvement and developments with the latest understanding of the underlying physical processes as well as more sophisticated measurements. Recently the wind input and dissipation functions have been further improved (Ardhuin et al., 2010) and validated on a remarkable data set in global and coastal waters (Ardhuin et al., 2010, 2012). The WWM II has basically two main parameterizations for the wind input and dissipation: the first one was used at the ECMWF (The European Centre for Medium-Range Weather Forecasts) and the details were given in Bidlot et al. (2002), and a second and more recent one was proposed by Ardhuin et al. (2010), which includes dominant wave-breaking in the dissipation term and also an alternative to treat shallow water wave-breaking ( $S_{br}$ ) with one dissipation term only (Fillipot et al., 2010). In this study, we have used the wind input and dissipation terms given by Ardhuin et al. (2010). The conservative approach for shallow water wave-breaking of Battjes and Janssen (1978) is also available in WWM II. Wave dissipation by bottom friction is modeled based on the results obtained from the JONSWAP experiment (Hasselmann et al., 1973); an

alternative formulation of the bottom friction is given by Mathisen and Madsen (1996).

The latest version of WWM II was verified in Roland (2009) for laboratory experiments, analytical solutions, and field observations with good results using the alternative numerical schemes. A detailed description of WWM II, including numerical schemes as well as physical processes, can be found in Roland (2009).

#### 2.4 Modeling wave-current interaction

In the current version of the coupled model, three aspects of current-wave interaction are considered: (1) wave-induced radiation stress based on the formulation of Longuet-Higgins and Stewart (1964); (2) wave-enhanced surface stress as well as mixing due to the surface wave-breaking (e.g., Craig and Banner, 1994); (3) wave-enhanced bottom stress (e.g., GM79). Brief descriptions of these aspects, which are included in our model simulations, are given in this section.

##### 2.4.1 Wave-induced radiation stress

Since the original paper by Zhang and Baptista (2008a), the ocean circulation model, SELFE, has evolved into a comprehensive modeling system that can be configured in many different ways; e.g., hydrostatic or non-hydrostatic options; 3D bottom deformation as occurred during seismically or landslide-generated tsunamis; in 2D or 3D configuration; in Cartesian (i.e., map projection) or spherical coordinates. The descriptions of these new features are presented in the previous section. The 3D

Reynolds-averaged Navier-Stokes equations with hydrostatic assumption, wave-induced radiation stress and under Cartesian coordinates that are used in this study can be presented as follows:

$$\frac{D\mathbf{u}}{Dt} = \frac{\partial}{\partial z} \left( \nu \frac{\partial \mathbf{u}}{\partial z} \right) - g\nabla\eta + \mathbf{F} \quad (2.35)$$

and the continuity equation:

$$\nabla \cdot \mathbf{u} + \frac{\partial w}{\partial z} = 0 \quad (2.36)$$

where  $D$  denotes the material derivative,  $\mathbf{u}$  is the horizontal velocity,  $\eta$  is the surface elevation,  $\nabla = (\partial/\partial x, \partial/\partial y)$  is the horizontal gradient operator,  $g$  is the gravitational acceleration,  $w$  is the vertical velocity, and the explicit term in Eq. (2.35) is given by:

$$\mathbf{F} = \nabla \cdot (\mu \nabla \mathbf{u}) - f\mathbf{k} \times \mathbf{u} - \frac{1}{\rho_0} \nabla p_A + \alpha g \nabla \varphi + \mathbf{R}_s \quad (2.37)$$

where  $\mathbf{k}$  is a unit vector of the  $z$ -axis (pointing vertically upward),  $f$  is the Coriolis factor,  $\alpha$  is the effective earth-elasticity factor,  $\varphi$  is the earth tidal potential,  $\mu$  and  $\nu$  are the vertical and horizontal viscosities ( $\text{m}^2\text{s}^{-1}$ ) respectively that may be solved from turbulence closure schemes (e.g. GOTM; Zhang and Baptista, 2008a),  $\rho_0$  is reference water density (in this paper, reference density is set as  $1000 \text{ kg m}^{-3}$ ),  $\rho$  is water density, and  $p_A$  is the atmospheric pressure. It should be noted that SELFE treats all terms in Eq. (2.35) semi-implicitly except for  $\mathbf{F}$ ; in other words, the radiation stress terms ( $\mathbf{R}_s$ ) are treated explicitly. The finite-element formulation outlined in Zhang and Baptista (2008a) is applied to the additional radiation stress terms when the wave-induced stresses are considered in the model run.

The radiation stress term  $R_s$  (a net momentum of flux produced by wave transformation in shallow water) is parameterized with different formulations (Mellor, 2003, 2005, 2008, 2011a, b; Xia et al., 2004) and there is still a great deal of controversy on the vertical profile of the stress (Bennis and Ardhuin, 2011; Mellor 2011a, b; Bennis et al., 2011). At the first stage of model development, we simply adopted the simplest radiation stress formulation originally proposed by Longuet-Higgins and Stewart (1962, 1964), although we have also implemented other options and the more sophisticated vortex-force formulations will be implemented in the near future.

The wave-induced stresses (gradient of the radiation stress) according to Longuet-Higgins and Stewart (1964) in the x- and y-directions can be estimated in the linear form, accounting for the mean flow momentum as given in Mastenbroek et al. (1993):

$$\left\{ \begin{array}{l} \mathbf{R}_s = (R_{sx}, R_{sy}) \\ R_{sx} = -\frac{1}{\rho_0 H} \frac{\partial S_{xx}}{\partial x} - \frac{1}{\rho_0 H} \frac{\partial S_{xy}}{\partial y} \\ R_{sy} = -\frac{1}{\rho_0 H} \frac{\partial S_{xy}}{\partial y} - \frac{1}{\rho_0 H} \frac{\partial S_{yy}}{\partial x} \end{array} \right. \quad (2.38)$$

with  $S_{xx}$ ,  $S_{xy}$ ,  $S_{yy}$  being the components of the radiation stress tensor, defined for an irregular wave spectrum according to Battjes (1974) as:

$$\begin{aligned}
S_{xy} &= \int_0^{2\pi} \int_0^{\infty} N_{(\sigma,\theta)} \sigma \frac{c_g(\sigma)}{c_p(\sigma)} \sin(\theta) \cos(\theta) d\theta d\sigma \\
S_{xx} &= \int_0^{2\pi} \int_0^{\infty} N_{(\sigma,\theta)} \cdot \sigma \cdot \left[ \frac{c_g(\sigma)}{c_p(\sigma)} (\cos^2(\theta) + 1) - \frac{1}{2} \right] d\theta d\sigma \\
S_{yy} &= \int_0^{2\pi} \int_0^{\infty} N_{(\sigma,\theta)} \cdot \sigma \cdot \left[ \frac{c_g(\sigma)}{c_p(\sigma)} (\sin^2(\theta) + 1) - \frac{1}{2} \right] d\theta d\sigma
\end{aligned} \tag{2.39}$$

where  $H=h+\eta$  is the total water depth,  $\theta$  is the angle between the x-axis and the dominant wave direction, and  $C_g$  and  $C_p$  are group and phase velocities. Note that the stress is uniform in the vertical dimension under this formulation.

While vertically varying radiation stress formulations have been developed (e.g. Mellor, 2003, 2005, 2008, 2011a, b; Xia et al., 2004), some formulations (e.g. Mellor, 2003; Xia et al., 2004) contain errors (Sheng and Liu, 2011) and others (e.g. Mellor, 2008) require additional efforts for incorporation into our coupled modeling system. Hence, these vertically varying formulations are not considered in this study.

#### 2.4.2 Wave-enhanced surface stress

When considering the effect of wave-enhanced surface stress, the total surface stress is estimated based on the actual sea state using the theory of Janssen (1991) and the extension made to it (e.g., sheltering of the young waves) in Ardhuin et al. (2010).



The total stress is passed to the current model in order to account for the surface stress and the enhanced mixing due to the wave-breaking is expounded upon in Craig and Banner (1994).

The wave decay due to the wave dissipation at the cost of whitecapping and depth-induced breaking also results in transfer of momentum from waves into the currents that can be parameterized using effective shear stress (Kim et al., 2008) and “roller” (Warner et al., 2008; Uchiyama et al., 2010). All these effects can be implemented in our modeling system easily but we do not consider their effects in this study. More recent and sophisticated formulations of wave-turbulence (e.g. Ardhuin and Jenkins, 2006; Babanin, 2011; Janssen, 2011) will be considered in the future development of the coupled modeling system.

#### 2.4.3 Wave-enhanced bottom stress

In shallow water regions, the wave-induced bottom stress in the wave bottom boundary layer plays an important role in sediment transport and can thus significantly enhance bottom shear stress. The formulation of wave-enhanced bottom stress we adopted in this study was originally proposed by Grant and Madsen (GM 79) and later modified by Mathisen and Madsen (1996) and implemented by Zhang et al. (2004) for the prediction of tide and wind-driven circulation in the Singapore Straits. When the effects of wave-enhanced bottom stress are considered, the original bottom roughness (i.e., the sediment diameter or ripples height,  $z_0$ ), will be replaced

with an apparent roughness  $z_{ob}$  as given below. The quadratic law adopted in SELFE (the same as in Eq. (2.10)) is:

$$\begin{aligned} \{\boldsymbol{\tau}_{bx}, \boldsymbol{\tau}_{by}\} &= \rho_0 C_D (u^2 + v^2)^{1/2} \{u, v\} \\ C_D &= [\kappa / \log(z_b / z_0)]^2 \end{aligned} \quad (2.40)$$

where  $\kappa = 0.4$  is the von Karman constant,  $z_b$  is the height from the bottom to the top of the bottom computational cell, and  $z_0$  is the bottom roughness related to the sediment grain size in the fixed bed without ripples.

The direction of the current  $\theta_c$  can be obtained as  $\tan \theta_c = \tau_{bx} / \tau_{by}$ , and the total magnitude of the current bottom shear stress is  $\tau_b = \sqrt{\tau_{bx}^2 + \tau_{by}^2}$ . Therefore, the angle between wave and current  $\theta_{wc}$  can be defined as  $\theta_c - \theta_w$ .

The maximum wave bottom stress is defined as:

$$\tau_w = 0.5 \rho_0 f_w U_w^2 \quad (2.41)$$

where  $U_w$  is the orbital velocity amplitude:

$$U_w = \frac{a_w \omega}{\sinh kH} \quad (2.42)$$

where  $a_w$  is the wave amplitude,  $\omega$  is the angular frequency. The combined wave-current friction factor,  $f_{wc}$ , is a function of the relative strength of currents and waves, specified by (Zhang et al., 2004):

$$\gamma = \frac{|\tau_b|}{\tau_w}$$

$$C_\gamma = \left(1 + 2\gamma |\cos \theta_{wc}| + \gamma^2\right)^{1/2}$$
(2.43)

And  $f_{wc}$  is given by

$$f_w = C_\gamma \exp \left[ 5.61 \left( \frac{C_\gamma U_w}{30z_0\omega} \right)^{-0.109} - 0.73 \right].$$
(2.44)

Eqs. (2.42), (2.43), and (2.44) are solved iteratively for  $(\gamma, c_\gamma, \tau_w)$  by first assuming  $\gamma = 0, C_\gamma = 1$  to obtain an initial estimate of  $\tau_w$  from Eq. (2.44) and (2.41). With this value of  $\tau_w$ , the values of  $\gamma$  and  $c_\gamma$  are updated using Eq. (2.43) and the procedure is repeated until the  $\gamma$  converges to within two significant digits. Convergence is usually achieved within a few iterations. After these quantities are found, the apparent roughness is given by:

$$z_{0b} = \delta_{wc} \left( \frac{\delta_{wc}}{z_0} \right)^{-\sqrt{|\tau_b|/(C_\gamma \tau_w)}}$$
(2.45)

where the wave boundary layer thickness  $\delta_{wc}$  is given by:

$$\delta_{wc} = \frac{\sqrt{\frac{C_\gamma \tau_w}{\rho_0}}}{\omega} \exp \left[ 2.96 \left( \frac{C_\gamma U_w}{30z_0\omega} \right)^{-0.071} - 1.45 \right].$$
(2.46)

The apparent roughness  $z_{0b}$ , as given by Eq. (2.45), should be used to replace  $z_0$  in Eq. (2.40). Previous studies (e.g., Zhang et al., 2004) indicate that this apparent roughness can be much larger than  $z_0$  even with modest waves inside estuaries.

## 2.5 Model coupling procedure

We first parallelized WWM II using the same domain decomposition scheme as that used by SELFE (see details in Section 2.2.6). The usage of the same subdomains in the two models can eliminate the need for interpolation and simplify the exchange of information between current and wave models, resulting in better efficiency. The WWM II is then recast as a subroutine inside SELFE. Due to very different time stepping schemes used in SELFE and WWM II, the time steps used in the two models are kept different in order to take advantage of each model's efficiency, and information exchange between the two models occurs at a pre-specified interval. During the information exchange, the sea surface elevation, wet/dry flags, and surface horizontal velocities are passed from SELFE to WWM II, and the calculated radiation stress, total surface stress, and the wave orbital velocity (needed in the GM79 model) are returned to SELFE. The robustness of both models has proved to be crucial for successful application of the coupled model to large field-scale tests (see Chapter 3).

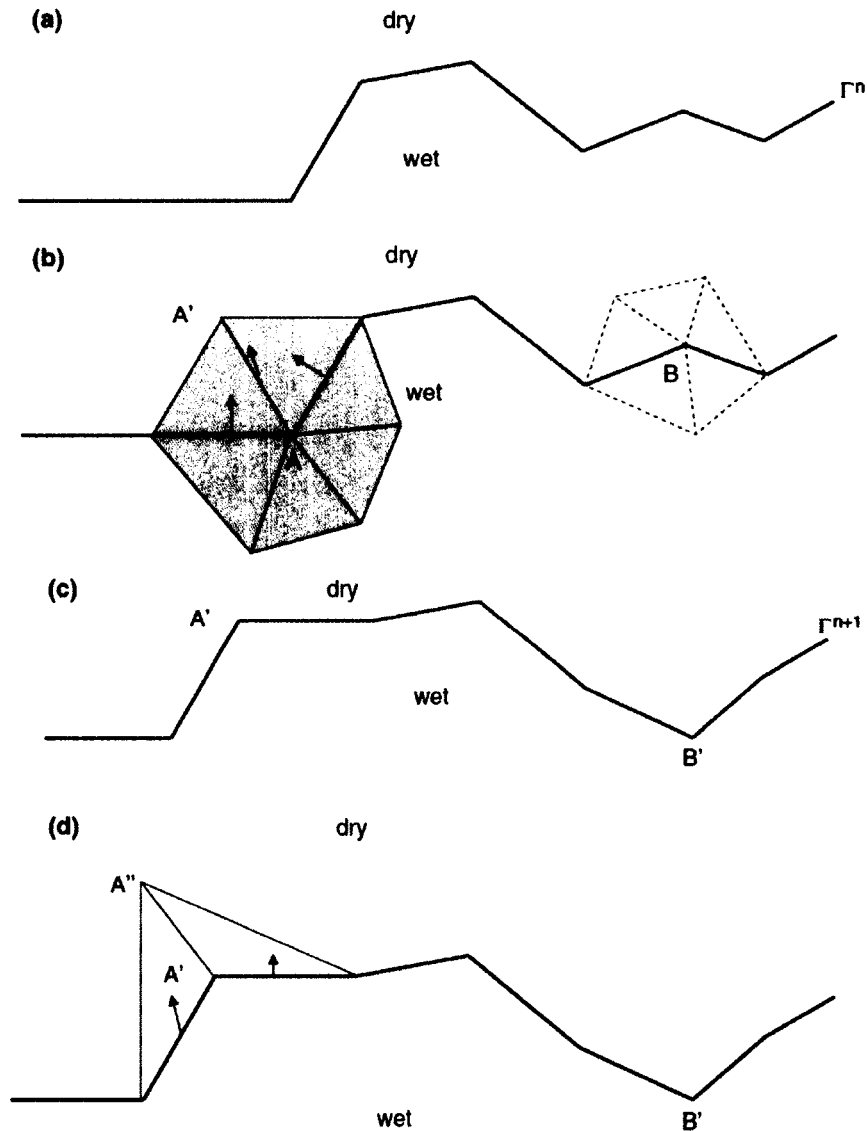
## 2.6 Conclusions

The evolution of surface waves is influenced by the ambient currents on both global and local scales. The actually available spectral wave models are continuously evaluated (e.g., Bidlot et al., 2002) and these models are at a stage where it is not easy

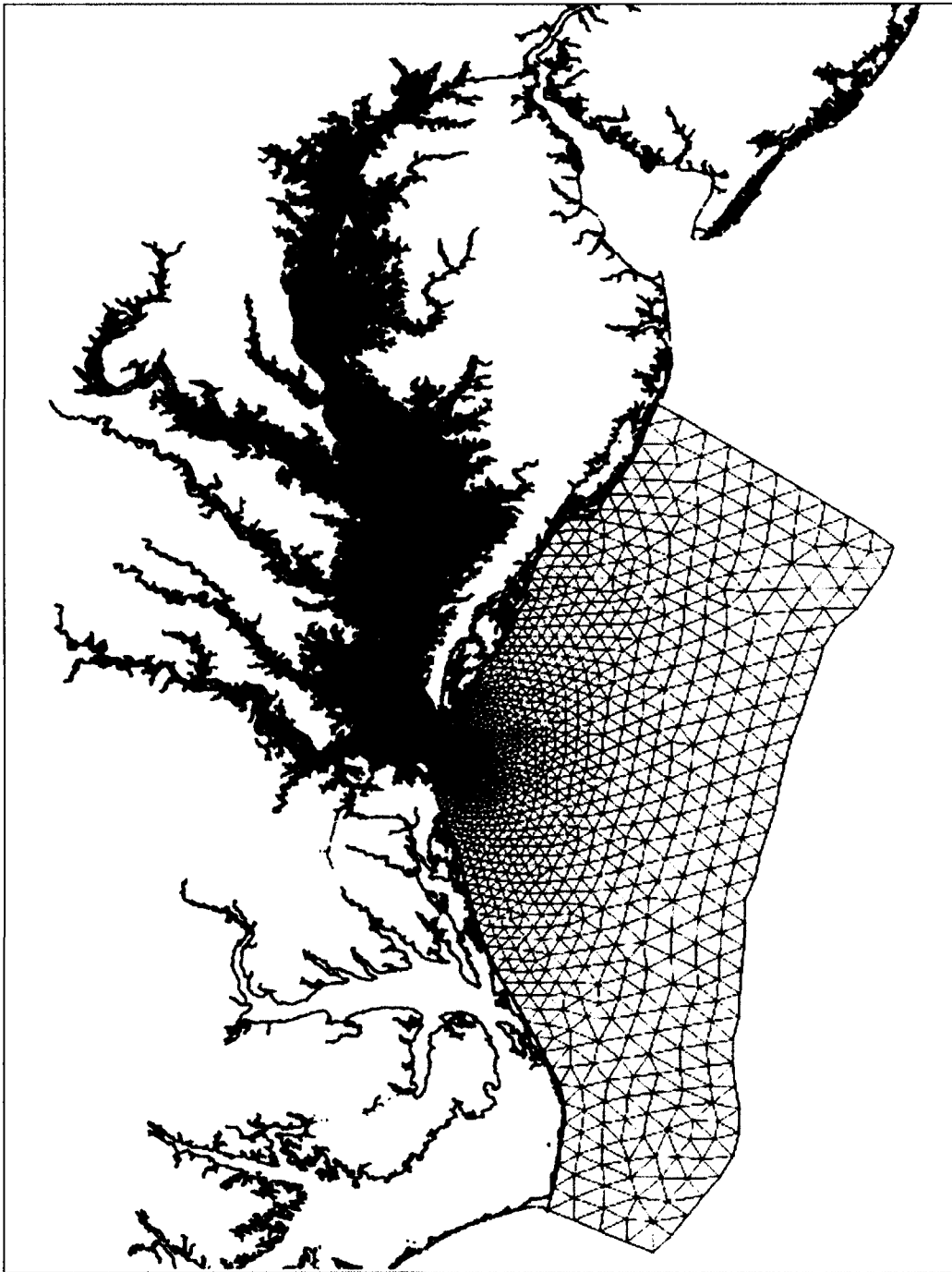
to make further improvements if the effect of currents is neglected, either on coastal or ocean scales.

In the coastal zones, surface waves induce coastal circulation and can have a strong influence on the total water levels, which are important for the coastal morphology and the coastal defense structures and, of course, give a feedback to the wave itself.

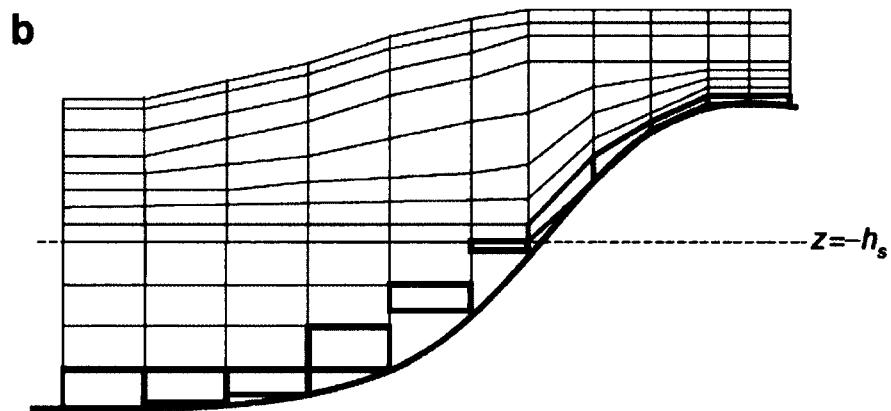
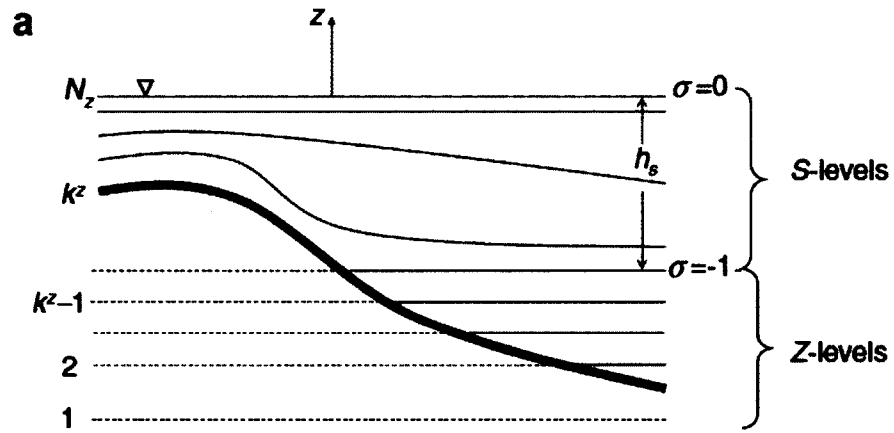
In this chapter, we present the new development of a fully coupled wave-current interaction model based on a 3D hydrodynamic model (SELFE) and the spectral wave model (WWM II), both implemented on unstructured grids, which makes the coupled model effective in multi-scale applications without grid nesting. Three effects of current-wave interaction are considered in our coupled model: (1) wave-induced radiation stress based on the formulation of Longuet-Higgins and Stewart (1964); (2) wave-enhanced surface stress as well as mixing due to the surface wave-breaking (e.g., Craig and Banner, 1994); (3) wave-enhanced bottom stress (e.g., GM79). The two models are tightly coupled with the same domain decomposition but with different time-stepping schemes to ensure maximum efficiency and flexibility. Our modeling framework represents a basis for the future research into the important topic of wave-current interactions, the wave propagation in inhomogeneous media (e.g. Liao et al., 2011; Toledo et al., 2012) and the improvement and validation of the physical framework for phase-averaged surface wave models. We carefully verified our coupled model and the detailed tests are presented in the next chapter.



**Figure 2-1** The wetting and drying scheme in SELFE. (a) Initial wet/dry interface at step  $n$ ; (b) evaluate wet/dry status for interfacial nodes based on new elevation at step  $n + 1$ ; (c) update the wet/dry interface, and iterate between (b) and (c); (d) final extrapolation of elevations along the final interface (or "coastline"). Note that this figure is re-plotted from Zhang and Baptista (2008b).



**Figure 2-2** Example of horizontal triangular grid used in SELFE model. Note that this figure is re-generated from Cho (2009).





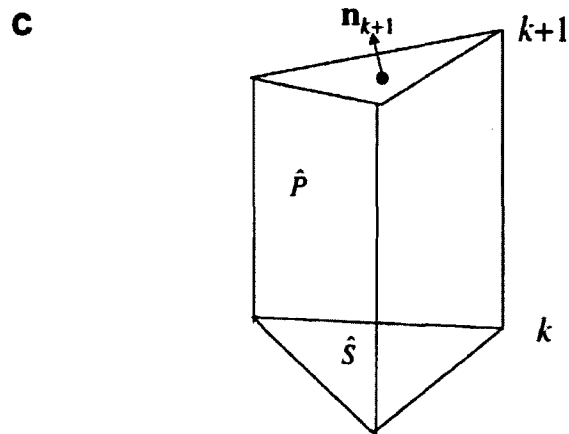


**Figure 2-3** A vertical grid of hybrid coordinate system used in SELFE. (a) a schematic view; (b) vertical view; (c) a unit of computational triangular prism with uneven bottom and top surfaces. Note that this figure is re-plotted from Zhang and Baptista (2008a).

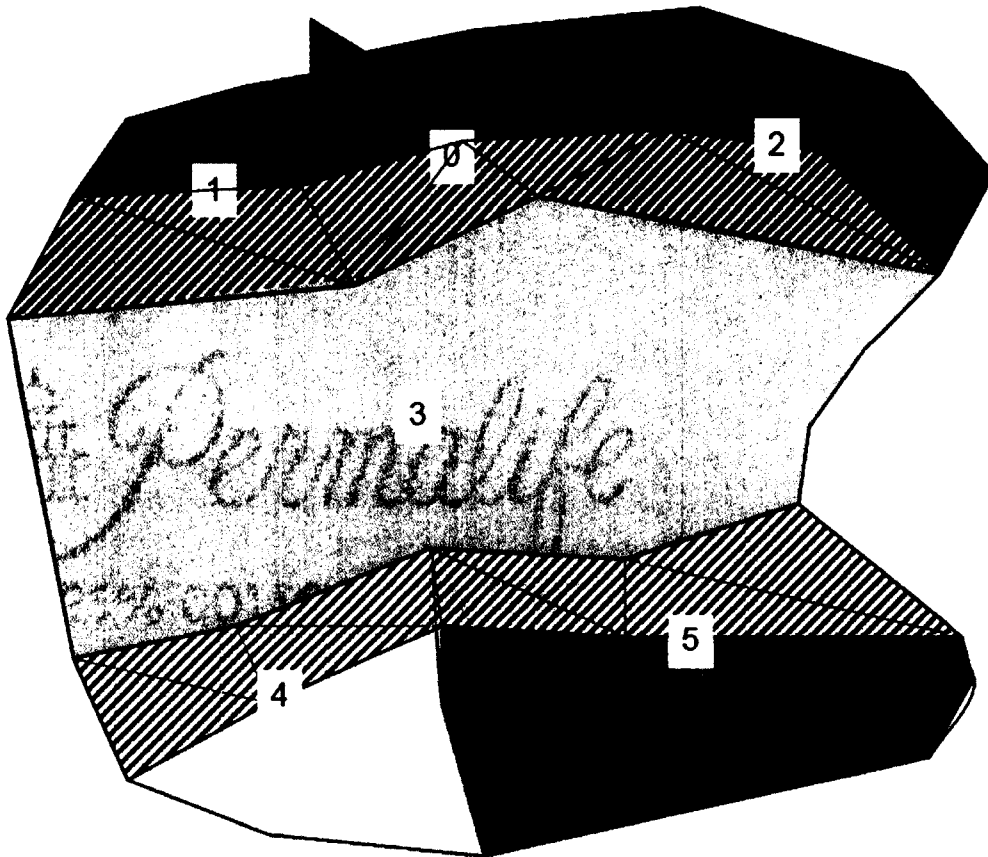


**Figure 2-4** A schematic view of domain decomposition used in SELFIE. Each color (number) presents each sub-domain on different computing node. Each sub-domain is augmented with 1 layer of ghost elements (gray regions) where exchange the information between different sub-domains.

## CHAPTER III. Model calibration

### 3.1 Introduction

In the previous chapter, we introduced the basic physical mechanisms and numerical methods of our coupled model. Then the model was carefully tested using analytical solutions of current-induced shoaling and refraction on wave action, analytical solutions of wave set-up on a linearly sloped beach profile, and several laboratory experiments taken from the ONR Test Bed Project (Ris et al., 2002). Although primarily proposed to validate spectral wave models alone, this Test Bed contains many valuable cases for the validation of a fully coupled wave-current model as well.

We have selected some of these cases for the validation of the current modeling system; in particular, we have compared wave-induced set-up based on the laboratory experiment of Boers (1996), as well as wave-breaking and eddy formation behind a submerged wave breaker based on the HISWA wave tank experiment of Dingemans (1987); we have also investigated the performance of the coupled model in wave blocking conditions as measured in the laboratory by Lai et al. (1989). In addition, we have investigated the performance of the coupled model for extra-tropical and tropical storm events, and here we will present the results for two tropical storms: the 2003 Hurricane Isabel making landfall along the U.S. East Coast and the 2004 Hurricane Ivan in the Gulf of Mexico. Detailed discussions are included in each subsection below.

### 3.2 Model verification – analytical solutions and laboratory experiments

#### 3.2.1 Current induced shoaling and refraction on wave

For the verification of current-induced shoaling and refraction, a deep water situation was considered where a monochromatic wave train with a period of 5.0 s and wave height of 1.0 m enters from the southern boundary of the computational domain. Three test cases are considered: (a) wave propagation in the same direction as the current; (b) wave propagation opposite to the direction of the current; and (c) for the slanting current case, the wave propagates with an angle of  $60^\circ$  to the x-axis into a current field, which is parallel to the x-axis with a constant positive gradient in the propagation direction. The computational domain consists of a rectangular basin that is 4 km long and 1 km wide. In Case (a) and Case (b), the speeds of currents are parallel to the y-axis and increased from the southern boundary to the northern boundary (ranging from 0.0 to 1.0 m/s). On the other hand, in the Case (C), the current is parallel to the x-axis. The directional distribution was set to  $2^\circ$  in order to be able to reproduce a nearly monochromatic wave at the deep water boundary. The directional resolution was kept constant with  $d\theta = 2^\circ$ . The settings of these three cases are shown in Fig. 3-1 schematically.

The analytical solutions for the following and opposing currents can be calculated (Phillips, 1977) with:

$$\frac{H^2}{H_1^2} = \frac{c_1^2}{c(c+2U)} \quad (3.1)$$

where

$$\frac{c}{c_i} = \frac{1}{2} + \frac{1}{2} \left(1 + 4 \frac{U}{c_i}\right)^{\frac{1}{2}} \quad (3.2)$$

and  $H_i$  and  $c_i$  are the incident wave height and incident wave celerity,  $H$  and  $c$  are the local wave height and the local wave celerity, and  $U$  is the current velocity. For the slanting current case, the analytical solutions for wave direction and wave height are (Jonsson, 1993):

$$\theta = \arccos\left\{\frac{gk_i \cos(\theta_i)}{[\omega - Uk_i \cos(\theta_i)]^2}\right\} \quad (3.3)$$

$$H = H_i \sqrt{\frac{\sin(2\theta_i)}{\sin(2\theta)}} \quad (3.4)$$

Here,  $\omega$  is the absolute radian frequency, and  $k_i$  and  $k$  are the incident and the local wave numbers, separately.  $\theta_i$  and  $\theta$  are the incident and local wave directions. The results are presented in Fig. 3-2. The agreement with linear theory is good in the first two cases (following and opposing currents); the computational errors are less than 1% for the significant wave height. For the slanting current case, the computational error is slightly larger than the first two cases; the error is less than 2% in significant wave height and less than  $0.1^\circ$  in direction. Overall, the results are acceptable as a first step of coupled model development.

### 3.2.2 Analytical solution for the wave set-up

Longuet-Higgins and Stewart (1964) gave an analytical solution for wave set-up on a gently sloping beach. In the simple 1D steady-state problem, the balance of forces is between the pressure gradient and the radiation stress and can be written as:

$$g \frac{\partial \eta}{\partial x} = -\frac{1}{\rho_0 H} \frac{\partial E(2n-0.5)}{\partial x}. \quad (3.5)$$

where E is the total wave energy per unit surface area, and  $n = \frac{1}{2} \left( 1 + \frac{2kH}{\sinh 2kH} \right)$ . The

solution is given in two separated zones: inside and outside the surf zone with the boundary defined as  $x = x_B$  (see Fig. 3-3). Outside the surf zone ( $x \geq x_B$ ), we have:

$$\eta = -\frac{a^2 k}{2 \sinh 2kh} \quad (3.6)$$

In addition, the conservation of wave energy leads to:

$$a^2 = \frac{n_0 k}{nk_0} a_0^2 \quad (3.7)$$

where variables with the subscript “0” are the quantities related to the incident wave.

Inside the surf zone ( $x \leq x_B$ ), the wave amplitude is proportional to the local water depth:

$$a = \beta(h + \eta), \quad (3.8)$$

where  $\beta=0.41$  is a wave-breaking constant in terms of wave amplitude as given by Xia et al. (2004).

If we assume a long-wave dispersion relation within this zone (i.e.  $n=1$ ), we then have:

$$\eta = \frac{1}{1 + \frac{3\beta^2}{2}} (h_B - h) + \eta_B \quad (3.9)$$

where the subscripts “B” denote quantities at  $x = x_B$ .

Matching the two solutions of Eqs. (3.6) and (3.9) leads to 4 equations for 4 unknowns  $(h_B, \eta_B, a_B, k_B)$ , which can be reduced to one equation for  $k_B$ :

$$k_B^{10} - \frac{8}{c_0} \left( 1 + \frac{2}{\beta^2} \right) \hat{k} k_B^5 + \frac{16}{c_0} \hat{k}^4 = 0 \quad (3.10)$$

where  $c_0 = a_0^2 n_0 / k_0$ ,  $\hat{k} = \omega^2 / g$ . After  $k_B$  is solved from Eq. (3.10), the complete solution can be constructed within each zone. The solution, however, exhibits a sharp jump near the breaking point  $x = x_B$ , due to the use of the long-wave dispersion relation above. If we have not assumed the long-wave dispersion relation in each zone, the unknowns can still be found by solving the original nonlinear equation system mentioned above. The latter approach is used here and the nonlinear equations are solved with an iterative method inside Matlab.

To test our SELFE-WWM II coupled model, we impose a train of monochromatic waves with an amplitude of 9 cm and a period of 1.5 s at the right-hand boundary for WWM II (for SELFE, the elevation calculated from the analytical solution is imposed there); the initial elevations and velocities are set to 0. The coupling time step (0.05s) is chosen to be the same as the time step used in SELFE, and the explicit  $N$ -scheme (a kind of RD scheme; readers can find more details in Roland, 2009) is used in WWM II with the sub-timestep being determined by the local CFL condition. The horizontal grid has a uniform resolution of 12.5 cm in  $x$  (Fig. 3-4) and 9 evenly distributed  $\sigma$  levels are used in the vertical grid. To remain consistent with the analytical solution, no bottom friction was used in this test. The total simulation time is 1 hour in order to reach a steady state.

A first check of the coupled model is on whether a steady-state solution is reached as predicted by the analytical solution. It can be seen from Fig. 3-5 that the surface elevation at a location close to the shoreline ( $x=0.38\text{m}$ ;  $h=0.038\text{m}$ ) reaches a steady state; it takes about 0.6 hours for the initial high-frequency oscillations to dissipate before converging to a steady state, which is an indication of the monotonicity and consistency of the coupled model. The modeled steady-state results compare very well with the analytical solutions for both wave height and wave-induced set-up (Fig. 3-6).

### 3.2.3 Wave set-up and wave-breaking of Boers (1996)

In the work of Boers (1996), depth-induced wave-breaking and wave-induced set-up were examined under laboratory control experiments. Boers investigated the evolution of random uni-directional wave trains in a laboratory flume and measured wave spectra and surface elevation as the waves propagate towards a bar-through profile as often found in natural conditions (see Fig. 3-7). Observed wave spectra, as well as wave-induced set-up, are available at a large number of locations, making this a valuable test case for the validation of the wave-current coupled model. There are three cases for this lab test with different wave boundary conditions, given in terms of the one-dimensional wave spectra (Fig. 3-8), and characterized by different mean wave lengths and wave heights.

The main challenge in this test is related to the complex bottom profile and the inclusion of the inundation zone; as a result, a steady state condition cannot be



reached if either the current or the wave model has stability issues. Therefore, the very fact that a steady state condition is reached in our coupled model, at a location very close to the shoreline, is testimony to the stability and robustness of both current and wave models (Fig. 3-9).

The coupled model is run on a uniform grid of 5-cm resolution in the horizontal and 9 evenly distributed  $\sigma$  levels in the vertical grid. The coupling time step is 0.1 sec and consistent with the time step used in SELFE. The lab-measured wave spectra (Fig. 3-8) and historic time-series elevation are imposed at the boundary for WWM II and SELFE, respectively. Since no information is provided for the bottom roughness, we used a constant bottom roughness of 1 mm over the entire model domain. The WWM II was set up to account for the quasi-resonant wave-wave interactions, bottom friction based on the JONSWAP formulation, and wave-breaking according to Battjes and Janssen (1978). For the wave-breaking formulation we had to reduce the default dissipation rate by 50% to 0.5 and set a fixed maximum wave height to a depth ratio of 0.8 in contrast to the default value of 0.73. The near-resonant interactions had to be re-tuned and we reduced the coefficient suggested by Eldeberky (1996) and Dingemans (1998) to 0.5 in order to not overestimate the transfer of low-frequency energy towards the higher harmonics. Even though the downshift of the average period ( $tm02$ ) is well predicted on average, the model does not reproduce the downshifts in the vicinity of strong wave-breaking dissipation (Fig. 3-10). The reason for this overestimation is probably because the approximation made by Eldeberky is for flat-bottom topography and therefore the estimation of the

near-resonant nonlinear transfer based on this approximation is not expected to be very accurate (Dingemans, 1998), especially in this test case. The wave-induced set-up is extremely sensitive to the spatial gradients of the wave spectrum, and since the model exaggerates the gradients of the total energy, the coupled model overestimates the wave-induced set-up consistently (Fig. 3-10).

The modeled significant wave heights and steady-state set-up profiles for the three laboratory cases compared well with the measured data (Fig. 3-10). The model tends to overpredict the set-up in the surf zone, but the reasons for this may be explained by the fact that we used a constant radiation stress profile (Section 2.4.1) and there was a strong sensitivity of the wave-induced forces on the wave height gradients in the wave model.

#### 3.2.4 HISWA experiment of Dingemans (L51 test, 1987)

To test our coupled model in a 2D configuration, the ONR (Office of Naval Research) test L51 was used. The laboratory experiment of Dingemans (1987) was performed in a rectangular basin with a flat bottom and with a submerged breakwater (Fig. 3-11a). The north and south boundaries parallel to the  $x$ -axis are fully reflective and a target JONSWAP spectrum with a peak period of 1.25 sec and height of 0.10 m was generated by the wave maker at the left-hand side boundary while, at the right-hand side boundary, a passive wave absorber was installed. The mean wave direction is along the  $x$ -axis with a directional spread of approximately  $25^\circ$ . The waves propagate across the breakwater with a significant loss of energy, generating a

relatively large high-frequency spectral peak. The breaking waves also generate a mean circulation in the rectangular basin.

The wave spectra derived from the laboratory data are imposed in the wave model at the left boundary, and a Neumann-type boundary is used on both the north and south boundary of the basin while the east boundary condition is set to be fully absorbing. In this test, we used 72 directional bins ( $0^\circ$  to  $360^\circ$ ) and 24 frequency bins (0.315Hz to 3.125Hz). As far as the current model is concerned, the basin is completely closed with fully reflective boundaries since the wave maker and the absorber operate at a higher frequency. The horizontal grid we used for this test is shown in Fig. 3-11b (the resolution of this grid is 40 cm). As in the previous tests, we used 9 evenly distributed  $\sigma$  levels in the vertical grid. The coupling and SELFE time step is chosen to be 0.5 sec, and the total simulation duration is 2500 sec, as a steady state condition is attained after approximately 800 sec.

The modeled steady-state surface velocity compares very well with the laboratory measurements, both qualitatively and quantitatively (Fig. 3-12). In particular the location of the eddy and the vortices are both well simulated. The direction of the eddy indicates that the wave overtopping is the dominant process in this case as opposed to the diffraction/refraction effects as in the case shown in Nicholson et al. (1997).

The modeled wave heights also compare reasonably well with the experimental results, and capture the wave-breaking process as waves propagate over the breakwater (Fig. 3-13). Unsurprisingly, the largest error occurs on the down-wave

side of the breakwater. The errors at the 3 gauges nearest to the left boundary indicate the errors in the wave boundary condition. The laboratory dataset also includes other types of measurements (e.g., vertical profiles of velocity) and will be used for further study as the coupled model incorporates more 3D formulations (e.g., 3D radiation stress profile).

### 3.2.5 The wave blocking experiment of Lai et al. (1989)

The last laboratory experiment used in this study investigates the capability of the coupled model to predict the wave decay under blocking conditions. The experiment conducted by Lai et al. (1989) investigated the evolution of unidirectional random waves running against an opposing current that was intensified by an underwater bar (Fig. 3-14). The current velocity reaches a maximum amplitude of 24 cm/s over the bar, which is sufficient to block a large portion of the wave spectra imposed on the boundary. The waves propagate from left to right and are blocked on the toe of the bar.

The grid used in this study has a uniform resolution of 2 m in the cross-shore direction and 0.02 m in the direction of wave propagation, and six uniformly distributed  $\sigma$  levels are used for the vertical discretization. The coupled model uses the same time step of 0.1 sec, and the total simulation time is 10 minutes, which is sufficient to produce a convergent steady-state solution (see Fig. 3-15).

The wave spectra from the data of the 6 measurement stations (locations are shown in Fig. 3-14), where gauge 1 is at the left-hand boundary, are shown in Fig. 3-

16. The results are compared to the spectral balance as proposed by Ardhuin et al. (2010). It can be clearly seen that the high-frequency portion of the spectra that is blocked by the strong counter-current vanishes in the phase-averaged model, whereas in the flume wave energy is still present. In the vicinity of the spectral peak of the measurements, it can be seen that the model is able to shift correctly the wave spectra in frequency space, and the peak of the measured and modeled wave spectra are very near to each other. However, the dissipation of wave energy is strongly over-estimated. One reason for that may be given by the fact that, near the blocking point, part of the wave energy is reflected as shown in Shyu and Phillips (1990) and the decay rate in blocking conditions is different due to the intense generation of turbulence.

The most significant implication of this comparison is that our fully coupled model, SELFE-WWM II, was able to reach a convergent solution, and therefore it serves as a good basis for future investigation of possible new formulations that are able to improve the results under strong blocking conditions. This is very important, especially for practical applications in tidal estuaries and other current-dominated regions where strong currents are present and are directed against the wave propagation.

### 3.3 Model verification – field events

#### 3.3.1 Hurricane Isabel (2003) in the Chesapeake Bay

Hurricane Isabel was the costliest and deadliest hurricane during the 2003 Atlantic season. Isabel formed near the Cape Verde Islands from a tropical storm on September 6, 2003 in the tropical Atlantic Ocean, moved northwestward, and steadily strengthened to reach peak winds of 165 mph on September 11, 2003. After fluctuating in intensity for four days, Isabel gradually weakened and made landfall on the Outer Banks of North Carolina as a Category 2 hurricane with winds of 105 mph on September 18, 2003. Isabel quickly weakened over land and became an extratropical storm over western Pennsylvania the next day (Wikipedia.org). The total damage due to Isabel was about \$3 billion with 16 fatalities, mostly in North Carolina and Virginia. The track of Hurricane Isabel is shown in Fig. 3-17. Based on Cho et al. (2012), Isabel was defined as a western-type storm, which passed to the west of the Bay and created the highest surge in the northern part of the Bay (Pore, 1960, 1965; Wang et al., 2005; Shen et al., 2005, 2006a, 2006b). Under this type of storm, the up-estuary local wind tends to penetrate deeper into the water column, which reduces stratification by reversing gravitational circulation (Cho et al., 2012).

In order to accurately capture the wave dynamics from the deep ocean to near-shore and to account for the remote wind effect during Hurricane Isabel (Shen et al., 2006; Cho et al., 2012), the model domain used in this test (Fig. 3-18a) includes a large part of the mid-Atlantic Bight from Georgia to New Jersey, with higher

resolution (1 km) inside the Chesapeake Bay (Fig. 3-18b) where extensive observations (water levels, winds, and wave characteristics such as significant wave heights, peak wave periods, mean wave periods, and peak wave directions) are available (Table 3-1; Fig 3-19). Note that the definitions of wave characteristics that are used for model-data comparison can be found in Appendix B.

The atmospheric forcing we used in this study is a blend of the NARR wind (North America Regional Re-analysis; normally with 32-km resolution; more details can be found at <http://www.esrl.noaa.gov/psd/data/gridded/data.narr.pressure.html>) and the high-resolution WRF wind (with approximately 4-km resolution) that we obtained from the NWS (National Weather Service). Fig. 3-20 shows a comparison between modeled and measured winds at Chesapeake Light buoy (Station CHLV2, Fig. 3-19). As can be seen, the modeled wind errors are generally small, although larger errors can be found during several transition regimes (e.g., around Sept. 18, 2003) during and after Hurricane Isabel.

The model grid for this case has about 26k nodes (Fig. 3-18a) in the horizontal and 34  $S$  levels in the vertical grid (with stretching parameters  $\theta_f=6$  and  $\theta_b=0.5$ ). The current and wave models are coupled using a time step of 50 sec, and the smaller time step (by the SELFE standard) was used to reduce splitting errors in WWM II. The dual kriging ELM is used to obtain high-order accuracy for the momentum advection in SELFE. For WWM II, we used 36 direction and 36 frequency bins, with the cut-off frequencies being 0.03 and 1 Hz (these were the default settings for all wave model runs in this study). The wind growth and dissipation formulations in WWM II are

from Ardhuin et al. (2010). At the offshore open boundary, the integrated wave parameters were prescribed based on the hindcast results produced by the WWIII (Wave Watch III) from the IOWAGA project (Integrated Ocean Waves for Geophysical and other Applications; <http://wwz.ifremer.fr/iowaga>). Tides were forced on the open-ocean boundary with the seven dominant astronomical tidal constituents and included the diurnal  $O_1$ ,  $K_1$  and  $Q_1$  constituents and the semidiurnal  $M_2$ ,  $N_2$ ,  $S_2$  and  $K_2$  constituents, using data from Le Provost's FES95.2 global model (Le Provost et al., 1998; Mukai et al., 2002). In addition, tidal potential functions are forced within the model domain for the same constituents. Periods, tidal potential constants, and the earth elasticity factors, which reduce the magnitude of the tidal potential forcing due to the earth tides, are listed in Table 3-2. Finally, the nodal factor and equilibrium argument for boundary and interior domain forcing tidal constituents are based on the starting time of the simulation.

Prior to storm surge simulation, the SELFE model was calibrated first with respect to the bottom frictional coefficient by simulating mean tide characteristics during Hurricane Isabel. The model was forced by 7 main tidal constituents at its open boundary, namely  $O_1$ ,  $K_1$ ,  $Q_1$ ,  $M_2$ ,  $N_2$ ,  $S_2$  and  $K_2$ . Earth tidal potential of each tidal constituent was also applied to interior cells of the model domain. The simulation of tide using a time step of 50 s started from 9/8/2003 UTC and lasted for 35 days. The simulated hourly tidal levels of the last 30 days were used for comparison with predicted tides at tidal gauge stations around Chesapeake Bay area from NOAA CO-OPS dataset (Table. 3-1). Chesapeake Bay has the tidal



characteristics of a reflected, dampened Kelvin wave, with a larger tidal range along the Eastern Shore than along the Western Shore (Hicks, 1964; Carter and Pritchard, 1988; Zhong and Li, 2006; Guo and Valle-Levinson, 2007). The mean tidal range decreases from 0.9 m at the Bay's entrance to a minimum of 0.27 m from Plum Point to Annapolis, MD, and then increases to 0.55 m at Havre de Grace, MD, near the head of the Bay. The model tidal calibration run reproduced these characteristics properly. Harmonic analysis results for four major tidal constituents ( $M_2$ ,  $S_2$ ,  $N_2$ , and  $K_1$ ) are shown in Tables 3-3 and 3-4. The model results have a high correlation and low error compared with observations. The dominant  $M_2$  constituent has an ARE value of 4.1% and a RMSE value of 1.6 cm. These results indicate that the simulation of tide by the SELFE model is overall satisfactory around the Chesapeake Bay region.

The fully coupled model runs 24 times faster than real time on 48 CPUs of NASA's Pleiades cluster in this case. In order to ascertain the effects from the waves, SELFE alone is run to simulate the storm surge without the wave effects. In addition, in order to elucidate the issues associated with the coupled 3D wave-current model, we conducted simulations with both 2D and 3D SELFE, with and without wave effects.

One of the major differences between 2D and 3D SELFE lies in the different bottom drag formulations used. In SELFE, we applied the quadratic stress at the bottom boundary and assumed a logarithmic bottom boundary layer in 3D mode. After the calibration for modeled tides, the initial distribution of the bottom roughness height is chosen as 1 mm outside the Chesapeake Bay and 0.1 mm inside for 3D

mode; the modified Grant and Madsen formulation (Section 2.4.3) is then used to dynamically adjust the wave-enhanced bottom friction. For the 2D mode, we used a fixed uniform Manning coefficient of 0.025, and the modified Grant and Madsen formulation is not applied therein.

The modeled wave characteristics (significant wave height,  $H_s$ ; peak wave period,  $T_p$ ; mean wave period,  $T_{m02}$ ) are found to be similar with the 2D and 3D modes and both of them compare well with the NDBC buoy data (Fig. 3-21), except at Buoys 41008 and 44008. Note that since Buoys 41008 and 44008 are very close to the open boundary, the results there mainly reflect the boundary condition from WWII. Overall, the modeled wave results indicate that the coupled model adequately simulated the wave characteristics during Hurricane Isabel around the Chesapeake Bay region.

The upper Bay is also affected by other types of wave dynamics, such as limited fetch, and is more sensitive to the atmospheric forcing such as local wind stress. Therefore, here we only focus on the lower Bay region. The modeled surge tides, as predicted by the 2D modes with and without waves, are shown in Fig. 3-22 at lower Bay stations. The wave effects, mostly due to the radiation stress (note this is for 2D case), account for up to a 20-cm increase in the total water set-up, which leads to a reduction of the average errors from 5.6% to 3.8% for the calculated surge heights. Overall, for the 2D mode, wave set-up accounts for to 5% of the observed peak surge elevation inside the Chesapeake Bay.

On the other hand, the addition of the 3D effects leads to some very interesting results. Without the waves (i.e., with SELFE alone), the addition of the vertical dimension from 2D to 3D SELFE generally results in a higher surge (Fig. 3-23; green circle – 2D without wave; green line – 3D without wave) due to the more accurate Ekman dynamics (e.g., Ekman Spiral) included in the 3D mode; similar results have also been obtained for Hurricane Ike in the Gulf of Mexico as well as many other tropical and extratropical storms (SURA test bed project, 2011). The 3D results slightly over-predicted the surge peaks at all stations in the lower Bay region (Fig. 3-23). Adding the full wave effects into the 3D model (including wave-induced radiation stress, wave-induced surface stress, and wave-enhanced bottom stress), however, decreases the simulated water level (Fig. 3-23 (blue line)), which is contrary to the 2D results we have presented above. This is because, inside the Bay, the wave-enhanced bottom friction effects (calculated from the modified GM79 formulation; Chapter 2.4.3) play a dominant role in our simulation. Indeed, with the GM79 formulation removed, the waves would have induced a higher surge peak (Fig. 3-23 (black line)), most of which is attributed to the radiation stress. The apparent bottom roughness ( $z_{ob}$ ) estimated by the GM79 formulation shows more than an order of magnitude increase from the initial 0.1 mm to several centimeters. The net set-down in the 3D mode with and without waves has fortuitously reduced the errors from 8.2% to 6.1% due to the initial overprediction. It is also interesting to note that the 2D and 3D results with wave effects added are generally close to each other, although the

surge peaks from the 3D mode are slightly higher at Gloucester Pt. and Sewells Point (Fig. 3-23 (blue diamond – 2D with wave; blue line – 3D with wave)).

As explained in Wolf (2009), many different (and sometimes opposing) physical processes are at play in 3D, some of which are still under active research; e.g. wave-induced surface stress and turbulence and wave bottom friction (in shallow waters), and depth and current refraction of waves by surge water levels and currents. The results we have shown here further highlight the need to close the knowledge gap between the simple 2D and more “complete” (and presumably better) 3D wave-current interaction models. It is our hope that the preliminary 3D results presented here will be further validated and improved after a more consistent framework, such as that proposed in Ardhuin et al. (2008), is implemented in our coupled model. At the moment, various components of the physical formulation in the model for radiation stress, surface stress and turbulence, and wave bottom boundary layers are not entirely consistent as explained in Bennis and Ardhuin (2011). While other theoretical frameworks have been proposed in the community (e.g., Uchiyama et al., 2010), currently lacking is a comprehensive suite of tests to assess the skill of the 3D models under complicated conditions that include all known mechanisms. We are in the process of carrying out such analyses and the results will be presented in the near future.

Sheng et al. (2010) also studied the same event using a wave-current coupled model (CH3D-SSMS, with the current model being 3D), and showed that the addition of the wave effects has led to a higher (and more accurate) surge. Their conclusion is

consistent with our 2D results, but not with the 3D results, where we have found a reduction of surge heights when the wave effects are added. The main differences between our and their 3D coupled model include: (1) they used a lookup table for wave-induced bottom stress; (2) the underlying wave and current models used in their paper are based on structured grid, thus having limited ability to resolve the detailed features, especially tributaries, in the Chesapeake Bay that are important for wave propagation; (3) the grid domain used in their study did not include the mid-Atlantic Bight; however, it has been proven that surge caused by Isabel was contributed by both remote and local wind forcings and, thus, a large model domain is a necessity for predicting storm surge accurately inside the Chesapeake Bay (Shen et al., 2006a). Further research is warranted on this once a self-consistent 3D framework (e.g., Ardhuin et al., 2008) is implemented in the model.

### 3.3.2 Hurricane Ivan (2004) in the Gulf of Mexico

Hurricane Ivan, attaining Saffir-Simpson Scale Category 5 status in the Caribbean Sea on 12 September 2004, entered the Gulf of Mexico and weakened to a Category 4 hurricane on 14 September 2004. It then weakened further before making landfall at the border between Alabama and Florida (Fig. 3-24) as a Category 3 hurricane on 16 September 2004 (Weisberg and Zheng, 2008). Hurricane Ivan produced severe storm surges of about 2.4 m around Dauphin Island and 2.1 m within Mobile Bay. Coupled with large waves (Wang et al., 2005), Ivan caused extensive damage to coastal and inland structures, highways and bridge systems, and forests

(Hagy et al., 2006; Sallenger et al., 2006), making it one of the most destructive hurricanes ever to hit the Alabama and Florida area. Hurricane Ivan caused an estimated \$18 billion 2004 USD (\$22.1 billion 2012 USD) in damages to the United States, making it the fifth costliest hurricane ever to strike the States. Our main focus of this test is to examine the significance of wave-current interaction on storm surge under strong current conditions in very shallow water regions.

As an illustration of model performance and to corroborate the findings from the results of Hurricane Isabel, we have run our coupled model on a super-regional grid covering the entire Gulf of Mexico, the U.S. East Coast, and the Caribbean Sea with 600K nodes and 31 vertical levels in order to simulate Hurricane Ivan (2004) in the Gulf of Mexico. The mesh resolves the northern part of the Gulf of Mexico with element edge lengths as fine as 100 m (Fig. 3-25). The model setup basically was similar to that for the Isabel 3D case (see Section 3.3.1).

Before the Ivan storm surge simulation, the simulation of tides along the U.S. East and Gulf Coasts was carried out to verify the SELFE model by using this super-regional grid. The model was forced by 7 main tidal constituents at its open boundary, namely  $O_1$ ,  $K_1$ ,  $Q_1$ ,  $M_2$ ,  $N_2$ ,  $S_2$  and  $K_2$ . Earth tidal potential of each tidal constituent was also applied to interior cells of the model domain. The simulation of tide using a time step of 50 sec started from 9/1/2004 UTC and lasted for 30 days. The simulated hourly tidal levels of the last 25 days were used for comparison with predicted tides at 22 tidal gauge stations around the Gulf of Mexico and the other 10 stations along the U.S. East Coast from the NOAA CO-OPS dataset (Fig. 3-26a and Fig. 3-26b).

Tables 3-5 and 3-6 show the correlation coefficients between computed and NOAA-predicted tides during the period from 9/6/2004 to 9/30/2004 in the Gulf of Mexico and along the East Coast, respectively. It can be seen that the model adequately simulated tidal elevation around the Gulf of Mexico with correlation coefficients ( $R^2$ ) ranging from 0.63 to 0.94 except at Cyremort Point, LA and New Canal Station, LA (Table 3-5) because the resolution is insufficient on the south shore of the Lake Pontchartrain (Dietrich et al., 2010). The simulated tides along the East Coast match the predicted tides very well with correlation coefficients greater than 0.88 (Table 3-6). These results indicate that the simulation of tide by the SELFE model using this super-regional grid is overall satisfactory along the U.S. East Coast and in the Gulf of Mexico.

For the validation of the wave model during Hurricane Ivan, the time series of the hindcast results at NDBC buoys (Fig. 3-27) are shown for the significant wave height (Fig. 3-28) and for the peak period (Fig. 3-29); the model-data comparisons are reasonable and generally better than those for Isabel. For the effect of wave-induced set-up, we focused our analysis on the station of Dauphin Island (Fig. 3-30) for the sake of brevity; a similar comparison was also conducted by Roland et al. (2009) using the coupled 2D wave-current model SHYFEM-WWM II. The model results for the water level elevation during Hurricane Ivan clearly show similar behavior patterns to those for Isabel. Without the effect of wave-enhanced bottom stress, the coupled model overpredicted the forerunner (Fig. 3-30 (blue solid line)); adding the wave boundary layer based on the GM79 formulation leads to a net reduction of the surge

peak and a better forerunner. It is interesting to note that the results from the fully coupled model (including wave-induced radiation stress, wave-induced surface stress, and wave-enhanced bottom stress) are close to those from SELFE alone, with the latter being slightly more accurate during the period of surge peak. Again, we expect further improvement to the fully 3D coupled model once a consistent 3D framework is implemented therein.

### 3.4 Efficiency of the coupled model

As we mentioned before, the key issues of operational storm surge forecast are the efficiency and scalability of the model. We conducted several benchmark tests to evaluate the efficiency of our coupled model and the results are presented in this section.

The parallel performance of our coupled model was evaluated on ECMWF's high-performance cluster (C1A/B). The scaling on the 600k mesh we used for the Hurricane Ivan case was good up to 32 compute nodes (with 64 cores on each node; 2048 cores altogether), on IBM Power 6 architecture with 50% hyper-threads (Fig. 3-31). Note that the definition of speed-up was relative to a run using 2 compute nodes (128 cores) without hyper-threading. The run was made with a coupling time step of 180 sec for which the peak performance on 2048 hyper-threading cores was approximately 110 times faster than real-time using 16 sub-iterations for the explicit scheme used in WWM II in order to fulfill the stability conditions. It can be seen that the domain decomposition technique leads to linear scaling behavior for the WWM II



up to 2048 cores. For SELFE alone, the scaling is also linear but with a somewhat smaller slope. The uses of hyper-threading resulted in a jump with respect to the efficiency in WWM II as well as the coupled model. This is due to the fact that the network traffic was reduced by a factor of 2, clearly indicating the efficiency of the implementation on hyper-threading platforms.

In the SURA test bed project, we also conducted benchmark runs on NSF/Teragrid's Ranger cluster by using the same setups to compare the efficiency between three models: ADCIRC, FVCOM, and SELFE. The results of the timing test are listed in Table 3-7. It should be noted that, in these three models, SELFE is the only one using a semi-implicit scheme, which means we can use a much larger time step compared with ADCIRC and FVCOM. As shown in Table 3-7, the total wall-clock time of a 10-day run for SELFE is only 107 mins when using 512 computational cores on Ranger. On the contrary, it took 266 mins for FVCOM and 378 mins for ADCIRC, almost 4 times slower than SELFE, to finish the timing test run. Moreover, the maximum performance of SELFE can be reached when using 256 computational cores (95 mins, not listed here). This result indicates that the performance of the SELFE model is sufficient for forecasts of large storms and only requires a reasonable computational power that is less than that of the other two models.

### 3.5 Conclusions

The coupled model we presented in Chapter 2 has been demonstrated to be accurate and robust, in addition to being efficient, through a series of stringent tests consisting of two analytical solutions, three laboratory experiments, and two cross-scale field tests. In addition to the tests presented in this chapter, we have also successfully applied our coupled model to other field scale tests, included in the context of the on-going IOOS-sponsored super-regional test bed for storm surge inundation (see details in Chapter 4 and 5), as well as forecasting the recent Hurricane Irene (2011).

Our results for the 3D wave-current coupled model also highlight the need to further understand the delicate inter-play of different and often opposing physical processes included in such complex nonlinear models, as the end results are not always easy to interpret. A consistent physical formulation for the wave-current interaction, such as that shown in Arduin et al. (2008), will help radiate more light on the explanation on the 3D results presented in this chapter.

Since the efficiency of our wave-current coupled model is good and only requires little computational resource, we advocate the use of wave-current coupled models in all scientific and engineering studies, especially the regions inside the surf zone. Neglecting the wave-current interactions is an assumption that can hardly be justified in wave-dominated coasts and downstream portions of estuaries.

Table 3-1 Station information and availability of observations during Hurricane Isabel used in this study.

Station ID	Station Name	Coordinates (degree)		Observations*		
		Latitude (N)	Longitude (W)	Water Level	Winds	Waves
NOAA						
8570283	Ocean City Inlet, MD	38.328	75.092	X		
8571892	Cambridge, MD	38.573	76.068	X	X	
8573364	Tolchester Beach, MD	39.213	76.245	X	X	
8574680	Baltimore, MD	38.267	76.578	X		
8575512	Annapolis, MD	38.983	76.48	X		
8577330	Solomons Island, MD	38.3	76.452	X		
8594900	Washington, DC	37.873	77.022	X		
8632200	Kiptopeke Beach, VA	37.167	75.988	X	X	
8635150	Colonial Beach, VA	38.252	76.96	X		
8635750	Lewisetta, VA	37.987	76.463	X	X	
8636580	Windmill Point, VA	37.615	76.29	X		
8637624	Gloucester Point, VA	37.247	76.5	X		
8638610	Sewells Point, VA	36.947	76.33	X	X	
8638863	Chesapeake Bay BT, VA	36.967	76.113	X	X	
8639348	Money Point, VA	36.778	76.302	X	X	
8651370	Duck Pier, NC	36.183	75.747	X	X	
NDBC						
44004		38.484	70.433		X	X
44008		40.502	69.247		X	X
44009		38.464	74.702		X	X
44017		40.692	72.048		X	X
44025		40.25	73.166		X	X
41001		34.7	72.73		X	X
41002		32.382	75.415		X	X
41008		31.4	80.87		X	X
41025		35.01	75.4		X	X
CHLV2		36.91	75.71		X	X
VIMS						
GP	Gloucester Point, VA	37.247	76.5	X		X

Table 3-2 Principal tidal constituents with periods (hours), tidal potential constants (m), and associated effective earth elasticity factors.

Species, j	n	Constituent	$T_{jn}$ (h)	$C_{jn}$ (m)	$\alpha_{jn}$
1	1	$K_1$	23.934470	0.141565	0.736
	2	$O_1$	25.819342	0.100514	0.695
	3	$Q_1$	26.868357	0.019256	0.695
2	1	$M_2$	12.420601	0.242334	0.693
	2	$S_2$	12.000000	0.112841	0.693
	3	$N_2$	12.658348	0.046398	0.693
	4	$K_2$	11.967235	0.030704	0.693

Table 3-3 Comparison of observed and predicted mean tidal amplitudes at 11 selected tidal gauge stations.

Stations	M2		S2		N2		K1	
	OBS	PRE	OBS	PRE	OBS	PRE	OBS	PRE
(unit: m)								
CBBT	0.38	0.37	0.07	0.09	0.09	0.09	0.06	0.07
Kiptopeke	0.38	0.37	0.07	0.08	0.08	0.08	0.06	0.07
Gloucester Point	0.35	0.31	0.07	0.07	0.07	0.07	0.05	0.05
Windmill Point	0.17	0.16	0.03	0.04	0.04	0.04	0.03	0.03
Lewisetta	0.18	0.18	0.03	0.04	0.04	0.04	0.02	0.03
Solomon's Island	0.16	0.17	0.02	0.03	0.03	0.04	0.03	0.04
Cambridge	0.23	0.22	0.03	0.04	0.04	0.05	0.05	0.05
Annapolis	0.13	0.12	0.02	0.02	0.03	0.03	0.06	0.06
Baltimore	0.16	0.17	0.02	0.02	0.04	0.04	0.07	0.07
Tolchester Beach	0.17	0.19	0.03	0.04	0.04	0.04	0.07	0.07
ARE* (%)		4.1		22.6		5.8		11.7
RMSE* (m)		0.016		0.01		0.005		0.006

\* ARE: mean absolute relative error; RMSE: root-mean-square error. Definitions of these statistical skill assessments can be found in Appendix A.

Table 3-4 Comparison of observed and predicted mean tidal phases at 11 tidal gauge stations.

Stations	M2		S2		N2		K1	
	OBS	PRE	OBS	PRE	OBS	PRE	OBS	PRE
(unit: degrees)								
CBBT	235.3	235.3	255.9	255.9	218.1	218.1	109.1	109.1
Kiptopeke	247.9	251.7	270.8	271.7	229.2	234.6	119.3	120.5
Gloucester Point	268.3	267	288.7	287.8	250.9	249.2	125.6	125.7
Windmill Point	317.3	326.6	334	344.7	297.2	309.8	148.7	159.4
Lewisetta	33.8	30.6	54.7	54.3	7.6	11.1	205	210.8
Solomon's Island	54.2	47.9	70.5	74.3	32.4	27.8	243.7	238.4
Cambridge	114.7	91.6	139	120.2	94	72.1	269.4	252.2
Annapolis	147.2	133.1	175	157.7	126	115	283.3	272.2
Baltimore	193.9	191.2	213.4	216.8	173.4	170.5	296.6	281.5
Tolchester Beach	202.7	194.4	227.4	222	176	173	287.9	277.5
ARE* (%)		6.1		3.7		10.3		3.2
RMSE* (deg)		9.8		9.1		9.2		9.7

\* ARE: mean absolute relative error; RMSE: root-mean-square error. Definitions of these statistical skill assessments can be found in Appendix A.

Table 3-5 Locations of NOAA stations around Gulf of Mexico used in the Hurricane Ivan case and the statistical analysis for the comparisons between modeled and NOAA predicted tide.

#	Location	Longitude	Latitude	Grid Node	Correlation Coefficient
	City, State	Dec Deg	Dec Deg	#	Manning Coefficient = 0.025
1	Calcasieu Pass, LA	-93.3429	29.7682	539669	0.91
2	Lake Charles, LA	-93.2217	30.2236	1207579	0.76
3	Freshwater Canal Locks, LA	-92.3050	29.5550	746226	0.94
4	Cypremort Point, LA	-91.8800	29.7134	892292	<b>0.30</b>
5	Lawma, Amerada Pass, LA	-91.3381	29.4496	768264	0.79
6	Port Fourchon, LA	-90.2091	29.1122	525506	0.88
7	New Canal Station, LA	-90.1134	30.0272	1144526	<b>0.26</b>
8	Grand Isle, LA	-89.9545	29.2676	441647	0.93
9	Shell Beach, LA	-89.6733	29.8681	668799	<b>0.63</b>
10	Pilots Station East, LA	-89.4074	28.9319	258357	0.93
11	Bay Waveland Yacht Club, MS	-89.3258	30.3264	420372	0.91
12	Gulfport Harbor, MS	-89.0817	30.3600	334930	0.93
13	Pascagoula NOAA Lab, MS	-88.5630	30.3679	243627	0.83
14	Dock E, Port of Pascagoula, MS	-88.5054	30.3477	240773	0.91
15	Dauphin Island Hydro, AL	-88.0603	30.2485	214500	0.91
16	Panama City, FL	-85.7113	30.0972	214538	0.79
17	Apalachicola, FL	-84.9773	29.7136	217994	0.73
18	Cedar Key, FL	-83.0317	29.1350	230412	0.93
19	Clearwater Beach, FL	-82.8317	27.9783	209986	0.94
20	Naples, FL	-81.8239	26.1434	207293	0.93
21	Key West, FL	-81.8259	24.5573	190261	0.83
22	Vaca Key, FL	-81.1210	24.7294	178258	<b>0.70</b>

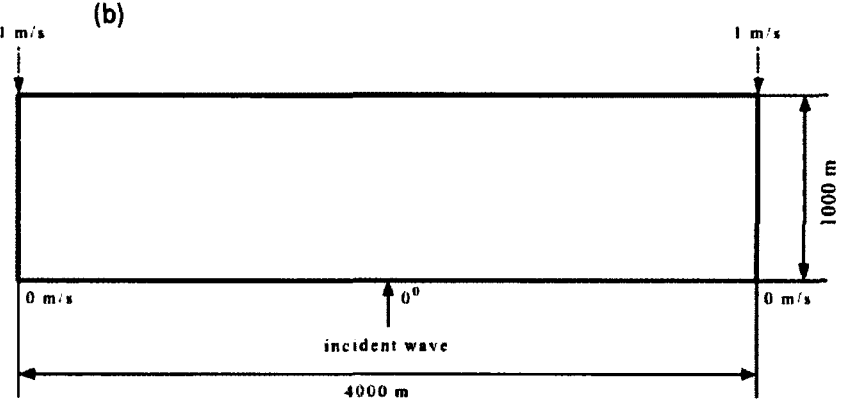
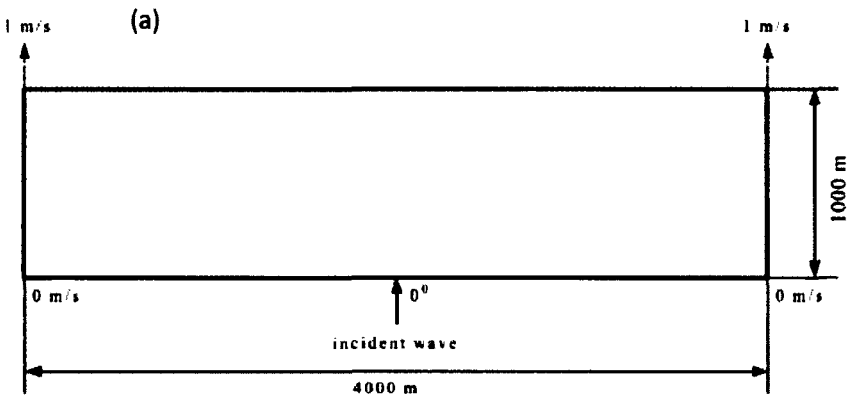
Table 3-6 Locations of NOAA stations along East Coast used in the Hurricane Ivan case and the statistical analysis for the comparisons between modeled and NOAA predicted tide.

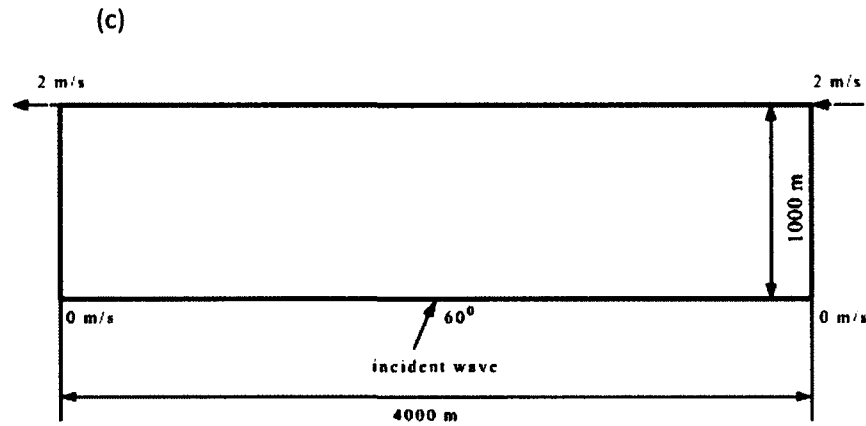
#	Location	Longitude	Latitude	Grid Node	Correlation Coefficient
	City, State	Dec Deg	Dec Deg	#	Manning Coefficient = 0.025
1	Trident Pier, FL	-80.5917	28.4150	131814	0.98
2	Fort Pulaski, GA	-80.9017	30.2236	138966	0.90
3	Charleston, SC	-79.9250	32.7817	121966	0.88
4	Springmaid Pier, SC	-78.9183	33.6550	119577	0.98
5	Wrightsville Beach, NC	-78.7867	34.2133	119591	0.99
6	Duck, NC	-75.7467	36.1833	90909	0.98
7	CBBT, VA	-76.1133	36.9667	115943	0.99
8	Atlantic City, NJ	-74.4183	39.3550	92348	0.99
9	Sandy Hook, NJ	-74.0083	40.4667	106079	0.99
10	Newport, RI	-71.3267	41.5050	81699	0.96



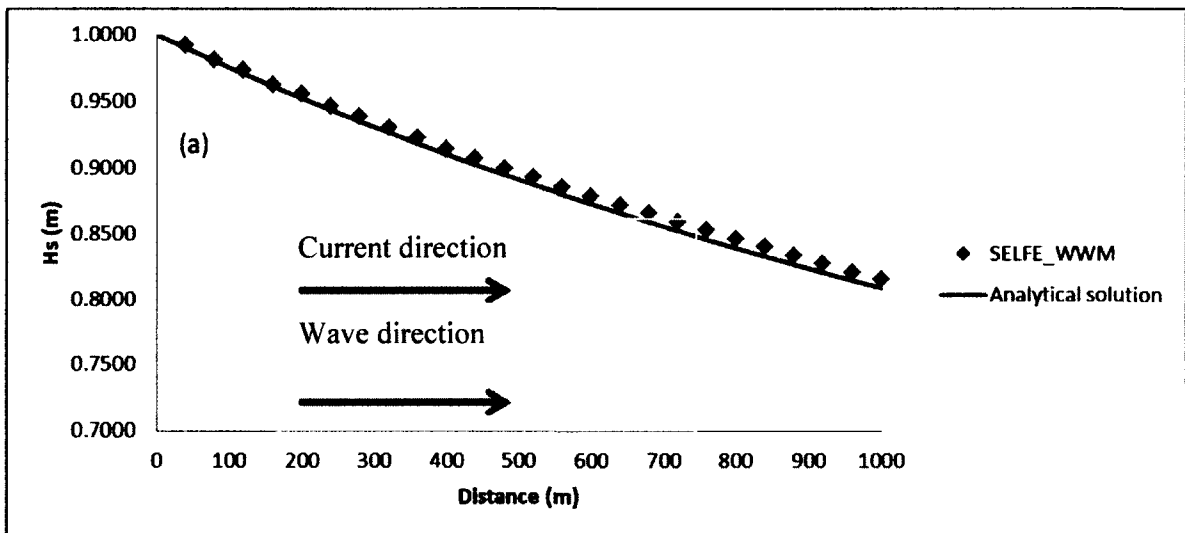
Table 3-7 Results of Timing tests for the model efficiency of three models: ADCIRC, FVCOM, and SELFE.

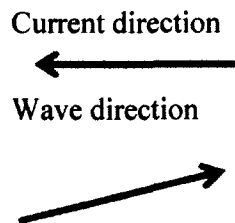
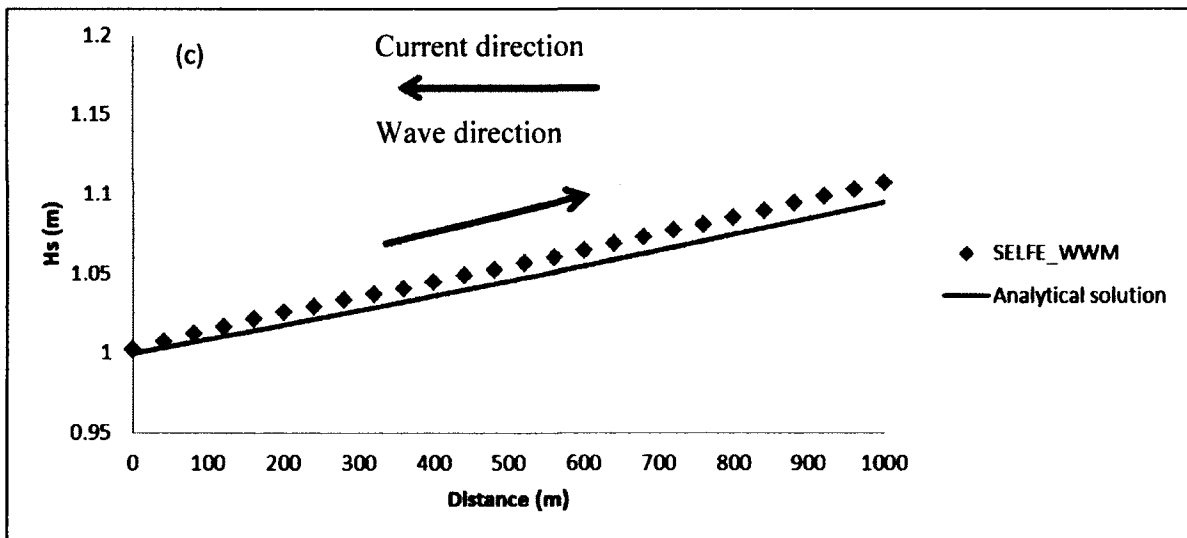
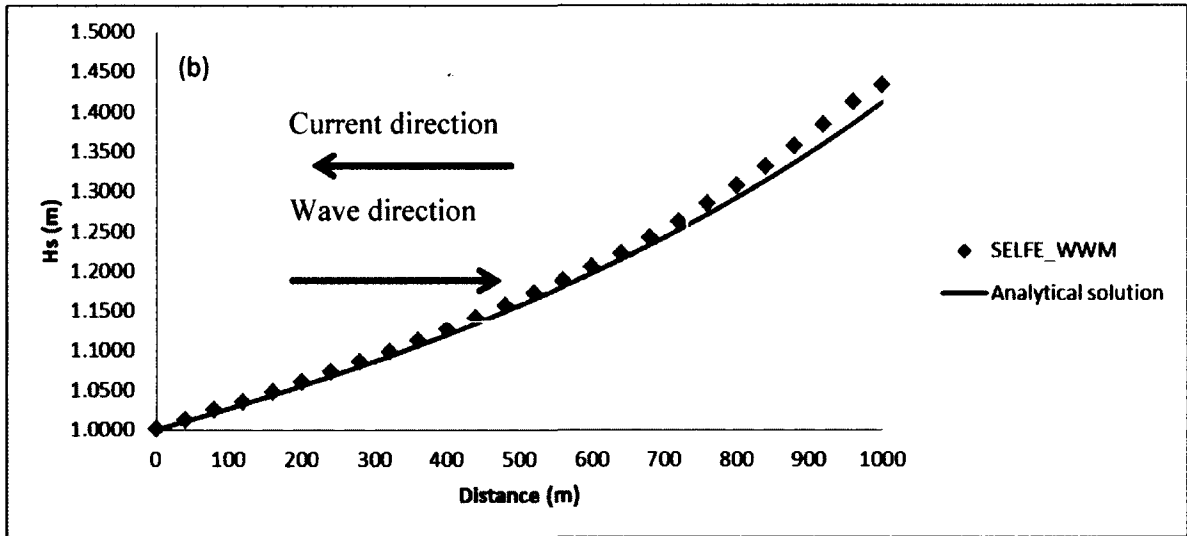
<b>MODEL</b>	<b>Run ID</b>	<b>dt (sec)</b>	<b>Cores</b>	<b>Simulation Days</b>	<b>Wall Time (min)</b>
ADCIRC	timing test	1	512	10	378
FVCOM	timing test	1.2	512	10	266
SELFE	timing test	120	512	10	107





**Figure 3-1** Schematic of the surface wave propagation in a domain with ambient water current. (a) Following current case; (b) opposing current case; and (c) slanting current case.





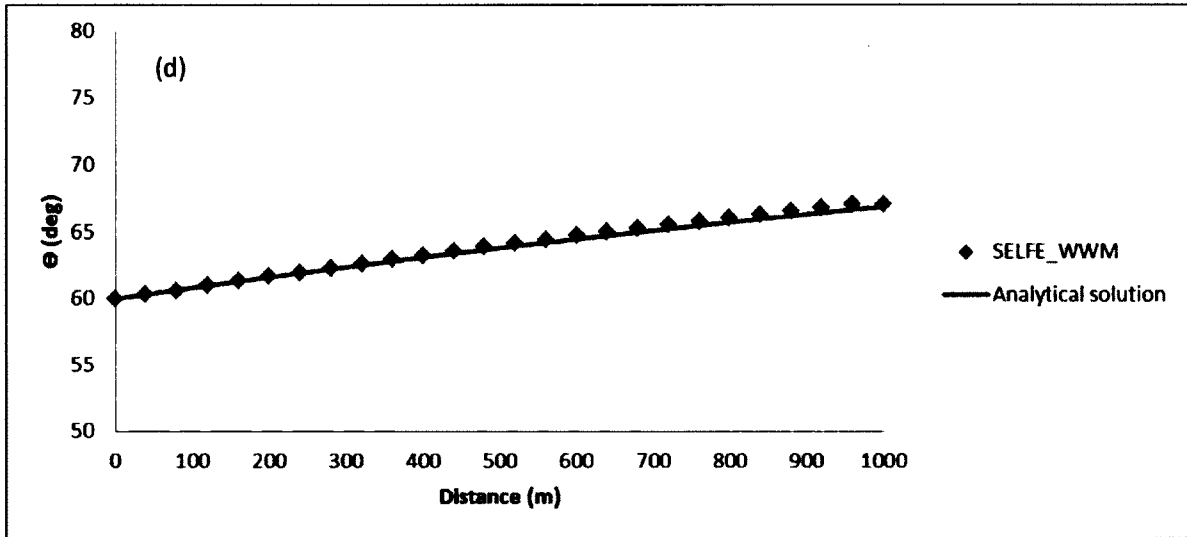


**Figure 3-2** Comparisons of SELFE-WWM II with the analytical results for (a) following current field; (b) opposing current field; (c) slanting current field (significant wave height); and (d) slanting current field (wave direction).

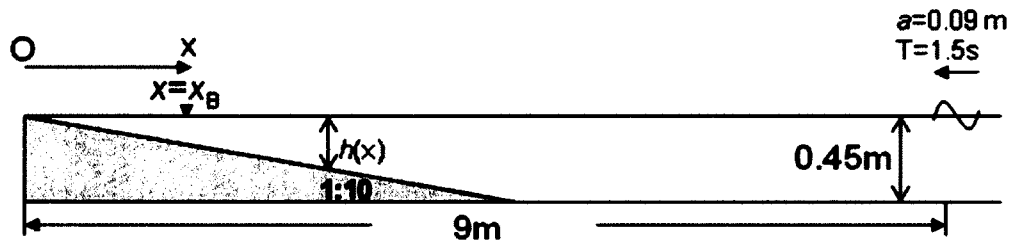


**Figure 3-3** Sketch of sloping beach used in the Longuet-Higgins and Stewart wave set-up test.



**Figure 3-4** Top view of the grid domain used in the Longuet-Higgins and Stewart wave set-up test.

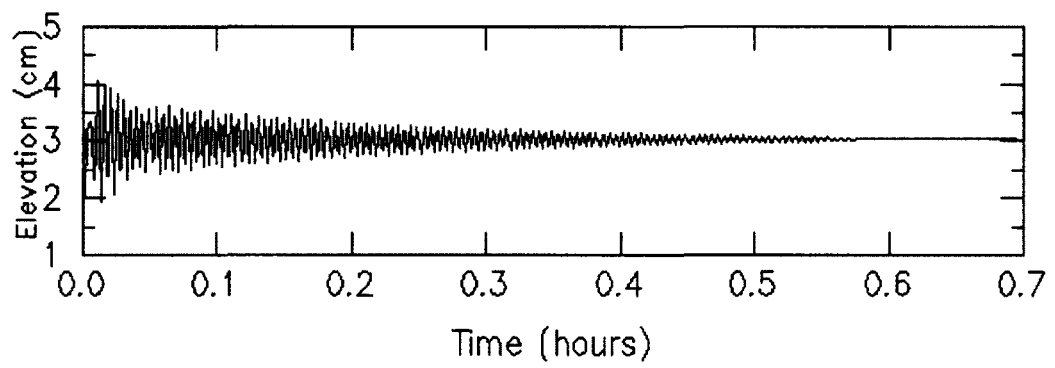


**Figure 3-5** Convergence to steady state for elevation at  $x=0.38\text{m}$  ( $h=0.038\text{m}$ ).

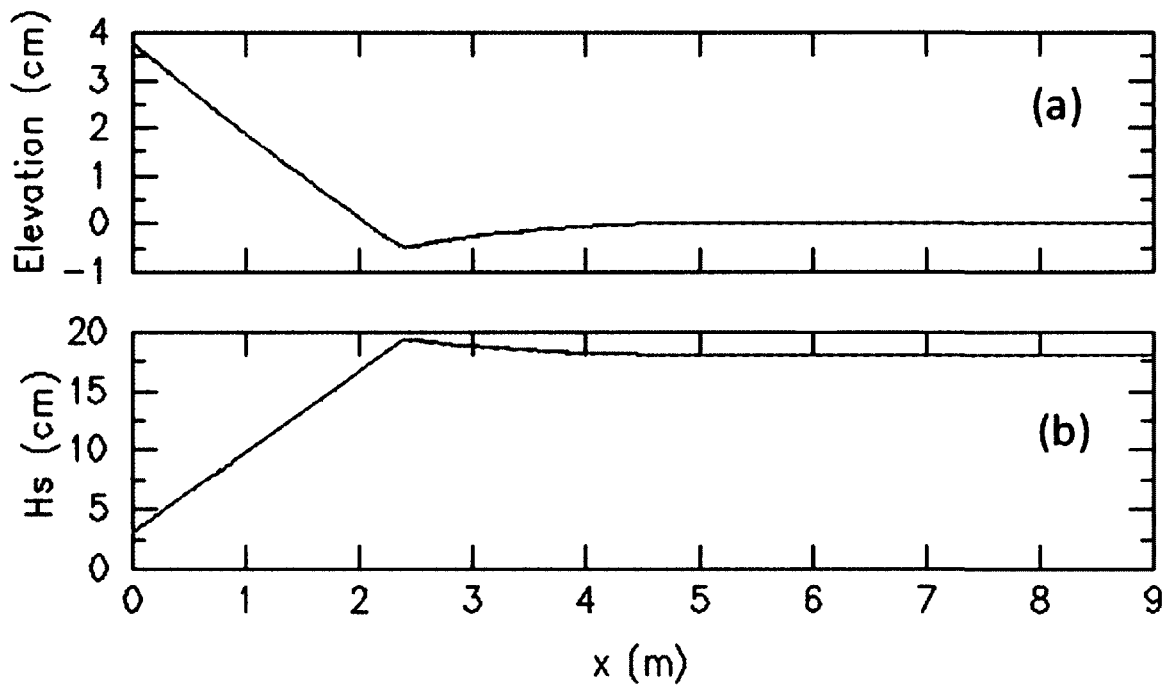


**Figure 3-6** Comparison of analytical (dotted line) and numerical solutions (red solid line) for (a) wave-induced set-up and (b) significant wave height.



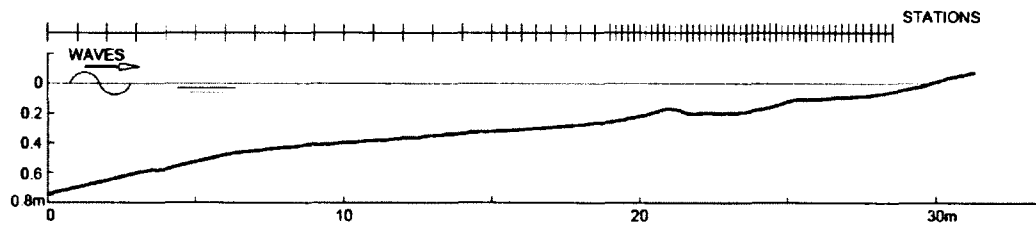


**Figure 3-7** Sketch of Boers (1996) laboratory set-up.

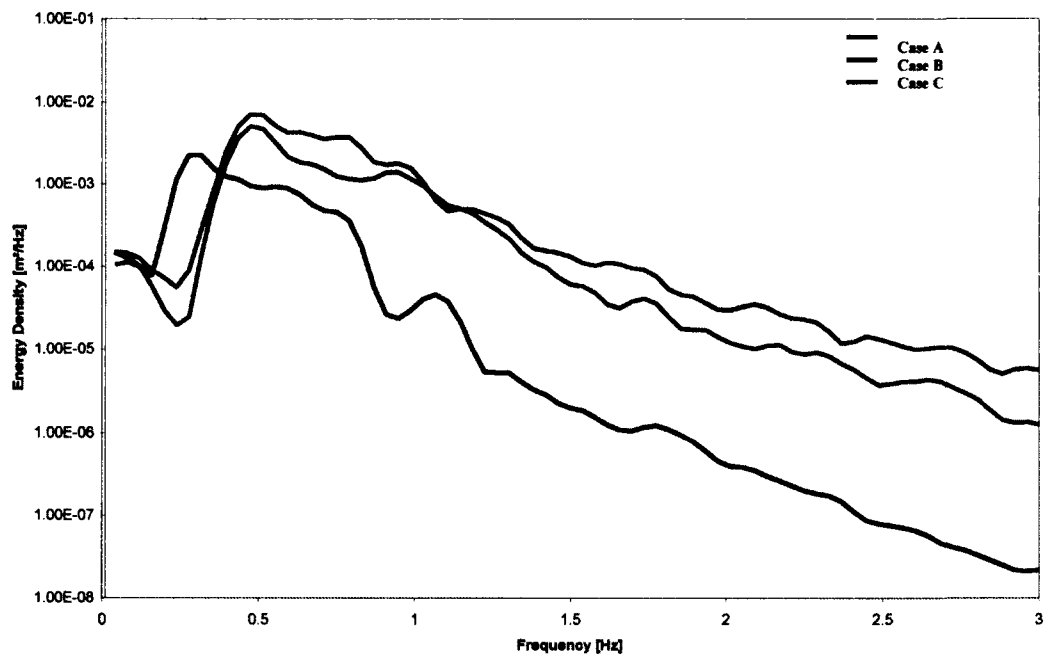


**Figure 3-8** Wave boundary conditions for Boers (1996) laboratory set-up.

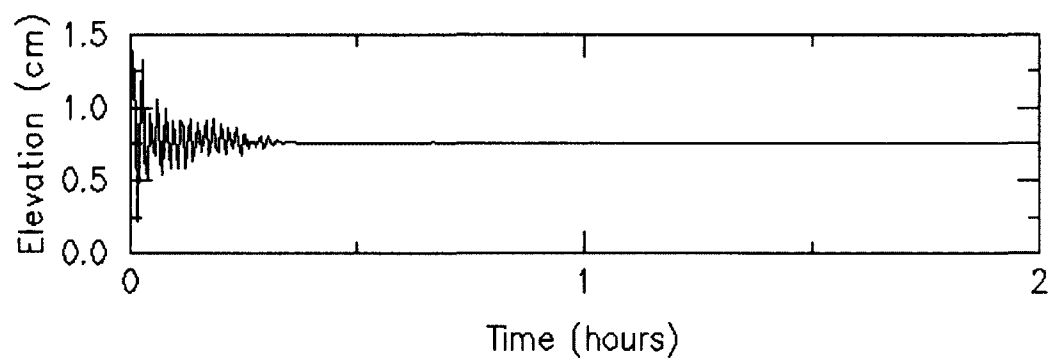


**Figure 3-9** Convergence to a steady state for elevation for the test of Boers (1996) laboratory set-up: Case A at  $x=28.6$  m.

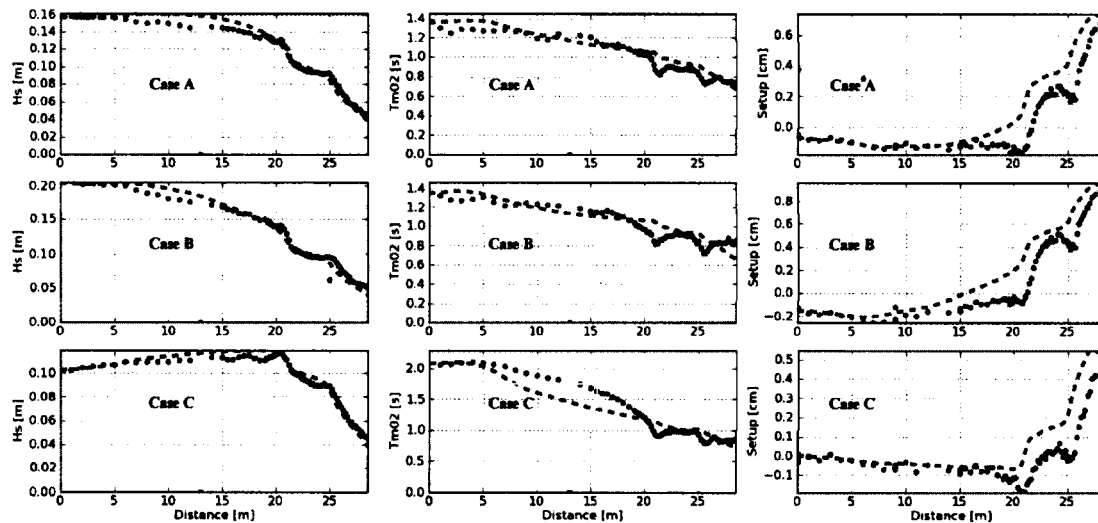
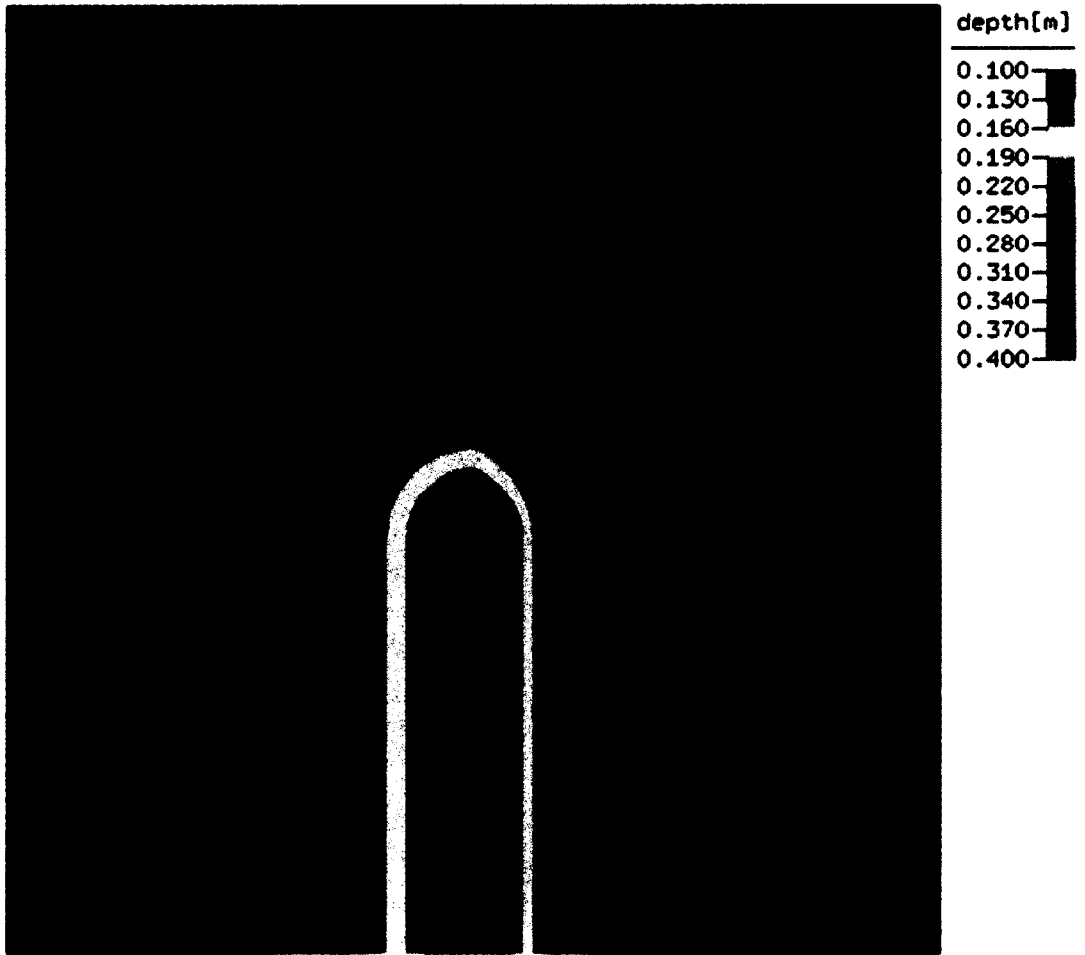
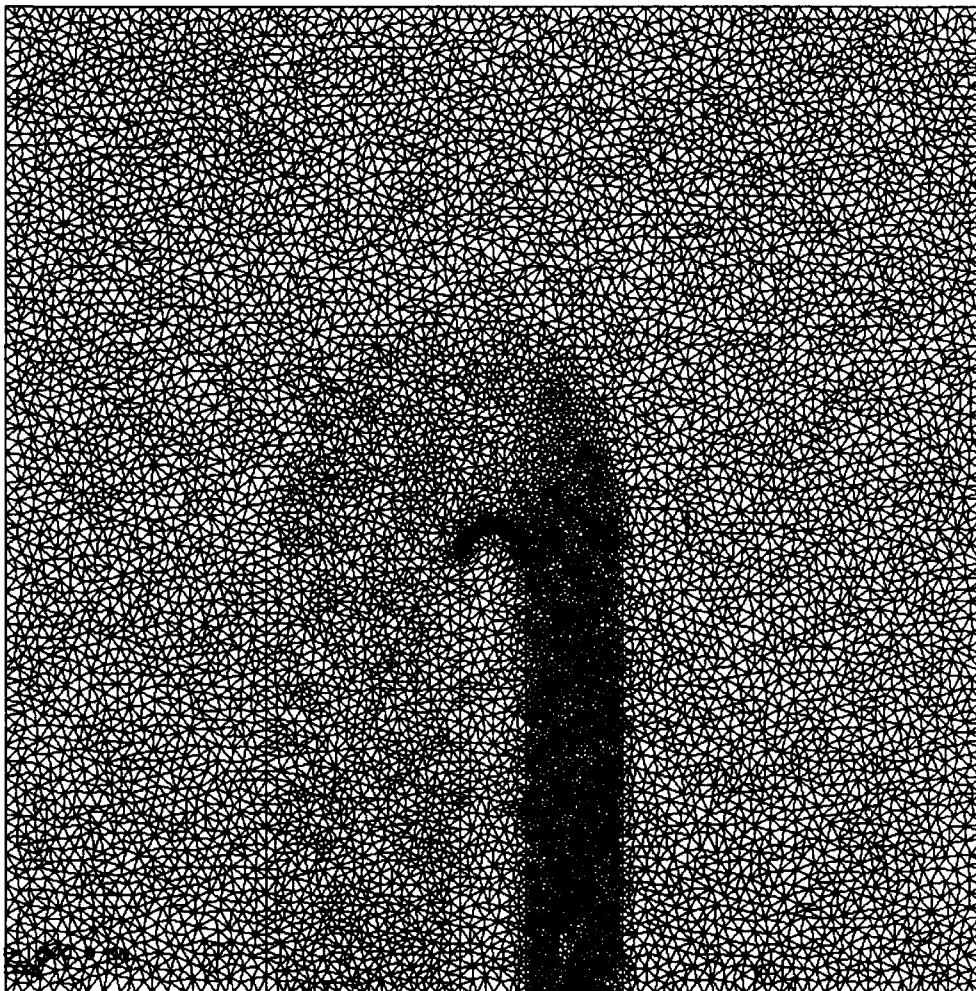


**Figure 3-10** Comparison of wave heights, zero down crossing periods (average period), and wave-induced set-up for the three investigated cases between lab data (dots) and model results (dashed lines) under steady state conditions.

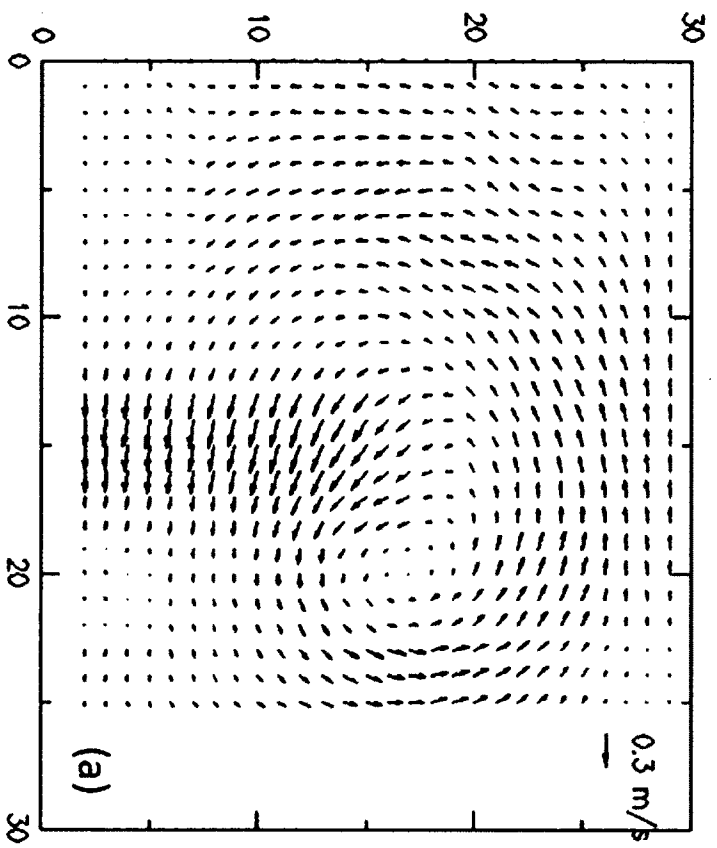
(a)

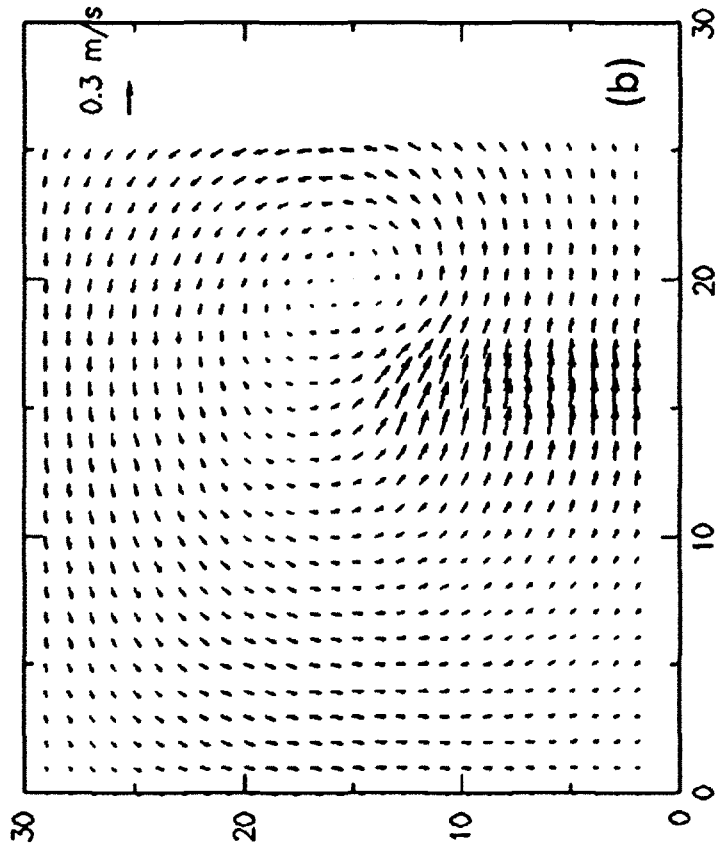


(b)

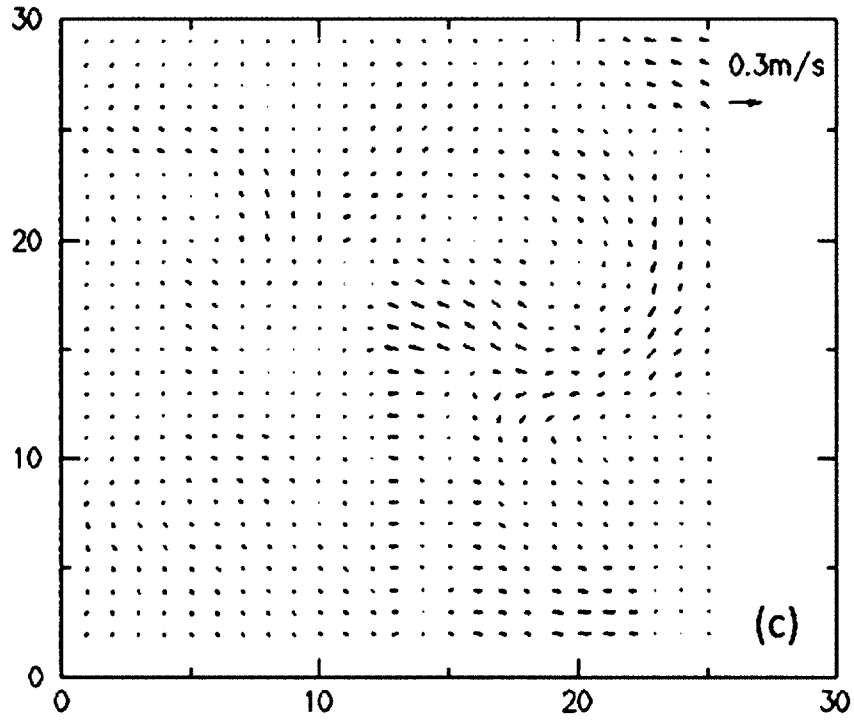


**Figure 3-11** (a) Topography of HISWA Experiment of Dingemans (L51 test); (b) Top view of the grid domain used in L51 test.

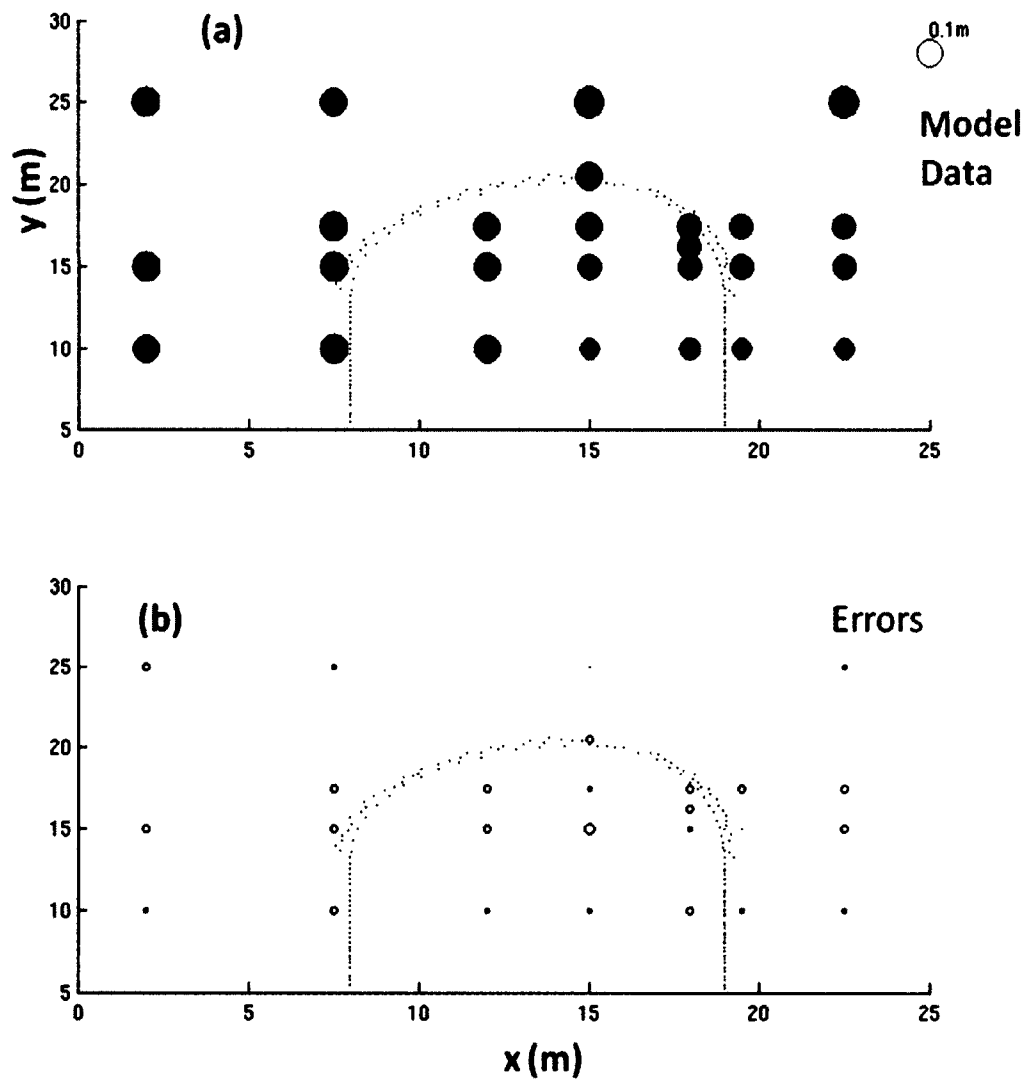




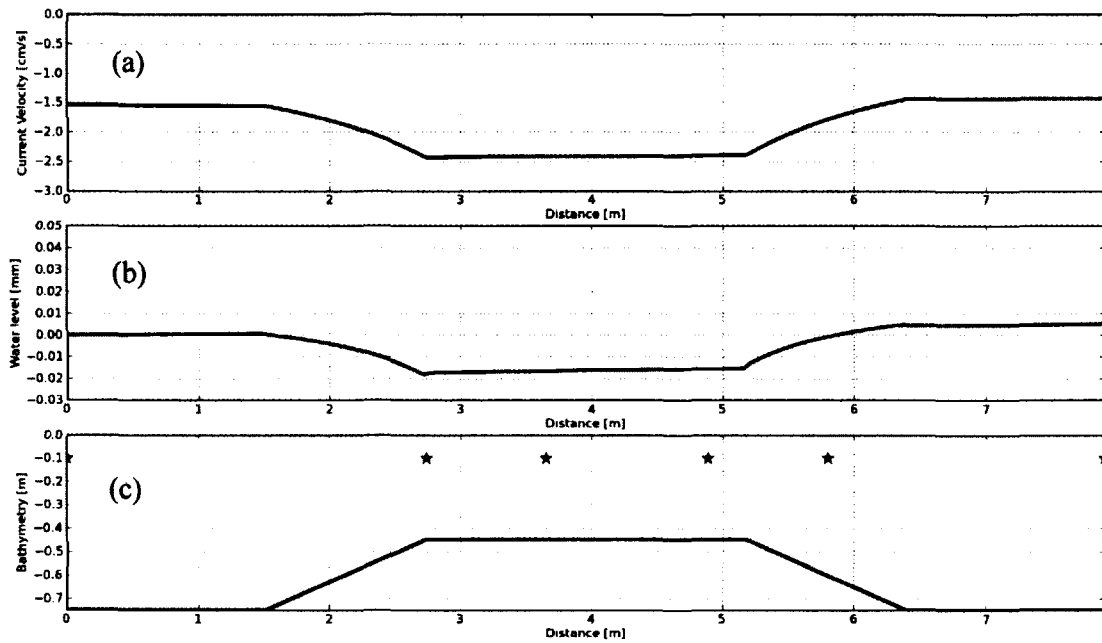




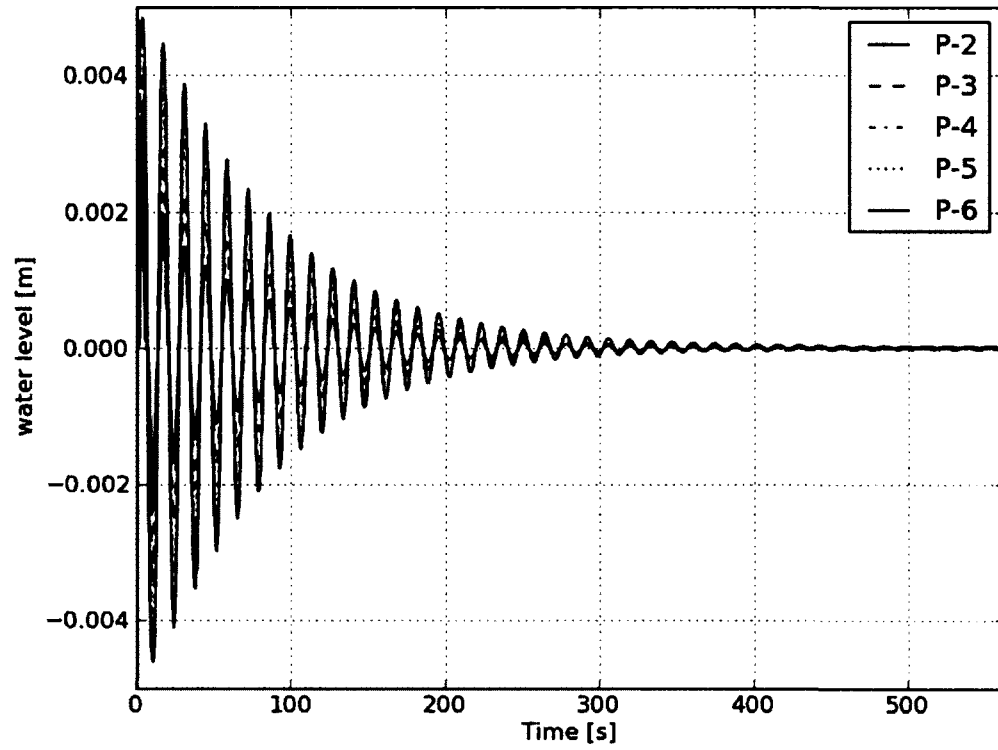
**Figure 3-12** Comparison of wave-induced surface currents from (a) laboratory data; (b) model results; (c) absolute errors ((b)-(a)).



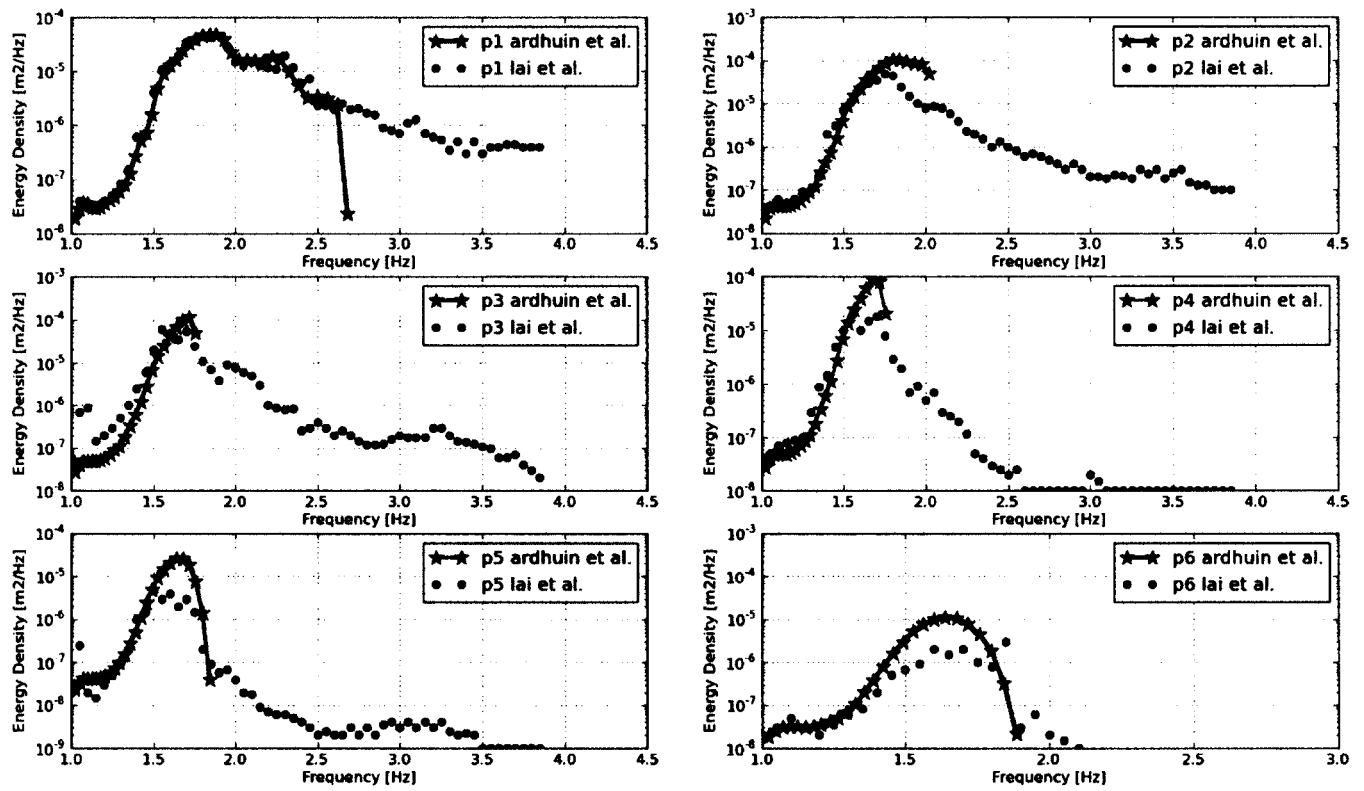
**Figure 3-13** (a) Comparison of  $H_s$  at 26 stations between the laboratory data (red dot) and model results (blue circles); the scale is shown at the upper right corner, and the dotted line is 0.4 m isobaths; (b) absolute errors (model-data).



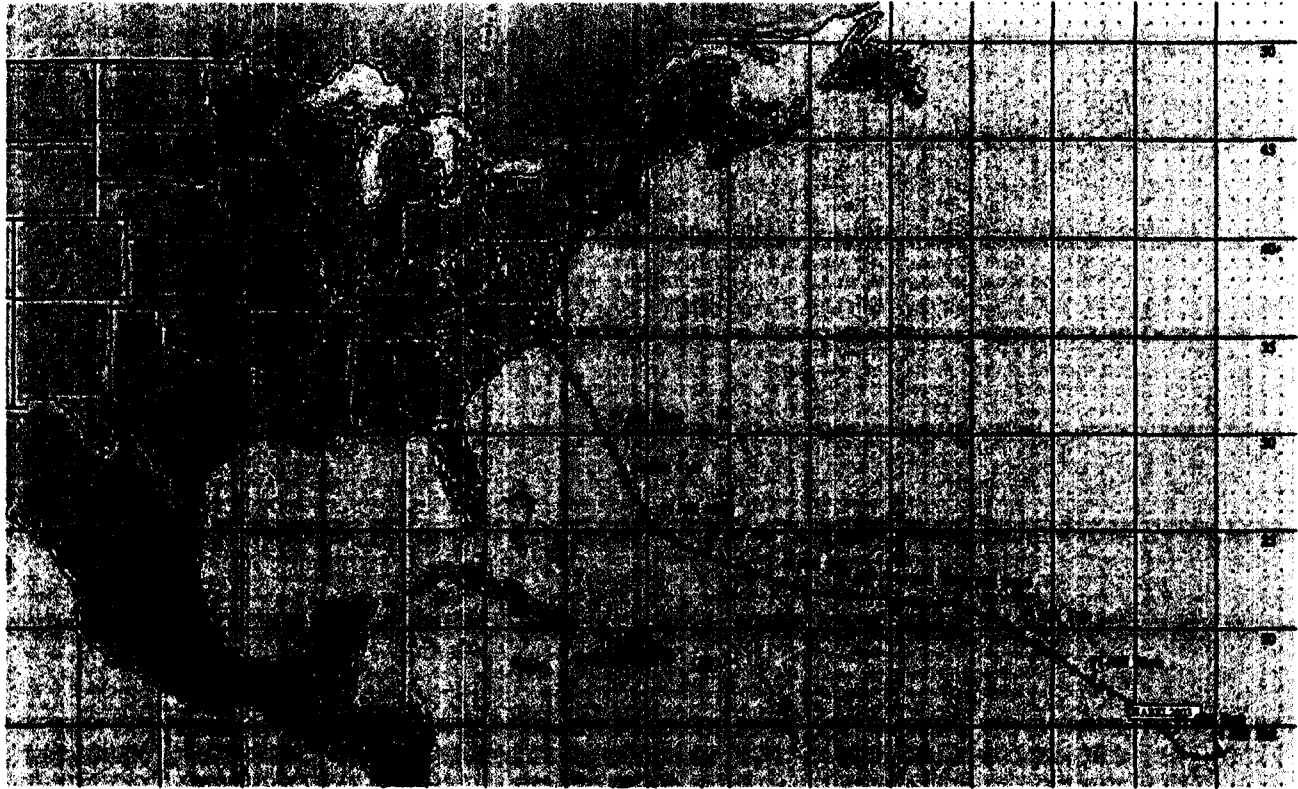
**Figure 3-14** Along-channel profiles of the Lai et al. (1989) experiment (a) current velocity, (b) water level, and (c) bathymetry. The station locations P-1 to P-6 are marked with a star from left to right increasing station number.



**Figure 3-15** Convergence history of elevation along the 5 measurement locations (see Fig. 3-14).

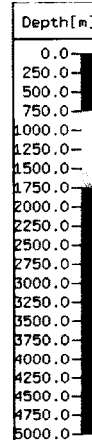


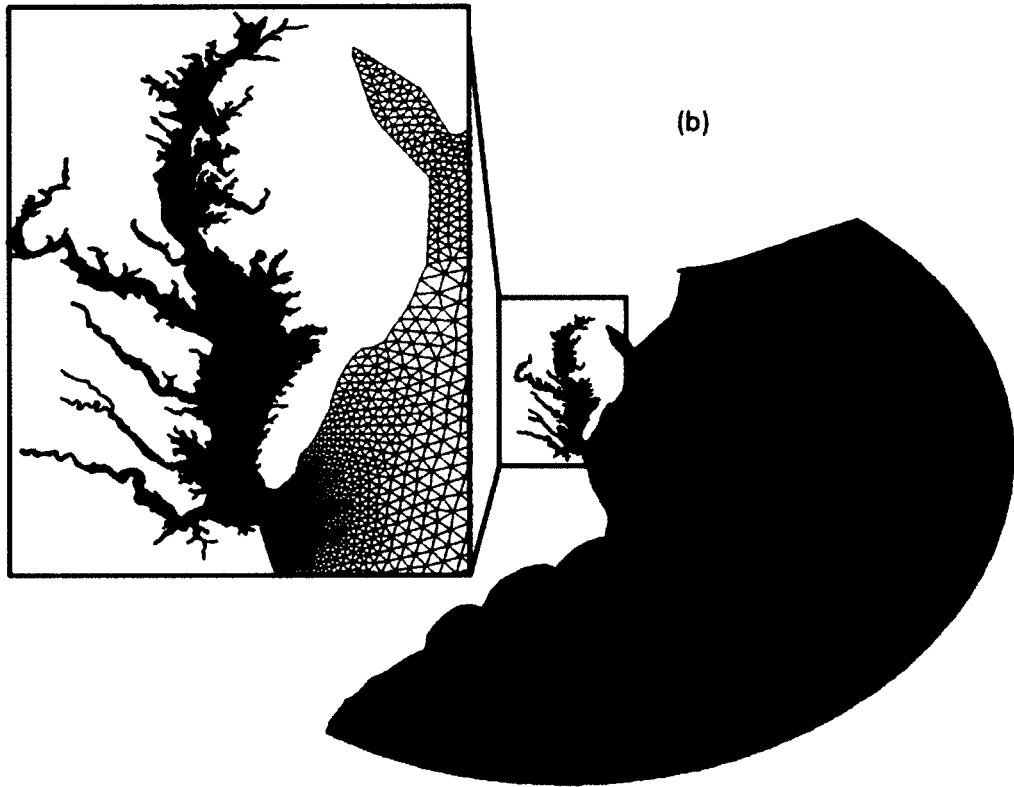
**Figure 3-16** Measured (dashed) and computed wave spectra (solid) at the given locations (see Fig. 3-14) in a logarithmic scale.



**Figure 3-17** Track of Hurricane Isabel (from [www.erh.noaa.gov](http://www.erh.noaa.gov)).

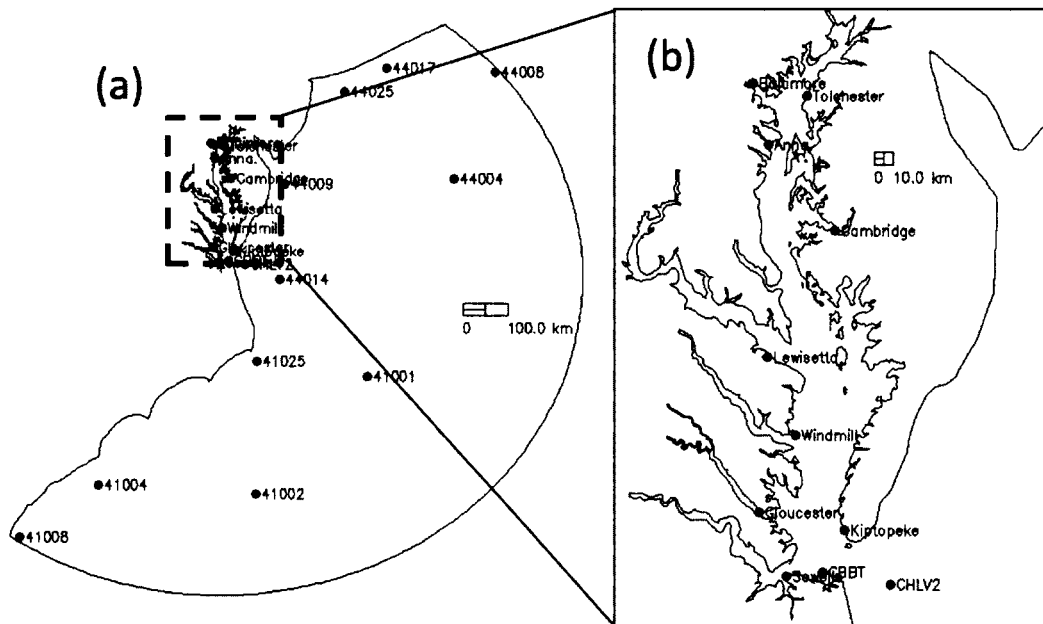
(a)



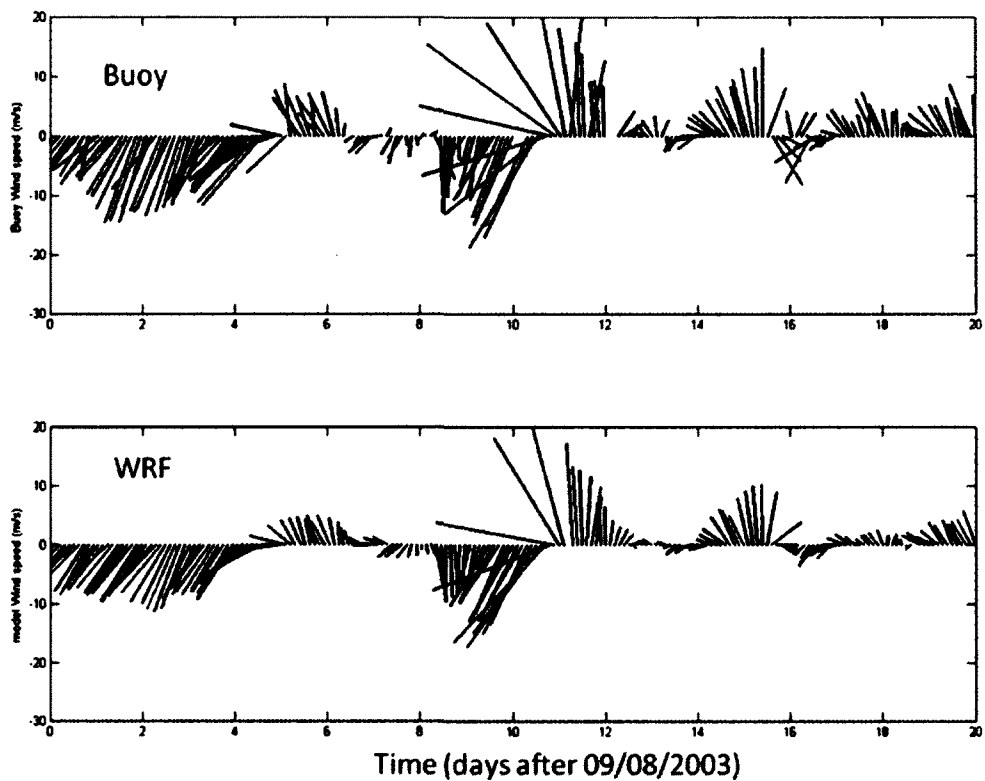


**Figure 3-18** (a) Bathymetry in the whole computational domain, and (b) zoom-in of the Chesapeake Bay area with the computational mesh.

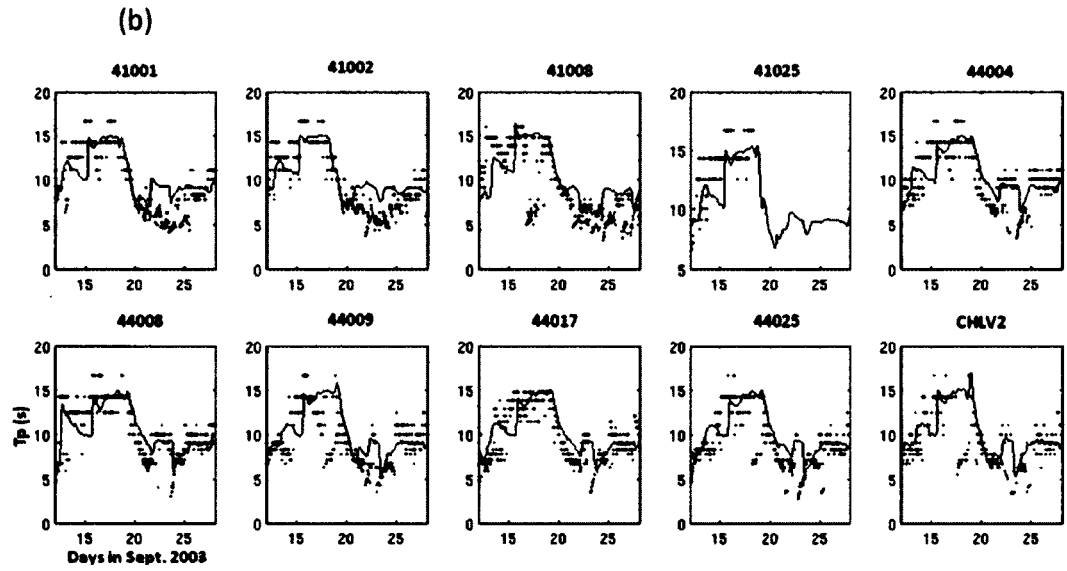
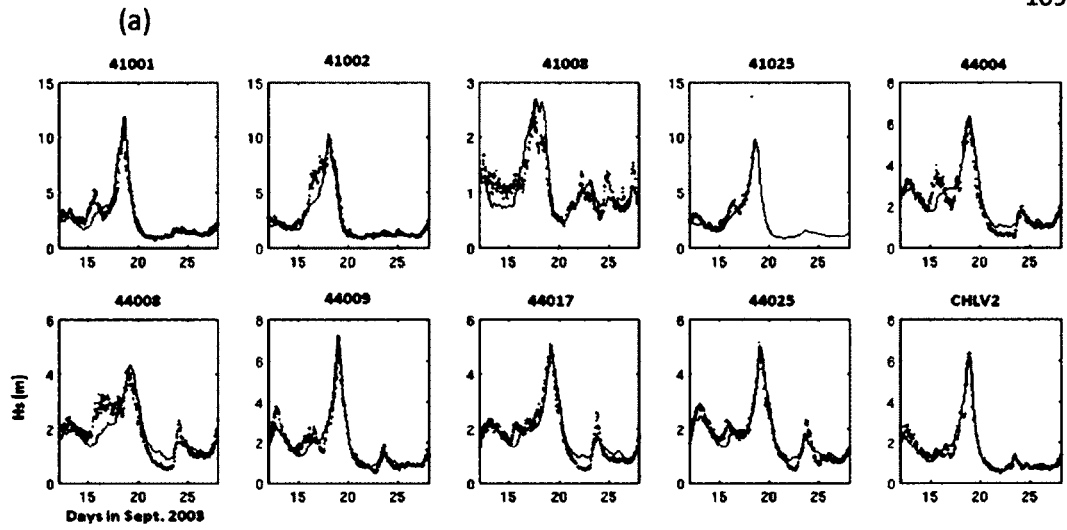




**Figure 3-19** (a) Locations of the wave buoys, and (b) tidal gauges inside the Chesapeake Bay area.



**Figure 3-20** Comparison between modeled and measured wind at Chesapeake Bay Light buoy (CHLV2, Fig. 3-19).



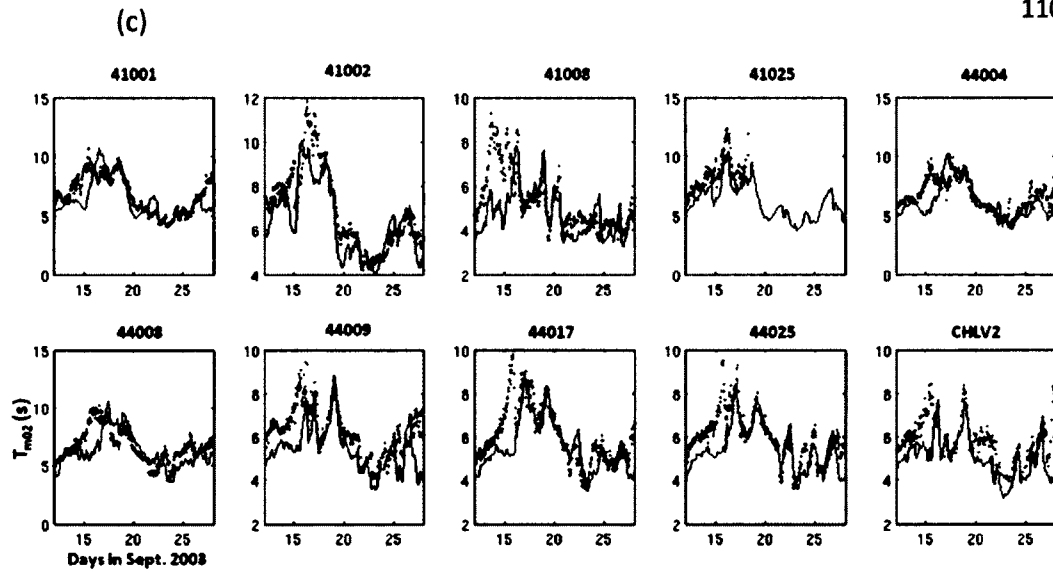


**Figure 3-21** Comparison of (a)  $H_s$ ; (b)  $T_p$ ; and (c)  $T_{m02}$ , between modeled results (solid lines) and buoy observation (circles).

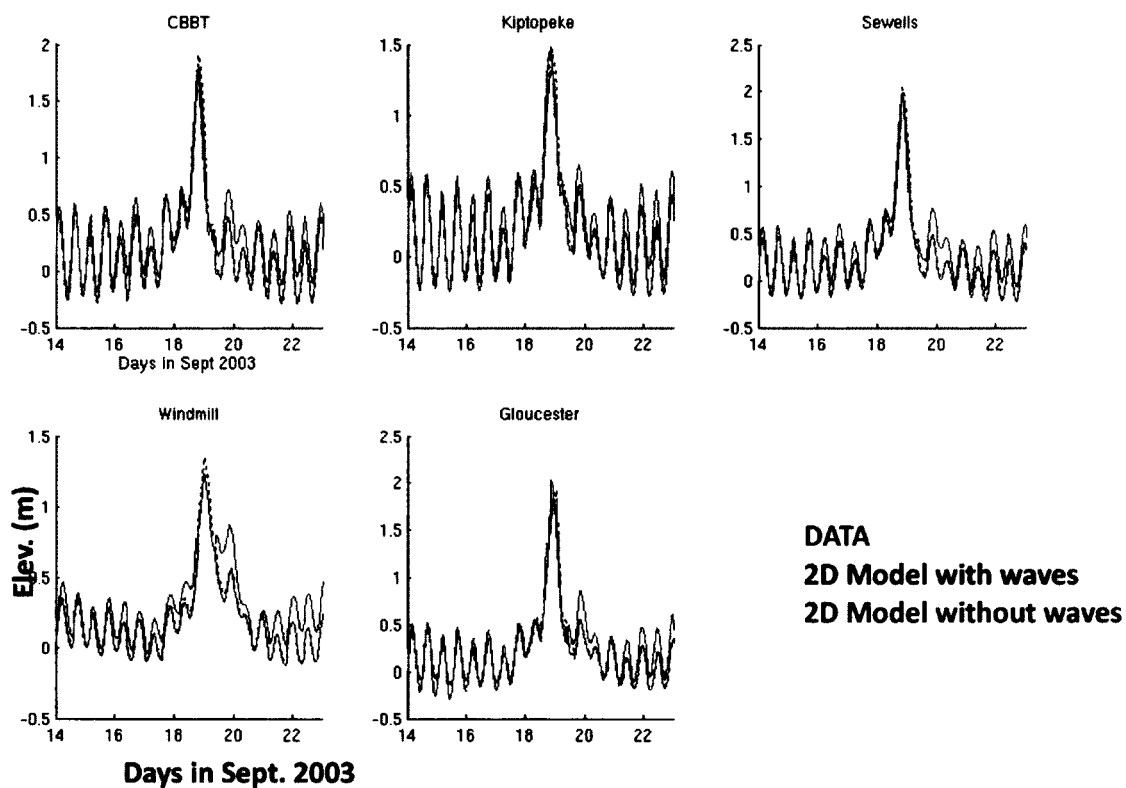


**Figure 3-22** Comparison of elevations predicted from 2D mode with/without waves. Close-ups near the surge peaks can also be seen in Fig. 3-23. Note that the observation has a gap near the maximum surge peak at Station Windmill Pt.

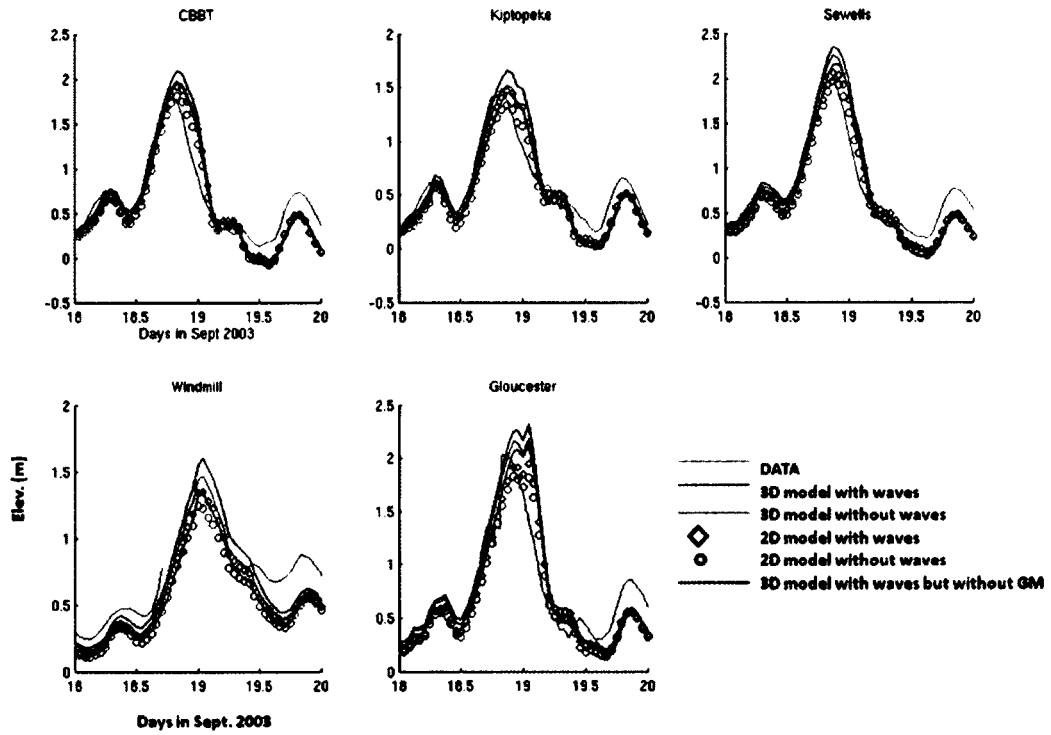


**Figure 3-23** Comparison of elevations predicted from 2D and 3D modes with/without waves effects.

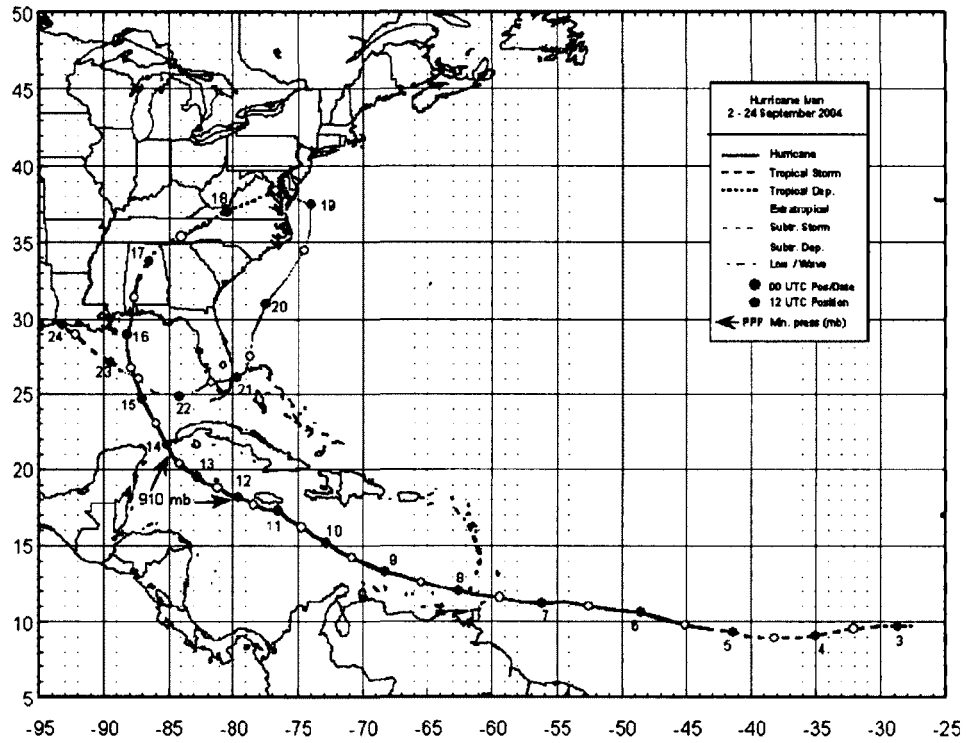


**Figure 3-24** Best track for Hurricane Ivan, 2-24 September 2004 (from Stewart, 2005, Tropical Cyclone Report Hurricane Ivan, NHC).

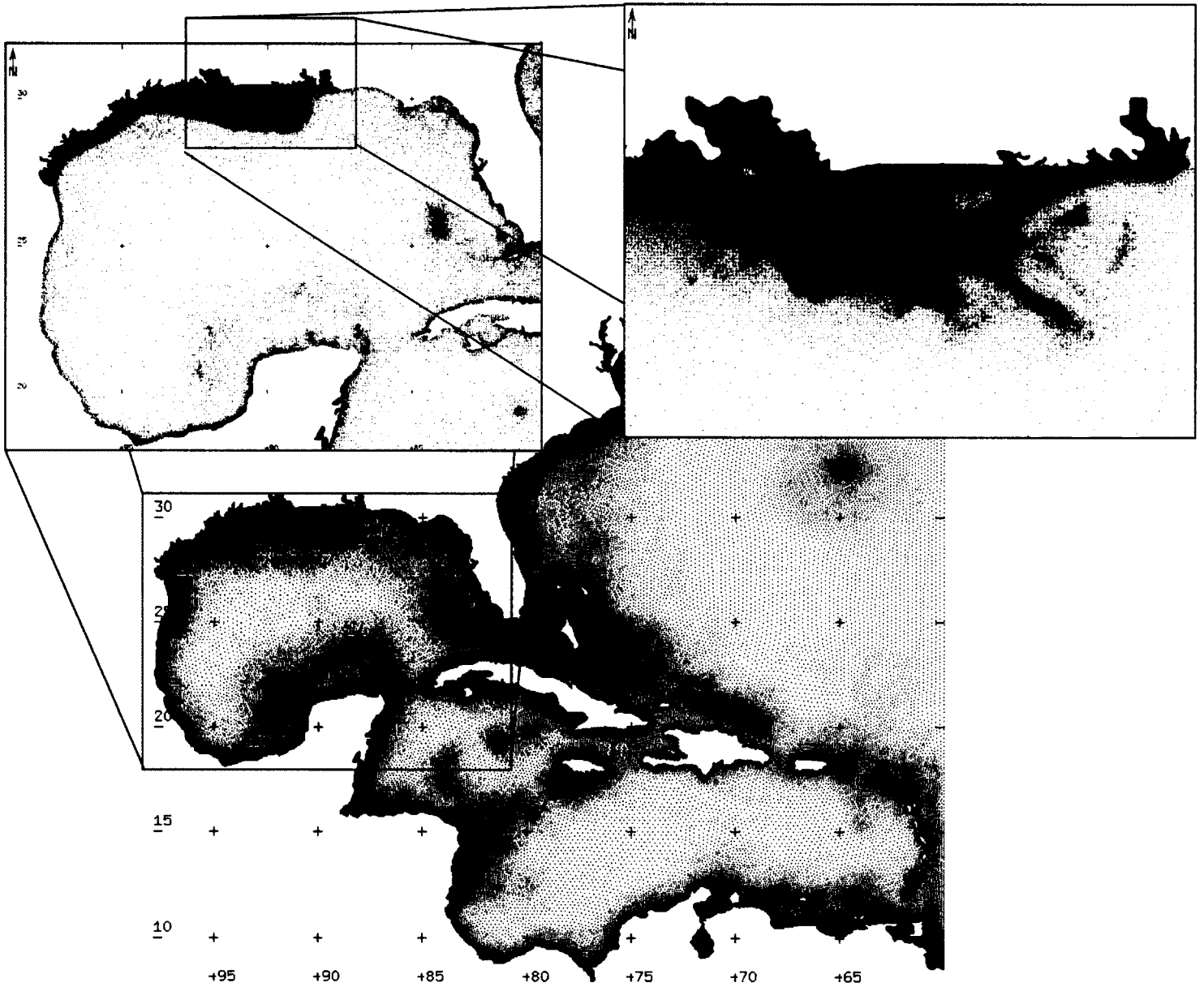
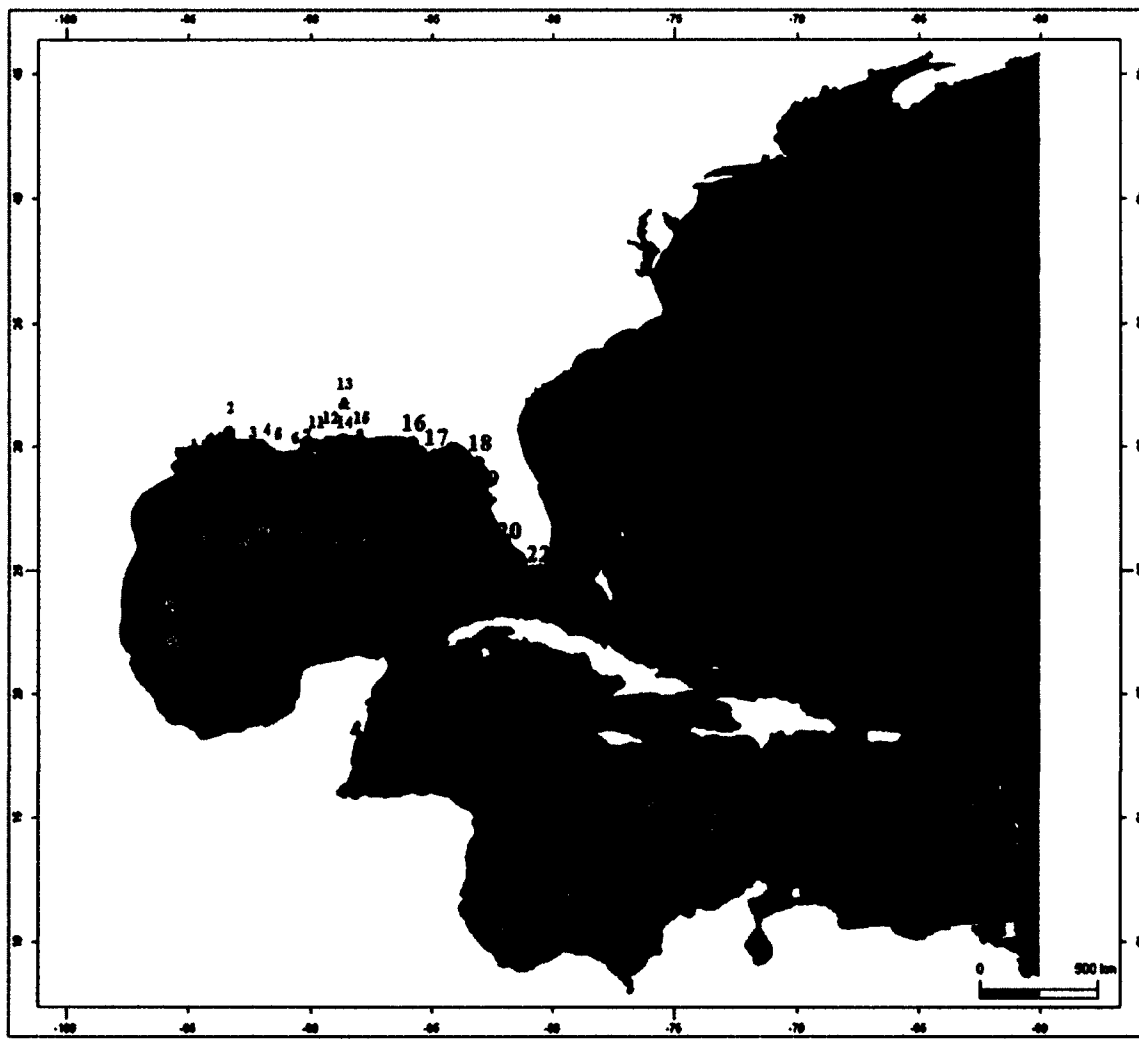


**Figure 3-25** Model domain and grid for Hurricane Ivan



(a)



Legend

1	Calcasieu Pass, LA
2	Lake Charles, LA
3	Freshwater Canal Locks, LA
4	Cypremort Point, LA
5	Lawma, Amerde Pass, LA
6	Port Fourchon, LA
7	New Canal Station, LA
8	Grand Isle, LA
9	Shell Beach, LA
10	Pilots Station East, LA
11	Bay Waveland Yacht Club, MS
12	Gulfport Harbor, MS
13	Pascagoula NOAA Lab, MS
14	Dock E, Port of Pascagoula, MS
15	Dolphin Island Hydro, AL
16	Panama City, FL
17	Apalachicola, FL
18	Cedar Key, FL
19	Clearwater Beach, FL
20	Naples, FL
21	Key West, FL
22	Vaca Key, FL



(b)

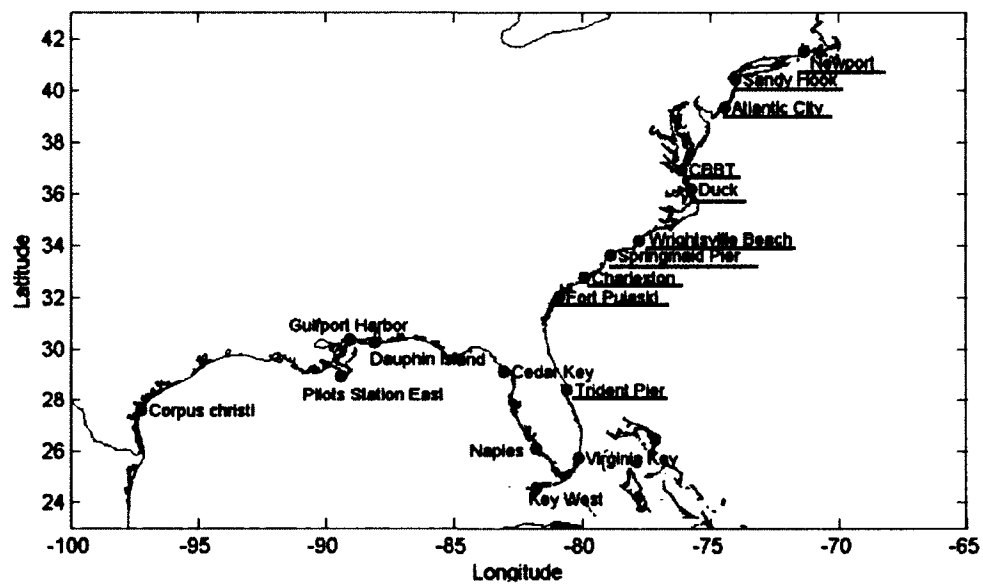


**Figure 3-26** (a) Model domain with bathymetry (m) and locations of 22 NOAA tidal gauge stations around Gulf of Mexico and (b) 10 NOAA tidal gauge stations (red under line) along East Coast we use to compare with model results.

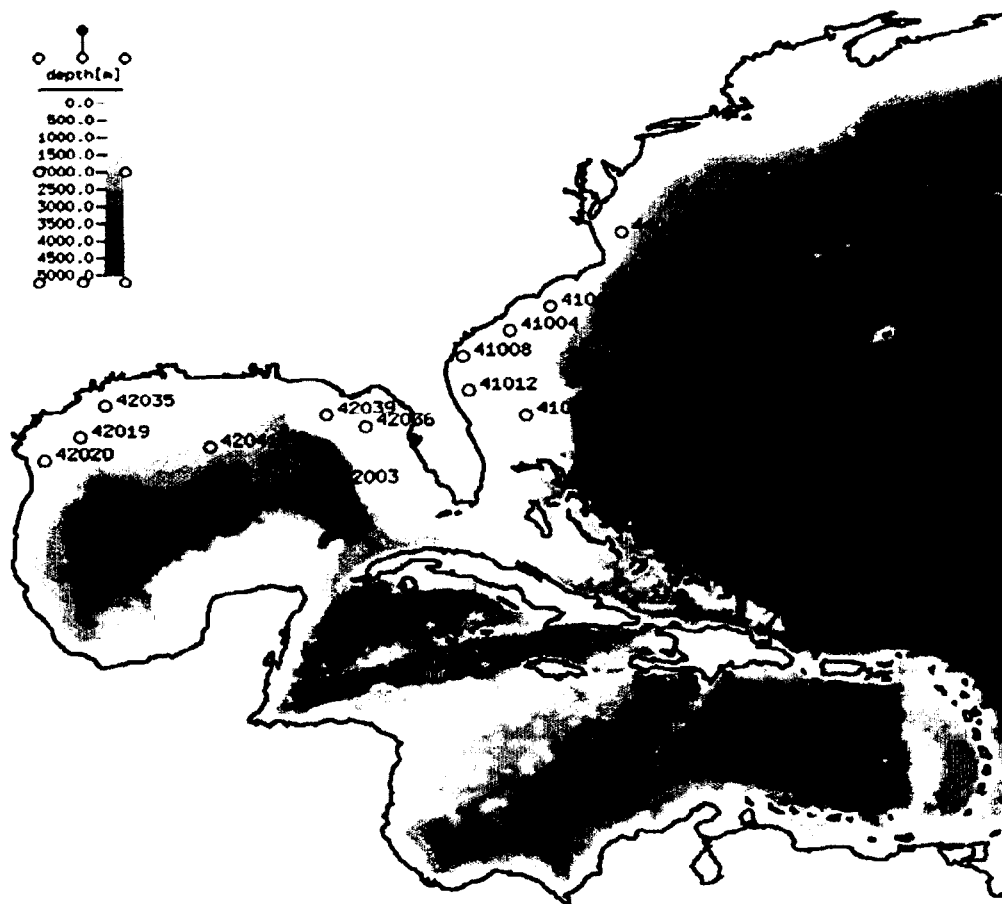
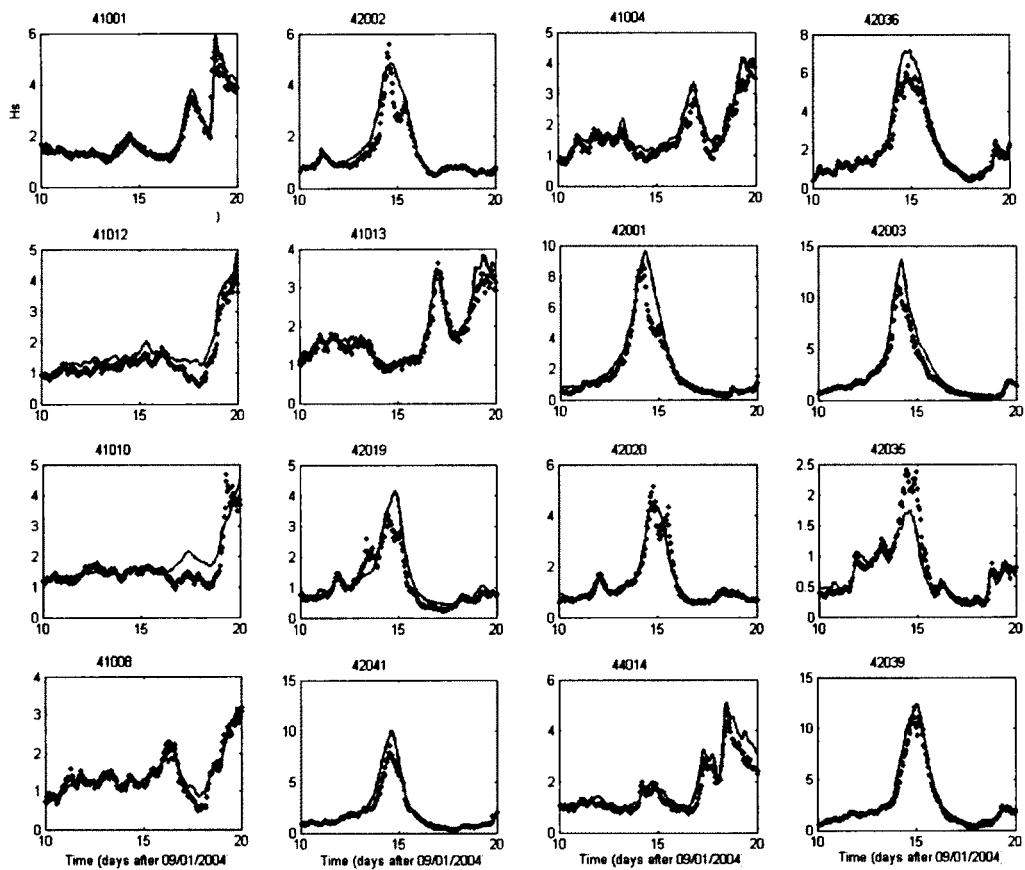
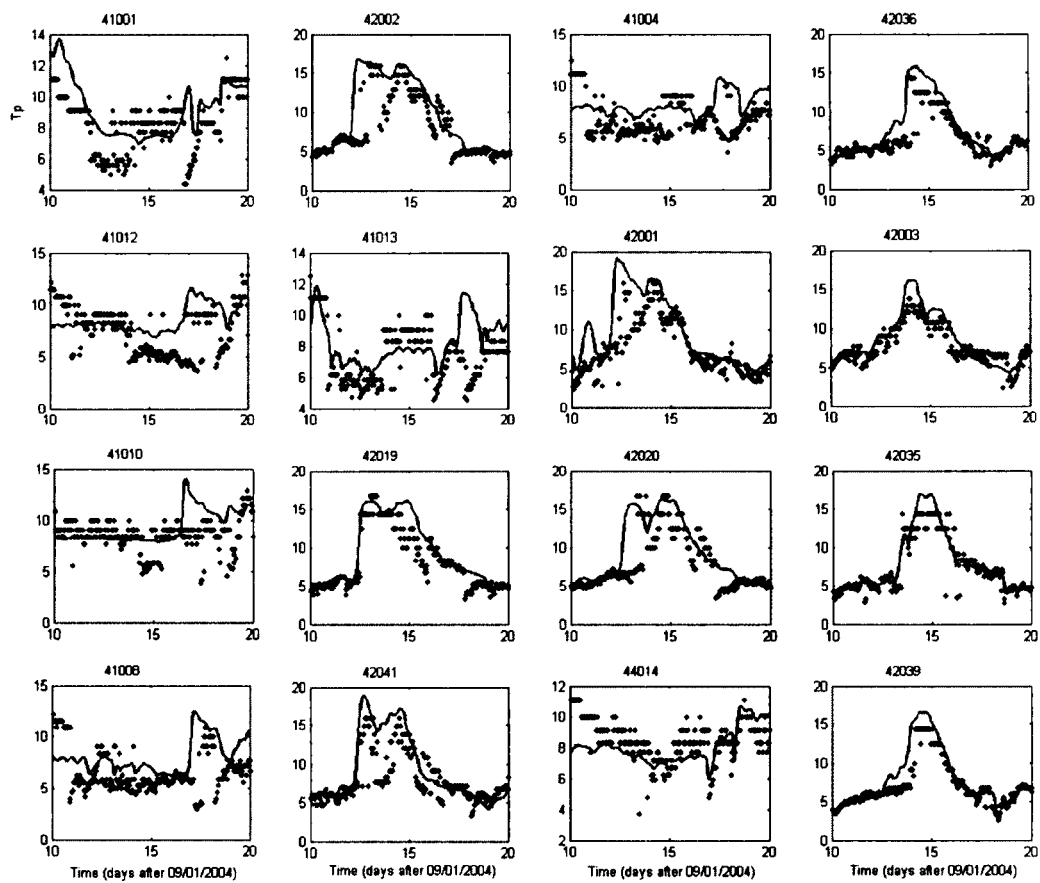


Figure 3-27 Location of NDBC buoys in Gulf of Mexico used in the comparison.



**Figure 3-28** Comparison of significant wave height between model (solid lines) and buoy observation (circles) for the Hurricane Ivan case.



**Figure 3-29** Comparison of peak period between model (solid lines) and buoy observation (circles) for the Hurricane Ivan case.

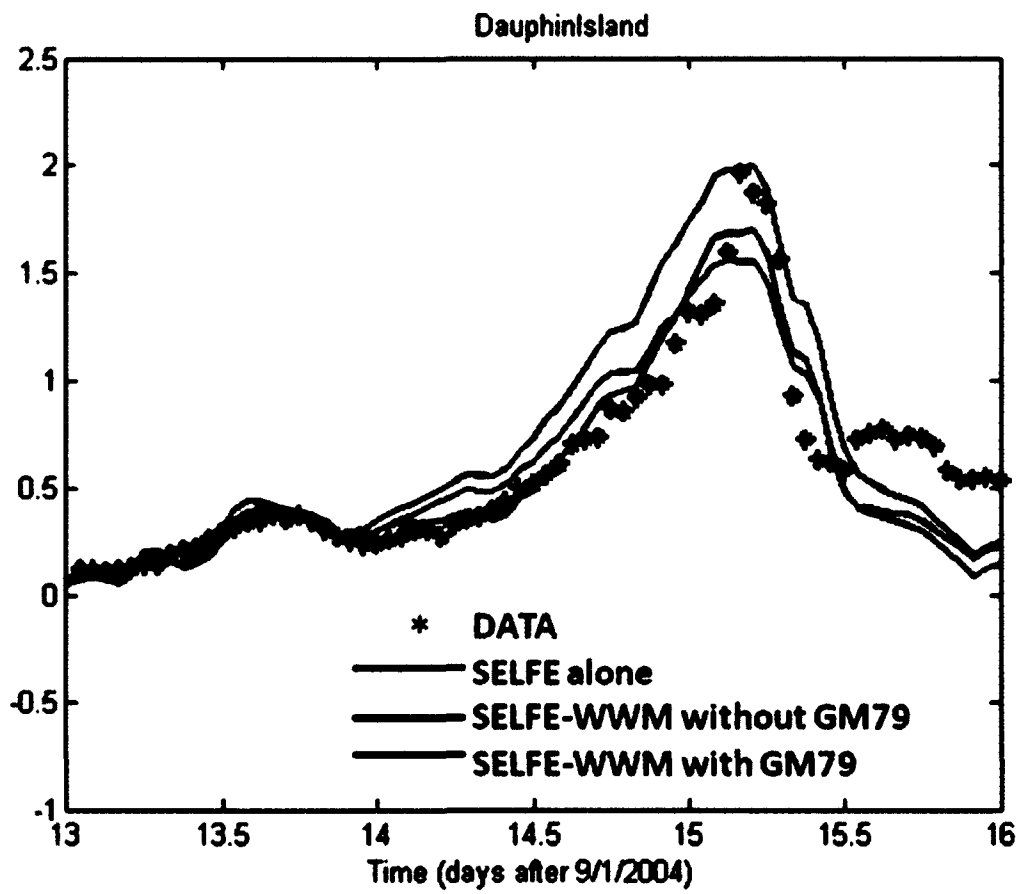


**Figure 3-30** Comparison of storm surge between modeled results and observations at Dauphin Island during the Hurricane Ivan.

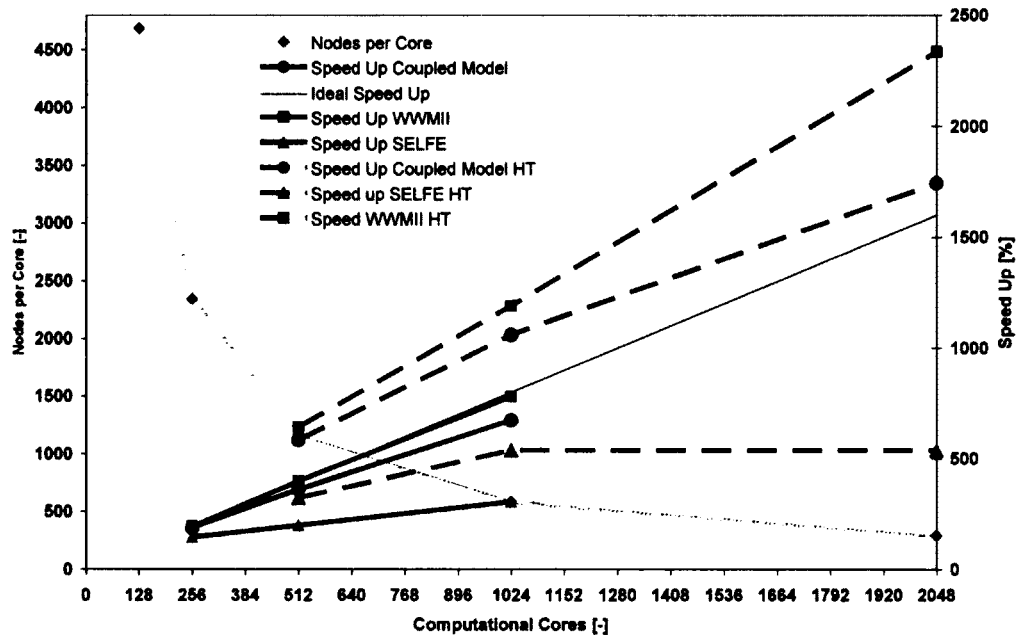


Figure 3-31 Overview of the speed up of the coupled mode, SELFE and WWM II on the C1A/C1B high performance computer at ECMWF.

CHAPTER IV. The effect of bottom boundary layer dynamics on the forerunner simulation during 2008 Hurricane Ike in the Gulf of Mexico

4.1 Introduction

Western Louisiana and northern Texas (LATEX) Coasts are constantly under a threat by tropical storms (e.g., hurricanes) because of their geographic locations along the northern Gulf of Mexico (Fig. 4-1b). Wind-driven coastal surge from these hurricanes was the most important contributor to total water level, associated with coastal flooding (Bunya et al., 2010). The primary storm surge caused by local wind stress will peak around the time of landfall, with the largest surge found to the right side of the hurricane track in the northern hemisphere (Kennedy et al., 2011).

Along the U.S. East and Gulf Coasts, smaller increases in surface water level have been found up to several days before a hurricane makes landfall. This so-called *forerunner* is well-known in the Gulf of Mexico but, in the past, oceanographers and coastal engineers usually ignore this phenomenon due to the relatively smaller amplitude ( $< 1$  m) compared with the primary surge (Bunpapong et al., 1985). However, recently larger forerunners (1-1.5 m) were reported during Hurricane Dennis (2005) and Hurricane Ike (2008) while the centers of the storms were still far from the Gulf Coasts and winds were relatively weak and shore-parallel (Morey et al., 2006; Kennedy et al., 2011).



The time series of the water level anomaly (observed water surface level minus predicted tide) collected from NOAA tidal stations for the 2008 Hurricane Ike are shown in Fig. 4-2 (locations are shown in Fig. 4-1b). The water level anomaly, with a maximum of 4 m at the tidal gauges shown, was largest on the right side of the landfall (Station 8770570, Sabine Pass North). The peaks of the water level anomaly occurred as Hurricane Ike approached the LATEX Coasts, and the surge at landfall thus fits well with prevailing descriptions of storm surge being forced by local wind stress (usually dominant along the cross-shelf direction when the hurricane is close to the shoreline; Fig. 4-3). Based on the observations (Fig. 4-2), large forerunners were also found one day before landfall. Winds at these times were parallel to the shore and relatively weak (Fig. 4-3); this local wind did not play an important role in contributing to these large forerunners. Potential explanations of the forerunners' existence include wave set-up, large scale seiching modes, and Ekman set-up (Kennedy et al., 2011). It has been demonstrated that the large forerunner observed during Hurricane Ike occurred as a result of first Ekman set-up due to the shore-parallel wind along the broad LATEX shelf and then reached the geostrophic balance due to the slow-moving speed of Hurricane Ike. Based on Kennedy et al. (2011), this forerunner surge, due to an approximately geostrophic balance between Coriolis force acting on the along-shelf current and the across-shelf pressure gradient (e.g., Freeman et al., 1957; see schematic explanation in Fig. 4-4), can be calculated from simplified across-shelf steady-state momentum equations as:

$$\frac{\Delta\eta_c}{\Delta y} = \frac{fU}{g} \quad (4.1)$$

where  $\eta_c$  is the across-shelf Ekman set-up,  $y$  increases along a transect toward the shoreline,  $f$  is the Coriolis parameter,  $g$  is gravitational acceleration, and  $U$  is the depth-averaged along-shelf velocity. Thus, a large Ekman set-up will be forced by strong shore-parallel winds generating rapid along-shelf currents over a broad shelf; for example, a depth-averaged current of 1 m/s at 30 degrees north latitude would force an Ekman set-up of 1.5 m on a 200-km-wide continental shelf. This number is close to the observed water level anomaly during the forerunner period (Fig. 4-2b). It should be noted that actually Eq. (4.1) is a classical geostrophic equation since it shows the balance between the Coriolis force and the cross-shore pressure gradient and the classical theory of Ekman dynamics should include frictional forces (Ekman, 1905). Theoretically, if the water depth exceeds the Ekman depth then, under steady-state conditions, the bottom and surface Ekman layers will be generated by a wind stress on the ocean surface and a geostrophic interior will occur between bottom and surface Ekman layers. Based on Ekman (1905), in this study we defined the Ekman set-up as a balance between frictional forces, Coriolis forces, and the cross-shore pressure gradient.

We followed the procedure presented in Kennedy et al. (2011) by using our wave-current coupled model and conducted similar numerical experiments: with and without Coriolis forcing and attained very similar results (Fig. 4-4 and Fig. 4-5). Fig. 4-4 shows that, one day before landfall, there would have been essentially no forerunner in the absence of Coriolis forcing. It should be noted that, although the agreement shown in Fig. 4-4 is reasonable, it is not perfect, with simulations under-

estimating the magnitude of the forerunner. One possible explanation pointed out in Kennedy et al. (2011) is due to the poorly known bottom friction coefficients. Based on Eq. (4.1), Ekman set-up is heavily dependent on the magnitude of along-shore current, which is very sensitive to the bottom boundary, especially the drag coefficient in the inner-shelf or shallow water regions. They found that agreement can be improved by decreasing the bottom drag coefficient, which they believe is consistent with the smooth and muddy bottom inside the LATEX shelf. However, this kind of explanation is only appropriate for the forerunner stage, because reducing the bottom drag coefficient in the model tends to cause an overprediction of the surge during the primary surge stage (Fig. 4-5). This implies that the bottom drag coefficient, usually determined by the bottom sediment grain size in the near-bed, actually varies with time in the natural world.

Typically, the bottom drag coefficients are determined during the calibration of models, through the comparisons of computed and observed tidal currents. In most cases, bottom drag coefficients are specified by constant bottom roughness and the bottom stresses are described using the log-profile of the wall. However, it has been known that a number of dynamics have significant effects on bottom boundary layer (BBL). Previous works (Grant and Madsen, 1979; Grant et al., 1984; Glenn and Grant, 1987; Styles and Glenn, 2000; Zhang et al., 2004) indicate that the presence of surface waves over rough bottoms significantly increases the bottom friction. In addition, due to the increased bottom friction, the thickness of the bottom boundary layer is considerably larger than previously estimated (Grant and Madsen, 1986).

Thus, during a strong wind wave condition (for example, in a storm), the majority of the water column over the shelf is frictionally dominated.

Although the effects of wave-current interactions are accepted as being important to the BBL dynamics on shelf, there are other processes that are known as being important to shelf BBL dynamics, especially the bottom drag coefficient (or the thickness of the BBL). One important process is density stratification in the water column. It is well-known that the water column on the continental shelf region generally exhibits vertical density gradients associated with gradients in temperature, salinity (fair weather conditions), and suspended sediment (extreme weather conditions, e.g., tropical storms). Under a stable stratification, vertical mixing is dampened, since shear production of turbulence is partially suppressed by work against buoyancy forces. As a result, the diffusion of momentum and mass within the boundary layer is reduced. In this case, the BBL is reduced in thickness, the boundary shear stress is decreased, and the veering angle is increased (Grant and Madsen, 1986). In this study, we are focusing on the density stratification produced by suspended sediment because the upper layer of the water column should be well-mixed under the strong wind condition. For example, along the Louisiana Coast, for a cold-front passage sampled in 2001, a well-mixed water column in terms of salinity and temperature during pre-front conditions has been found; at the same time, high-concentration sediment suspensions during storm conditions significantly enhance the stratification in the lower part of the water column (Fig. 4-6). In addition, cross-shelf wave attenuation on the shallow shelf was observed, and was greatest during storm

events coinciding with the times of formation of near-bottom high-concentration sediment suspensions (Kineke et al., 2006). Sediment-induced stratification is important to the bottom boundary dynamics on wind-driven shelves and may have significant impacts on forerunner and storm surge prediction.

The pioneering works of the effects of suspended sediment stratification on the oceanic BBL have been done by Smith and McLean (1977a, b) and Adams and Weatherly (1981). The latter authors developed a near-bottom quasi-steady flow model for a BBL subject to suspended sediment-induced stratification. These models couple the conservation of mass and momentum through the effect of the mass field on the vertical mixing of momentum. Near the boundary, an alternative to the Richardson number is the non-dimensional stability parameter  $z/L$ . Here  $L$  is the Monin-Obukov length ( $L = -\frac{\rho u_*^3}{g} < \rho' w' >$ , where  $\rho'$  and  $w'$  are the fluctuating density and turbulence vertical velocity, respectively). This dimensional stability parameter expresses the ratio of turbulence kinetic energy dissipated by buoyancy forces to that produced by mean shear in the vicinity of the boundary where the production is equal to  $u_*^3/\kappa z$ . The introduction of this stability parameter allows a useful analogy between log-linear atmospheric models of stably stratified shear flows in the surface layer and suspended sediment stratification in the ocean. Thus, the effect of the suspended sediment-induced stratification on the velocity profile in the boundary layer is similar to the results from atmospheric models for stratification due to surface heating (Grant and Madsen, 1986). Model results indicate that the BBL response to a gradient of suspended sediment concentration is to reduce turbulence

kinetic energy, and bottom stress is reduced approximately 45% (Adams and Weatherly, 1981). Later Wang (2002) and Byun and Wang (2005) considered the effects of tidally induced suspended sediment stratification in the BBL and the effects on sediment transport, respectively.

Existing formulations of mud-induced wave dissipation are based on the assumption that mud-induced wave dissipation is important only for long wave (low-frequency waves; shallow water waves), which reach deep enough into the water column. Bottom sedimentary fabric should have negligible effects on short waves (e.g. wind waves), which interact weakly with the bottom. However, Sheremet and Stone (2003) found significant short wave dissipation in the muddy Louisiana inner shelf. Strong bottom sediment reworking during a storm event suggests that this effect (dampening of short wave) is related to sediment resuspension processes. In fact, in the case of a strong wind condition (e.g., a tropical storm), the effect of the sediment-induced stratification on the flow is strongly tied to the wind waves. For the suspended sediment-induced stratification, the wave effects are extremely important since the large bottom shear stresses are associated with the waves. As a result, large amounts of sediment are suspended and may induce strong stratification (Grant and Madsen, 1987). Observation data show that wave and current activity resuspended large quantities of sediment, and caused a *lutocline* located at about 1 m above the bottom on the muddy Louisiana inner shelf during Hurricane Claudette (Sheremet et al., 2005). A *lutocline* is a sediment-induced pycnocline (Kirby and Parker, 1977). Recent studies show that the sediment-induced stratification is important for the

kinetic energy balance throughout the water column (Safak et al., 2010). They did model-observation comparisons and the model results suggested that sediment-induced stratification effects are on the same order of magnitude as turbulent dissipation, and thus play a significant role in the turbulence kinetic energy balance within the tidal (current) boundary layer. All these works imply that the BBL dynamics could be strongly affected by the sediment-induced stratification during extreme weather events.

Despite the fact that there are plenty of model studies about the effects of suspended sediment stratification on a BBL in the shelf regions, published models have not considered sediment-induced stratification on storm surge simulations. With the numerical model, we can evaluate the contributions of BBL sediment stratification on storm surge during storm weather conditions. The objective in this study is to develop a numerical model with coupled current-wave-sediment transport-BBL processes to investigate the effects of sediment-induced stratification on the forerunner during Hurricane Ike in the Gulf of Mexico. This chapter is constructed as follows: A brief description of the current and wave model is presented (details can be found in Chapter 2) and the details of the sediment transport model and bottom boundary layer sub-model are described in Section 4.2. Section 4.3 provides a description of the numerical experiments setup; the validation of current-wave-sediment transport-BBL model and ideal test cases are also shown in this section. Section 4.4 presents the model results as well as the discussions of the sediment-

induced stratification effects on the BBL. A practical approach is described in Section 4.5. The summary and conclusions of this study are provided in Section 4.6.

## 4.2 Model description

In this study, we have built a storm surge modeling system that couples the state-of-the-art circulation model SELFE (Zhang and Baptista, 2008), wave model WWM II (Roland, 2009), and sediment transport-BBL model (Warner et al., 2008). A detailed description of our 3D wave-current model, including governing equations as well as the coupling procedure, can be found in Chapter 2. In this section we focus on the descriptions of algorithms for sediment transport and the BBL we implemented in our coupled model SELFE-WWM II.

### 4.2.1 Sediment transport model

In order to consider the effect of sediment-induced stratification, the model should have the capability to represent suspended-sediment transport in the water column. To simplify the problem, in this study we consider only single-sized non-cohesive sediment with a constant settling velocity  $w_s$ . The three-dimensional equation describing the scalar transport is given by:

$$\frac{\partial C}{\partial t} + \frac{\partial}{\partial x}(uC) + \frac{\partial}{\partial y}(vC) + \frac{\partial}{\partial z}(wC) = \frac{\partial}{\partial z}(K_h C) + C_{source} \quad (4.2)$$

where  $C$  represents a tracer quantity (here  $C$  is suspended sediment). We know that temperature, salinity, and sediment suspended in the water column are transported by



solving the advection-diffusion equation. However, for suspended sediment, an additional source/sink term is needed (last term on the right-hand side of Eq. (4.2)) for vertical settling and exchange with the seabed as:

$$C_{source} = -\frac{\partial w_s C}{\partial z} + E \quad (4.3)$$

Where  $w_s$  is the vertical-settling velocity (positive upwards);  $E$  is the erosional flux. The erosion source term in Eq. (4.3) is parameterized following Ariathurai and Arulanandan (1978) as:

$$E = E_0 (1 - \phi) \frac{\tau_{sf} - \tau_{ce}}{\tau_{ce}}, \text{ when } \tau_{sf} > \tau_{ce} \quad (4.4)$$

where  $E_0$  is the bed erodibility constant ( $\text{kg m}^{-2}\text{s}^{-1}$ );  $\phi$  is the porosity (volume of voids/total volume);  $\tau_{ce}$  is the bottom critical erosion stress;  $\tau_{sf}$  is the total skin friction bottom stress (maximum combined wave+current). There is considerable uncertainty involved with the choice of  $E_0$  in Eq. (4.4). Since we are only interested in a qualitative description of the BBL effect on the forerunner simulation, the exact values in suspended sediment concentration is not our major concern. We therefore set  $E_0$  to a constant  $5 \times 10^{-4} \text{ kgm}^{-2}\text{s}^{-1}$ . This value is the default for non-cohesive sediment used by Community Sediment Model in ROMS (<https://www.myroms.org/wiki/index.php/sediment.in>). A constant  $E_0$  assumes that there is an unlimited suspended-sediment bed load for erosion.

The density of clear seawater usually is determined by the equation of state. When considering the effects of suspended sediment on the density field, the equation of state for seawater density becomes:

$$\rho = \rho_{water} + \frac{C}{\rho_s}(\rho_s - \rho_{water}) \quad (4.5)$$

where  $\rho$  is clear seawater density and  $\rho_s$  is sediment density. Eq. (4.5) allows the model to simulate processes where sediment density influences hydrodynamics (e.g., sediment-induced stratification).

#### 4.2.2 Bottom stress calculations for sediment transport

It is known that the treatment of the BBL is important for the circulation model solution because it determines the stress exerted on the flow by the bottom, which enters the Reynolds-averaged Navier-Stokes equations as a boundary conditions for momentum in the x- and y-directions:

$$v \left( \frac{\partial u}{\partial z}, \frac{\partial v}{\partial z} \right)_b = (\tau_{bx}, \tau_{by}). \quad (4.6)$$

Determination of the BBL is even more important for the sediment-transport formulations because bottom stress determines the suspension rate for the suspended sediment (Eq. (4.4)).

Similar to Warner et al. (2008), in this study we implement two methods for representing BBL processes: (1) simple drag coefficient expressions and (2) more complex formulations that represent the interactions of wave and currents over a sea bed. The drag-coefficient method implements a formulation for a logarithmic profile.

The logarithmic formulation assumes that flow in the BBL has the classic vertical logarithmic profile. Conceptually, the BBL can be viewed as a two-layered system: an inner layer with strong velocity shear close to the bottom and an outer layer making up the remainder of the boundary layer. In the overlap region, the velocity profile is logarithmic for a neutrally stable boundary layer that can be defined by a friction velocity and bottom roughness length as:

$$U = \frac{u_*}{\kappa} \ln\left(\frac{z_b}{z_0}\right) \quad (4.7)$$

where speed  $U = \sqrt{u^2 + v^2}$ ,  $z_b$  is the thickness of the bottom cell,  $z_0$  is a constant (but possibly spatially varying) bottom roughness height (m),  $\kappa = 0.4$  is the von Karman constant, and  $u_*$  is the friction velocity defined as  $u_* = \sqrt{\tau_b / \rho_0}$ . Bottom stresses based on the logarithmic profile assumption are calculated as:

$$\tau_{bx} = \kappa^2 u U / \ln^2\left(\frac{z_b}{z_0}\right) \quad (4.8)$$

$$\tau_{by} = \kappa^2 v U / \ln^2\left(\frac{z_b}{z_0}\right) \quad (4.9)$$

The advantage of the simple drag-coefficient method for the bottom stress calculation is that the velocity and the vertical elevation of that velocity are used in Eqs. (4.8) and (4.9). Since the vertical elevation of the velocity in the bottom computational cell will change spatially and temporally, the inclusion of the elevation provides a more consistent formulation.

A more complex routine is required to simulate BBL processes in the presence of waves and currents. The short (a few sec) oscillatory share of wave-induced motions in a thin (a few cm) wave-boundary layer will produce turbulence and generate large instantaneous shear stresses. The turbulence enhances momentum transfer, effectively increasing the coupling between the flow and the bottom and increasing the frictional drag exerted on the mean flow, averaged over many wave periods. The large instantaneous shear stresses usually dominate sediment resuspension. Resuspended sediments can cause sediment-induced stratification and significantly change the effective viscosity of the fluid.

The BBL parameterization implemented in the sediment-transport model is based on Grant and Madsen (1979) and Madsen (1994). This parameterization requires inputs of velocities  $u$  and  $v$  above the bottom cell, representative wave-orbital velocity amplitude  $U_b$ , wave period  $T$ , and wave propagation direction  $\theta$  (degrees, in nautical convention). The wave information is provided by the wave model WWM II. Additionally, the BBL model requires bottom sediment characteristics (median grain diameter  $D_{50}$ , sediment density  $\rho_s$ , and settling velocity  $w_s$ ); Bed stresses associated with mean current above the wave-boundary layer  $\tau_c$ , the pure wave motion  $\tau_w$ , and the maximum vector sum of the two  $\tau_{wc}$  from the previous time step are used as initial estimates for the next time step. The detailed procedure for BBL calculations in the BBL model can be found in Warner et al. (2008). The final step in the BBL calculations is to estimate the skin friction bottom stress that is used to determine sediment resuspension in Eq. (4.4).

In summary, the more advanced BBL routine for sediment transport model calculates current and wave-boundary bottom stresses under the combined influence of wave and currents. These stresses directly influence flow near the bottom and act as agents for sediment resuspension. The comparisons of different methods for bottom shear calculations are conducted and discussed in a later section.

#### 4.2.3 Modified bottom boundary conditions for sediment stratification

It has been recognized that the stratification induced either by sediment or other variables (e.g., water temperature) can lead to a significant change in BBL dynamics (Adams and Weatherly, 1981; Grant and Madsen, 1986; Soulsby and Wainwright, 1987; Wang, 2002; Byun and Wang, 2005; Taylor and Sarkar, 2008). In order to consider the effect of sediment stratification, the bottom boundary conditions of SELFE presented in Section 2.2.2 need to be modified. The velocity profile for a stably stratified logarithmic boundary layer is given by (Adams and Weatherly, 1981):

$$U = \frac{u_* (1 + AR_f)}{\kappa} \ln\left(\frac{z_b}{z_0}\right) \quad (4.10)$$

Where A is the empirical constant and can be provided from laboratory experiments. In this study we adopt A=5.5, which is equivalent to the value used by Adams and Weatherly (1981), Wang (2002), and Byun and Wang (2005).  $R_f$ , the flux Richardson number, referenced as an index for the vertical density, is expressed by:

$$R_f = -\frac{P_b}{P_s} = \frac{K_h}{\nu} R_i \quad (4.11)$$

where  $P_b$  and  $P_s$  are the buoyant production and the shear production of turbulent kinetic energy, respectively;  $K_h$  is the vertical eddy diffusivity ( $m^2s^{-1}$ );  $\nu$  is the vertical eddy viscosity ( $m^2s^{-1}$ );  $R_i$  is the gradient Richardson number. These terms can be presented by:

$$\begin{aligned} P_b &= -K_h N^2 \\ P_s &= \nu \left[ \left( \frac{\partial u}{\partial z} \right)^2 + \left( \frac{\partial v}{\partial z} \right)^2 \right] \\ R_i &= \frac{N^2}{\left( \frac{\partial u}{\partial z} \right)^2 + \left( \frac{\partial v}{\partial z} \right)^2} \end{aligned} \quad (4.12)$$

where  $N^2$  is the buoyancy frequency squared including the contribution of the sediment-induced stratification. SELFE adapts the Generic Length Scale (GLS) turbulence closure through the General Ocean Turbulence Model (GOTM) suggested by Umlauf and Burchard (2003; 2005), taking the advantages from most of the level 2.5 closure schemes ( $k-\epsilon$  (Rodi, 1984);  $k-\omega$  (Wilcox, 1998); Mellor and Yamada, 1982). Detailed descriptions can be found in Section 2.2.3. The  $k-\epsilon$  turbulence scheme was used to calculate vertical eddy viscosity and vertical diffusivity. The critical flux Richardson number  $R_{fc} = 0.21$  that was chosen to represent the turbulence is completely suppressed by the stratification (slippery BBL).

In real-world observations, current velocity profiles are used to estimate shear velocities,  $u^*$ , and roughness lengths,  $z_0$  (e.g., Eq. (4.7)). The effects of strong density stratification due to near-bed suspended sediment on the estimates of  $u^*$  are significant (Cacchione et al., 1995) and reduced bottom drag has been observed under this condition (King and Wolanski, 1996; Dyer et al., 2004). Substituting Eq. (4.10)

into Eq. (2.9) and Eq. (2.10), the bottom drag coefficient in a sediment-induced stratification BBL can be given by:

$$C_D = \left[ \frac{1}{\kappa / (1 + AR_f)} \ln\left(\frac{z_b}{z_{ob}}\right) \right]^{-2} \quad (4.13)$$

where  $z_{ob}$  can be equal to  $z_0$  (without the effect of wave-current interaction in the

BBL) or  $z_{ob} = \delta_{wc} \left( \frac{\delta_{wc}}{z_0} \right)^{-\sqrt{|\tau_b|/(C\tau_w)}}$  (with the effect of the wave-current interaction in

the BBL). Note that the  $R_f$  used in Eq. (4.13) is the value calculated at the bottom computational cell.

In Eq. (4.13), the bottom drag coefficient is reduced by the stratification induced by suspended sediment near the bed. In SELFE, Eq. (4.13) is adopted to compute the bottom drag coefficient and bottom friction stress (Eq. (2.9) and Eq. (2.10)) for the density-stratification BBL case. In a well-mixed BBL case (when  $R_f=0$ ), Eq. (4.13) reverts to the traditional form of Eq. (2.10).

#### 4.2.4 Modified surface boundary conditions for wave-enhanced wind stress

In Chapter 2 we presented the default option of the wind drag coefficient in SELFE as a function of the wind speed at a 10-m elevation (Pond and Pickard, 1998). However, it is well-known that, in reality, the drag coefficient is not only a function of wind speed, but also depends on the stage and motion of the waves (e.g., Donelan et al., 1993). When considering the effects of wave-current interaction, there are two options for the calculation of wave-enhanced surface stress in our coupled model. The

first one is based on the actual sea state (wave age) using the theory of Janssen (1991). The second one is based on the motion of the waves. For example, in regions where the winds and waves are moving in the same direction, wind drag coefficient will be relatively small. However, in regions where the winds are blowing opposite to the direction of wave propagation, the wind drag coefficient will be larger due to the additional roughness of the sea surface (Dietrich et al., 2011b). The sector-based wind drag coefficients we used in this study are based on recent research (Powell, 2006; Dietrich et al., 2011b). Fig. 4-7 shows the variability in the wind drag coefficient based on the storm sectors. In this study, we choose the sector-based wind drag coefficient as the default for all simulations we present later.

### 4.3 Validation and setup of coupled wave, current, and sediment-transport-BBL model

#### 4.3.1 Model domain and grid

The model domain we used in this study is based on Xu et al. (2010) and shown in Fig. 4-1a. This domain encompasses the U.S. East Coast, a portion of the Northern Atlantic Ocean, the Gulf of Mexico, and the Caribbean Sea. The model grid, with 57,344 nodes, 163,786 edges, and 106,389 elements, extends from  $-98^{\circ}\text{W}$  to  $-60^{\circ}\text{W}$  in longitude and from  $41^{\circ}\text{N}$  to  $8^{\circ}\text{N}$  in latitude. Resolutions of grid cells range from 50 m near the coast to 29 km along the open ocean. In the open ocean, model topography was interpolated from the ETOPO1 global relief dataset from NOAA



(resolution is about 1-minute. Model topography in coastal regions was interpolated from the U.S. coastal relief dataset with a 3-second resolution from NOAA (<http://ngdc.noaa.gov/mgg/bathymetry/>). Both relief datasets are referenced to mean sea level.

It should be noted that water levels are increased at the beginning of the storm tide simulation to account for the vertical datum and the intra-annual mean sea surface variability of the Gulf of Mexico. The computed water levels in SELFE are relative to local mean sea level, and they are adjusted to the North American Vertical Datum of 1988 updated to the 2004.65 epoch, NAVD88 (2004.65), by adding 0.125 m (Bunya et al., 2010; SURA test bed project, 2011). A further adjustment is required because of the intra-annual fluctuation in sea level due to the thermal expansion of the Gulf and other processes (Dietrich et al., 2011c). In this study, based on long-term observations at Dauphin Island, Mississippi, and Grand Isle and Eugene Island, Louisiana, a steric increase of 0.151 m in the averaged water levels in September was found (SURA test bed project, 2011). Thus, the combined increase in water levels for Hurricane Ike is  $0.125 \text{ m} + 0.151 \text{ m} = 0.276 \text{ m}$ .

#### 4.3.2 Circulation model validation – 3D Ekman motion

It has been demonstrated that the Ekman dynamic is an important process that drives the water exchanged between very near-shore regions and the outer continental shelf during a storm surge event (Shen, 2009; Kennedy et al., 2011). Moreover, it is a known fact that the Ekman dynamic is a kind of three-dimensional process (e.g., the

Ekman spiral), so theoretically the 3D model should resolve the Ekman layer more accurately and can simulate the Ekman transport more realistically than the 2D model. The validation of our current model SELFE, based on the comparisons between model results and analytical solutions of 3D Ekman motion, is presented in this section.

Away from the equator, a steady wind blowing over an ocean leads to ocean velocities that are not parallel to the direction of the wind. Ekman motion (Ekman-layer dynamics) is used to describe this expected behavior, under the following assumptions: a) steady wind ( $\tau^x$  and  $\tau^y$ ), blowing over an infinitely deep, flat-bottom, and wide ocean, with constant density, and b) motion based on the balance of friction (e.g., wind stress and vertical eddy diffusivity) and Coriolis force. By these assumptions, we can obtain the following equations and boundary conditions in the surface Ekman layer:

$$-fv = \mu \frac{\partial^2 u}{\partial z^2} \quad (4.14)$$

$$fu = \mu \frac{\partial^2 v}{\partial z^2} \quad (4.15)$$

$$\text{Surface } (z = 0): \rho\mu \frac{\partial u}{\partial z} = \tau^x, \rho\mu \frac{\partial v}{\partial z} = \tau^y \quad (4.16)$$

$$\text{Bottom } (z = -\infty): u=0, v=0 \quad (4.17)$$

Assuming  $\rho$  and  $\mu$  are constant, the analytical solution to this problem is:

$$u = \frac{\sqrt{2}}{\rho f d} e^{z/d} \left[ \tau^x \cos\left(\frac{z}{d} - \frac{\pi}{4}\right) - \tau^y \sin\left(\frac{z}{d} - \frac{\pi}{4}\right) \right] \quad (4.18)$$

$$v = \frac{\sqrt{2}}{\rho f d} e^{z/d} \left[ \tau^x \sin\left(\frac{z}{d} - \frac{\pi}{4}\right) + \tau^y \cos\left(\frac{z}{d} - \frac{\pi}{4}\right) \right] \quad (4.19)$$

Eqs. (4.18) and (4.19) show that the surface current flows at  $45^\circ$  to the right (left) of the wind direction in the northern (southern) hemisphere, and the deviation increases over depth in a spiral pattern known as the Ekman spiral.

Eqs. (4.18) and (4.19) are the analytical solutions for steady-state Ekman motion in the ocean. However, it should be noted that, in the real world, speed and direction of the wind changes continuously so the analytical solutions of unsteady Ekman dynamics were further built (e.g. Lewis and Belcher, 2004). First, consider the time-dependent Ekman equation for the wind-driven ocean currents:

$$\frac{\partial U}{\partial t} + ifU = \frac{\partial}{\partial z} \left( \mu \frac{\partial U}{\partial z} \right) \quad (4.20)$$

where  $U(z, t) = U + iV$  is the complex horizontal velocity for the wind-driven (Ekman) components in the  $x$ - $y$  plane. Analytical solutions to Eq. (4.20) can be obtained subject to the appropriate boundary and initial conditions. The ocean is assumed to be initially at rest (i.e.,  $U = 0, t \leq 0$ ). Then, for time  $t > 0$ , we apply a constant wind stress to the ocean surface and the surface boundary condition becomes:

$$\rho \left( \frac{\partial}{\partial z} \left( \mu \frac{\partial U}{\partial z} \right) \right) = \tau_s, \text{ at } z = 0. \quad (4.21)$$

Although there are different ways to specify the bottom boundary condition, a no-slip boundary condition,  $U = 0$ , at  $z = -H$  was applied as the lower boundary condition to solve Eq. (4.20).

By applying a Laplace transform, the general solution of Eq. (4.20) can be given by the inverse Laplace transform (e.g. Abramowitz and Stegun, 1972; Lewis and Belcher, 2004):

$$U(z, t) = \frac{1}{2\pi i} \int_{c-i\infty}^{c+i\infty} e^{st} U(z, s) ds, \quad c \geq 0. \quad (4.22)$$

Detailed derivations for Eq. (4.22) can be found in the Appendices in Lewis and Belcher (2004). Considering a case when eddy viscosity is constant ( $\mu = \text{constant}$ ) and a finite depth  $-H$  with the no-slip boundary condition, one can get an analytical solution for the time-dependent Ekman current velocities in finite-depth water:

$$U(z, t) = U_c \left[ \frac{(1-i \sinh[\frac{(1+i)(z+H)}{d}])}{\cosh[\frac{(1+i)H}{d}]} + \frac{2de^{-ift}}{H} \sum_{n=0}^{\infty} \frac{(-1)^{n+1} \exp[-\alpha_n t] [(\frac{\alpha_n}{f}) - i] \sin[k_n(H+z)]}{[(\alpha_n/f)^2 + 1]} \right] \quad (4.23)$$

where  $d = \sqrt{2\mu/f}$  is the depth scale of the Ekman layer,  $\alpha_n = (n + 1/2)^2 \pi^2 \mu / H^2$ ,  $k_n = (n + 1/2)\pi/H$ , and  $U_c = \tau_s / \rho \sqrt{2f\mu}$  is the scale for the surface velocity, which equals to the surface velocity given by the classic Ekman theory (steady-state, constant eddy viscosity, infinite water depth, and constant wind); The first term in the square brackets is the steady-state current for Ekman flow in finite depth and the second term is the transient. At short times, when  $ft \ll 1$ , Eq. (4.23) simplifies to the non-rotating solution, with momentum diffused downwards to generate a unidirectional current. At later times, when  $ft \gg 1$ , the Coriolis force deflects the current southwards. Qin (2011) developed a 1-D vertical numerical model to calculate the time-dependent Ekman current velocity in finite-depth water and good agreements were found between numerical simulations and analytical solutions, which verified that Eq. (4.23) could be useful to study the transient motions of Ekman layers as well as their effects on ocean circulation.

The wind-driven horizontal transport in the surface Ekman layer has components given by:

$$U = \int_{-\infty}^0 u dz = \frac{1}{\rho f} \tau^y \quad (4.24)$$

$$V = \int_{-\infty}^0 v dz = \frac{-1}{\rho f} \tau^x \quad (4.25)$$

Eqs. (4.24) and (4.25) show that the wind-driven transport in the surface Ekman layer (Ekman transport) is oriented perpendicularly to the wind stress. Although the preceding mathematical model of surface Ekman layer is highly idealized, it is useful to test the accuracy of the circulation model. Here we consider a rectangular ( $100 \times 100 \text{ km}^2$ ), flat-bottom (50-m depth) ocean, and apply a steady, uniform south wind ( $15 \text{ m s}^{-1}$ ). The latitude is roughly at  $45^\circ\text{N}$ , which translates to a Coriolis parameter of  $10^{-4} \text{ rad/s}$ . In the vertical, we use 101 uniform pure S layers. Vertical eddy viscosity is uniform over depth ( $10^{-4} \text{ m}^2 \text{ s}^{-1}$ ) as well as the density of water ( $\rho=1000 \text{ kg m}^{-3}$ ). Uniform water level (MSL) is imposed at all open boundaries. We also turn off advection, horizontal diffusion, and bottom friction in order to get “pure” model results to compare with analytical solutions.

Fig. 4-8 and Fig. 4-9 show that the model results (blue line) match the analytical solutions (red line) closely (except for the velocities near the bottom due to the bottom boundary conditions as shown in Fig. 4-9). The speed of the surface current is approximately 1% of the wind magnitude, and decreases exponentially with depth. The surface current flows are almost  $45^\circ$  to the right of the wind direction, and the deviation increases over depth in a spiral pattern.

Notice that one important element related to this study is neglected from the Ekman-layer formulations we described above: the presence of vertical density stratification. The gradual change of density with height hinders vertical movements, thereby reducing vertical mixing of momentum by turbulence; it also allows the motions at separate levels to act less coherently and to generate internal gravity waves. As a consequence, stratification reduces the thickness of the Ekman layer and increases the veering angles of the velocity with height (e.g., Adams and Weatherly, 1981). The Ekman dynamic, in terms of total transport across the shelf, may be significantly affected by the strong stratification in the water column. We will present an additional test case for the effects of density stratification on cross-shelf Ekman transport as well as Ekman set-up in a later section.

#### 4.3.3 Tidal validation during Hurricane Ike in the Gulf of Mexico

The tides are relatively weak in the Gulf of Mexico, with mixed diurnal and semidiurnal tides on the Florida shelf up to Apalachicola, Florida; diurnal tides are the dominant components between Panama City Beach, Florida and Port Fourchon, Louisiana; and mixed tides again start from Point au Fer Island, Louisiana to Port Isabel, Texas. Overall, the tidal amplitudes of the dominant constituents in the Gulf of Mexico are less than 0.2 -0.4 m (Bunya, 2010).

The tidal simulation is carried out to verify the long wave propagation in our model domain. The SELFE open boundary is forced by 8 tidal constituents, namely  $M_2$ ,  $K_2$ ,  $N_2$ ,  $S_2$ ,  $K_1$ ,  $O_1$ ,  $P_1$  and  $Q_1$ . These tidal constituents are obtained from the

ADCIRC 2DDI tidal database (Mukai et al., 2002). The earth tidal potential of each tidal constituent was also applied to interior cells of the model domain. The simulation of tide using a time step of 90 sec started at 5/19/2008 0000 UTC and ended at 9/01/2008 0000 UTC, a total of 105 days with the first 30 days for spin-up. The reason for a 105-day run is in order to remove the effect of the inertia wave on the diurnal tide in the Gulf of Mexico. The model results from the last 75 days are used for the comparison and the harmonic decomposition is conducted using “T-tide” with a 38-constituent decomposition.

The harmonic analysis of computed 30-min tidal levels during the last 75 days of the simulation at 58 NOAA CO-OPS tidal gauge stations that cover the state of Florida (FL), Alabama (AL), Mississippi (MS), Louisiana (LA), and Texas (TX), is conducted to compare simulated amplitudes and phases of six major harmonic constituents ( $M_2$ ,  $S_2$ ,  $N_2$ ,  $K_1$ ,  $M_4$ , and  $O_1$ ) with those in the NOAA data-set (Fig. 4-10 and Fig. 4-11). In order to quantify the comparison, six statistics considered in this study are as follows: (a)  $R^2$ , which indicates the correlation between the modeled and the observed data squared; (b) Slope of the best fitting line  $y = mx$  through the modeled and observed data; (c) Standard deviation,  $\sigma$ , which shows how much variation of modeled data exists from the observed data; (d) Average error,  $\bar{\epsilon}$ , between the observed and modeled data,

$$\bar{\epsilon} = \frac{1}{N} \sum_{i=1}^N (obs_i - mod_i); \quad (4.26)$$

(e) Average absolute error,  $|\bar{\epsilon}|$ , between the observed and modeled data,

$$\bar{\epsilon} = \frac{1}{N} \sum_{i=1}^N |obs_i - mod_i|; \quad (4.27)$$

(f) Normalized root-mean-square error,  $E$ , between the observed and modeled data,

$$E = \left[ \frac{\sum_{i=1}^N (obs_i - mod_i)^2}{\sum_{i=1}^N obs_i^2} \right]^{1/2}. \quad (4.28)$$

The  $R^2$  values of semidiurnal tides such as  $M_2$  and  $S_2$  along the Gulf Coast are greater than 0.80 for both amplitudes and phases except for the  $N_2$  tide ( $R^2=0.72$  for amplitude and 0.61 for phase). The average absolute difference of semidiurnal tide amplitudes are less than 0.02 m and the average difference of phases are  $1^\circ - 35^\circ$ . The  $R^2$  values of diurnal tide amplitudes such as the  $K_1$  and  $O_1$  constituents are relatively worse than those for semidiurnal tides: the correlation coefficients of modeled diurnal tides are around 0.40 for amplitude, but the phase results are relatively better ( $R^2=0.75$ ). Table 4-1 lists the statistics for the five groups of NOAA stations based on the five different States. Again the  $R^2$  values are greater than 0.78, indicating good matches between model prediction and observation, with the exception of amplitudes and phases along the Texas Coast, which the coarse-resolution grid is not fully able to resolve. These results indicate that the simulation of tide by SELFE is overall satisfactory in the Gulf of Mexico. It should be noted that, in the SURF test bed project for coastal inundation, we also conduct an inter-model tidal comparison between three different unstructured-grid models with the same tidal forcing and



model setup (Fig. 4-12). All three models (ADCIRC, FVCOM, and SELFE) perform about the same for both amplitude and phase. This implies that, if we would like to improve model skill for tidal simulation, it is essential to improve the mesh resolution in the coastal regions such as bays, channels, inlets, and estuaries.

#### 4.3.4 Atmospheric and wave forcing

Wind forcing for Hurricane Ike was taken from a H\*Wind post-storm reconstruction (Powell et al., 1998) and blended with large-scale winds using the Interactive Objective Kinematic Analysis (IOKA) system (Cox et al., 1995). The resulting wind fields combine all available wind observations into a common marine framework at a 10-m height. Winds fields are interpolated to 15-min intervals, starting at 1215 UTC 5 September 2008 (approximately 7.8 days before landfall (0700 UTC, 13 September)) and ending at 1200 UTC 15 September 2008. The spatial resolution of the wind field is  $0.02^\circ$ .

Wind and wave data collected during Hurricane Ike at 10 NDBC buoys (locations are shown in Fig. 4-13) are used to validate the wind field used in the model and modeled wave results. It should be noted that the NDBC data were assimilated into the wind field we used, but many other sources of data also influenced it. Comparisons between measured and simulated wind at buoys close to the storm track are shown in Fig. 4-14. The simulated winds compare quite well with the measured winds at these locations; these results indicate the model winds should represent the realistic wind fields appropriately.

Wave conditions along the open boundary of WWM II are provided by WAVEWATCH-III. WAVEWATCH-III, also known as WW3 (Tolman, 1999), is a third-generation wave model developed at NOAA/NVEP based on the WAM model (The Wamdi Group, 1988; Komen et al., 1994). Our wave model open boundary is forced by WW3 results such as significant wave height, peak frequency, zero down crossing frequency, mean wave direction, and mean directional spreading.

#### 4.3.5 Wave model validation

At the same 10 NDBC buoys (shown in Fig. 4-13), significant wave heights, peak wave periods, mean wave periods ( $T_{m02}$ ), and peak wave direction (in nautical coordinates) are used to validate our wave model as shown in Fig. 4-15. WWM II matches the timing and magnitude of significant wave heights, and the simulated peak wave period agrees very well with observations at the selected buoys. The modeled mean wave periods catch the transitions from wind sea to swell sea, and match observations at most of the selected stations, except the stations in the shallow water regions, which probably are not well-resolved in the mesh. The WWM II model also accurately modeled the peak wave direction during Hurricane Ike periods. Overall, the computed wave results match the qualitative behavior of Hurricane Ike, and their values lie within the scatter of the observations.

#### 4.3.6 Sediment-transport model validation –steady uniform open-channel flow

Warner et al. (2008) provided a benchmark test for exercising the model's ability to simulate vertical profiles of suspended sediment concentrations. The

simulation represents suspended sediment transport for steady horizontally uniform flow in a straight rectangular channel. The description of the model domain and the open boundary condition can be found in their paper; setups of model parameters for this test case are listed in Table 4-2. The comparisons between modeled results with the  $k-\epsilon$  turbulence closure model and analytical solutions (model run with parabolic profile of viscosity and the eddy diffusivity is determined from the turbulent Prandtl number ( $Pr$ ; ratio of eddy viscosity/eddy diffusivity)) are shown in Fig. 4-16. The model results, in terms of the vertical profile of velocity, diffusivity, and suspended sediment concentration, compared well with the analytical solutions. This test case gives us the confidence that the behavior of the sediment-transport model we have built for this study should be reasonable.

#### 4.3.7 Sediment model parameters used for the Hurricane Ike case

At most locations in the inner and middle LATEX shelf, the sediment contained more than 80% mud except at the sandy Trinity and Ship Shoals (20-30% mud) between the 5- and 10-m isobaths south of Atchafalaya Bay (Xu et al., 2011). In this study, we assume that initially the seabed is covered by smooth mud for which the median sediment size ( $SD_{50}$ ) is chosen as 0.01 mm. Given the fact that the seabed was mainly consolidated mud where water depths exceed 300 m in the Gulf of Mexico, we turn off the erosion when  $h > 300$  m in order to simplify the sediment transport calculations and to avoid unrealistically high erosion. This is appropriately given (a) for storm surge study, we usually focus on the inner shelf regions ( $h < 100$

m); and (b) sediment movement by wave resuspension in deep water only occurs once every 5 to 20 years (Curry, 1960).

The sediment-transport model described in Section 4.2.1 involves parameters of the sediment density  $\rho_s$ , porosity  $\phi$ , settling velocity  $w_s$  and the critical stress  $\tau_{ce}$ , for erosion. Sediment density was set to be  $2650 \text{ kg/m}^3$  and porosity was chosen as 0.8 based on measurements by Draut et al. (2005) and Allison et al. (2007). Sediment transport calculations are extremely sensitive to the settling velocities and it is well-known that settling velocity should not be constant in the real world. For example, flocculation critically impacts settling velocity and sediment transport near river-dominated muddy deltas (Geyer et al., 2004); however, there are few in-situ measurements of floc-settling velocity on the LATEX shelf. We therefore chose a typical value of  $w_s$  as  $1 \text{ mm s}^{-1}$  (Xu et al., 2011). Critical shear stress  $\tau_{ce}$  was held constant (0.11 pa), a value derived by Wright et al. (1997) for the Louisiana inner continental shelf. The important parameters for the sediment transport model used in this study are listed in Table 4-3.

#### 4.3.8 Experimental setup

Several numerical experiments for storm simulation were conducted and the setups are listed in Table 4-4. All numerical experiments were forced by the 8 tidal constituents, namely  $M_2$ ,  $K_2$ ,  $N_2$ ,  $S_2$ ,  $K_1$ ,  $O_1$ ,  $P_1$  and  $Q_1$ , at the open boundary. In addition, the earth tidal potential of each tidal constituent was also applied to interior cells of the model domain. Since the open boundary in our model domain is far away

from the Gulf Coast and storm surge is often relatively small at the open ocean, it is assumed that there is no storm surge at the model open boundary during the initial stage. The numerical experiments were conducted from 8/19/2008 0000 UTC to 9/8/2008 0000 UTC to spin-up the model. After this initializing phase, the model was further integrated for 8 days starting from 9/8/2008 0000 UTC to 9/16/2008 0000 UTC with atmospheric forcing (both wind and pressure fields).

Numerical simulations of vertical suspended sediment profiles are sensitive to the number and placement of vertical grid levels. As the number of vertical grid levels increases towards the bottom, the gradient of suspended sediment near the seabed can be better resolved. In this study, twenty layers with vertical stretching parameters ( $\theta_f = 3$  and  $\theta_b = 1$  in SELFE) in a pure s-coordinate were used to provide increased resolution near the seabed.

The first experiment was used for the validation of storm tide simulation, which can be seen as the “base case”. Typically, storm surge is mainly driven by an atmospheric pressure drop and the strong wind field induced by a hurricane. Based on that, we only consider the effects of atmospheric forcing in Experiment 1.

Experiment 2 was designed to examine the effects of the wave-current interaction on the storm surge simulation. This experiment consists of two model runs. In the first run (Exp. 2a), we only consider radiation stress and the BBL was not affected by wave-current interaction. In the second run (Exp. 2b), both radiation stress and wave-current bottom stress calculated from the modified GM model (see Section 2.4.3) were included.

Experiment 3 is similar to Experiment 1, except that the sediment-stratified BBL is added. This run is used to test the effect of sediment stratification on BBL through Eq. (4.13) for storm surge simulation. The density in the water column now is affected by the suspended sediment, according to Eq. (4.5). The simple drag-coefficient method for the bottom stress calculation in the sediment-transport model presented in Section 4.2.2 is used since, in this case, we do not consider wave effects.

Finally, Experiment 4, including all the effects (radiation stress, wave-current bottom stress, and sediment-induced stratification), was conducted to test the combined effects on storm surge simulation and the BBL response. The major difference between Experiments 3 and 4 is now that the wave-enhanced bottom stress is considered in both SELFE and the sediment-transport models, which should be extremely important for the distribution of suspended sediment as well as the BBL properties because, according to Eq. (4.4), erosion flux of bed sediment is very sensitive to the evolutions of bottom shear stress.

#### 4.4 Results and discussion

##### 4.4.1 Experiment 1: storm tide simulation (base case)

We compared SELFE-computed water levels against the NOAA CO-OPS-measured time histories and results are shown in Fig. 4-17. Modeled water levels at Shell Beach (8761305) along the east side of the Hurricane Ike track showed good agreement with measured values in terms of timing and hydrograph features. The

computed water levels at Pilots Station East (8760922) are underestimated from 9/10/2008 to 9/14/2008. This discrepancy, which is almost consistent in time, implies that there may be a discrepancy in datum levels. Modeled and measured data at Grand Isle (8761724) are well-matched. The difference of the maximum water level is approximately 0.30 m. The comparison at Lawma Amerda Pass (8764227) indicates that the model is underpredicting the peak of the forerunner by 0.62 m. Model results at Fresh Water Canal Locks (8766072) show that the model captures the hydrograph features, but tends to underpredict the forerunner. The surge peaks are well-matched at both Calcasieu Pass (8768094) and Sabine Pass North (8770570), but model results indicate that the forerunner and post-runner cannot be captured well in this run. The comparison at Galveston Pleasure Pier (8771510) indicates that the modeled storm tides are well-represented in the region that Hurricane Ike made landfall; the surge peak is overpredicted by about 0.60 m, and the forerunner is underpredicted by about 0.82 m. Notice that the forerunner surge during Hurricane Ike was as important as the primary surge because it caused early flooding of coastal regions, and contributed significantly to the total water level subsequently during the primary surge. Dangerous forerunners that occurred on wide, shallow shelves need to be considered for the future storm surge forecasting; therefore, it is valuable to study different effects on the forerunner in order to improve the model performance. Finally, the measured and simulated water levels at USGS Freeport (8772447) and Corpus Christi (8775870) are well-matched in terms of the hydrograph features. The difference between model and observation at these two stations may be attributed to the

insufficient grid resolution along the Texas Coast (USGS Freeport is located near the inlet and Corpus Christi is located outside the barrier island). The comparison of computed and observed time series of storm tides at 10 stations indicates that our model adequately simulated the major features of storm tides during Hurricane Ike.

#### 4.4.2 Experiment 2: effects of wave-current interaction on storm surge simulation

In regions with a wide and shallow continental shelf (e.g., LATEX Coasts), a traveling external surge may combine with tide, the locally generated surge, and waves under storm events and there can be a significant interaction between the current and waves. Wave properties such as wave height along the coast are highly controlled by water depth, so the effect of tides and surges on wave action must be included. On the other hand, waves contribute to the total water level by means of wave set-up through radiation stresses (Wolf, 2009). These processes are already well-understood and considered in many storm surge investigations (e.g. Bunya et al., 2010; Sheng et al., 2010; Kennedy et al., 2011). However, other interactions between currents and waves include the processes of surface wave-induced stress in which wave age affects the sea surface roughness and bottom wave-enhanced friction is also important, but the details of these processes are still not well-understood. In Experiment 2, two cases were conducted to evaluate the contributions of radiation stress (Fig. 4-18 (blue solid line)) and wave-enhanced bottom friction + radiation stress (Fig. 4-18 (green solid line)) over the entire period of storm surge. These results



were compared against the base case (Exp. 1, Fig. 4-18 (black solid line)) that did not include current-wave interaction.

Experiment 2a (blue solid line in Fig. 4-18) shows that including the wave radiation stress slightly increases the entire storm surge by 5 – 15% at the ten stations located along the LATEX Coast. This can be explained by the fact that the onshore component of wave radiation stress gradients, which produces a wave set-up that can contribute to the total water level. However, the modeled results with and without wave set-up (contributed by the wave-induced radiation stress) for forerunners (24 hours before Ike made landfall) showed only small differences at most of the stations in the Gulf of Mexico (Fig. 4-18). This finding is consistent with Kennedy et al. (2011). Fig. 4-19 shows the effects of wave radiation stress on the maximum computed water level for Hurricane Ike. The figure shows the difference between Exp. 2a (including wave radiation stress) and Exp. 1 (without wave effects). The largest differences ( $\sim 0.2$  m) are located in the regions where rapid wave transformation occurs through depth-limited wave-breaking, such as Atchafalaya Bay and Mississippi Delta. The weak contribution of wave set-up along the LATEX Coast (0.05 – 0.1 m) can be explained by the relatively broader continental shelf (compared with the Mississippi Delta) and expansive wetlands. The wave-induced set-up would be larger and more focused if the shelves were narrower or if the near-shore region had a steeper slope.

Model results of Experiment 2b (green solid line in Fig. 4-18) show that, when including both radiation stress and wave-enhanced bottom friction, the storm

surges are significantly underpredicted by 5-20% at the NOAA stations during Hurricane Ike. The modeled results indicate that the influence of the wave-enhanced bottom stress on the storm surge simulation is even more important than the wave set-up through wave radiation stress. Fig. 4-20 shows the effect of waves as the difference between the maximum water levels from Exp. 2b (full current-wave interaction) and Exp. 1 (base case). The largest differences ( $\sim -0.2$  m) are located along the LATEX Coast, and modest decreases ( $\sim -0.05$  m) occur near the 50-m isobath. This pattern can be explained as follows: near the oceanic bottom, there exist enhanced levels of turbulence due to wind-wave activities and the short-period oscillatory nature of wave orbital velocity leads to a thin wave boundary layer above the seabed in the near-shore regions. The high shear velocity within the wave BBL produces higher levels of turbulence intensities. The strong turbulence intensities within the wave BBL result in larger bottom shear stresses and have a stronger impact in the near-shore region than in deep water (Grant and Madsen, 1979; Grant et al., 1984; Grant and Madsen, 1986; Zhang et al., 2004).

#### 4.4.3 Experiments 3 and 4: effects of sediment-induced stratification on the forerunner

Based on the conclusions of Experiment 2 presented above, it is clear now that, although the breaking wave plays an important role, particularly near the shoreline, this breaking wave is not the major process to explain why the model tends to underestimate the large forerunner during Hurricane Ike. In this section, our

hypothesis of the effects of sediment-induced stratification on the forerunner and the BBL response will be investigated using Experiments 3 and 4.

The water levels simulated by Experiment 3 show the significant effect of sediment-induced stratification on the forerunner (Fig. 4-21). The modeled forerunners increased about 30% (compared with the base case) when considering the effect of sediment stratification on the bottom friction (Eq. (4.13)). Fig. 4-22 shows the difference between the maximum envelope of water during Ike obtained by Exp. 3 (considering the effect of sediment stratification on bottom friction) and Exp. 1 (base case) simulations. The larger differences ( $> 0.6$  m) are located near the western Louisiana Coast where water depth is shallower than 40 m. As we mentioned before, bottom friction plays an important role in shallow water regions; the increase of sediment stratification as well as Richardson number in the near-bottom water column (Fig. 4-25 (blue dot)) decreases the bottom friction coefficient. In a strongly stratified BBL, where the Richardson number is large, bottom friction decreases with the increase of alongshore current velocity (Fig. 4-26), suggesting that the Ekman set-up in a stratified environment becomes larger than in a clearly well-mixed water case. However, the water levels during the primary surge are overestimated in Exp. 3 around the areas where Ike made landfall. Potential explanations for that include the constant value of settling velocity used in the model, treatment of sediment class (only one class in the present model), and wave-current interaction over the seabed. The first two are poorly understood along the LATEX Coast and uncertainties will be increased for the calculation of sediment transport. The third one, interaction of

waves and currents over the seabed, is a key material for the determination of the bottom shear stress as well as the calculation of sediment transport because bottom stresses determine the resuspension rate for suspended sediment; a large amount of sediments are resuspended due to strong bottom stresses caused by wave-current interactions and, therefore, generate strong gradients close to the boundary. According to Experiment 2b, bottom shear stresses are highly affected by wave-current interactions. Also, recent studies indicate that the effect of bottom sediment-induced stratification is a function of the normalized near-bed wave orbital velocity (Conley et al., 2008). Based on all this information, including the interactions of wave and currents in the BBL for suspended sediment simulation is the most viable procedure to fix the over-shooting of the primary surge in Experiment 3 and improve the entire storm surge simulation of Hurricane Ike.

Results of Experiment 4 (including full wave-current interactions and effects of sediment stratification on bottom friction) are shown in Fig. 4-23. At most stations along the LATEX Coast, the modeled forerunner also matches well with measured data, and the over-shooting of the primary surge almost vanishes with the wave-current BBL dynamics. Fig. 4-24 shows the differences between the maximum envelope of water during Ike obtained by Exp. 4 (including full wave-current interaction and the effect of sediment-induced stratification) and Exp. 1. The distribution of Fig. 4-24 is similar to that of Fig. 4-22, except the difference is slightly larger along the West Louisiana Coast. The vertical profiles of suspended sediment simulated by the model at the location 30 km from Station 8771510 (see Fig. 4-1b,

green dot) for the period of 9/12/2008 0000 UTC to 9/14/2008 0000UTC (including forerunner, primary surge, and post-runner) are shown in Fig. 4-25. It is notable that an increase (decrease) of combined stress due to waves and currents (Fig. 4-27) increases (decreases) the bottom sediment concentration (Fig. 4-25) as well as the intensity of stratification, which is represented by the flux Richardson number  $R_f$  (Fig. 4-26). Fig. 4-27a and Fig. 4-27b show that the variation of combined stress due to waves and current is highly correlated with bottom orbital velocity. The vertical distribution of sediment concentration and the flux Richardson number  $R_f$  (Fig. 4-25 a-e, (blue dot); Fig. 4-26) indicate that a strong sediment-induced stratification occurs due to larger  $\tau_{wc}$  during the forerunner stage (Fig. 4-27a). Sediment-induced stratification vanishes due to the increase of  $\tau_{wc}$  in the stage of primary surge. On the contrary, without considering the effect of wave-current interaction on the calculation of bottom shear stress, the sediment erosion was based on a simple drag formulation (see Section 4.2.2) and the strong gradient of suspended sediment always existed at the bottom of the water column (Fig. 4-25 a-i (blue dot)) in both stages. Fig. 4-28 shows the snap-shot of vertical profiles of eddy diffusivity at 1200 UTC 09/12/2008 during the forerunner stage. The profiles show that a sediment-induced stratification reduced the maximum value of the eddy diffusivity by about 63%. The dampening of turbulence (i.e., a reduction in eddy diffusivity) results in the diffusion of momentum and the bottom friction is reduced compared with the well-mixed case (King and Wolanski, 1996). The new bottom shear stress that considered the effects of sediment-induced stratification for current model,  $\tau_{c\_mod}$  ( $\tau_{c\_expt3}$  and  $\tau_{c\_expt4}$ ), is shown

in Fig. 4-27a. The magnitude of  $\tau_{c\_expt4}$  is slightly smaller than that of the  $\tau_{c\_expt3}$  by 42% during the period of the forerunner, and then increases by 40% in the primary surge stage. This can explain why the over-shooting of the primary surge vanishes in Experiment 4 and the agreement of the forerunner is still good. It is also interesting to note that, in Fig. 4-26, after day 4.7, the maximum value of the flux Richardson number occurred in the middle layer of the water column. The presence of density stratification in the middle layer can also be expected to reduce the turbulence production and yield larger velocity (Fig. 4-29) in the middle layer compared with the well-mixed case (Dyer, 1986). Although there are no measured data to verify our model results, there are several previous studies that could support our finding: e.g. Sherwood et al. (2006) did field measurements under wave-dominated conditions and found that the log-profile method (adopted by developers of most ocean models) tends to overestimate shear velocity during strong stratification cases. This is consistent with our finding: the strong sediment-induced stratification during the forerunner causes the original log-profile method to overestimate bottom stress associated with the underprediction of the magnitude of the forerunner; agreement can be improved by considering the effects of stratification on the BBL.

From Eq. (4.1), the magnitude of the Ekman set-up is dependent on along-shore current, which is itself sensitive to bottom friction in shallow water regions. In Experiment 4, when including full wave-current interaction and the effects of sediment stratification on the BBL, the bottom friction is reduced, so the magnitude of the along-shore current is increased as well as cross-shore Ekman set-up during the

Hurricane Ike forerunner. On the other hand, based on BBL theory (e.g., Adams and Weatherly, 1981), the veering angle of the current vector is enhanced due to suspended sediment stratification (Fig. 4-29), and it may significantly increase the total water cross-shelf transport and contribute to the forerunner. Thus, in order to examine which dynamic dominates the magnitude of forerunner (Ekman set-up), we further calculate the mean of depth-averaged velocity in the LATEX inner-shelf (the region inside the 50-m isobath) during the Ike forerunner period (9/12/2008 0000 UTC – 9/13/2008 0000 UTC). The mean of depth-averaged velocity for each test, as well as the wind, are shown in Fig. 4-30. Although the vertical profiles of velocity vectors (Fig. 4-29) show a small increase in the turning angle (less than  $4^\circ$ ), the directions of mean depth-averaged velocities are still parallel to the shoreline and are close to each other. However, the magnitude of the along-shore current is quite different in each test. We then calculate the ideal Ekman set-up under the geostrophic balance based on Eq. (4.1) by using the modeled depth-averaged velocities from each case. Table 4-5 shows the results of an ideal forerunner based on the simplified across-shelf steady-state momentum equation (Eq. (4.1)) from each test. From the case including full wave-current interaction and sediment stratification (Exp. 4), we attained a set-up of 1.4 m on a 200-km-wide continental shelf. This value is very close to the observed water level anomaly during the Ike forerunner. These results indicate that, by including both wave-current interaction and sediment stratification, the magnitude of the along-shore current can be increased as well as the cross-shore sea surface set-up by 30% due to the decreasing of bottom shear stress and, hence,

yield better results for the forerunner simulation. Overall, Experiment 4 demonstrates the importance of wave-current coupling as well as the effects of sediment-induced stratification on the simulation of the dangerous forerunner.

Eq. (4.1) can be good to explain the formation of forerunner surge under steady-state. However, in the real world, the magnitude and direction of wind are changed with time so we should include the time variable in Eq. (4.1). Suppose a broad continental shelf with constant water depth  $D$ , and a uniform wind stress  $\tau_s$  is blown alongshore at the surface of sea from  $t=0$ , and the bottom stress is  $\tau_b$ . In the absence of any changes with the alongshore direction, and in the vicinity of the coast where the condition of no cross-boundary flow ( $v=0$ ) applies, then the typical momentum balance of the quasi-steady geostrophic component of arising sea level near the coast can be simplified as:

$$\frac{\partial u}{\partial t} = \frac{1}{\rho} \left( \frac{\partial F}{\partial z} \right) \quad \text{where } F = \tau_s - \tau_b \quad (4.29)$$

$$f u = \frac{-1}{\rho} \left( \frac{\partial P}{\partial y} \right) \quad (4.30)$$

Note that in Eq. (4.29) we neglect the Coriolis force because we assume the effect of Coriolis force is relatively small in the shallow water region under strong wind conditions although in Section 4.3.2 we have introduced the analytical solutions of unsteady Ekman dynamics. Integrating Eqs (4.29) and (4.30) from  $-D$  to surface, assuming  $u$  is constant with depth, and substituting  $P_z = P_A - \rho g(z - \eta)$  for  $\frac{\partial P}{\partial y}$ , then:

$$D \frac{\partial u}{\partial t} = \frac{F}{\rho} \quad (4.31)$$



$$fu = -g \left( \frac{\partial \eta}{\partial y} \right) \quad (4.32)$$

which leads directly to:

$$u = \frac{Ft}{\rho D} \quad (4.33)$$

$$\frac{\partial \eta}{\partial y} = \frac{-fu}{g} \quad (4.34)$$

Eq. (4.33) shows that the magnitude of alongshore current depends on the duration of wind. In particular, this current will eventually be limited by bottom friction ( $F = \tau_s - \tau_b$ ). Eq. (4.34) shows that a cross-shore sea surface set-up is in geostrophic balance with the alongshore current  $u$  with sufficient time. This set of equations (Eqs. (4.33) and (4.34)) can be used to describe the unique forerunner that occurred during Ike with time variation. Based on the observation (Fig. 4-2), the duration of shore-parallel wind is 1 day and the average magnitude of the wind is 15 m/s during the forerunner period. If we neglect the effect of the bottom shear stress term in Eq. (4.29) and assume a constant water depth  $D=30$  m in the LATEX shelf, then the magnitude of the alongshore current is 0.95 m/s and we can attain a sea surface set-up of 1.42 m on a 200-km-wide continental shelf. Overall, we can conclude that the large forerunner that occurred during Hurricane Ike along the LATEX shelf was due to (a) the long duration of shore-parallel wind (at least 1 day with the magnitude around 10-15 m/s) blowing along the broad continental shelf (200-km-wide in this case) generated cross-shore Ekman set-up and contributed to the forerunner surge; (b) this forerunner surge reached a geostrophic balance between the

Coriolis force acting on the along-shelf current and the across-shelf pressure gradient due to the sufficiently slow speed of Hurricane Ike.

#### 4.5 Practical approach

Although a three-dimensional current model coupled with wave, sediment-transport, and BBL sub-models including the effects of sediment-induced stratification can significantly improve model performance for the simulation of the Ike forerunner, too much computing resource is required to run a fully coupled model for storm surge simulation. It is fine for a hindcasting study since we are interested in the formation of the large forerunner as well as dominant mechanisms, but for the real-time forecasting, the efficiency of the model (i.e., its execution speed) is as important as accuracy. For example, the NHC (National Hurricane Center) produces a hurricane advisory every 3-6 hours during a tropical storm event, and when decision makers have a new hurricane advisory in hand, they would like to know the associated storm surge as well as the inundation, – immediately, if possible. In this section, a practical approach is presented to simplify the sophisticated model we described above. The simplified model is very efficient, and moreover it is still reasonable to represent the large forerunner in the Gulf of Mexico.

Fig. 4-27 shows that the varying of combined stress due to waves and currents is highly relative with bottom orbital velocity. Conley et al. (2008) indicated that the stratification effect is given as a function of the normalized orbital velocity. In their study, the parameter  $\Delta c$  is defined to quantify the effects of stratification:

$$\Delta c = \frac{C_{DS} - C_{NS}}{C_{DS}} . \quad (4.35)$$

Where  $C_{DS}$  ( $C_{NS}$ ) represents the sediment load integrated from the bed to 1 m above it for the simulations including (excluding) the sediment effect on seawater density. This parameter has the quality that it asymptotes to 1 as stratification becomes important and tends towards zero as the importance of stratification subsides. A similar approach is conducted to analyze our model results from Exp. 4, except we used the more common parameter, flux Richardson number  $R_f$ , instead of the self-defined  $\Delta c$ , to represent the effect of density stratification. Despite the large scatter, it is relatively clear that the effects of stratification are a function of the normalized orbital velocity (Fig. 4-31). This is a very important relationship since a simplified stratification parameter, as a function of orbital velocity, can be derived directly from the 3D wave-current coupled model. This derivation can be done instead of running the real sediment-transport model, since it is too expensive to conduct a 3D fully coupled wave, current, and sediment-transport model with a grid of over a million nodes for real-time storm surge forecasting.

In Fig. 4-31, basically the stratification parameter as a function of normalized orbital velocity can be separated into three regions and described independently: normalized orbital velocity below 300, normalized orbital velocity between 300 and 800, and normalized orbital velocity larger than 800. For the mid-range of normalized orbital velocity (300~800), the model results in the inner-shelf region from Exp. 4 indicate a good linear relationship ( $R^2=0.55$ ) between normalized orbital velocity and

sediment-induced stratification. Since the critical flux Richardson number  $R_{fc} = 0.21$  was chosen to represent the condition for which turbulence was completely suppressed by stratification (slippery BBL), the sediment-induced stratification met this maximum criterion when normalized orbital velocity is larger than 800. For weakly normalized orbital velocity ( $< 300$ ), there is no sufficient energy to resuspend sediment in the water column and therefore there is little stratification potential.

Given the understanding of the above relation, a simple index of density stratification as a function of normalized orbital velocity can be generated without running the sediment-transport model in the Gulf of Mexico. In the 3D wave-current coupled model, the flux Richardson number  $R_f$  can be obtained by:

$$R_f = 0.0 \quad \text{if } \frac{U_b}{w_s} < 300 \quad (4.36)$$

$$R_f = 0.0004 \left( \frac{U_b}{w_s} \right) - 0.126 \quad \text{if } 300 \leq \frac{U_b}{w_s} \leq 800 \quad (4.37)$$

$$R_f = R_{fc} \quad \text{if } \frac{U_b}{w_s} > 800. \quad (4.38)$$

This approach was adopted in the inner-LATEX shelf region (inside the 50-m isobath) to consider the effects of sediment-induced stratification on the BBL without running the real 3D sediment-transport model. Using the practical approach in the 3D wave-current coupled model and the cap for maximum and minimum bottom drag coefficient in the inner-LATEX area, the simulated water levels along the LATEX Coast in the northern Gulf of Mexico during Hurricane Ike were generally close to the results we attained from Exp. 4. Fig. 4-32 shows examples of the modeled water level along the LATEX Coast. Black solid lines represented the base case (without wave

and the effects of sediment-induced stratification); blue solid lines are the results obtained by Exp. 4 (full wave-current interaction and effects of sediment-induced stratification); the green solid lines are the results obtained by employing the practical approach. Basically the modeled forerunners based on the practical approach compared well with observed data and the patterns are similar to the results calculated by Exp. 4, whereas the results from the base case indicate the magnitude of forerunners is underestimated by about 30%. It is evident that, along the LATEX shelf, the under-prediction of the water level during the Ike forerunner was due to the overestimation of the bottom drag coefficient, which could be significantly revised by accounting for the effects of sediment-induced stratification on the BBL. Once the effects of sediment-induced stratification were considered through the simple practical approach we described above, the prediction skill for the water level became much improved in the LATEX regions during Hurricane Ike in 2008. The simple practical approach met our goal, and certainly proved our hypothesis: BBL dynamics are also important for the storm surge simulation. Note that the discrepancy between the practical approach and Exp. 4 (Fig. 4-32; green line and blue line) could be explained by the poor assumption in the third relationship we adopted (Eq. (4.38)) because the water column was not always stratified ( $R_f = R_{fc}$ ) when  $\frac{U_b}{w_s} > 800$  (Fig. 4-31). This can be further improved by using more appropriate assumptions during the largely normalized orbital velocity.

#### 4.6 Conclusions

A new three-dimensional storm surge modeling system coupling the unstructured grid current model SELFE (Zhang and Baptista, 2008), the wave model WWM II (Roland, 2009), and the sediment-transport model was developed to study the sediment resuspension effects and the BBL dynamics on the hindcast of the Ike forerunner in the Gulf of Mexico. A stability function to the bottom drag coefficient  $C_d$  is introduced to the bottom boundary condition in SELFE in order to consider the effects of sediment-induced stratification on the BBL.

The modeling system was implemented to the super-regional domain covering the entire U.S. East Coast, a portion of the Northern Atlantic Ocean, the Gulf of Mexico, and the Caribbean Sea and resulted in reasonable tidal and wave predictions in the northern Gulf of Mexico. When only considering atmospheric forcing, the primary surges associated with Ike are well-predicted along the LATEX Coast, but the model tended to underestimate large forerunners by 30%. Numerical experiments were then performed to screen the response of the forerunner development by different physical dynamics, such as the wave-current interaction or the effects of sediment-induced stratification on the BBL.

Breaking wave set-up through gradients of radiation stresses slightly contributes to the entire storm surge by 10%, and the total water levels were fully underpredicted with the combination of wave-induced radiation stress and wave-enhanced bottom shear stress. When the seawater density and the sediment concentration were coupled, the effect of sediment-induced stratification reduced the

magnitude of bottom shear stress as well as the thickness of the BBL. The modeled results that only consider the effects of sediment-induced stratification on BBL matched the Ike forerunner pretty well, but over-shooting occurred in the primary surge stage. Combining the effects of the full wave-current interaction and sediment-induced stratification produced the best model results. The sediments resuspended during the forerunner by the combined bottom stress due to waves and currents were only distributed in the near bottom with a thickness of a few meters. The thickness of the BBL and bottom friction was reduced by the establishment of a lutocline above the BBL due to the strong vertical gradients of sediment concentrations. On the other hand, the lutocline vanished and a well-mixed distribution of suspended sediment manifested during the primary surge stage (Fig. 4-33). As the stratification varied from the forerunner to the primary surge, the bottom friction variability was also predicted. The model therefore matched the forerunner without over-shooting during the primary surge. Note that the variability of the bottom drag coefficient  $C_d$  was not only a hypothesis, but has been observed in the field (e.g., Cheng et al., 1999). When the effects of sediment-induced stratification were properly represented by the flux Richardson number,  $R_f$ , then a positive linear relationship was displayed with wave orbital velocity normalized by settling velocity. The dependence of stratification on normalized orbital velocity was useful for simplifying the sophisticated modeling system. A practical approach was adopted in the 3D wave-current coupled model based on the relationship between normalized orbital velocity and sediment-induced stratification. By implementing the simple practical approach over the inner-LATEX

area, the predictions of the total water level were generally reasonable compared with measured data and results from the fully 3D wave-current-sediment-transport coupled model. Another interesting phenomenon in Fig. 4-33 is that, after the primary surge, our model did not simulate the response of water level correctly during the relaxation period (ADCIRC and FVCOM also have this same problem). During the relaxation period, the winds were relatively weak and all the other forces (e.g., baroclinic force due to water temperature or salinity, see Fig. 4-34, Bhagat (2009)) merge together and play important roles. Baroclinic adjustment can cause dramatically different results of water level during the relaxation period and should be further considered in the future study.

Finally, it should be stressed that the model simulation of sediment distribution and the BBL properties in this study are tentative without direct data-model comparison. Our results suggest that future field investigations should incorporate an effort to monitor water column and near-bed suspended sediment, in addition to detailed near-bed hydrodynamic measurements, in order to further understand the effects of sediment-induced stratification on BBL dynamics during storm events.



**Table 4-1** Statistic Comparisons of tidal amplitudes (in meters) and phases (in degrees) derived from harmonic analysis of simulated and NOAA predicted tidal levels (groups of stations based on different States).

	$R^2$	Slope	$\sigma$	$\bar{\epsilon}$	$ \bar{\epsilon} $	E
State Amplitudes						
FL	0.96529	1.080842	0.017343	-0.00823	0.011772	0.171634
AL	0.978793	1.063326	0.009433	-0.00458	0.008038	0.132745
MS	0.971922	1.053031	0.01071	-0.00394	0.00808	0.145613
LA	0.776199	0.983094	0.024416	0.00103	0.014284	0.407122
TX	0.481198	0.760318	0.034025	0.006584	0.021866	0.621271
State Phases						
FL	0.984236	0.961944	14.05314	5.825491	10.45416	0.08992
AL	0.466504	0.604691	75.70788	40.43465	67.58089	0.513484
MS	0.777539	0.813544	38.15308	22.64761	32.03011	0.309974
LA	0.779643	0.940086	55.70728	-1.76981	34.26291	0.326018
TX	0.670961	0.874074	63.73142	10.97739	46.13566	0.408912

**Table 4-2** Model parameters for sediment transport model validation – open channel flow case.

<b>Model parameter</b>	<b>Variable</b>	<b>Value</b>
Length, width, depth	Xsize, Ysize, depth	10000, 100, 10 m
Bottom roughness	$Z_0$	0.0053 m
Time step	dt	30 s
Simulation steps	Ntimes	1440
Settling velocity	$W_s$	1.0 mm s <sup>-1</sup>
Erosion rate	$E_0$	5×10 <sup>-5</sup> kg m <sup>-2</sup> s <sup>-1</sup>
Critical stress	$\tau_{ce}$	0.05 N m <sup>-2</sup>
Porosity	$\phi$	0.9
Inflow/ outflow boundary condition	u	1 m s <sup>-1</sup>

**Table 4-3** Model parameters for sediment transport model for storm surge cases.

<b>Parameter</b>	<b>Unit</b>	<b>Value</b>
$SD_{50}$	mm	0.01
$E_0$	$\text{kg m}^{-2}\text{s}^{-1}$	$5 \times 10^{-4}$
$\rho_s$	$\text{Kg m}^{-3}$	2650
$\tau_{ce}$	Pa	0.11
$Z_0$	m	0.001
$W_s$	$\text{mm s}^{-1}$	1
$\phi$		0.8

**Table 4-4** Setup of numerical experiments.

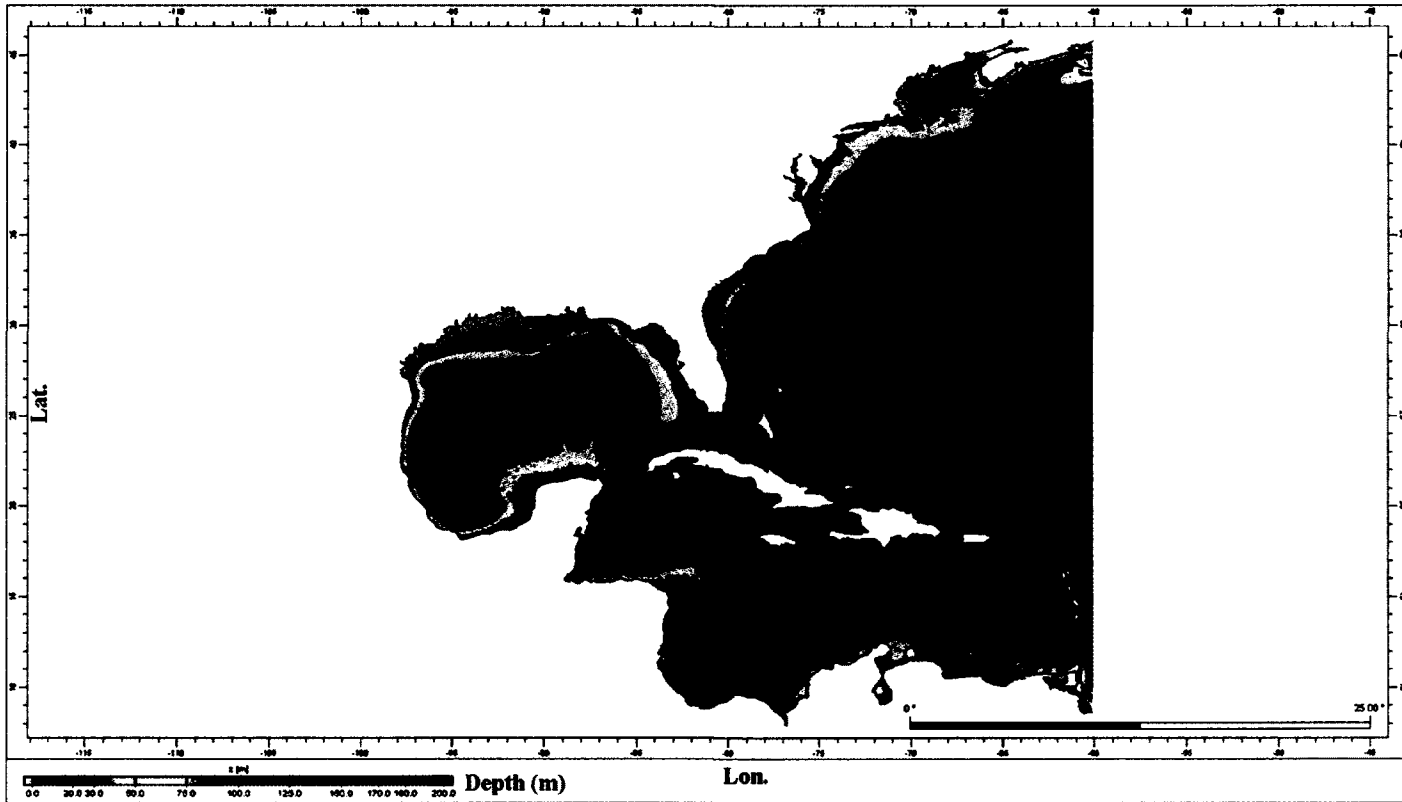
<b>Exp.</b>	<b>tide</b>	<b>wind</b>	<b>pressure</b>	<b>Radiation stress</b>	<b>Wave-enhanced bottom stress</b>	<b>Density effects</b>
1	on	on	on	off	off	off
2a	on	on	on	on	off	off
2b	on	on	on	on	on	off
3	on	on	on	off	off	on
4	on	on	on	on	on	on

**Table 4-5** Mean of depth-averaged velocity in the inner-LATEX shelf and results of ideal Ekman set-up based on Eq. (4.1) from each numerical experiment.

	<b>u</b>	<b>v</b>	<b>mag. (m/s)</b>	<b><math>\eta_c</math> (m)</b>
<b>Exp. 1</b>	<b>-0.66</b>	<b>-0.10</b>	<b>0.66</b>	<b>1.0</b>
<b>Exp. 2a</b>	<b>-0.67</b>	<b>-0.1</b>	<b>0.67</b>	<b>1.0</b>
<b>Exp. 2b</b>	<b>-0.50</b>	<b>-0.07</b>	<b>0.50</b>	<b>0.7</b>
<b>Exp. 3</b>	<b>-0.93</b>	<b>-0.14</b>	<b>0.94</b>	<b>1.4</b>
<b>Exp. 4</b>	<b>-0.90</b>	<b>-0.14</b>	<b>0.91</b>	<b>1.4</b>

(a)

### Grid Domain



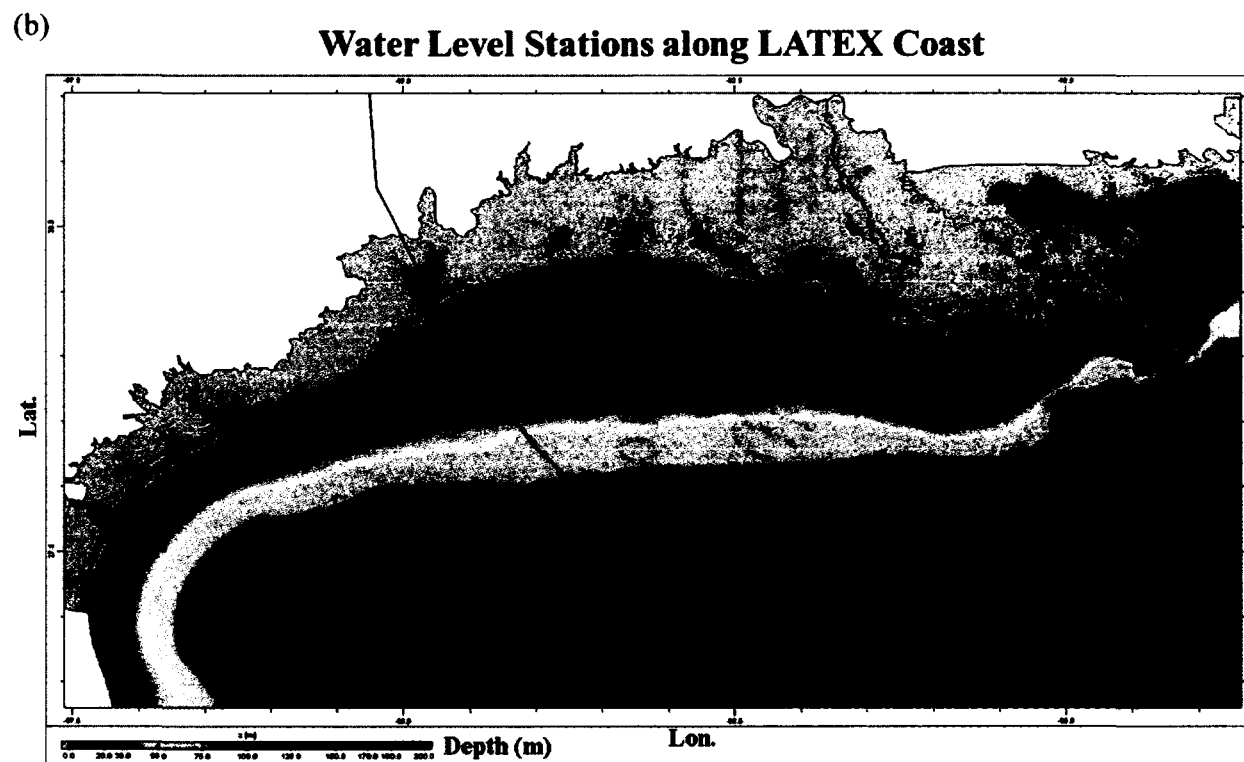
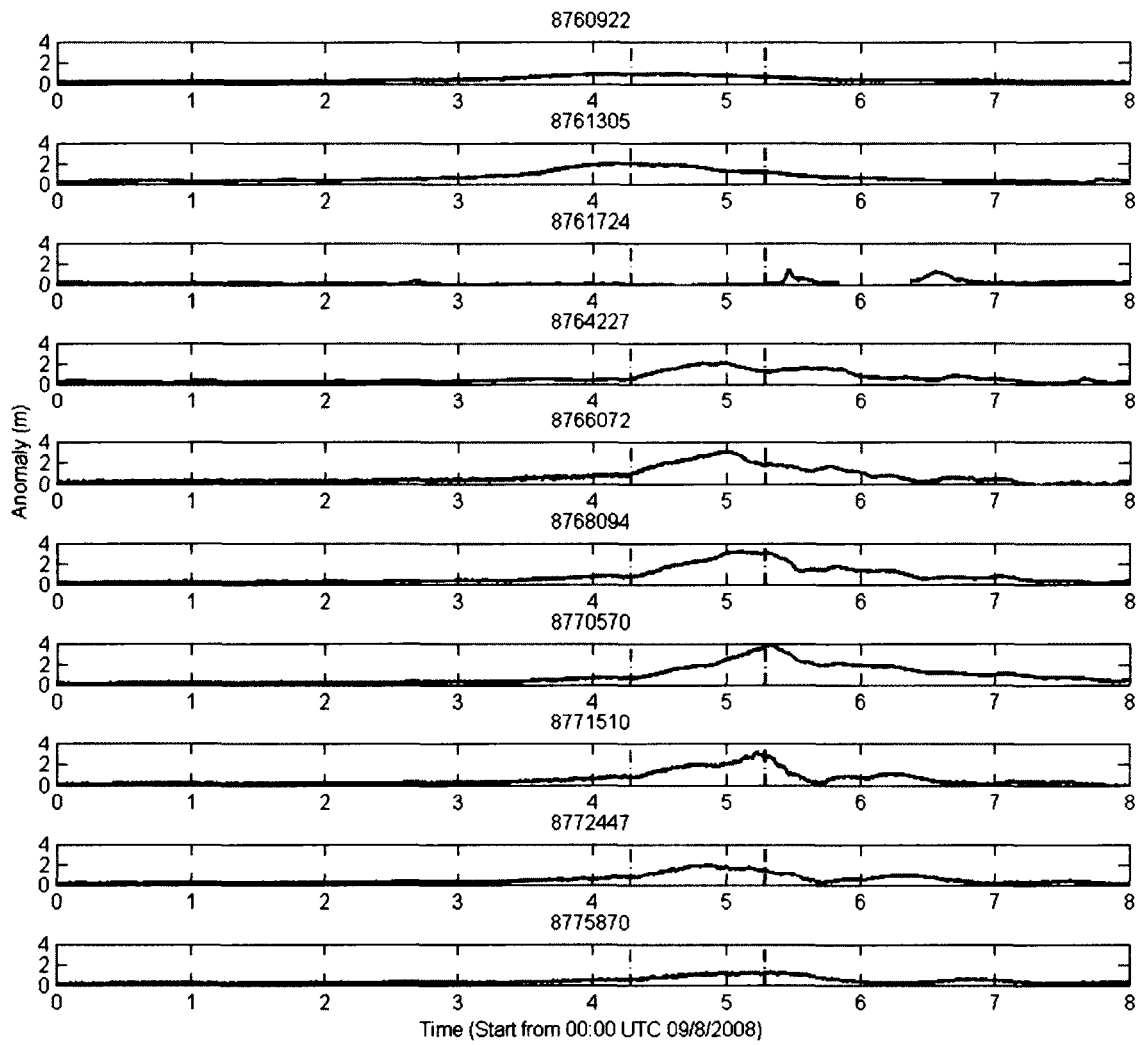


**Figure 4-1** (a) Model domain used in this study with bathymetry (m), and (b) Bathymetry of LATEX shelf, with tracks of Hurricane Ike (black curve). Black squares represent the locations of NOAA tidal stations used for the model validation. Green dot is 30 km from Station 8771510 and is used for the description of model vertical profile.

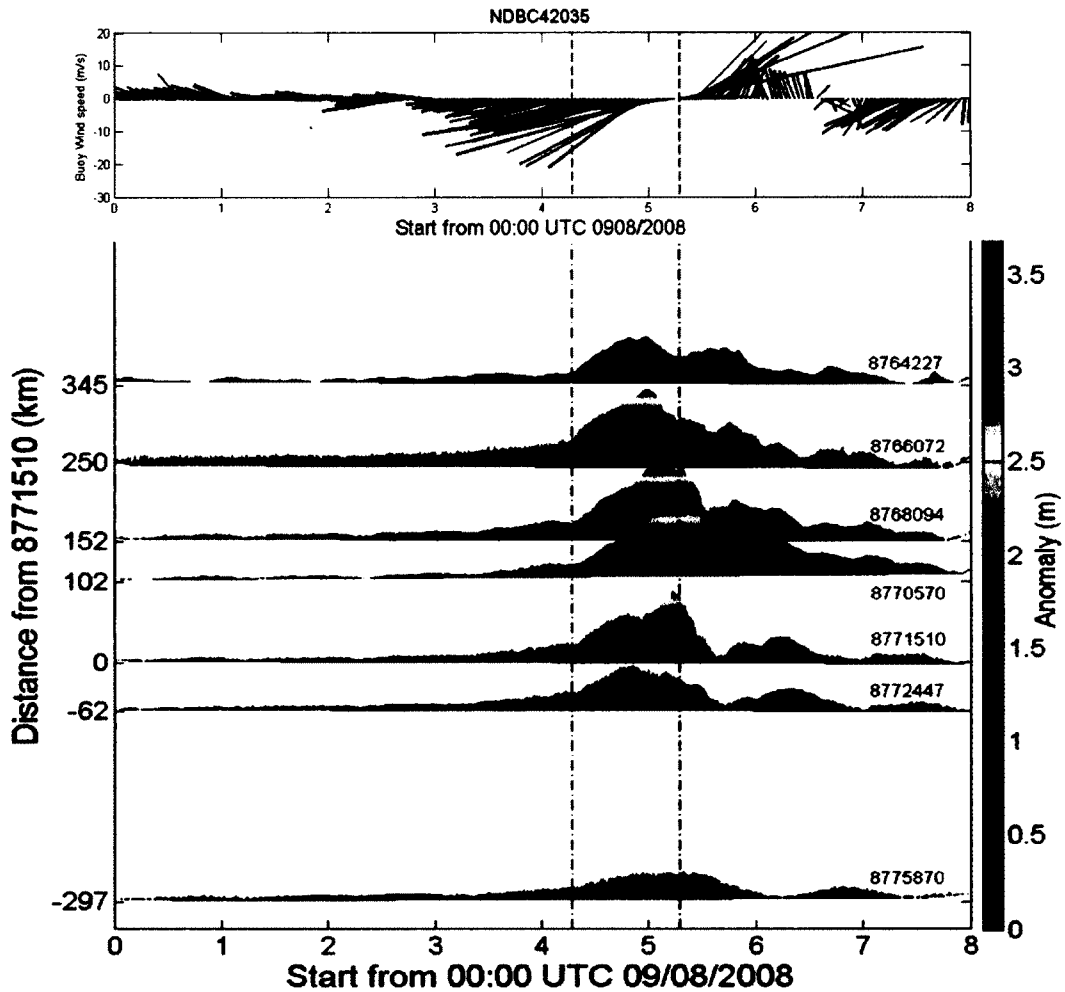
(a)

## Water Level Anomaly

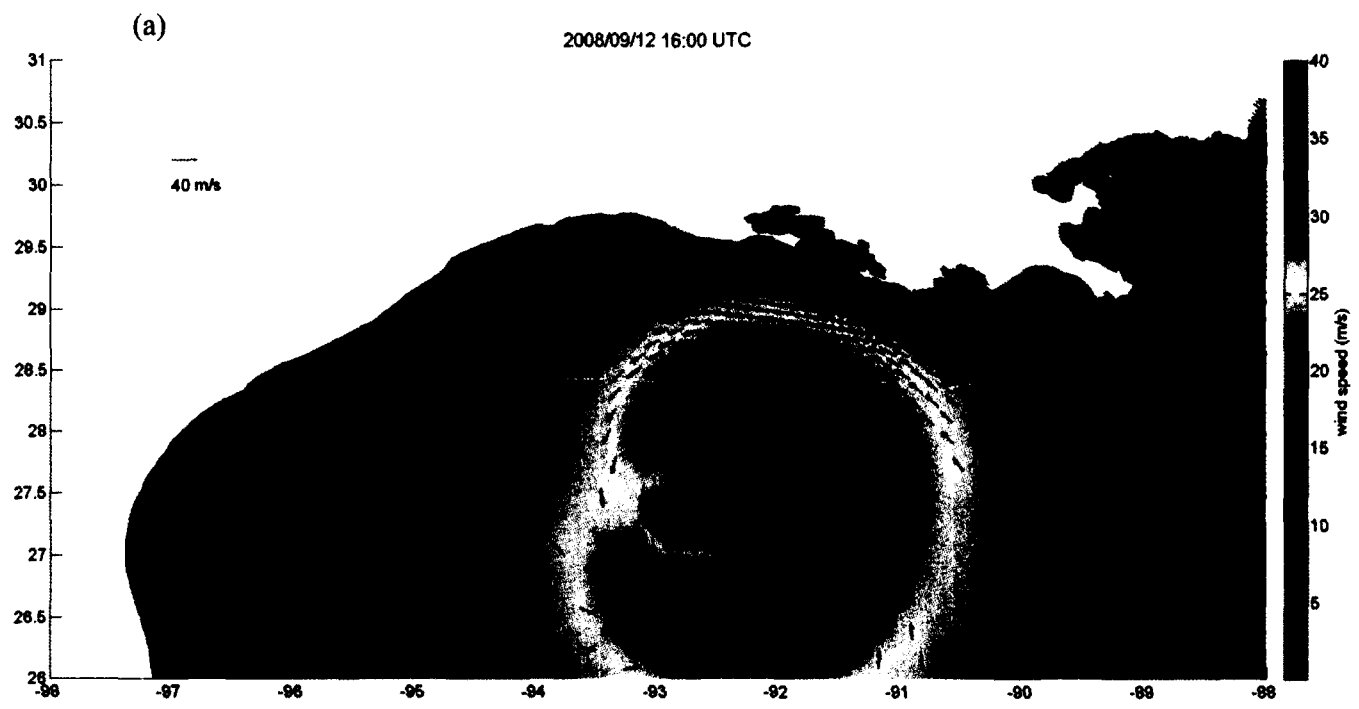


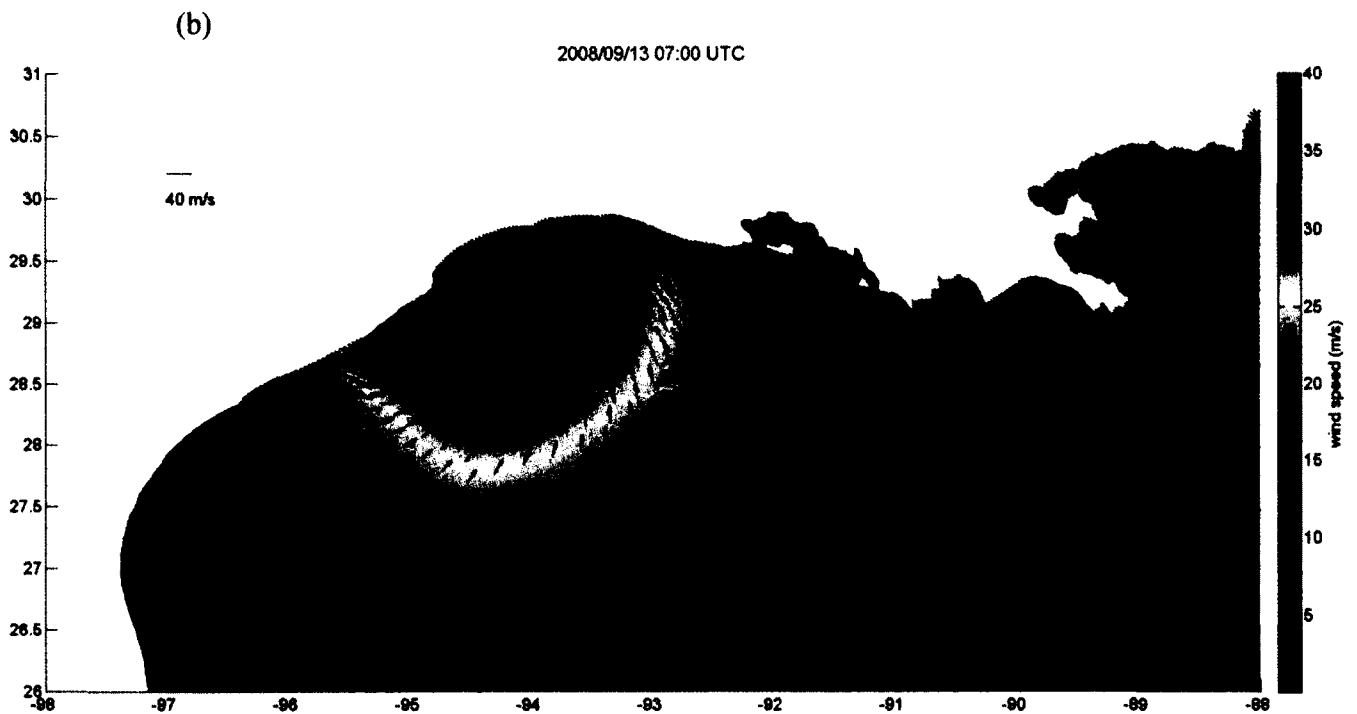


## (b) Observed wind and Water Level Anomaly

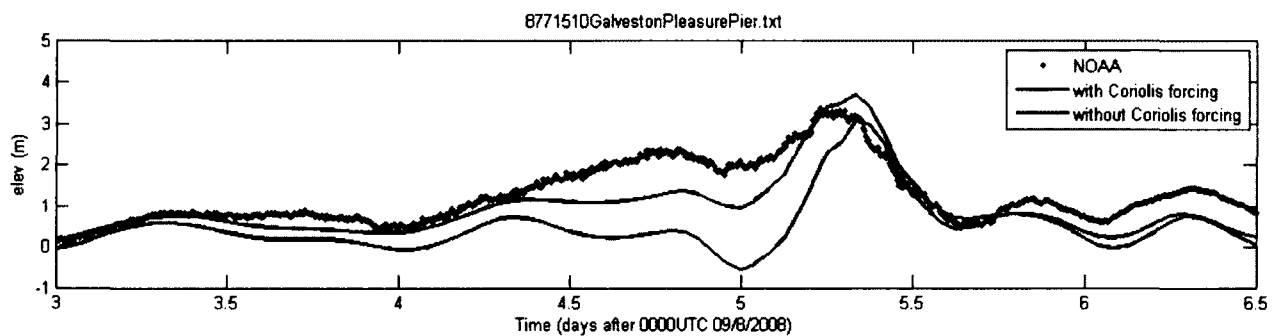


**Figure 4-2** (a) Time series of water level anomaly during Hurricane Ike at ten NOAA stations (observed water surface minus predicted tide). The black dashed line represents the date of landfall and the red dashed line represents 24 hours before landfall, and (b) Water level anomaly during Hurricane Ike along the LATEX Coast (observed water surface minus predicted tide). The black dashed line represents the date of landfall and the red dashed line represents 24 hours before landfall.

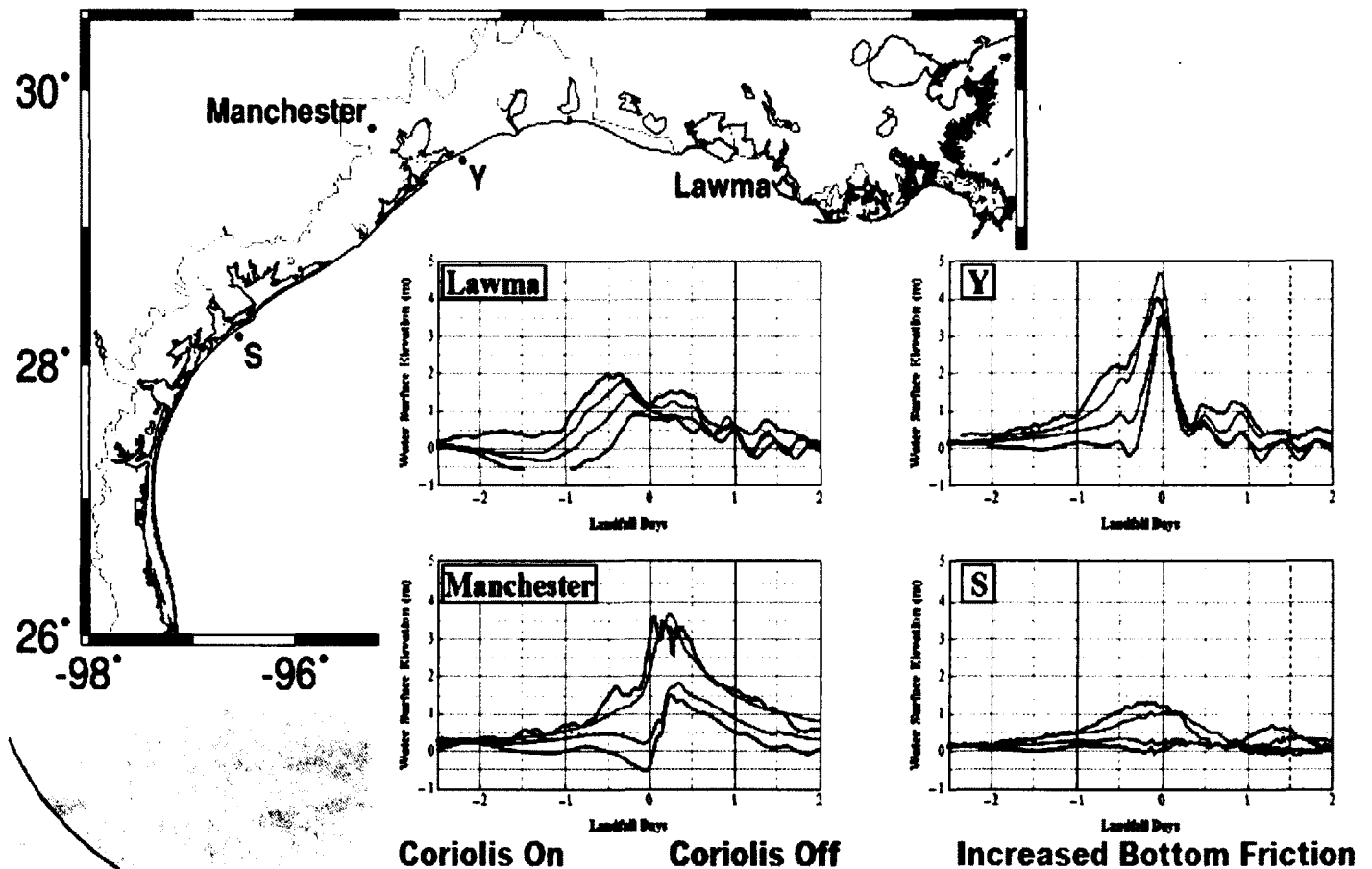




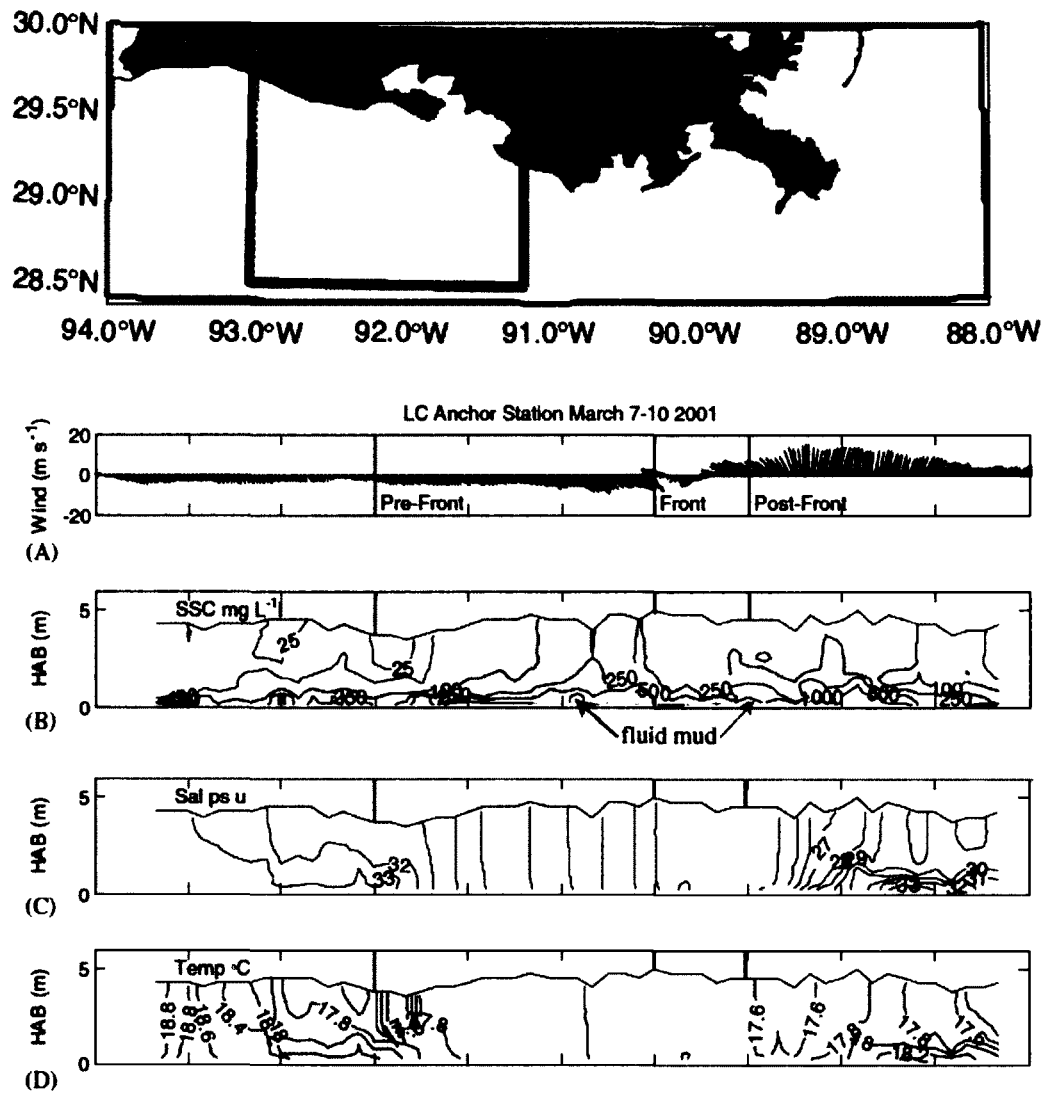
**Figure 4-3** Data assimilated wind field (a) at 12 hours before Hurricane Ike's landfall; (b) at time that Ike made landfall. The 50-m depth contour is given by the white line.

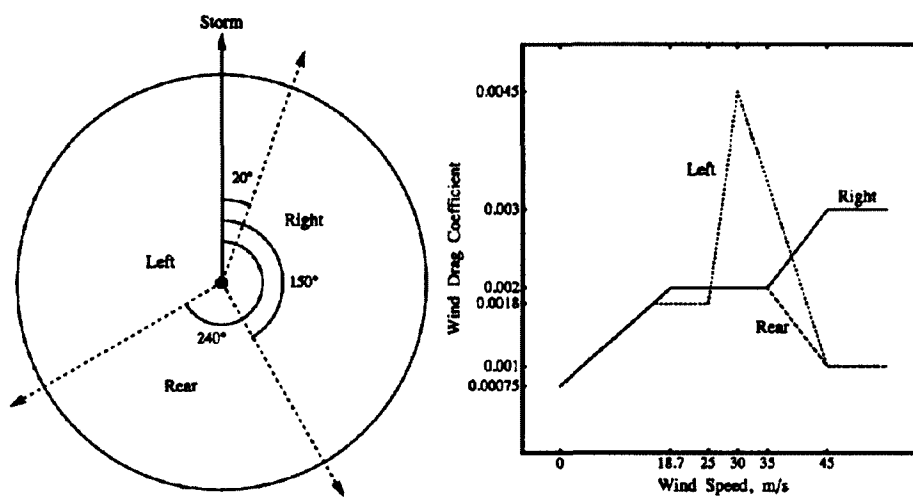


**Figure 4-4** Time series of measured (red dots) and computed water level with (black) and without (blue) Coriolis forcing at Station Galveston Pleasure Pier (8771510).

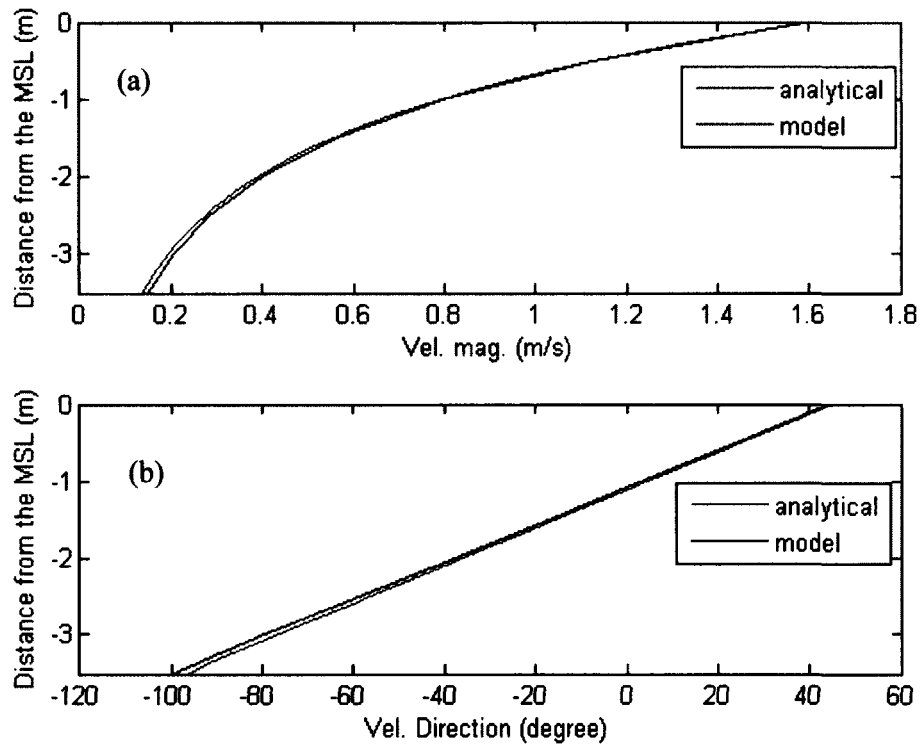


**Figure 4-5** Time series of measured (black) and computed water level with (red), without (blue) Coriolis forcing, and increased bottom friction (green) at Lawma, Gauge Y (High Island), Manchester Houston, and Gauge S (Locations are shown in map). Note that these results are presented by Kennedy et al. (2011).

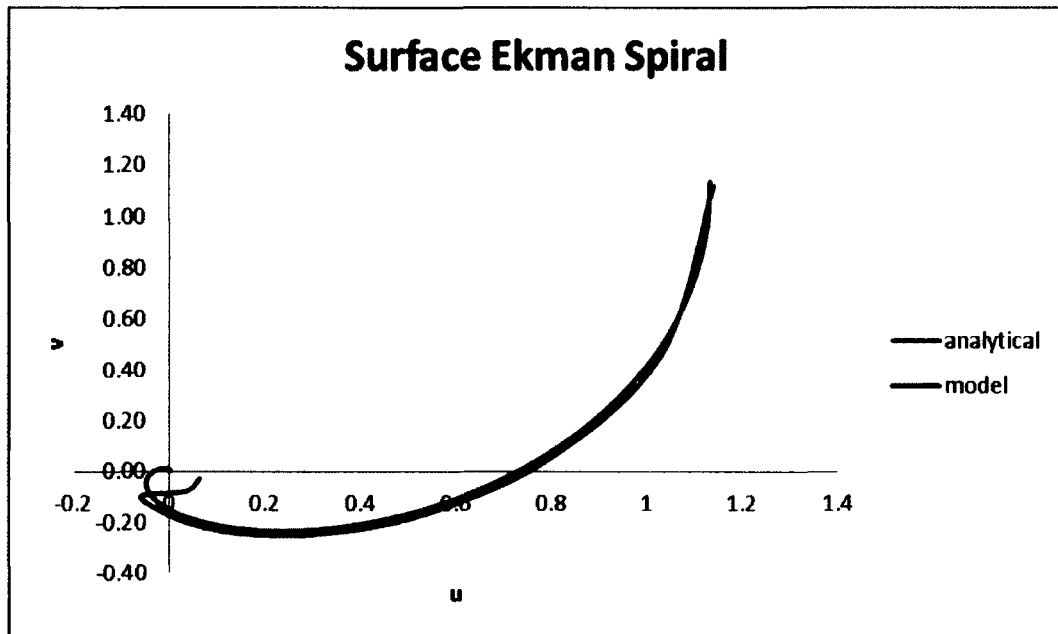




**Figure 4-7** Schematics of the azimuthal wind drag, showing (left) extents of sectors in relation to direction of storm movement, and (right) wind drag coefficient variability by storm sector. (This figure was re-plotted from Dietrich et al., 2011b).

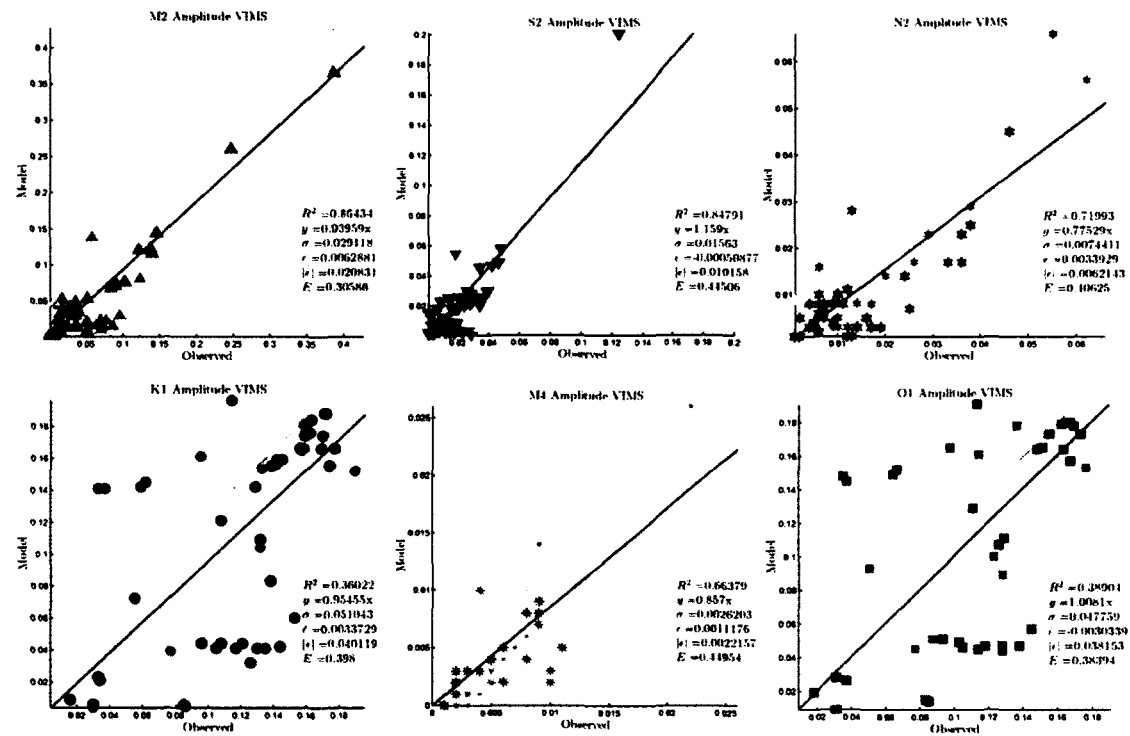


**Figure 4-8** Ekman motion test case – Magnitude (a) and direction (b) of velocity in the first 3m. The analytical solution is shown with red line, while the model results are shown with blue lines.

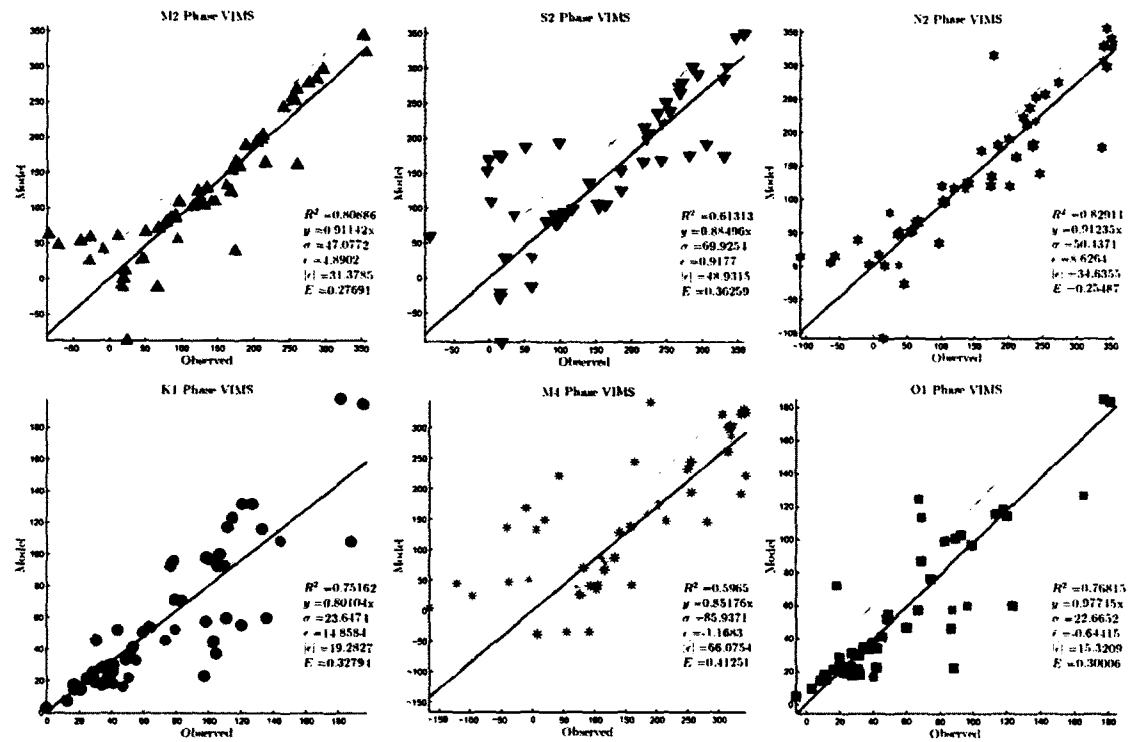


**Figure 4-9** Ekman motion test case – The velocity spiral in the surface Ekman layer. The analytical solution is shown with a red line, while the model results are shown with a blue line.

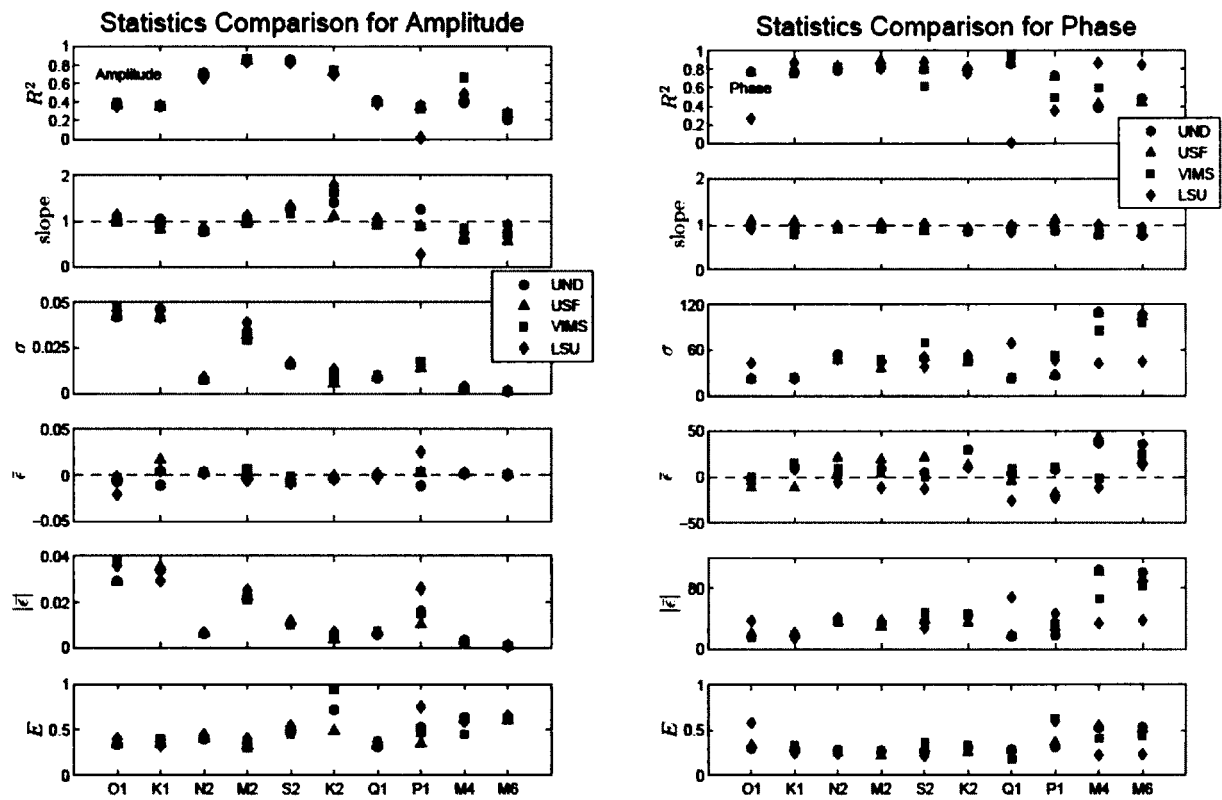




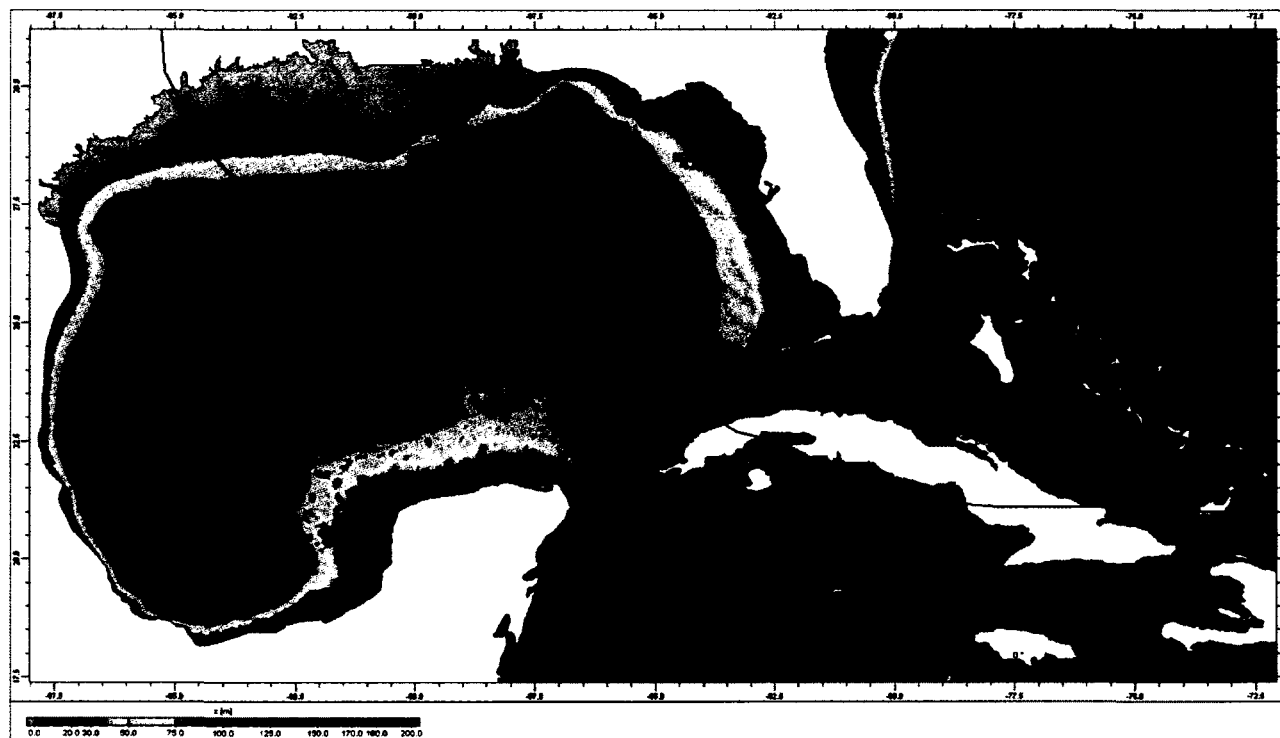
**Figure 4-10** Comparison of amplitudes as measured by NOAA and predicted by SELFE. Each figure represents each tidal constituent. The over- or under-predicted results are shown by color.



**Figure 4-11** Comparison of phases as measured by NOAA and predicted by SELFE. Each figure represents each tidal constituent. The over- or under-predicted results are shown by color.

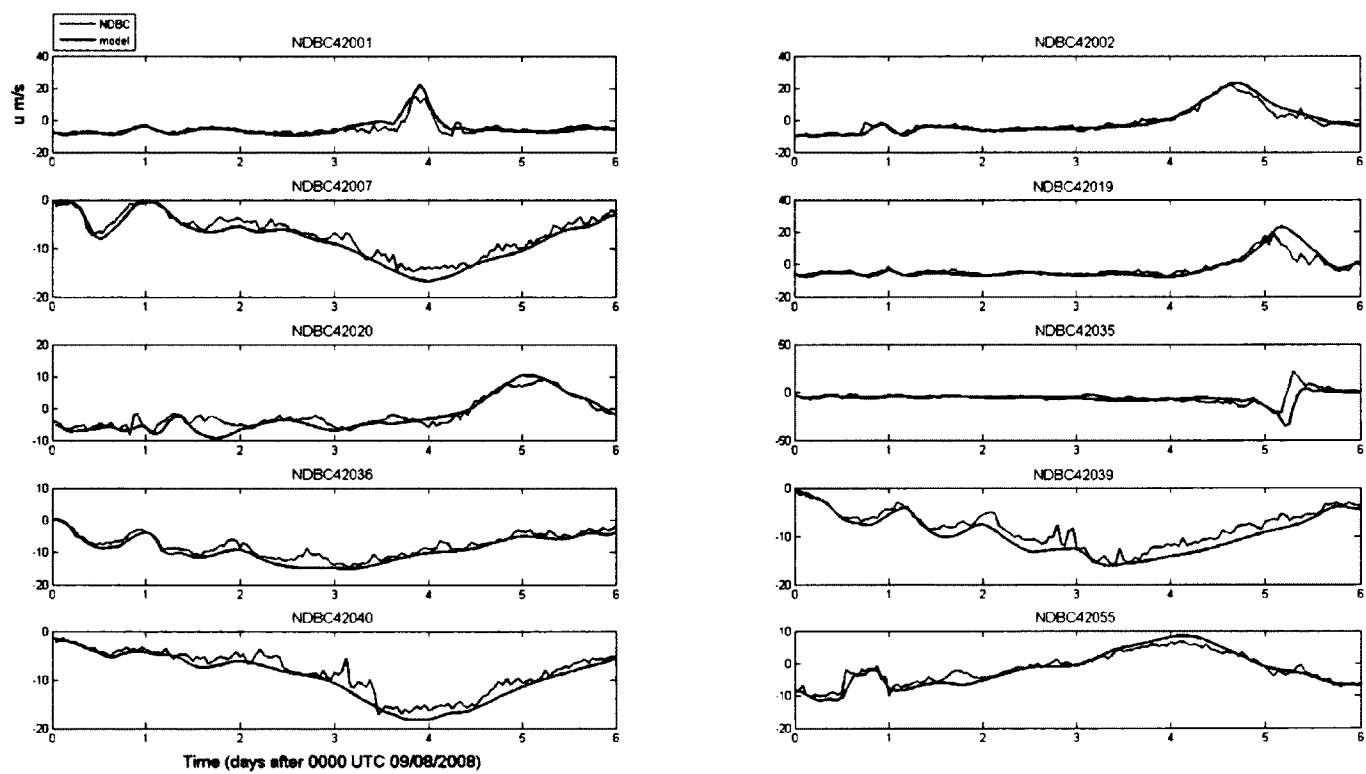


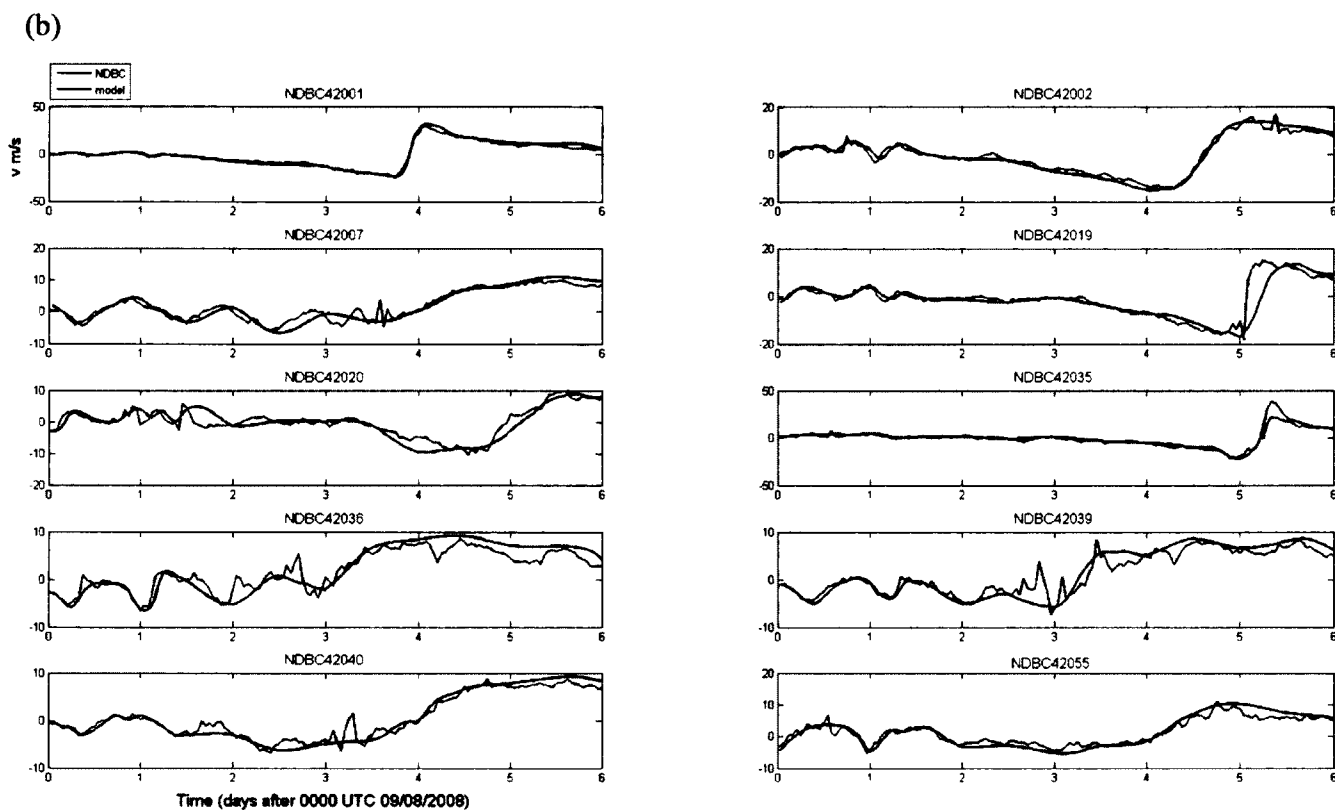
**Figure 4-12** Inter-model tidal comparison between four different unstructured-grid models with same tidal forcing and model setup.



**Figure 4-13** Locations of the NDBC buoys used for the validations of predicted wind and waves in the Gulf of Mexico during Hurricane Ike.

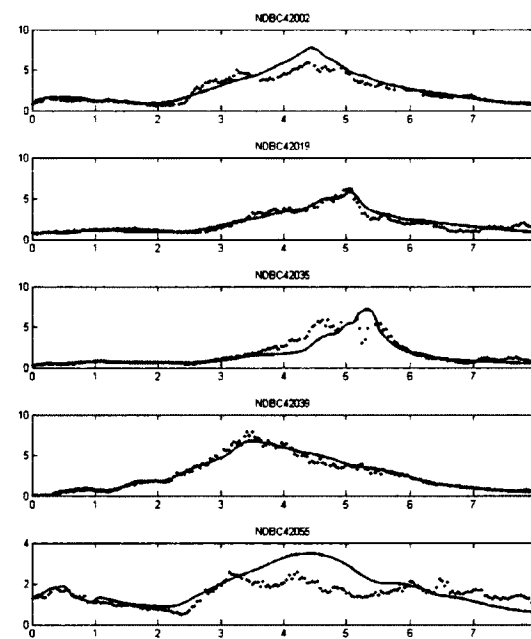
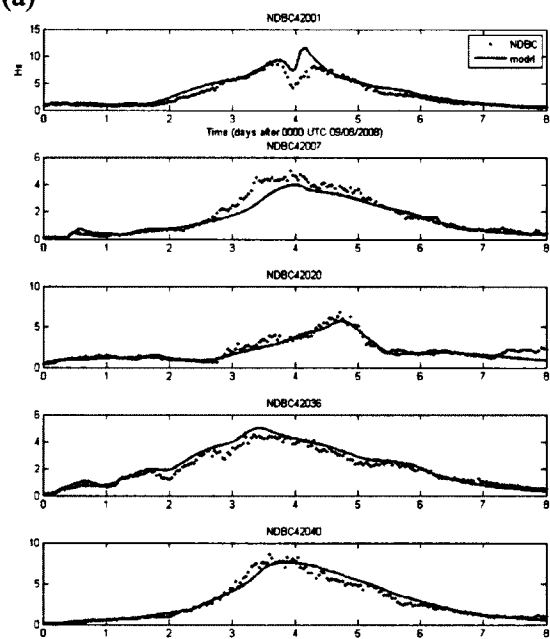
(a)

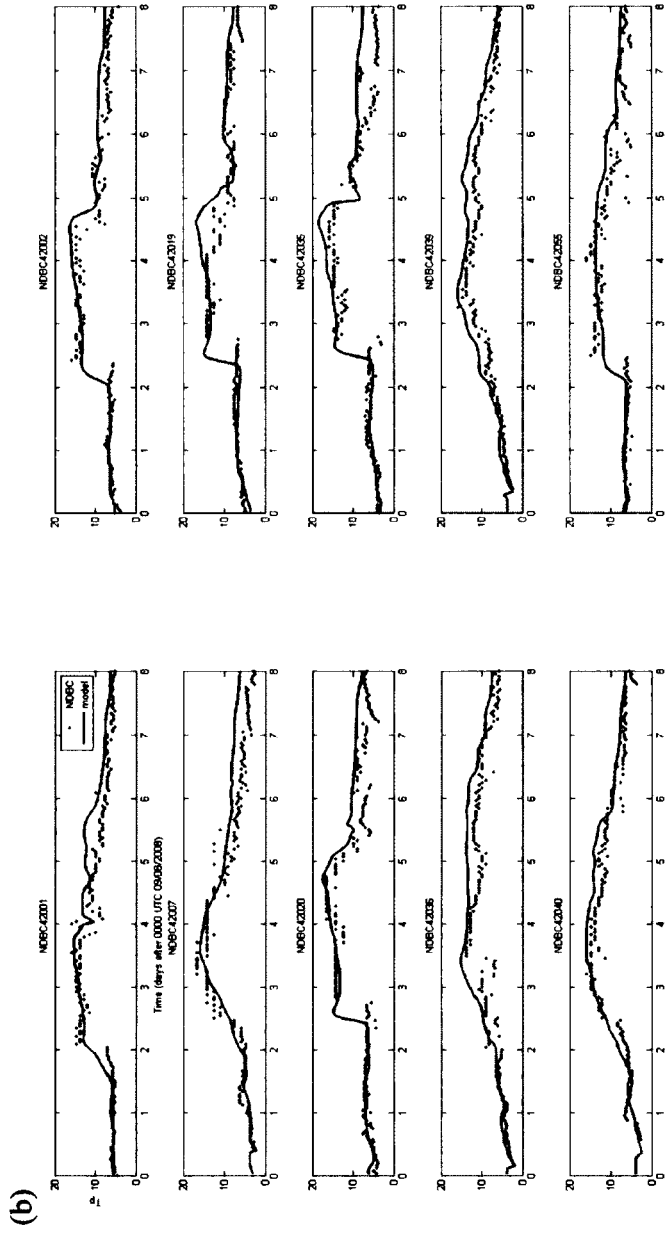




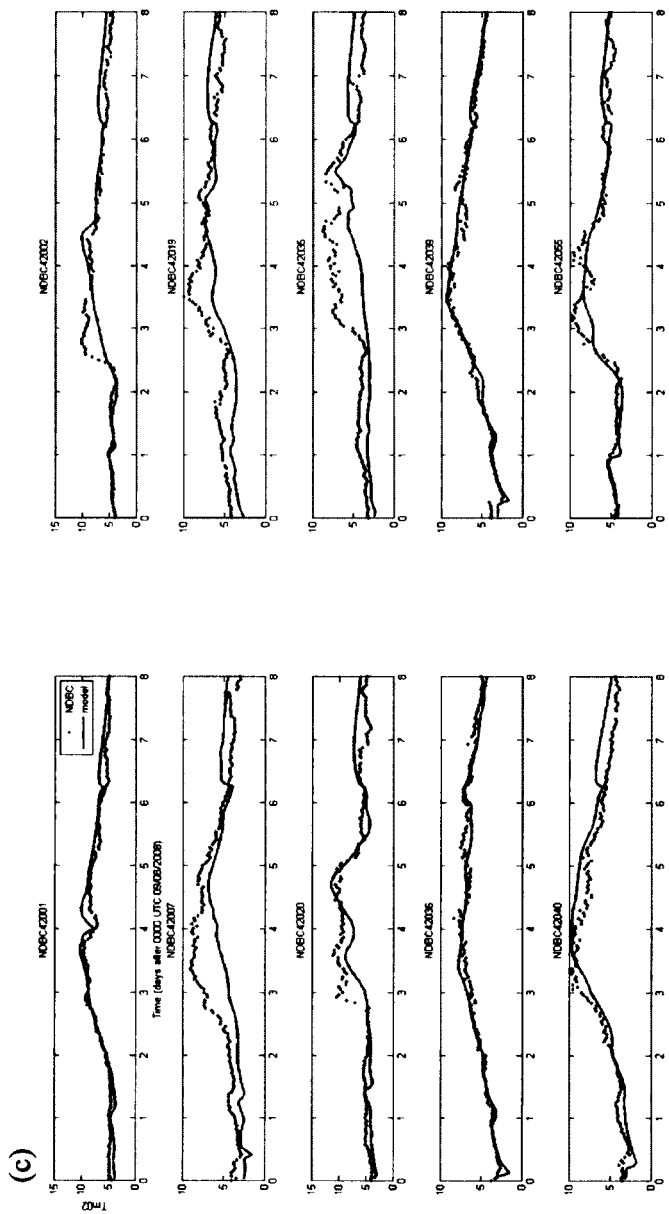
**Figure 4-14** Wind components (a)  $u$  directions; and (b)  $v$  directions during Hurricane Ike at 10 NDBC buoys. The measured data are shown with red lines, while the predicted results are shown with blue lines.

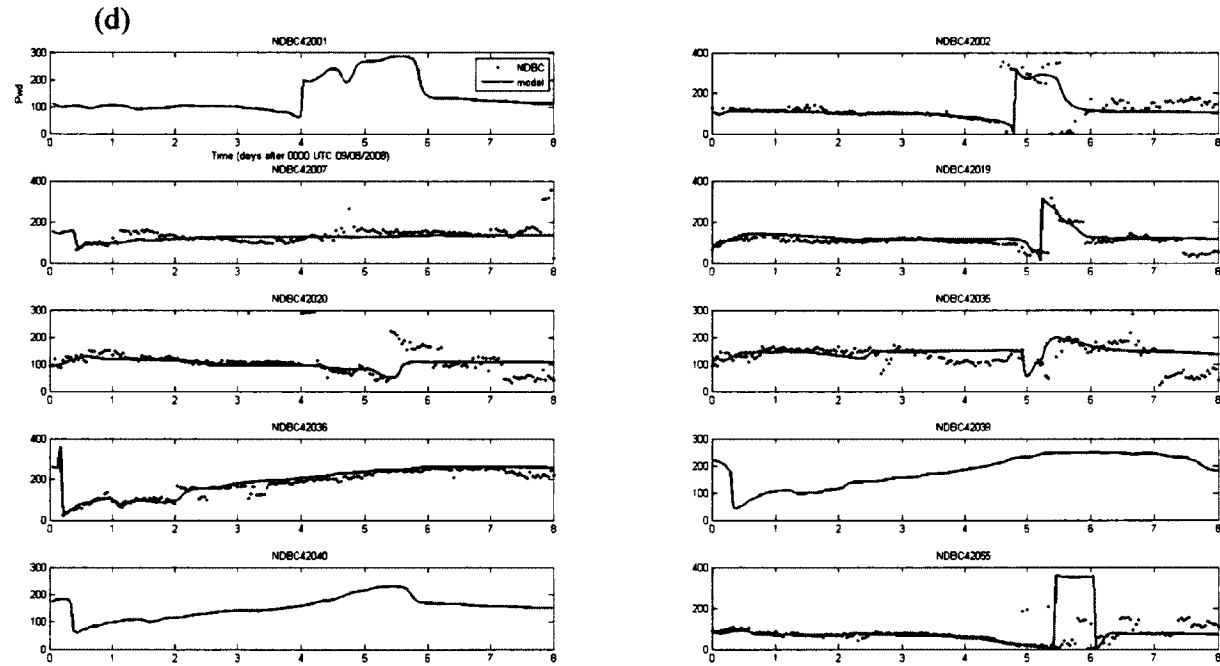
(a)



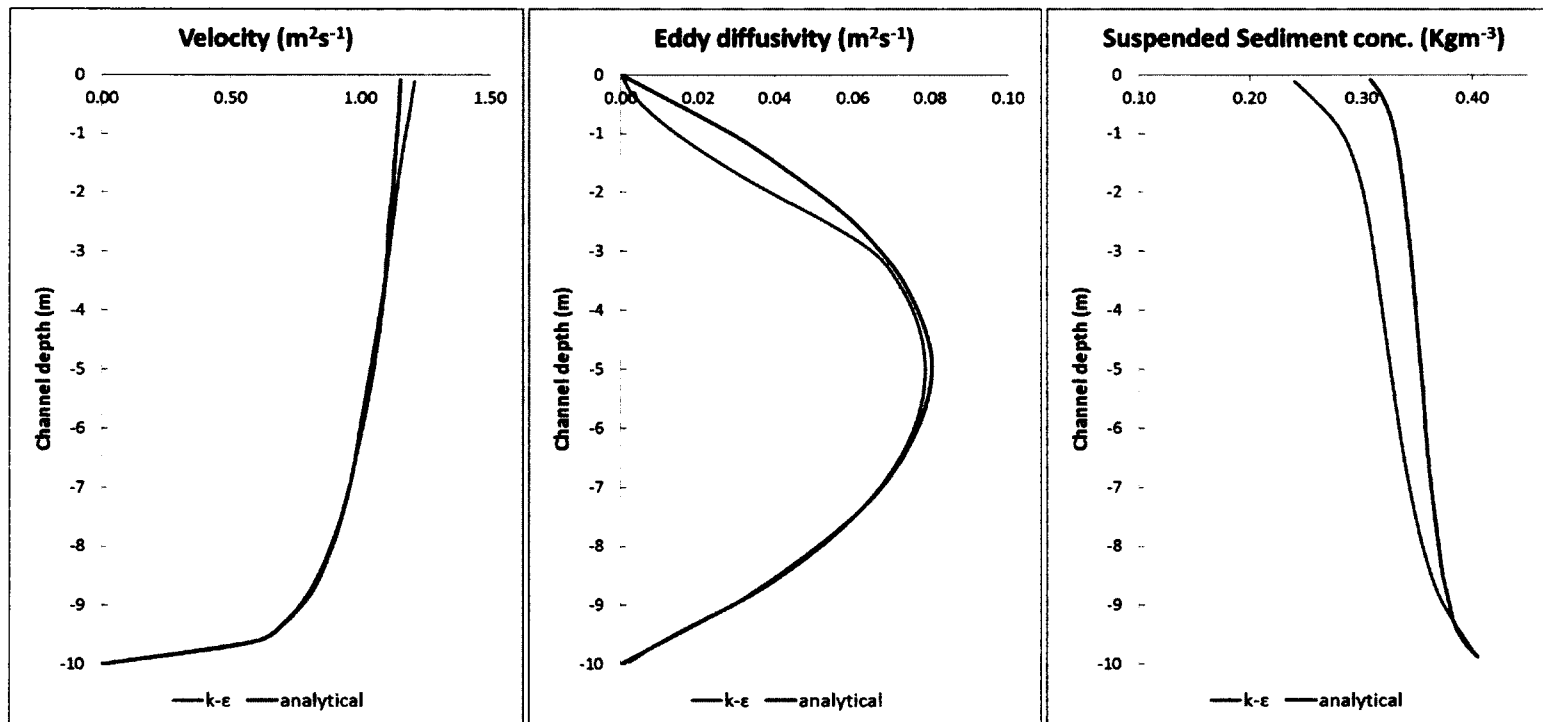




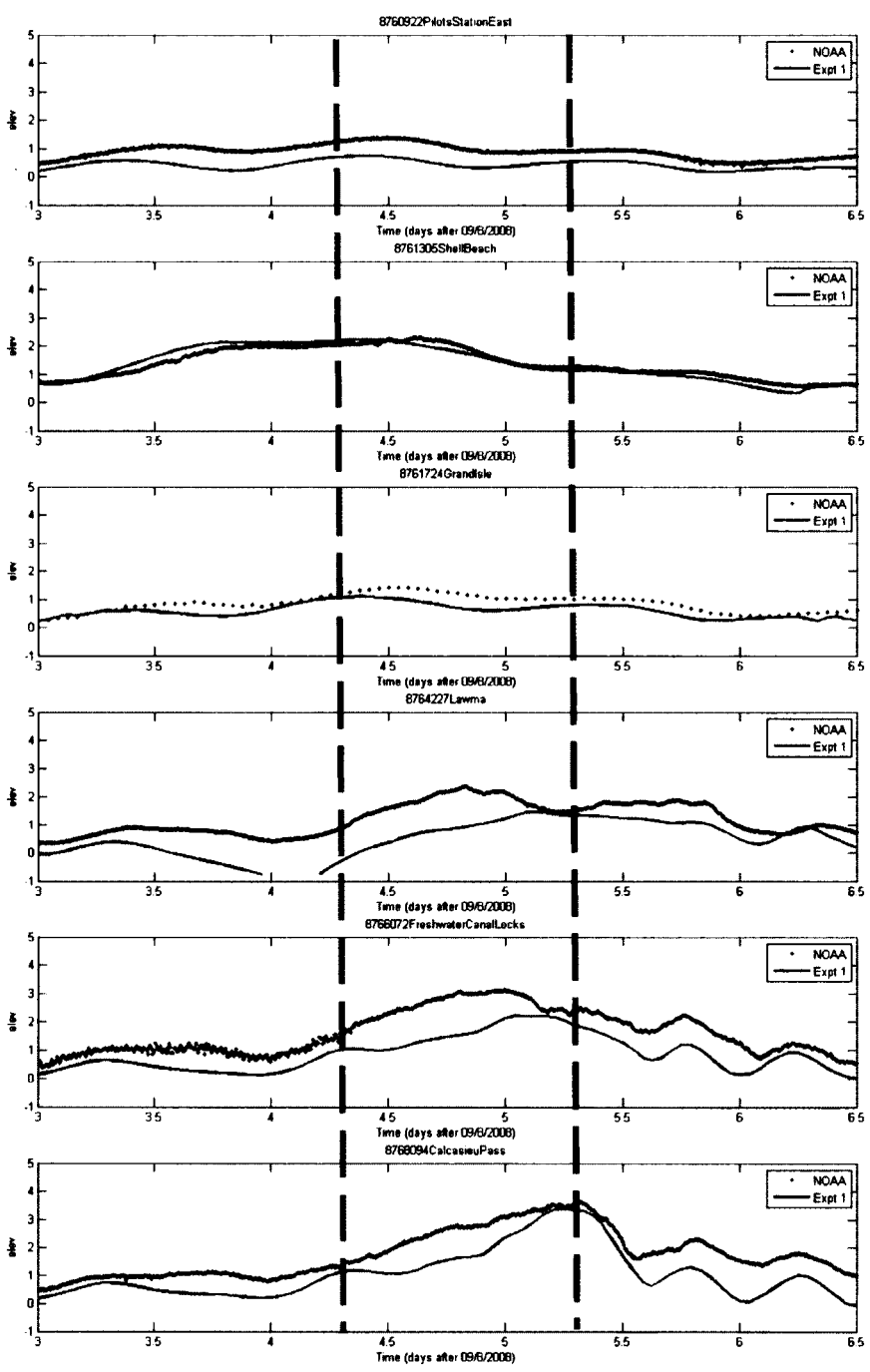


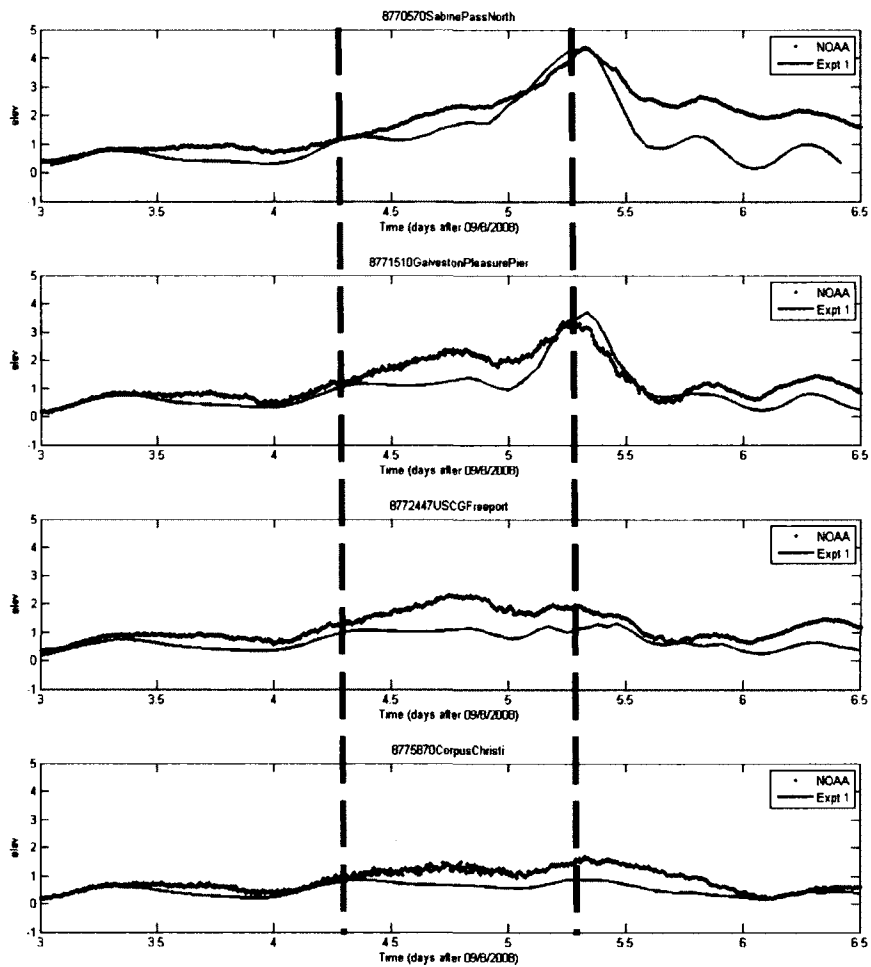


**Figure 4-15** Modeled wave characteristics during Hurricane Ike at 10 NDBC buoys. (a) Significant wave height (m); (b) peak wave period (sec); (c) mean wave period (sec); (d) peak wave direction (degrees). The measured data are shown with red dots, while the predicted results are shown with blue lines.

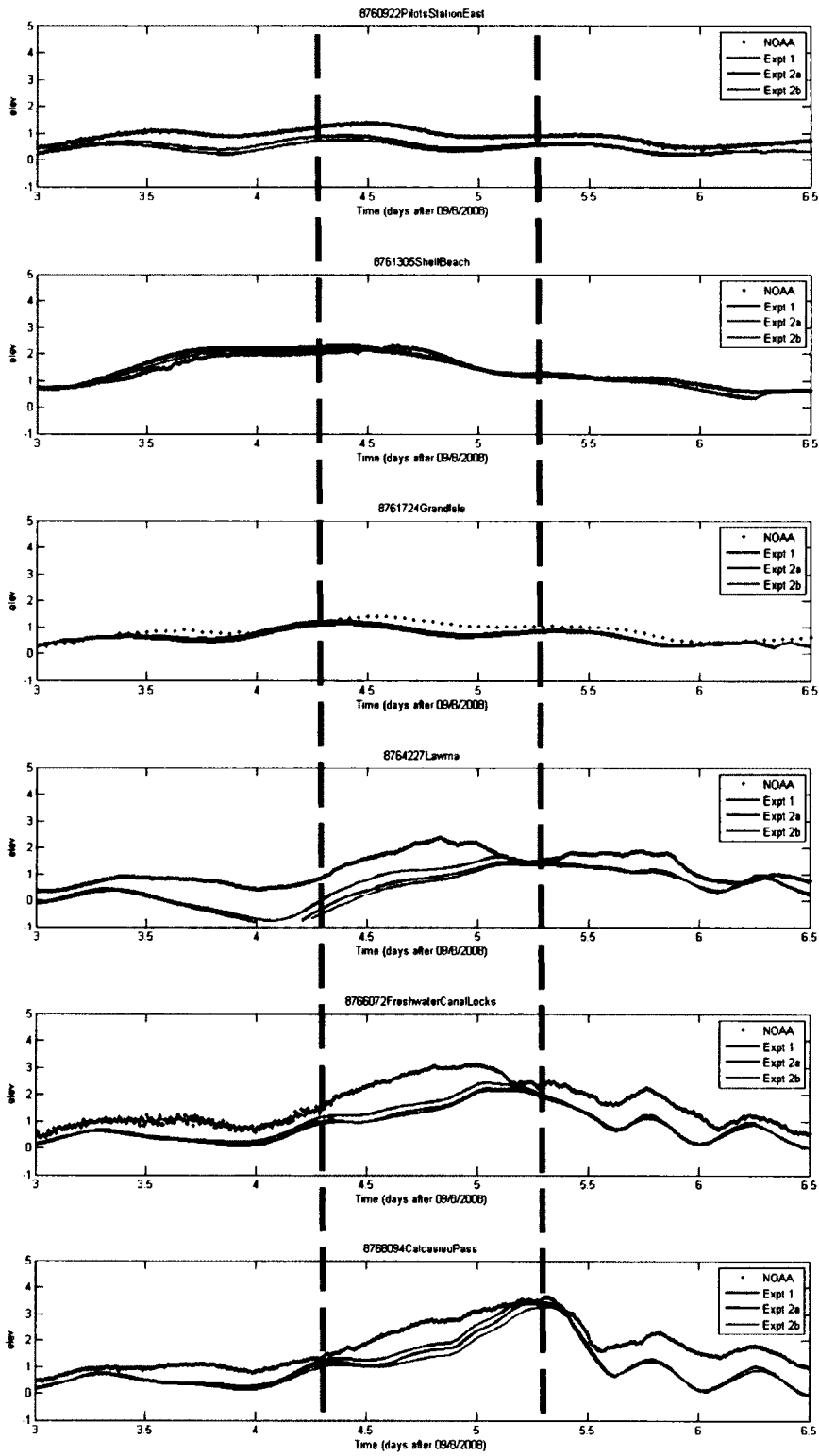


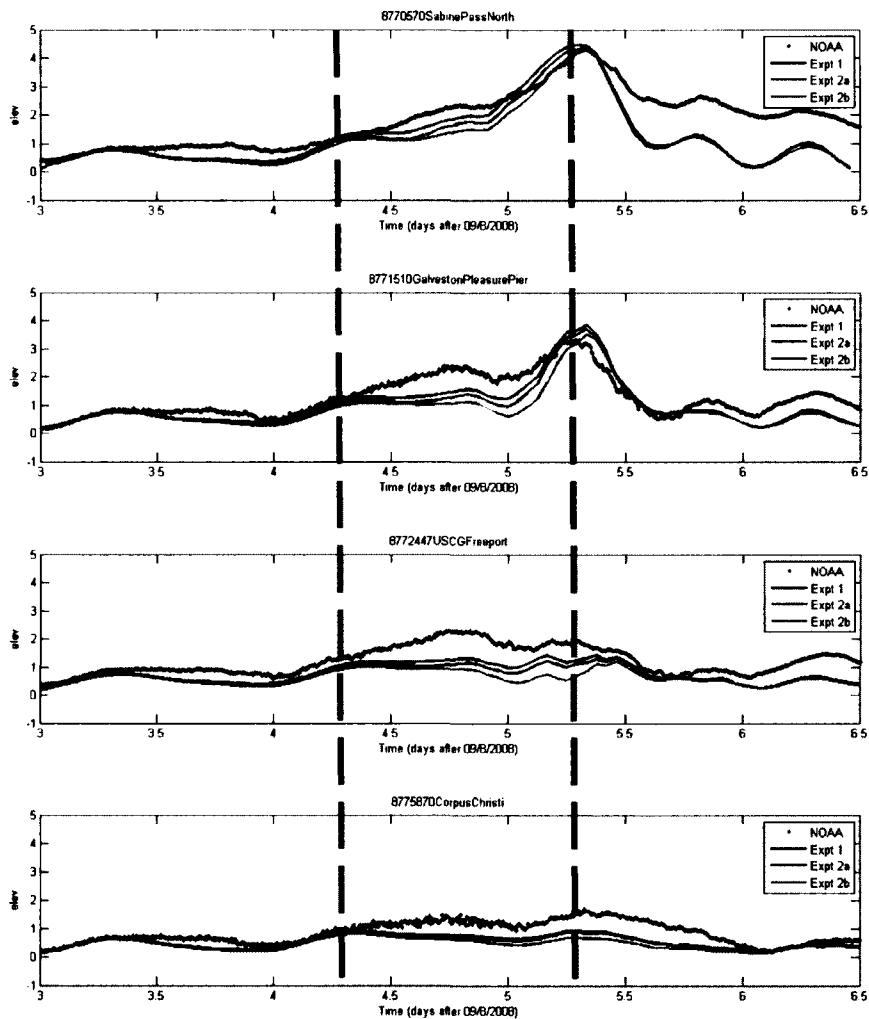
**Figure 4-16** Open channel test case -Vertical profiles of velocity, eddy diffusivity, and sediment concentration for two of turbulence closure options of analytical parabolic expression and  $k-\epsilon$ . Simulations used 21 vertical stretched levels.



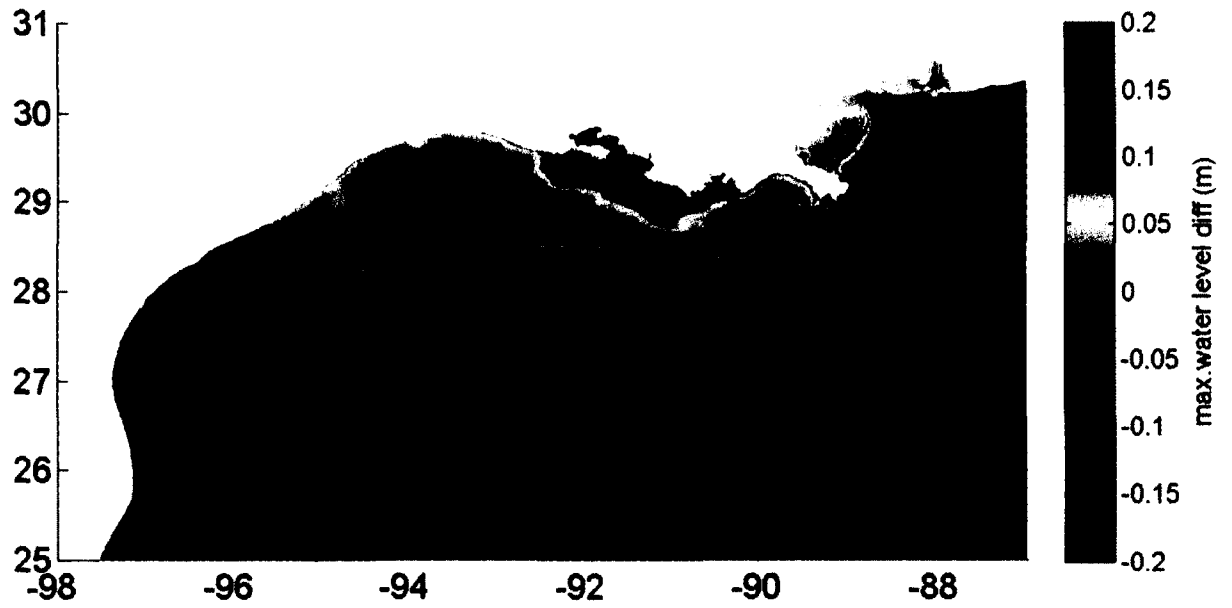


**Figure 4-17** Time series of modeled (Exp. 1, base case, blue line) and observed (red dots) storm tides for 10 stations in the LATEX shelf. The black dashed line represents the date of landfall and the red dashed line represents 24 hours before landfall. The unit of storm tide is in meters.



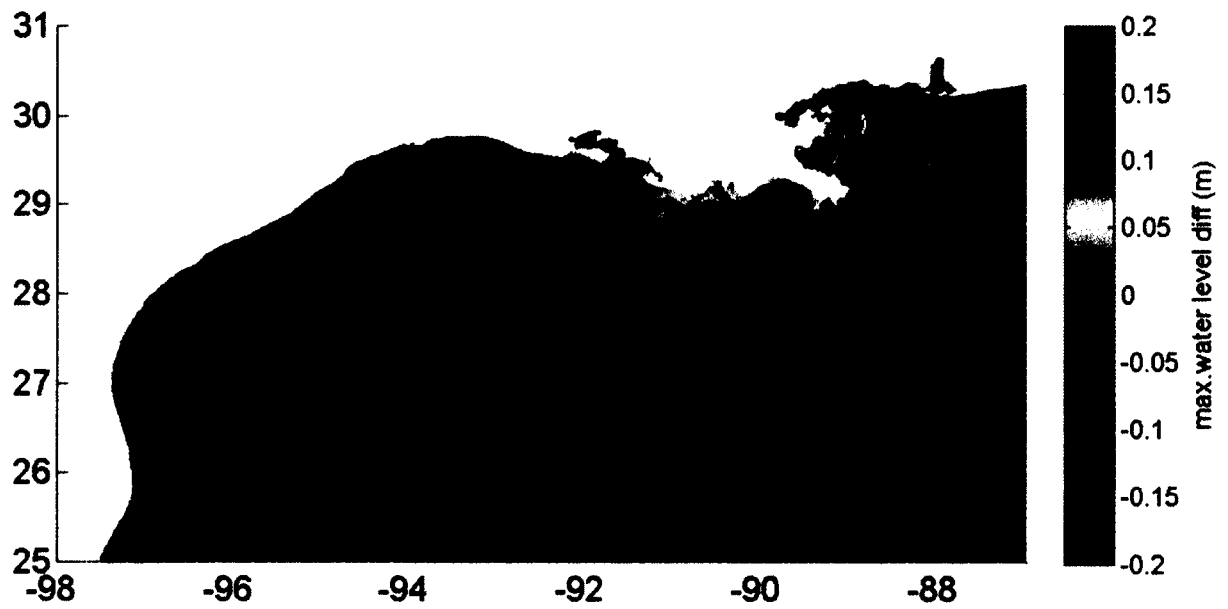


**Figure 4-18** Comparisons between Exp. 2a (blue line), Exp. 2b (green line), Exp. 1 (black line) and observed (red dots) storm tides for 10 stations in the LATEX shelf. The black dashed line represents the date of landfall and the red dashed line represents 24 hours before landfall. The unit of storm tide is in meters.

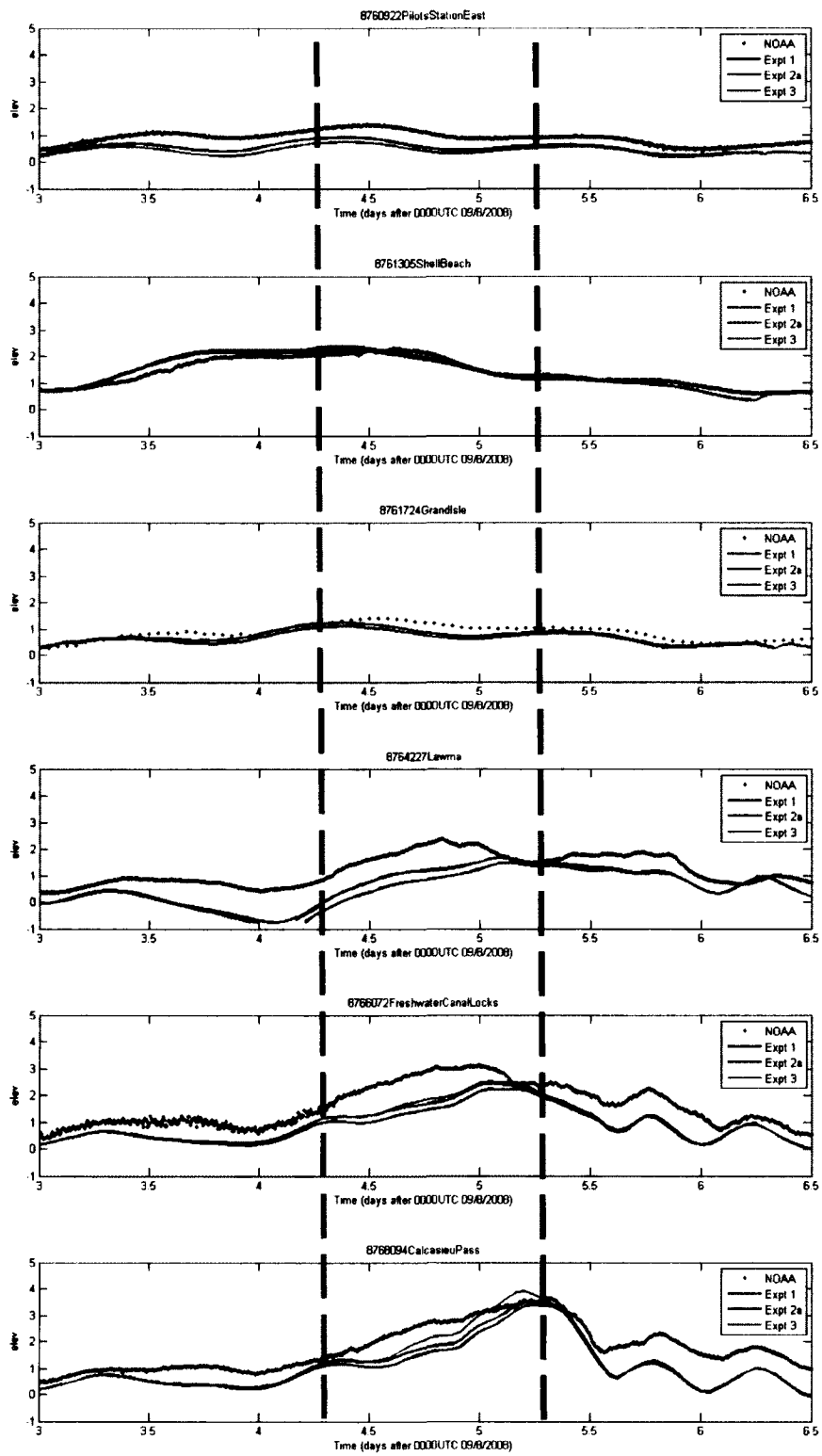


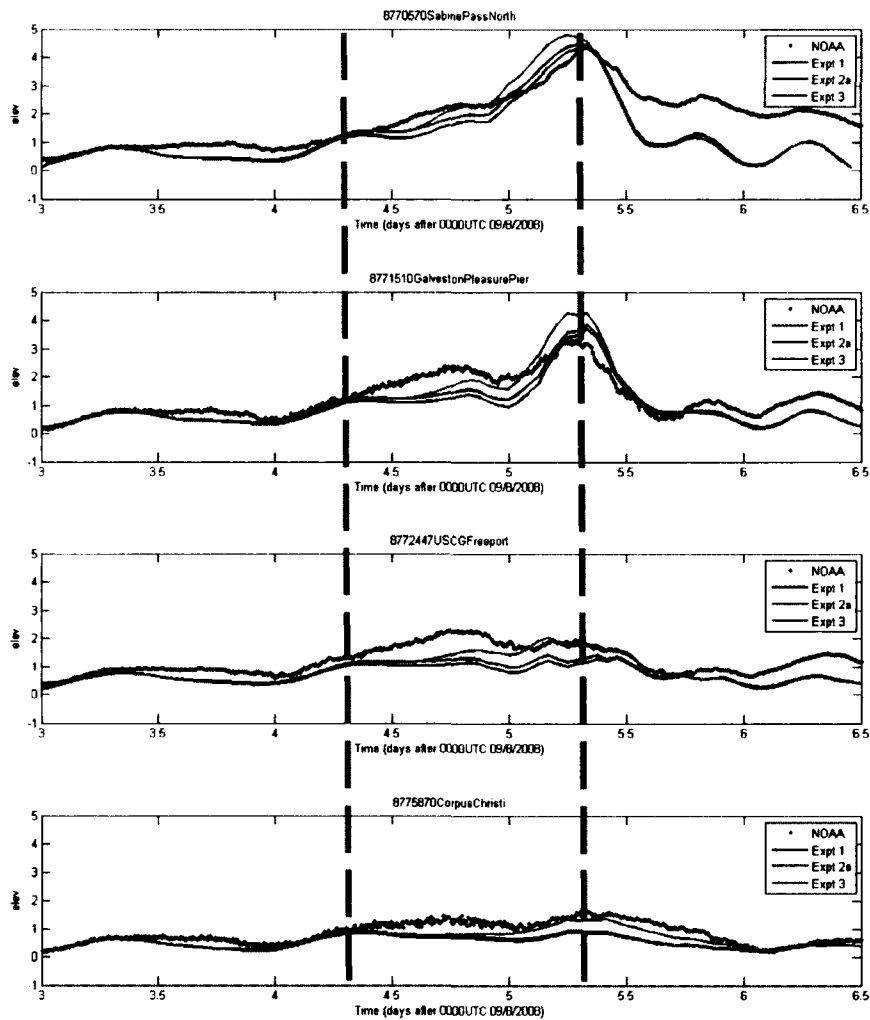
**Figure 4-19** Effect of wave set-up through radiation stress on the maximum water levels (m) during Hurricane Ike. The white line indicates the 50-m isobath line.



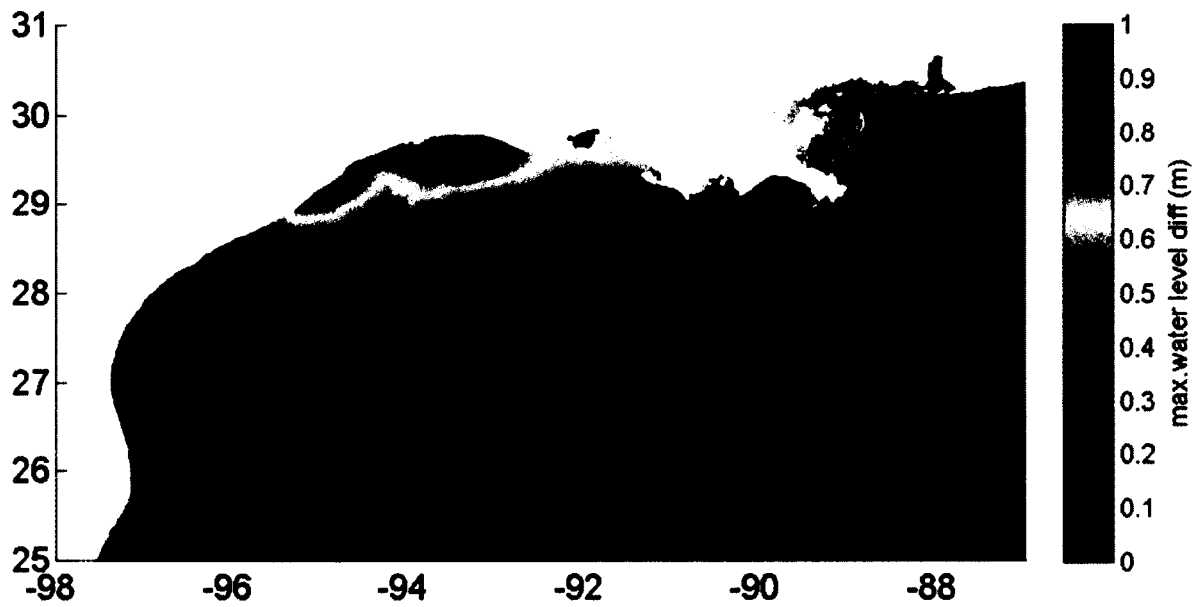


**Figure 4-20** Effect of wave set-up through radiation stress + wave-enhanced bottom stress on the maximum water levels (m) during Hurricane Ike. The white line indicates the 50-m isobath line.

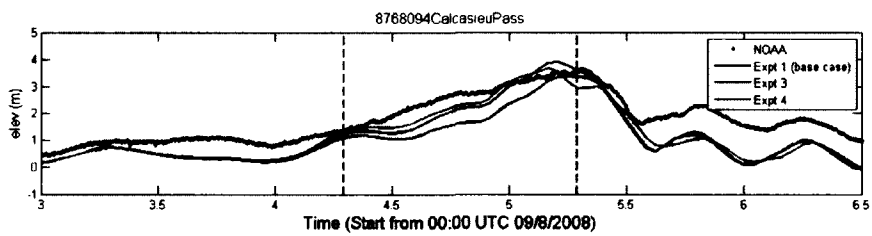
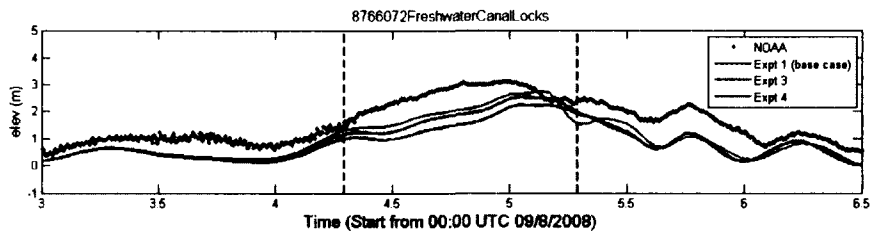
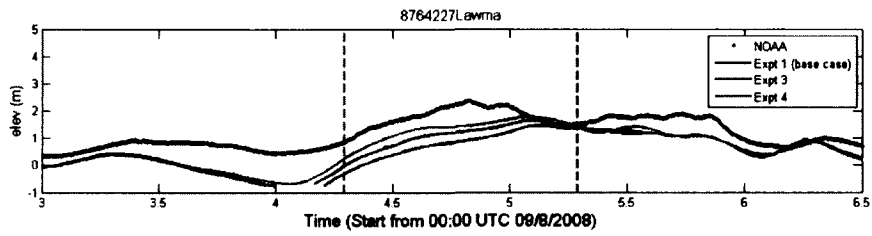
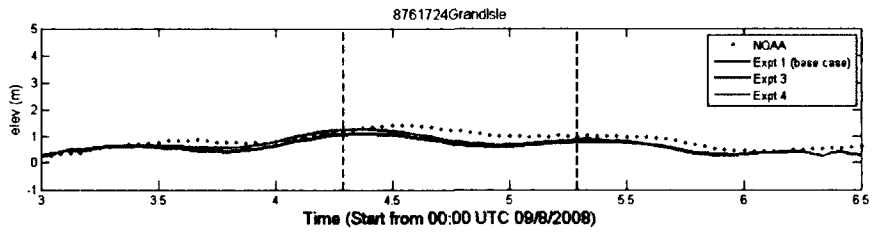
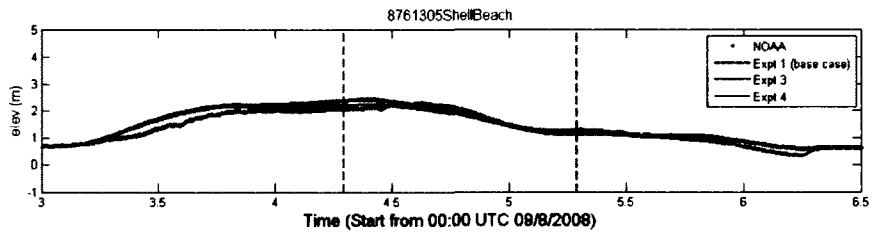
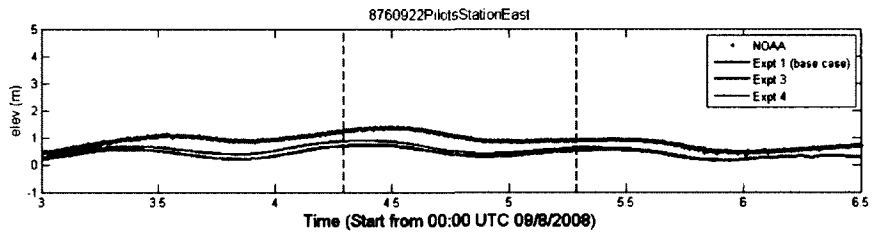




**Figure 4-21** Comparisons between Exp. 2a (blue line), Exp. 3 (green line), Exp. 1 (black line) and observed (red dots) storm tides for 10 stations in the LATEX shelf. The unit of storm tide is in meters. The black dashed line represents the date of landfall and the red dashed line represents 24 hours before landfall.



**Figure 4-22** Difference between the maximum envelope of water during Ike obtained by Exp. 3 (considering the effect of sediment stratification on bottom friction) and Exp. 1 (base case) simulations.



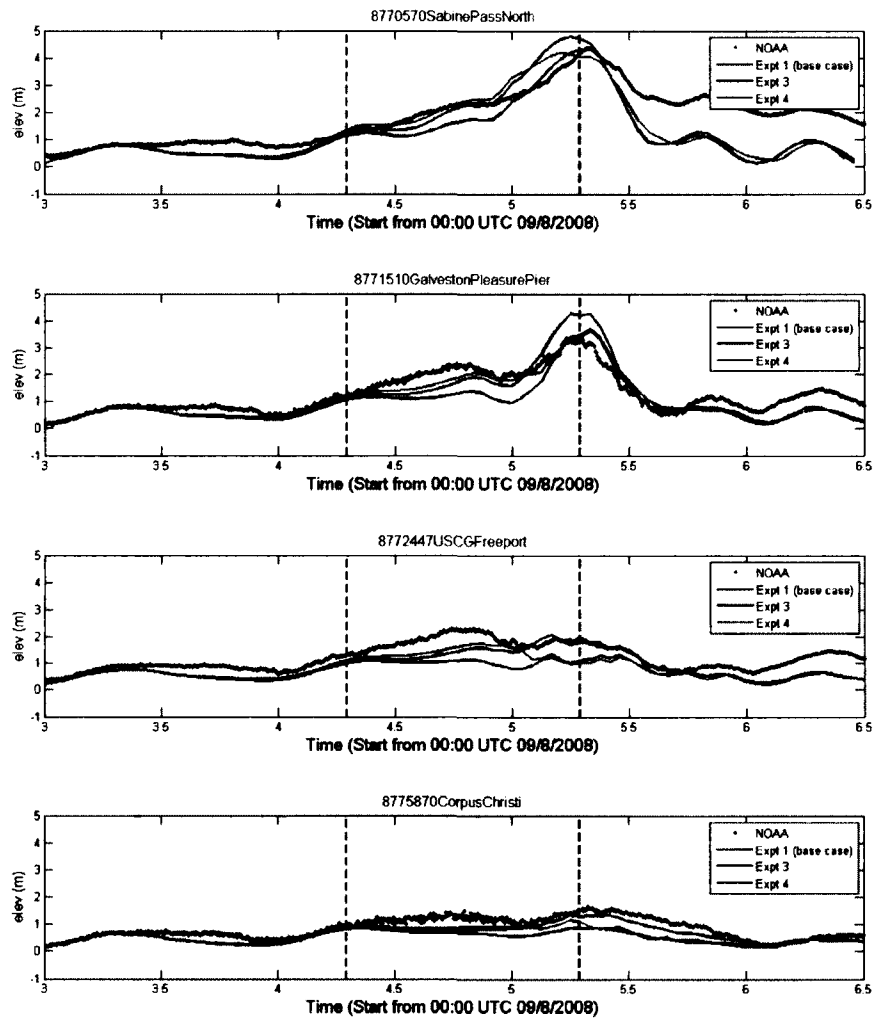


**Figure 4-23** Comparisons between Exp. 3 (blue line), Exp. 4 (green line), Exp. 1 (black line) and observed (red dots) storm tides for 10 stations in the LATEX shelf. The unit of storm tide is in meters. The black dashed line represents the date of landfall and the red dashed line represents 24 hours before landfall.

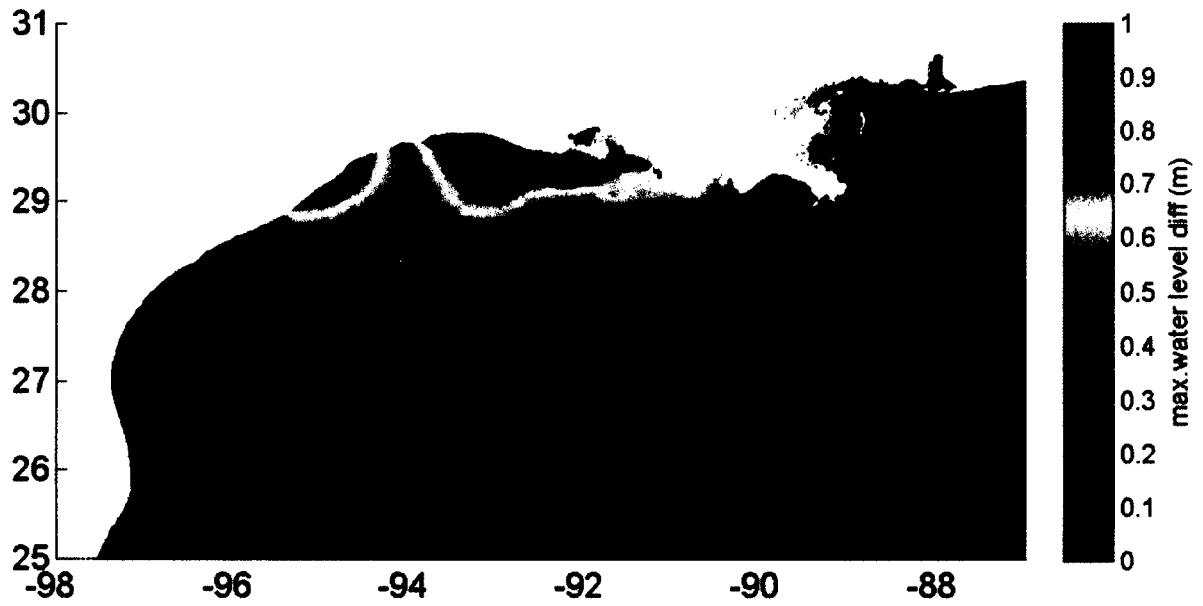


**Figure 4-24** Difference between the maximum envelope of water during Ike obtained by Exp. 4 (considering the full wave-current interaction and effect of sediment stratification on bottom friction) and Exp. 1 (base case) simulations.

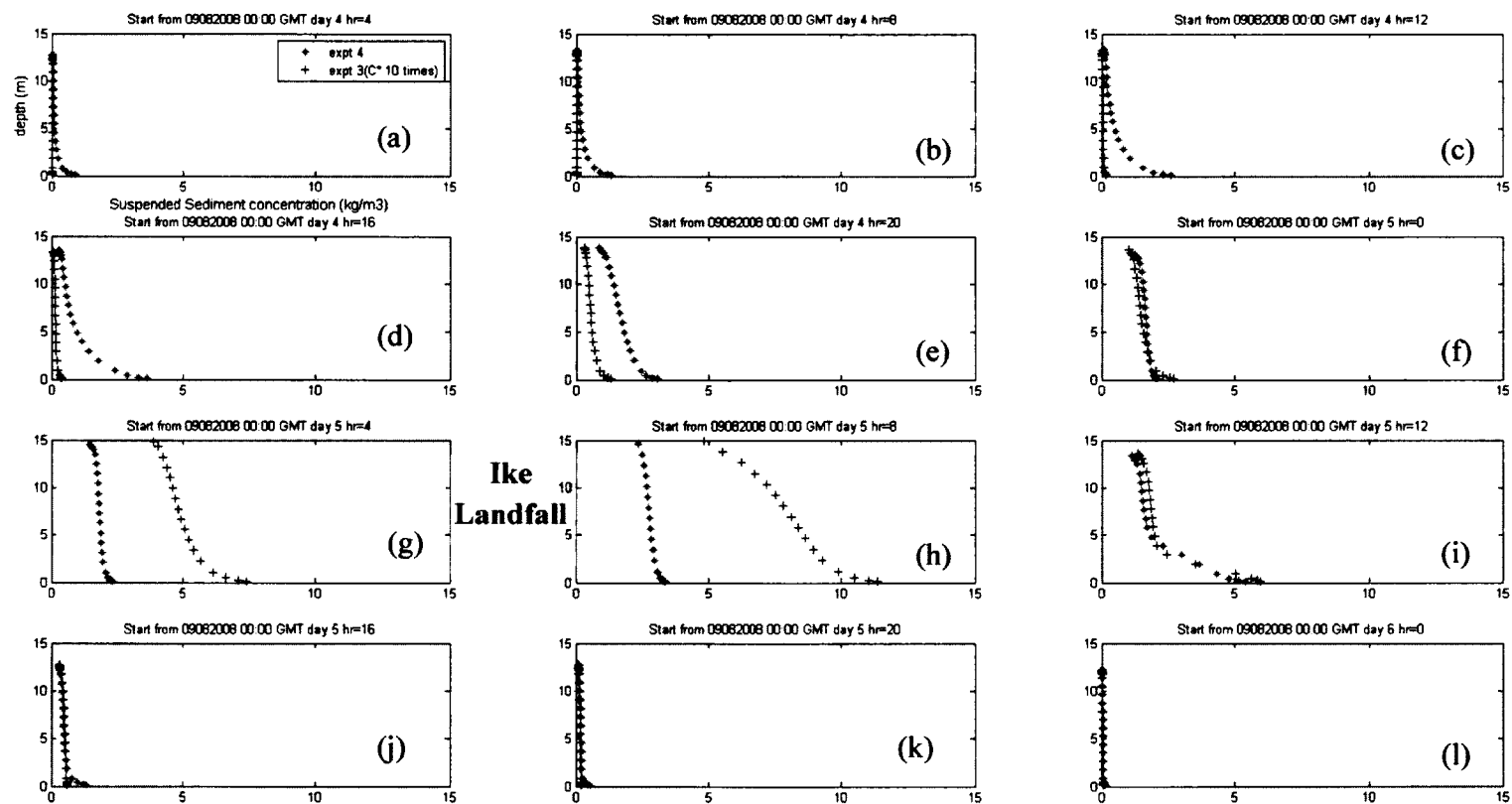




**Figure 4-25** Sediment vertical distribution (location is shown in Fig. 4-1b, green dot) in the water column for the period from 0000 UTC 9/12/2008 to 0000 UTC 9/14/2008 (including forerunner, primary surge, and post-runner). The sediment concentration was predicted by Exp. 3 (red dot) and Exp. 4 (blue cross), respectively. Notice that the concentration predicted by Exp. 3 is multiplied by 10 for visualization.

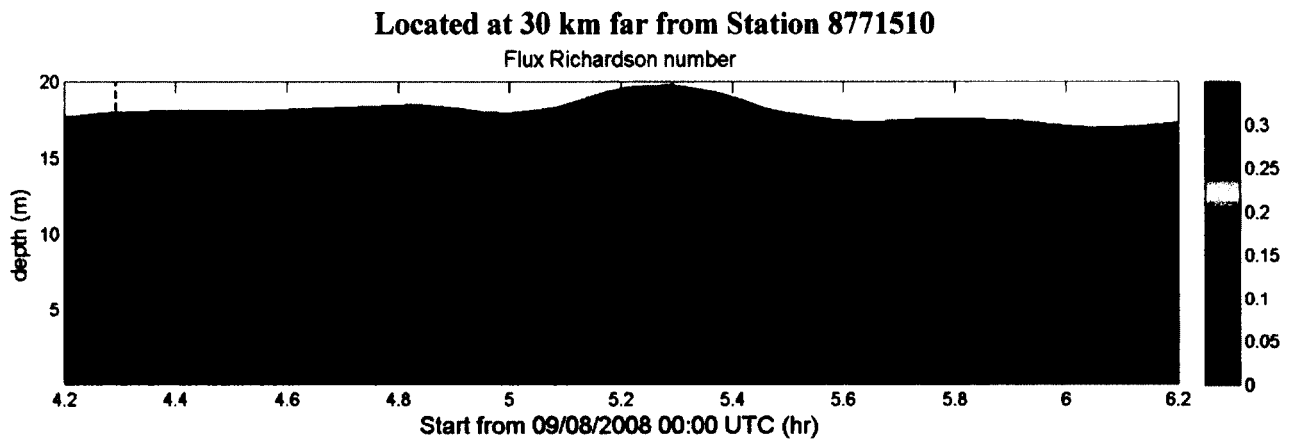


**Figure 4-26 (a)** Time series of the flux Richardson number  $R_f$  in the water column (Eq. (4.11)), at the location 30 km from Station 8771510 (see Fig. 4-1b, green dot) during the period from 0000 UTC 9/11/2008 to 1200 UTC 9/14/2008.

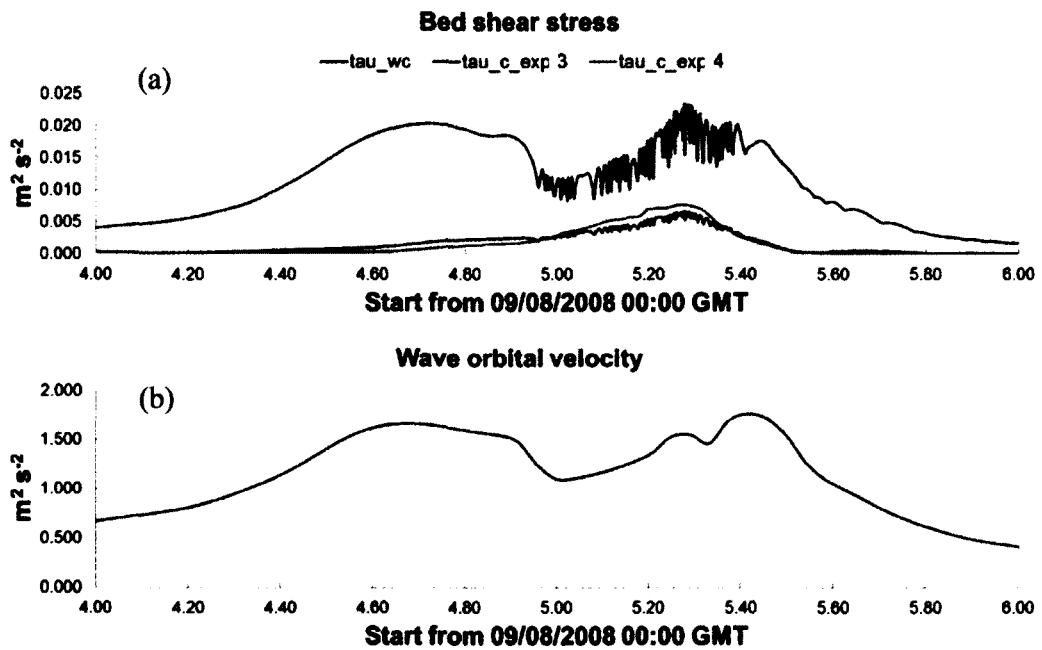


**Figure 4-27** (a) Time series of bottom stress due to current alone (red line) without stability function (Eq. (4.13)), combined bottom stress due to waves and current (blue line), and bottom stress due to current alone (green line) with stability function. Note that the green and red lines represent the stresses that were used in current model and the blue line represents the combined stress used in the sediment transport model; (b) Time series of wave orbital velocity at the location 30 km from Station 8771510 (see Fig. 4-1b, green dot) during the period from 0000 UTC 9/12/2008 to 0000 UTC 9/14/2008.

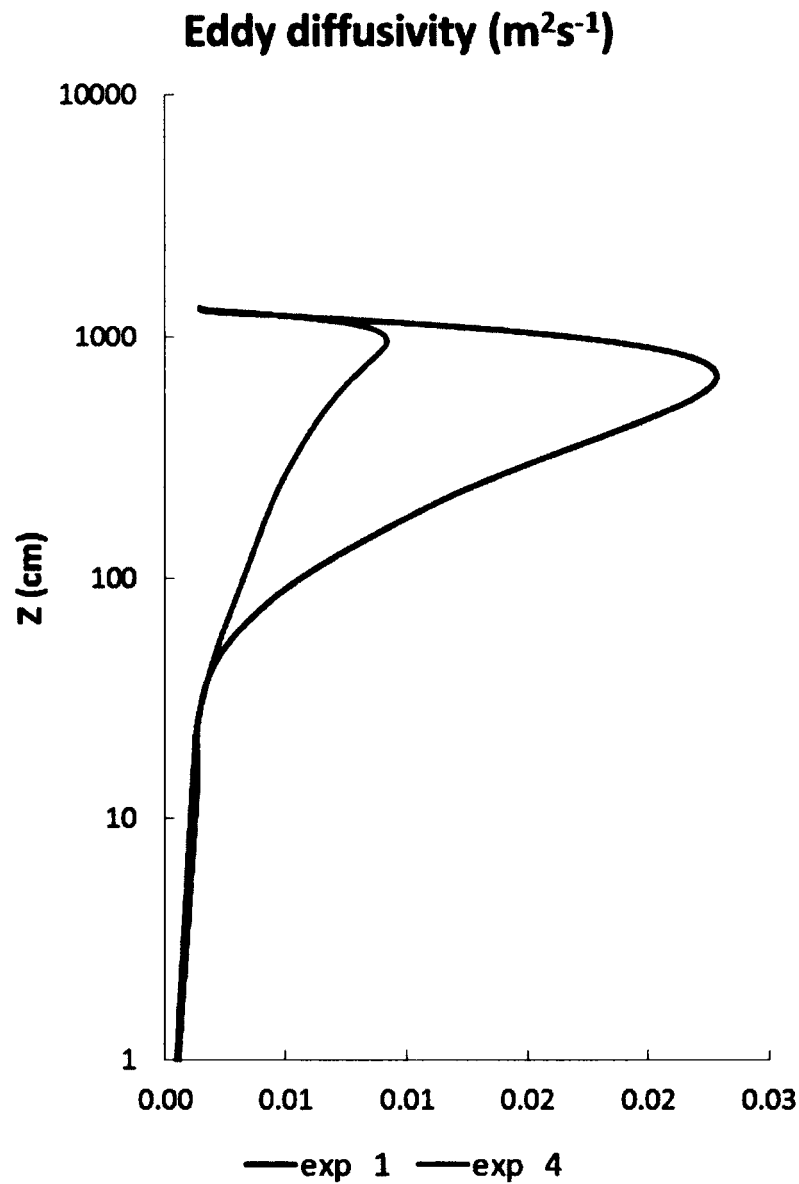


**Figure 4-28** Profiles of eddy diffusivity for the suspended-sediment-stratified BBL (Exp. 4, red line) and for the neutrally stratified BBL (Exp. 1, black line) at the location 10 km from Station 8771510 (see Fig. 4-1b, green dot) during Ike forerunner stage (Note that this plot represents a snap-shot at 12:00 UTC, 9/12/2008).

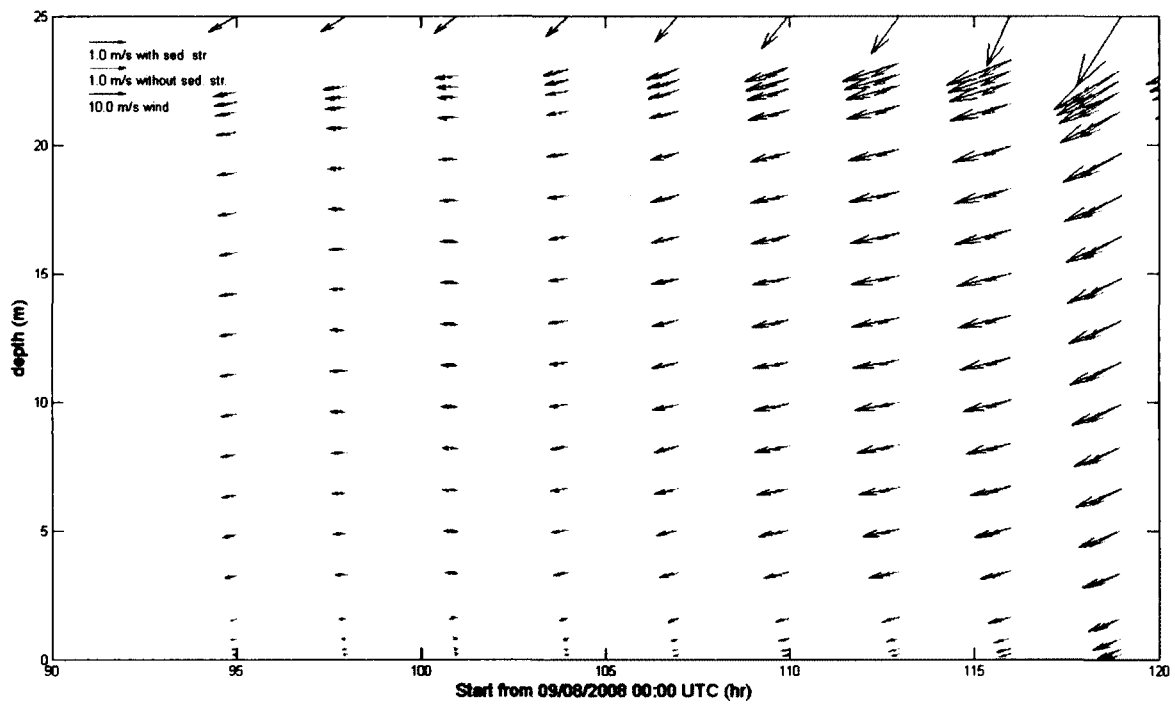


**Figure 4-29** Time series of horizontal velocity in the water column at the location 30 km from Station 8771510 (see Fig. 4-1b, green dot) during the Ike forerunner period from 1800 UTC 9/11/2008 to 1200 UTC 9/13/2008.

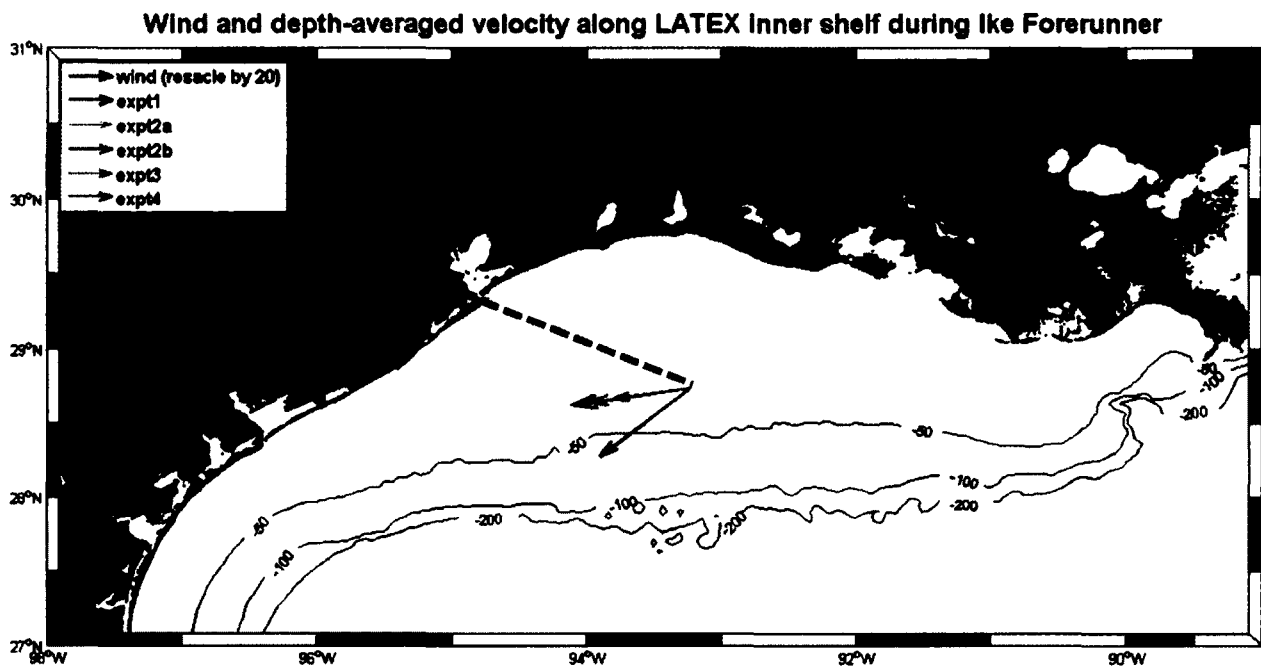


**Figure 4-30** Mean of depth-averaged horizontal velocity in the LATEX inner shelf during Ike forerunner period from each case.

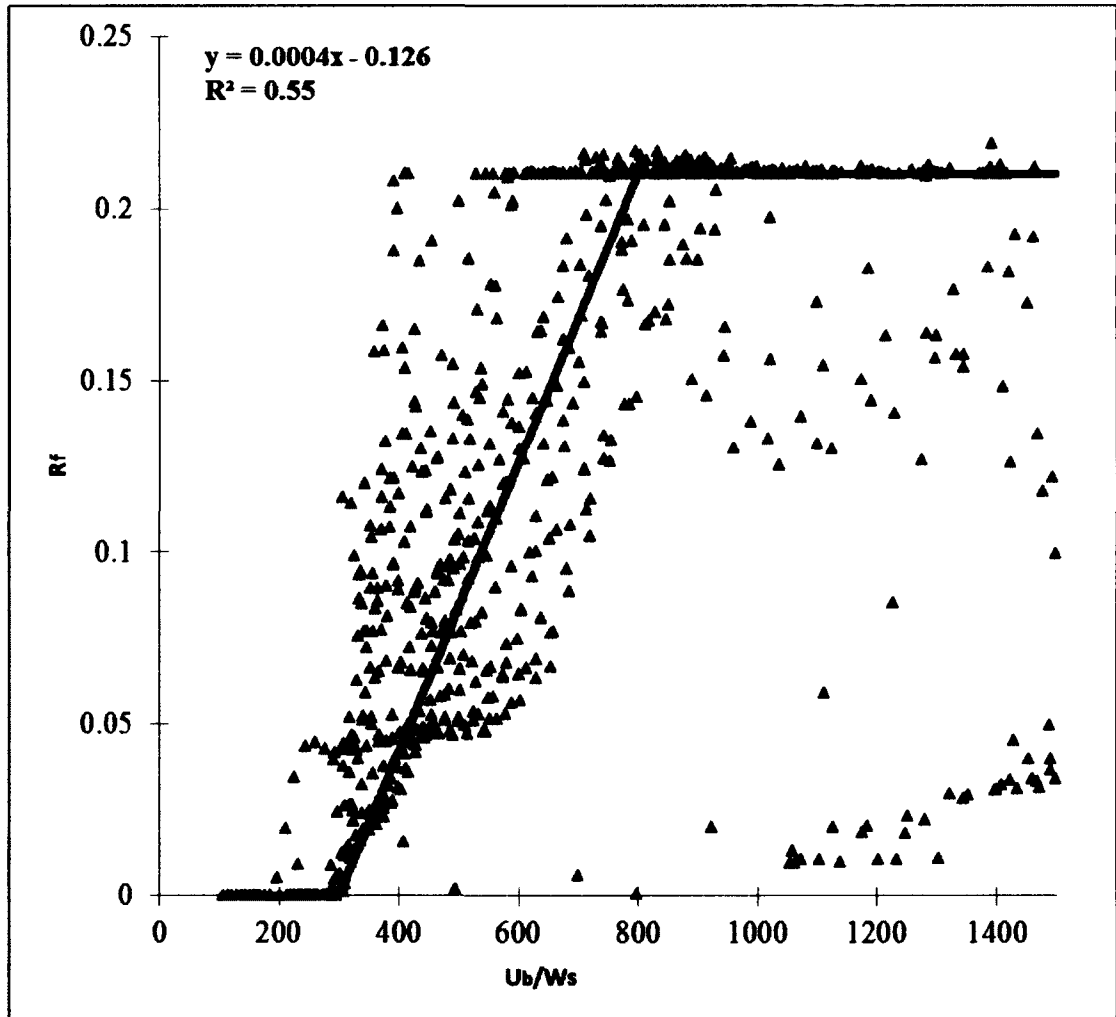


**Figure 4-31** Plots of the sediment-induced stratification (Exp. 4, during the period from 0000 UTC 9/12/2008 to 0000 UTC 9/14/2008) as represented by flux Richardson number  $R_f$  as a function of normalized orbital velocity. Black line is the best fit of the data.

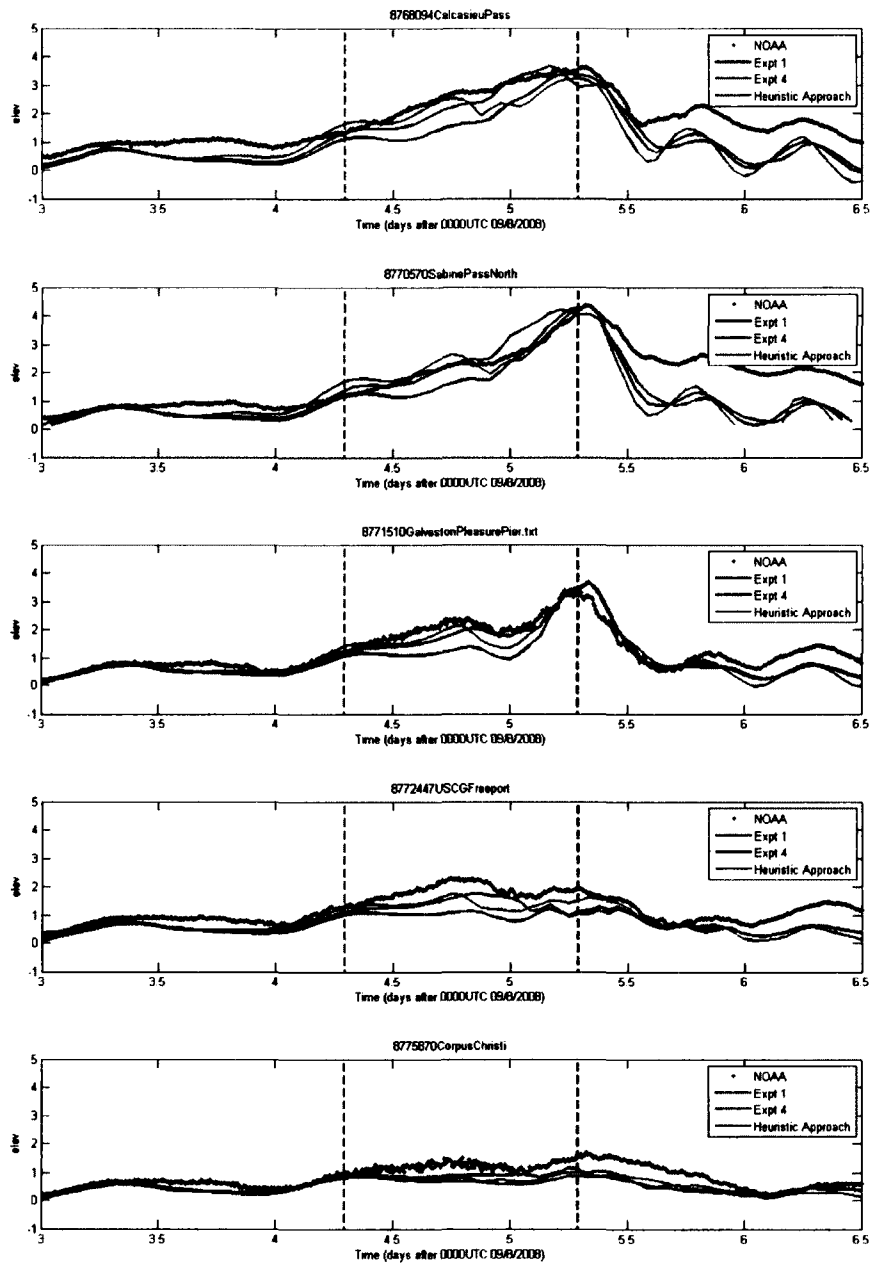


**Figure 4-32** Comparisons between Exp. 4 (blue line), practical approach (green line), Exp. 1 (black line) and observed (red dots) storm tides for 5 stations along the LATEX shelf. The unit of storm tide is in meters. The black dashed line indicates the date of landfall and the red dashed line indicates 24 hours before landfall.



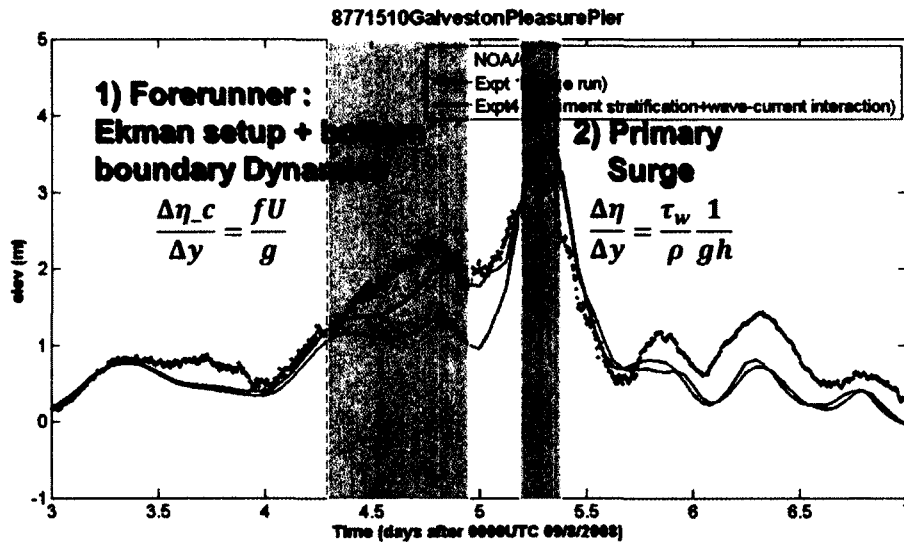


**Figure 4-33** Schematic of the two stages of the storm surge induced by Ike: (a) in the first stage, the forerunner surge was generated by the combination of Ekman set-up and BBL dynamics; (b) at the primary surge stage, the surge was mainly driven by the onshore directed winds (local wind effects).

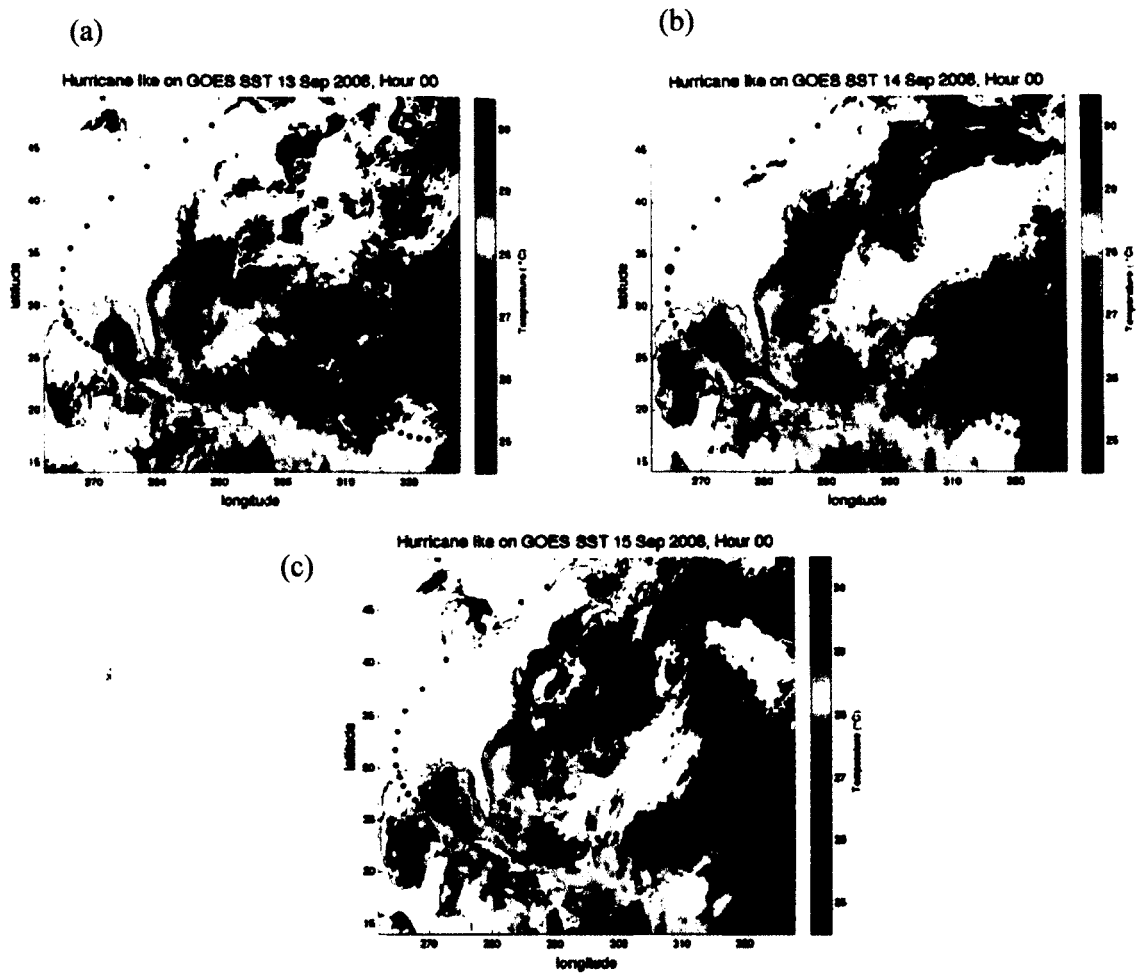


**Figure 4-34** Sea surface temperature (SST) during Hurricane Ike: (a) 7 hours before landfall; (b) 17 hours after landfall; (c) 41 hours after landfall. These plots were generated by Bhagat (2009) using GOES-SST data.

## CHAPTER V. The effects of wave-current interactions on coastal flooding in Scituate Harbor during the April 2007 Nor'easter

### 5.1 Introduction

There is no doubt that wind waves can have major effects on storm surges, and coastal currents in the ocean. In previous studies (e.g., Roland et al., 2012; see details in Chapter 2 and Chapter 3), the effects of wave-induced surface and bottom stress as well as wave set-up through radiation stress were introduced simultaneously in the dynamic coupling between waves and currents. Their study pointed out the need to consider fully wave-current interactions in a 3D ocean circulation model to study the complicated physical processes in the coastal regions and further improve the prediction skill for storm surge simulation.

In this chapter, a high-resolution, coupled SELFE-WWM II was applied in the Scituate Harbor, which is a small coast basin in the Gulf of Maine, to study the wave-current interaction and its effect on inundation during nor'easter events. Since SELFE-WWM II has a robust wetting-and-drying capability that allows us to simulate coastal inundation, it is in our interest to investigate the effects of the wave-current interaction and its effect on inundation in Scituate Harbor during the April 2007 Nor'easter. Section 5.2 provides brief descriptions of the April 2007 Nor'easter as well as the study location. Section 5.3 introduces the model setups and the numerical experiments performed. Section 5.4 describes the model validations and

results of experiments. The effects of the wave-current interaction on coastal inundation are presented in Section 5.5, followed by conclusions in Section 5.6.

## 5.2 Extratropical storm in the Gulf of Maine-April 2007 Nor'easter

A nor'easter is a large scale extratropical storm that occurs mostly along the East Coast of the United States. Due to its longer duration and larger spatial scale than those features of a tropical storm (e.g., hurricanes) a nor'easter can cause severe flooding in the coastal areas by bringing strong wind and heavy precipitation within a short period of time.

The April Nor'easter of 2007 (a.k.a., the Patriot's Day Storm) was a nor'easter that affected mainly the eastern parts of North America from April 15 to April 17, 2007. The Patriot's Day Storm will long be remembered not only for its devastating power, but also for its abnormally high spring tide plus a storm surge of nearly 0.9 meters that combined to produce a high tide of 4 meters. Observed wave heights reached nearly 10 meters in the Gulf of Maine during the April 2007 Nor'easter (Fig. 5-1; data are from GoMOOS buoys and NWS Gray, ME). The 3D wave-current fully coupled model we presented in the previous chapters can be used to simulate the abnormally high water level in the Gulf of Maine during the Patriot's Day Storm.

In the IOOS/SURA super-regional coastal modeling testbed project (SURA test bed project, 2011), one objective for the coastal storm surge and inundation team is to evaluate the effects of wave-current interactions on the model simulation of extratropical storm-induced inundation along the northeast coast of the U.S. Scituate,

MA (Fig. 5-2) was chosen as the extratropical testbed site for the SURA inundation project. The reasons are as follows: (a) the outer coast and harbor of Scituate experience severe flooding during strong nor'easter events; (b) the Taunton NWS (MA) Weather Forecast Office already had selected Scituate as a pilot site for the Northeast Coastal Ocean Forecast System (NECOFS, Fig. 5-3) development group to demonstrate an “end-to-end” inundation forecast system; and (c) with IOOS Northeast Regional Association of Coastal Ocean Observing Systems (NERACOOS) support, a high-resolution Scituate FVCOM inundation grid was developed and nested within the NECOFS regional GOM3 model system (Fig. 5-4; SURA test bed project final report, 2012). The benefit of this is that the high-resolution Scituate FVCOM inundation grid can be used as the common grid for the inter-model comparison as well as for the study of effects of wave-current interactions on inundation, and the lateral boundary conditions can be provided directly by NECOFS.

### 5.3 Model setup and experiments

#### 5.3.1 Model setup

In this study, the 3D coupled wave-current modeling system (see details in Chapter 2) is configured for Scituate Harbor and its adjacent area. As mentioned above, in order to resolve the hydrodynamics and more complicated topography of the relatively small harbor and its surrounding water, a high-resolution Scituate grid for inundation simulation (Fig. 5-4b) nested within the large GoM (Gulf of Maine)

regional grid was employed for this study. The Scituate domain (Fig. 5-4b), resolving more detailed geographic features in and around Scituate Harbor, has 5,620 nodes and 11,153 elements with a horizontal resolution between 10 m to 1000 m. As we are heavily interested in investigating the effects of wave-current interactions on inundation simulation, our coupled model was only used in the high-resolution Scituate domain. In other words, we did not use our coupled model in the large GoM domain. The large domain runs were conducted by the University of Massachusetts-Dartmouth (hereafter UMass Dartmouth/WHOI group) in the SURA testbed project, which provided lateral open boundary conditions such as water level, horizontal velocity, significant wave height, peak wave period, and peak wave direction to drive the high-resolution Scituate domain.

The Patriot's Day Storm impacted the northeastern region of the U.S. from April 15 to April 17, 2007. Time series of wind speed (WS), wind direction (WD), wave height (WH), dominant wave period (WP), surface, surface air pressure (BP, and air (blue) and water (red) temperature for the period April 10-21, 2007 are shown in Fig. 5-5 (data are recorded on the NDBC buoy 44013, and its location can be found in Fig. 5-7). Based on these records, the simulation period was started at 00:00 UTC, 1 April for model spin-up and completed at 00:00 UTC May 1 2007. The wind field used to drive our coupled model was a wind field from GoM-WRF (the meteorological model of NEOFS). The horizontal resolution for GoM-WRF is 9 km. In this study, eleven layers in a pure s-coordinate were used for the vertical grid domain and a time step of 30 sec was used for both the current and wave model.

### 5.3.2 Numerical experiments

In order to investigate the effects of wind waves on coastal inundations, two experiments are conducted in this study. The storm surge and inundation model run without wave-current interaction is referred to as Case A (base case). The experiment considering breaking wave set-up through radiation stress is referred to as Case B. A minimum water depth of 1 cm was set for the wetting/drying scheme.

## 5.4 Validations and results of experiments

### 5.4.1 Tidal validation in Scituate domain

Before running the storm surge and inundation simulation, a tidal simulation during May 2010 was conducted to verify the long wave propagation in the Scituate domain. The reason that May 2010 was selected for the tidal calibration was because a new water level gauge was installed inside Scituate Harbor (Fig. 5-6, Station F) and the water level data are available from this station. SELFE used the water level as well as flux time series provided by the large GoM domain as the forcing boundary condition for the Scituate domain. The simulation of tide using a time step of 30 sec that started from 5/1/2010 0000 UTC and ended at 5/31/2010 0000 UTC, a total of 30 days. The results of the modeled water level were used for the model-data comparison using “T-tide”, a public domain software for conducting tidal harmonic analysis (Pawlowicz, et al., 2002).

Five major harmonic constituents ( $M_2$ ,  $N_2$ ,  $S_2$ ,  $O_1$ , and  $K_1$ ) were used for tidal comparison between simulated and measured amplitudes and phases at the tidal gauge inside Scituate Harbor (Fig. 5-6). The results are shown in Table 5-1. The difference between modeled and measured amplitudes is generally smaller than 3 cm, except for the  $M_2$  tidal constituent (8.5 cm). For phase, the difference is also small ( $< 5^\circ$ ), except for the  $S_2$  tidal constituent ( $11.87^\circ$ ). Harmonic decomposition of the model elevation output showed that our model has strong prediction skills in both amplitude and phase for the major diurnal and semi-diurnal tidal constituents, indicating that the simulation of tide by SELFE is overall satisfactory in the Scituate domain. Note that this tidal comparison was conducted by the UMass Dartmouth/WHOI group in SURA testbed coastal storm surge and inundation team (UMass Dartmouth/WHOI group, 2012).

#### 5.4.2 Wave model validation in the Gulf of Maine

Although we did not run the large GoM application for storm surge and inundation simulation, a “wave-only” run was conducted in the GoM domain in order to evaluate our wave model WWM II because all known wave observational data are located outside of Scituate Harbor. Totals of 36 direction and 36 frequency bins, with the cut-off frequencies being 0.03 Hz to 1 Hz were used in this run. Also, data records from a total of 22 NDBC buoys (shown in Fig. 5-7) in the GoM were selected for model-data comparison. Wave characteristics such as significant wave heights, peak wave periods, mean wave periods ( $T_{m02}$ ), and dominant wave direction (in nautical



coordinates) are used to validate our wave model (Fig. 5-8). The WWM II wave model matches the timing and magnitude of significant wave heights, and the simulated peak wave periods agree well with the observations at the selected buoys. The modeled mean wave periods catch the transitions from wind sea to swell sea, and match the observation at most of the selected stations. The WWM II wave model also accurately modeled the dominant wave direction during the April Nor'easter 2007. In general, the comparisons indicate that modeled predictions of significant wave height, peak wave period, mean wave period, and peak wave direction are well simulated at selected buoys.

#### 5.5 The wave-current interaction and its effect on inundation

In this section, the effect of wave-current interaction on coastal inundation is analyzed from a set of numerical experiments: Case A and Case B, as described above.

It should be noted that, due to the lack of observed data in Scituate Harbor, we are not able to offer a complete and comprehensive model-data comparison in this study. Instead of the model-data comparison, an inter-model comparison was conducted to assess the qualitative accuracy our model results (UMass Dartmouth, 2012). More specifically, for each numerical experiment, surface water responses as well as depth-averaged velocities were compared between SELFE-WWM II and FVCOM-SWAVE at nine locations inside Scituate Harbor (Fig. 5-6) during the 2007 storm event to make sure our simulations were reasonable. The inter-model

comparisons at nine locations in Scituate for Case A (without the effect of surface waves) and Case B (with the effect of surface waves) are shown in Fig. 5-9 and Fig. 5-10, respectively.

In the case of the April Nor'easter 2007 without the wave-current interaction (Case A), FVCOM and SELFE predict nearly identical water surface responses throughout most of the Scituate model domain and specifically at nine designated model comparison locations (Fig. 5-9). Depth-averaged velocities at eight of nine stations are consistent between FVCOM and SELFE although they are more variable than surface water levels. At Station B, the depth-averaged velocity obtained by SELFE (red color) is much larger than the FVCOM prediction (blue color). The reasons for this variability are: (a) the two models compute velocity at different grid cell element positions (i.e., FVCOM –element centers; SELFE-element faces) and (b) the two models have different numerical approaches for their wetting/drying schemes. In general, SELFE and FVCOM present similar patterns of storm and inundation simulation without wave-current interaction in the Scituate domain.

#### 5.5.1 The wind wave effect on coastal currents

In the case of the 2007 storm, when with wave-current interaction is included in the model runs (Case B), FVCOM-SWAVE and SELFE-WWM II predict similar water levels and inundation at all nine designated comparison stations and generally throughout the Scituate domain. In this case, again no significant differences occur in the inter-model comparison for depth-averaged velocities at the selected stations.

However, larger differences were observed between the modeled velocities with and without wave-current interaction (Fig. 5-9 and Fig. 5-10) due to the development of relatively small scale velocity features through wave effects such as eddies, recirculation zones, and areas of significant lateral shear (Fig. 5-11).

#### 5.5.2 The wind wave effect on transport through the Harbor mouth

Wave-current interaction generates additional water transport into the Scituate Harbor and changes the magnitude and direction of velocity in near-shore regions (Fig. 5-11; Fig. 5-12, section B). Although the modeled surface water levels are just slightly increased (less than 3%) in and around Scituate, the patterns of flooding areas are changed significantly inside the Scituate Harbor, especially in the northern basin (Fig. 5-13).

#### 5.5.3 The wind wave effect on coastal inundation

As we mentioned above, the case without wave-current interaction predicts no inundation at the inland Station H while the case with wave-current interaction does have coastal inundation due to the enhanced vorticity of the eddy near the entrance and an additional water transport entering this area (Fig. 5-10, Station H; Fig. 5-14, and Fig. 5-15). High water marks for the Patriot's Day (April 2007) Storm suggest that the area around Station H was inundated, but unfortunately, there are no data to provide a time history or actual water levels in this area to verify our inundation simulation. The flooding areas were increased about 5% when considering wind wave effects (Table 5-2). These results show that including the wave-current interaction can

affect inundation predictions in near-shore and shallow water regions, even though there are no large differences in the surface water level. Note that in this study we only considered the effect of wave-induced radiation stress on inundation simulation. However, recent studies point out that other effects, such as wave-enhanced surface and bottom stresses by waves, also play significant roles for inundation simulation (e.g., Xie et al., 2008). Their effects should be accounted for during future studies to improve inundation prediction.

#### 5.5.4 Mechanism analysis

Based on our model results above, we can summarize that while the mean water level remained the same inside the Harbor when considering wind wave effects, the total inundation areas were increased. This phenomenon can be explained by invoking the vertically integrated fully coupled wave-current continuity and momentum equations (McWilliams and Uchiyama, 2008):

$$\frac{\partial \eta}{\partial t} + \nabla \cdot U = -\frac{\partial \bar{\eta}}{\partial t} - \nabla \cdot T^{St} \quad (5.1)$$

$$\begin{aligned} \frac{\partial U}{\partial t} + \bar{\nabla} \cdot (\bar{U}\bar{u}) + f\bar{z} \times U + gD\nabla\eta - \frac{\tau_s}{\rho} + \frac{\tau_b}{\rho} = & -\bar{u}(\nabla \cdot T^{St}) - (\bar{z} \times T^{St})(\bar{z} \cdot \nabla \times \bar{u} + \\ f) + \frac{Sk}{\rho\sigma} \end{aligned} \quad (5.2)$$

$$T^{St} = \frac{|A|^{2\sigma}}{4k\sinh^2[H]} \cosh[2Z]k \quad (5.3)$$

$$H = k(h + \eta + \hat{\eta}) \quad (5.4)$$

$$Z = k(z + h) \quad (5.5)$$

where  $k$  and  $\sigma$  are wavenumber vector and angular frequency of primary waves,  $T^{St}$  and  $\bar{\eta}$  are Stokes transport and quasi-static sea-level referred to as wave set-up,  $S$  is a non-conservative dissipation during wave-breaking, and  $\tau_b$  and  $\tau_s$  are the bottom and surface stress terms. Although we do not consider vortex-force representation explicitly in our model framework, it has been proved that radiation stress can be represented by the vortex force plus the Bernoulli's effect (Garrett, 1976). The vortex force signifies the interaction between the vortices of the flow and the Stokes drift. In our case, wind waves generated by the nor'easter affect the coastal current through the wave-induced vortex force (second right-side term in Eq. (5.2)) and enhanced eddies in the Harbor mouth (Fig. 5-11). Due to the increase of magnitude as well as the directional change on coastal current through the vortex force, the total water transport across the Harbor mouth increased (Fig. 5-12). The additional water transport caused by the wind wave should be contributed by the wave set-up (first right-side term in Eq. (5.1)) and the gradient of Stokes transport (second term on the right side in Eq. (5.1)). We assume that the gradient of Stoke transport should be relatively small inside the Harbor (first right-side term in Eq. (5.2)) because it is proportional to the square of the wave amplitude (Eq. (5.3)). The wave set-up, however, is compensated by the extension of the flooding areas in the shallow regions (Fig. 5-14; Fig. 5-15). This is why the flooding areas were increased while the mean water level did not change too much inside the Harbor when wind waves were included.

## 5.6 Conclusions

Based on SELFE-WWM II results, the inclusion of wave-current interaction in the models substantially strengthened and changed the direction of the velocity field in the coastal region outside of Scituate Harbor. As a result, the total transport through the entrance to Scituate Harbor also increased. The effect of wave-induced radiation stress generated additional water transport into Scituate Harbor and enhanced small scale eddy features within the harbor. While these do not translate to significant differences in mean water level inside the Scituate Harbor, it was shown that the total inundation areas were increased, as were the inundation frequencies in the southern and northern basins.

It should be noted that, in the northern basin of Scituate Harbor, the “Splash-over” - water driven by onshore winds and waves over the coastal sea walls, was a major contributor for flooding during the December 2010 Nor’easter (Beardsley et al., 2011). To the best knowledge of the author, so far this kind of process is not included in any of the wave-current coupled models. Further studies are needed in order to improve the model skill of inundation prediction.

**Table 5-1** Scituate tide amplitude comparison (5/1/2010 to 5/31/2010).

	OBS (m)	SELFE (m)	Diff (m)
M <sub>2</sub>	1.324	1.239	-0.085
N <sub>2</sub>	0.249	0.28	0.031
S <sub>2</sub>	0.166	0.19	0.024
O <sub>1</sub>	0.119	0.109	0.01
K <sub>1</sub>	0.136	0.128	0.008

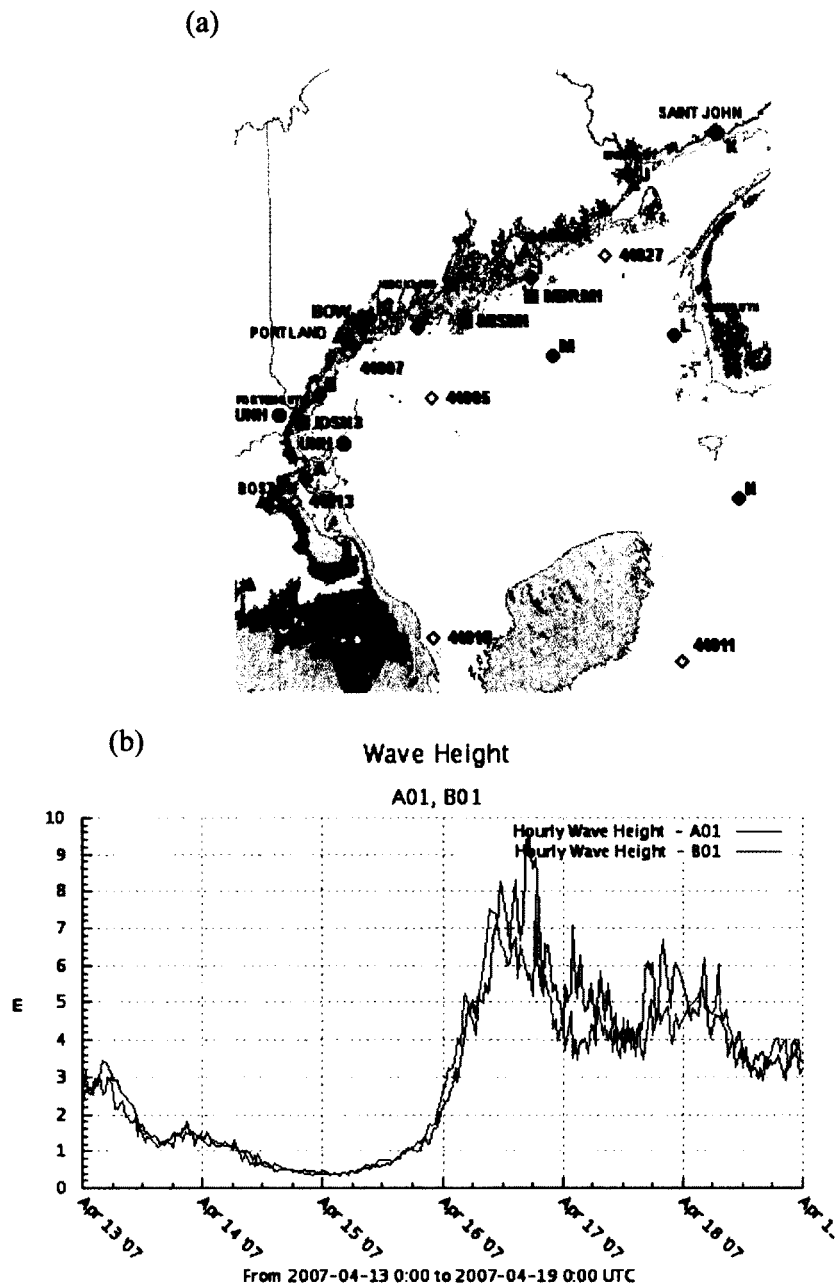
Scituate tide phase comparison (5/1/2010 to 5/31/2010).

	OBS (deg)	SELFE (deg)	Diff (deg)
M <sub>2</sub>	103.46	101.97	-1.49
N <sub>2</sub>	68.62	69.87	1.25
S <sub>2</sub>	141.30	153.17	11.87
O <sub>1</sub>	187.13	183.59	-3.54
K <sub>1</sub>	198.77	193.93	-4.84

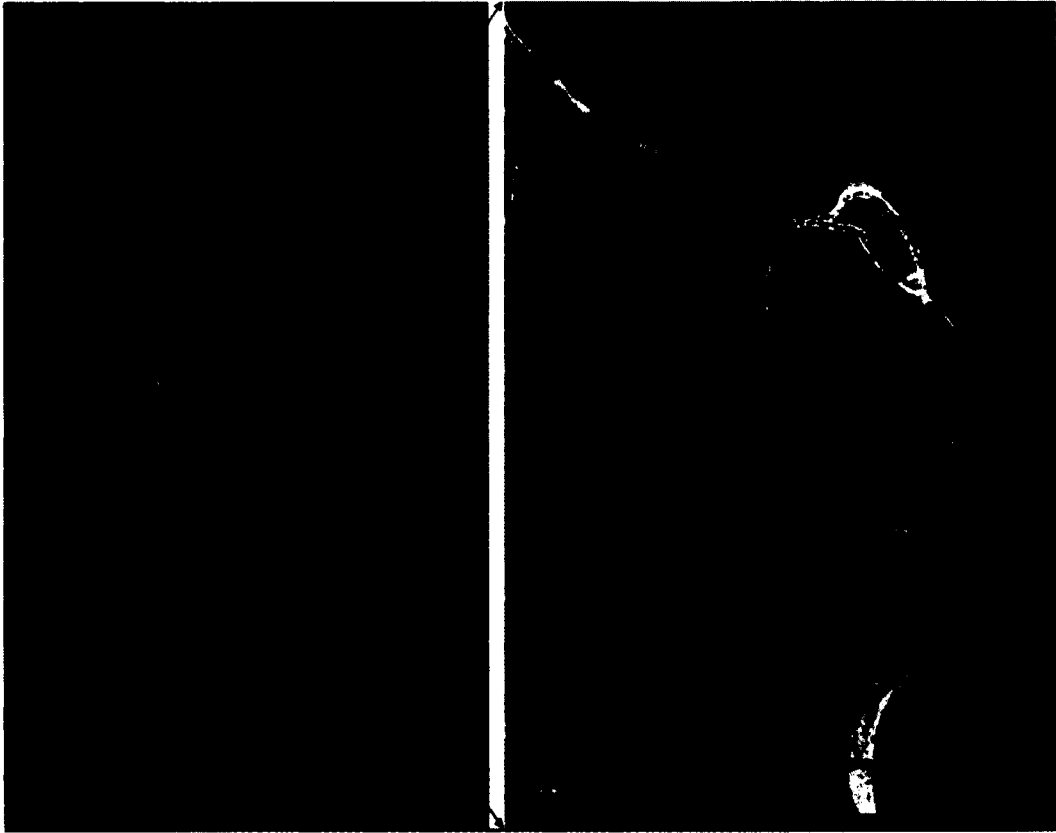
**Table 5-2** The comparison of flooding areas inside Scituate at 04:00 UTC 4/18/2007.

	<b>Inundated Areas (m<sup>2</sup>)</b>
Without wave	103797.2
With wave	108753.7
Diff (with wave-without wave)	4956.5
Diff (%)	5





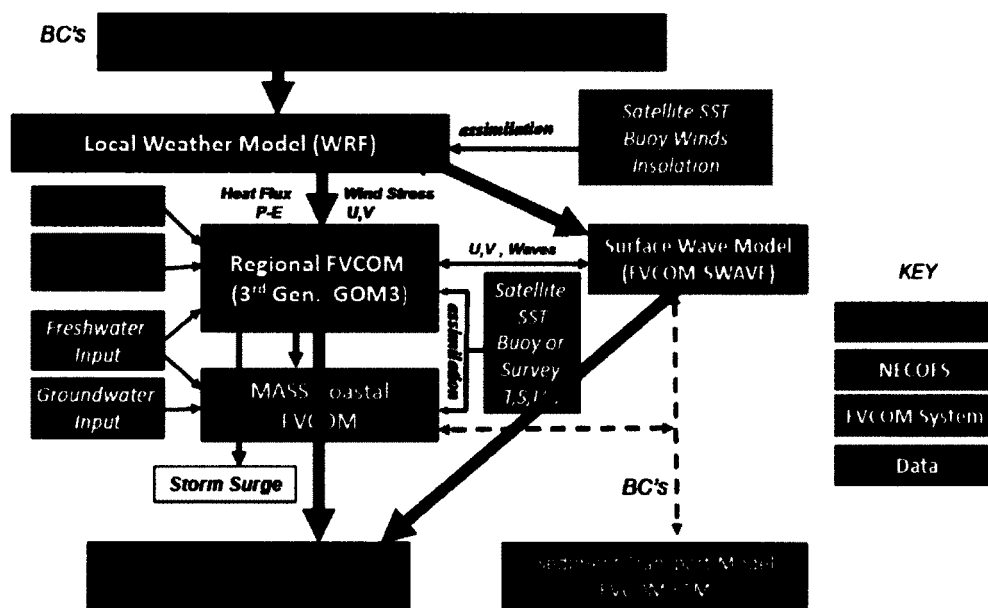
**Figure 5-1** (a) Locations of GoMOOS buoys (red point) in Gulf of Maine. (b) Observed wave heights from GoMOOS buoys at the (1) GoMOOS A01 - Massachusetts Bay and (2) GoMOOS B01 - Western Maine Shelf, for the period of the 2007 Patriot's Day Nor'easter.



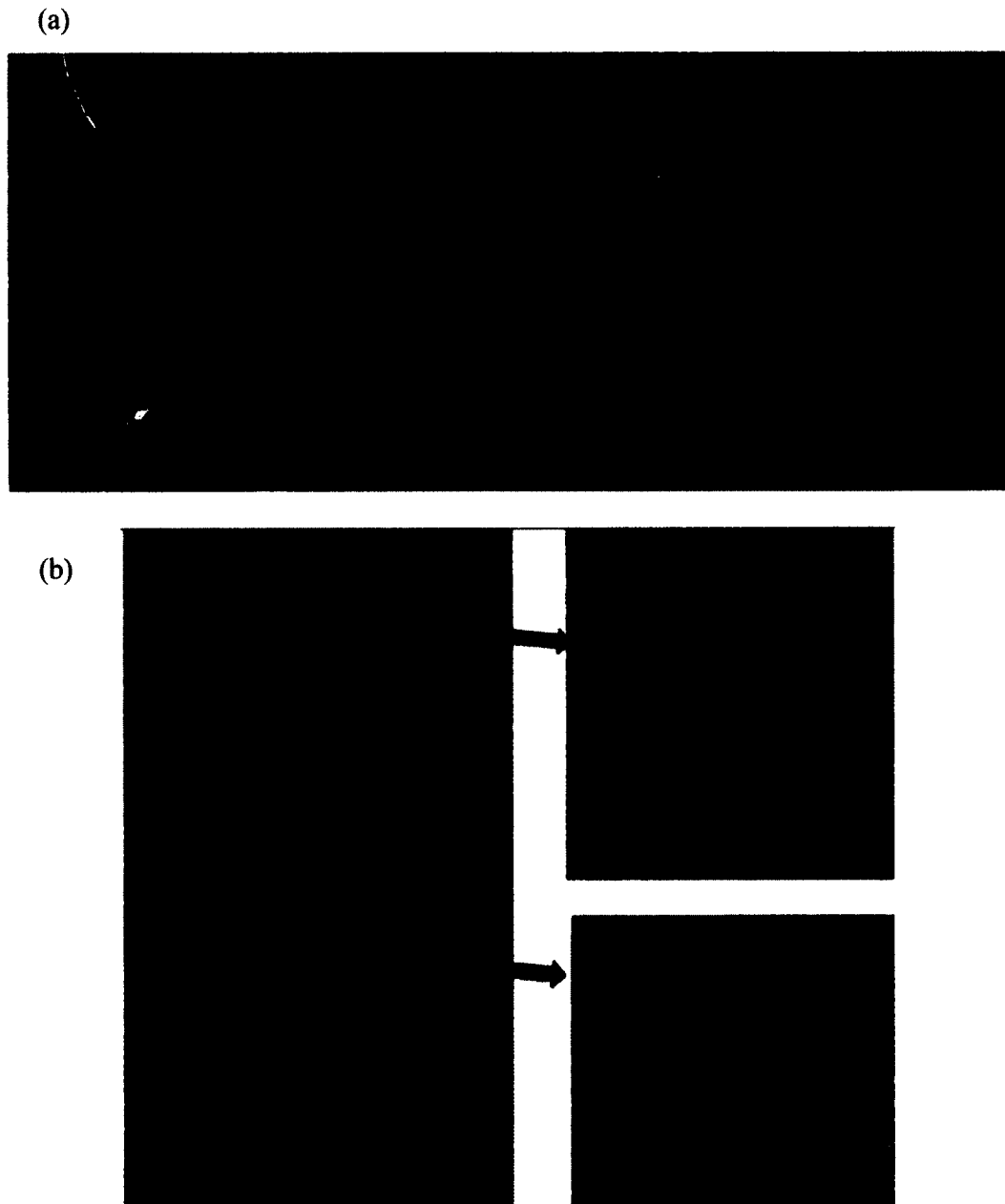
**Figure 5-2** The test site for this study: Scituate, Massachusetts.

## Northeast Coastal Ocean Forecast System (NECOFS) -

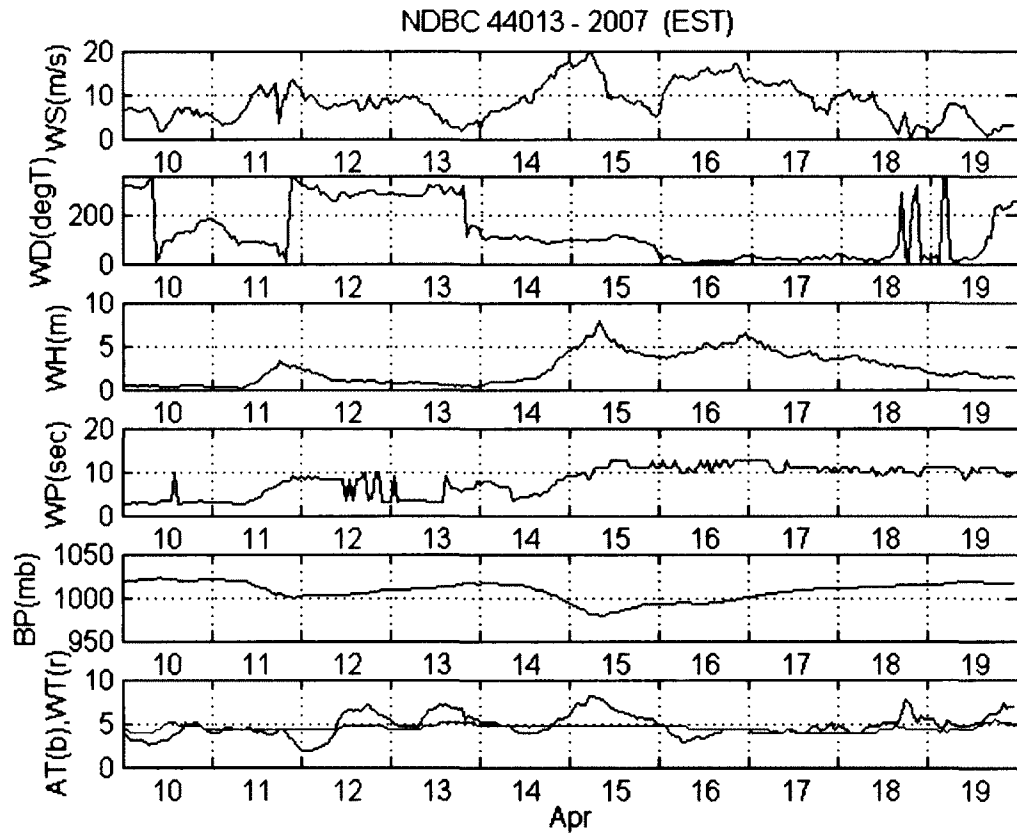
produces 3-day forecast of surface weather, waves, elevation,  
3D currents, temperature, salinity



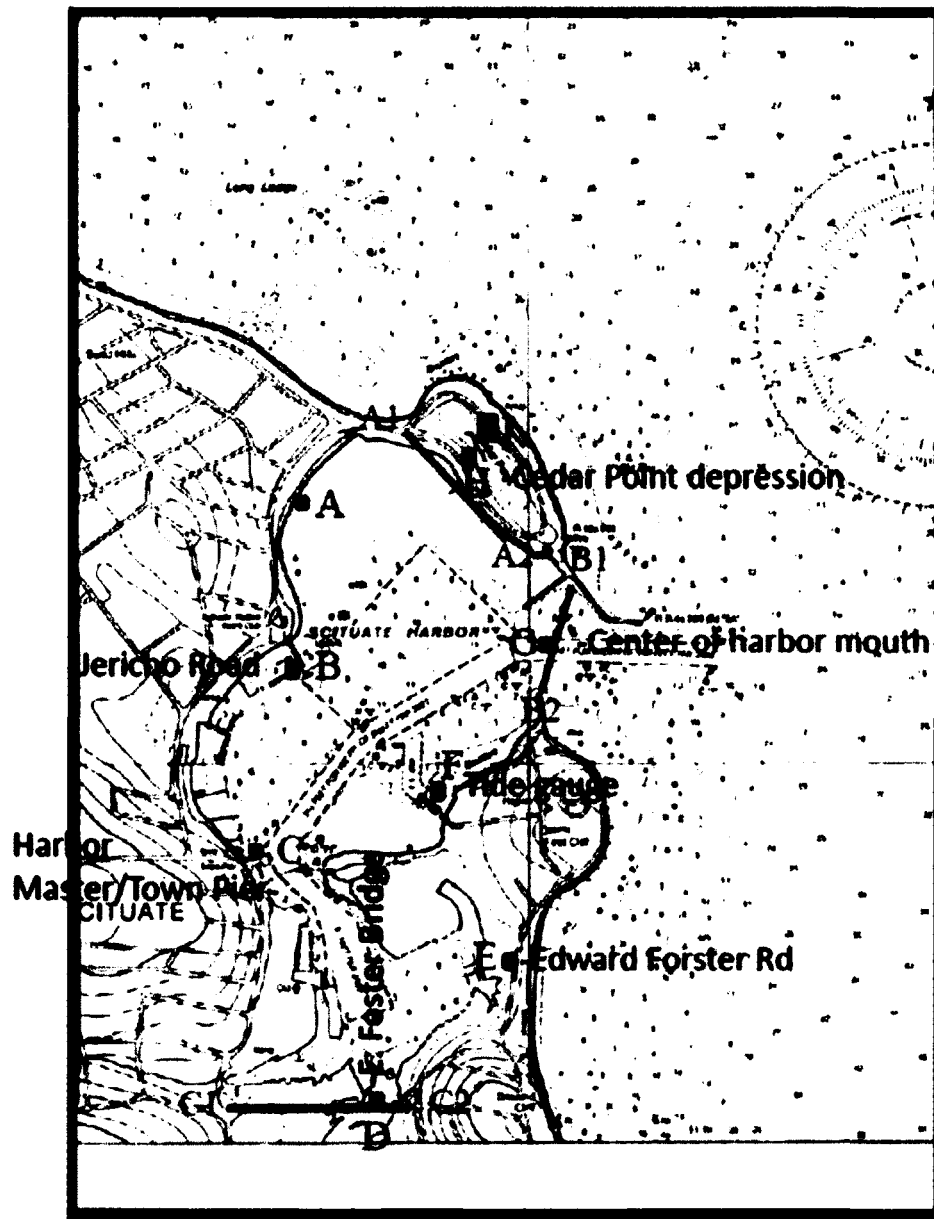
**Figure 5-3** Schematic diagram showing the components for Northeast Coastal Ocean Forecast System (NECOFS). More details can be found in [http://fvcom.smast.umassd.edu/research\\_projects/NECOFS/index.html](http://fvcom.smast.umassd.edu/research_projects/NECOFS/index.html). This figure was provided by UMass Dartmouth/WHOI group in SURA testbed (group members include R. Beardsley in WHOI, and C. Chen, Q. Xu, J. Qi, and H. Lin in UMass-Dartmouth).



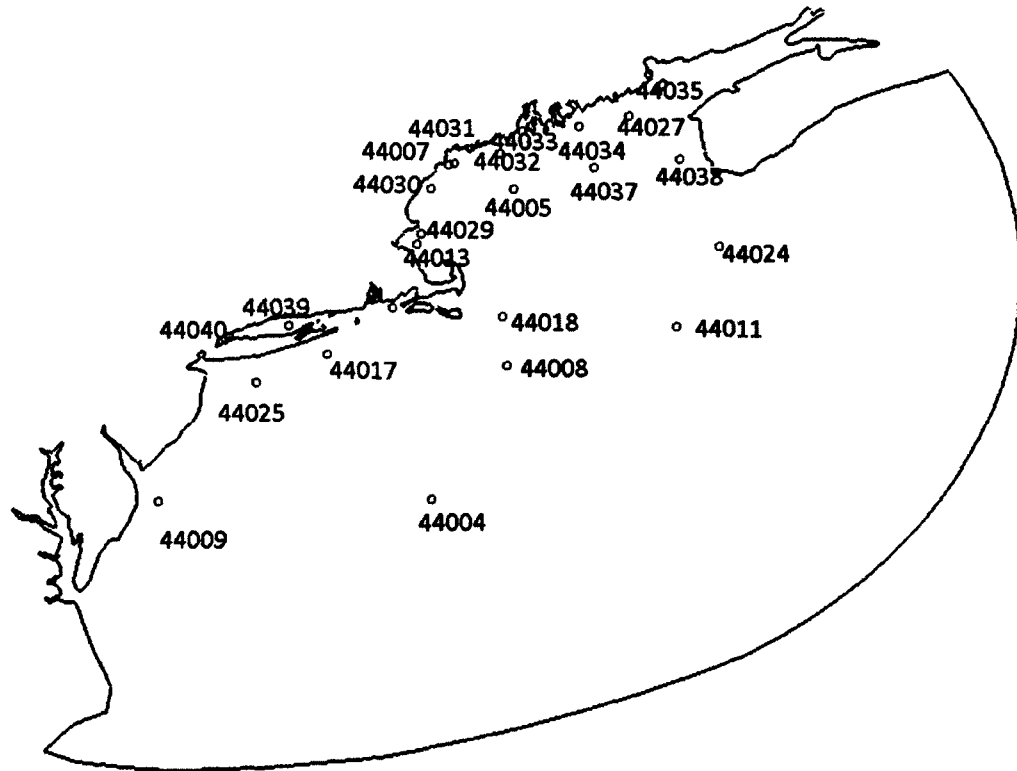
**Figure 5-4** (a) Nested, Scituate inundation grid (left) and the GoM regional FVCOM grid (right). The larger area model is used to drive the high-resolution Scituate inundation model in SURA test bed project (Figures are from SURA Semi-Annual Progress report of Super-Regional Modeling testbed); (b) zoom in to the high-resolution Scituate inundation grid.



**Figure 5-5** Time series of wind speed (WS), wind direction (WD), wave height (WH), dominant wave period (WP), surface, surface air pressure (BP, and air (blue) and water (red) temperature for the period April 10-21, 2007 (data are recorded on the NDBC buoy 44013, location can be found in Fig. 5-7).

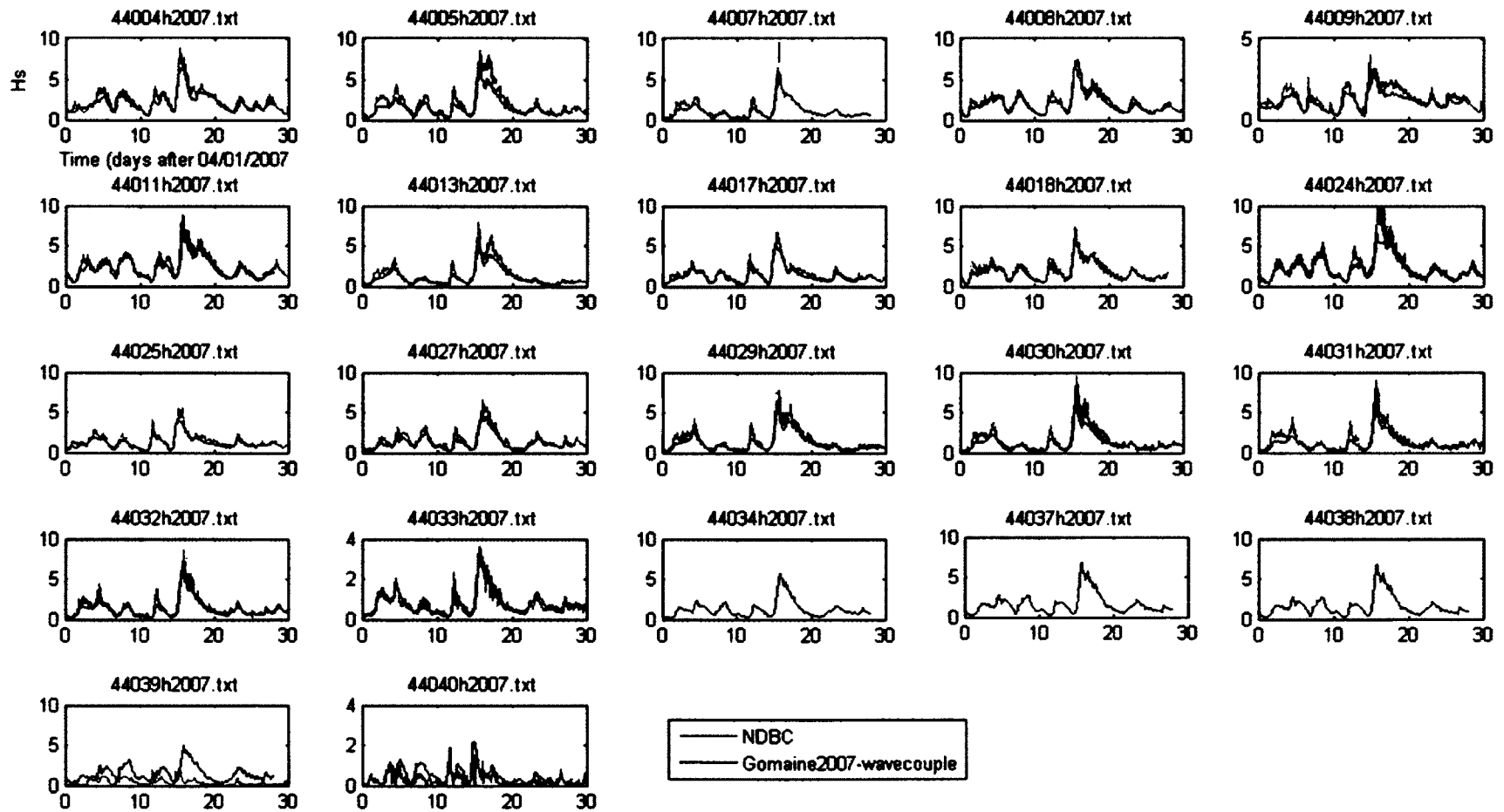


**Figure 5-6** Locations chosen for model data comparison (Station F) and inter-model comparison (Station A, B, C, D, E, G, H, and I) inside Scituate Harbor during April Nor'easter 2007. Time sequence of volumetric transport ( $\text{m}^3\text{s}^{-1}$ ) at three transects (red solid line) is calculated to study the effects of wave-current interaction on inundation.

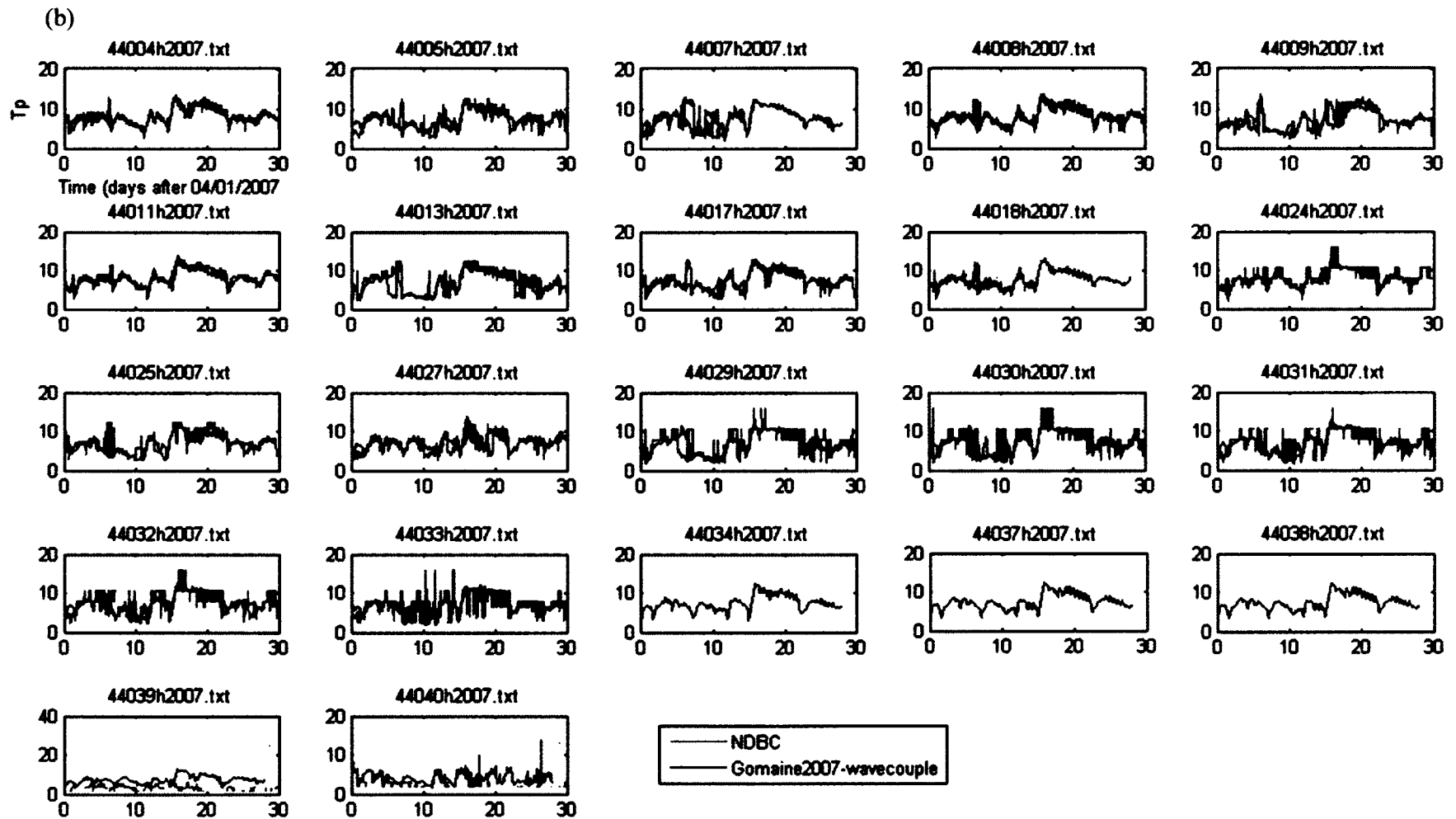


**Figure 5-7** Locations of the NDBC buoys used for the validations of predicted wave in the Gulf of Maine during April Nor'easter 2007.

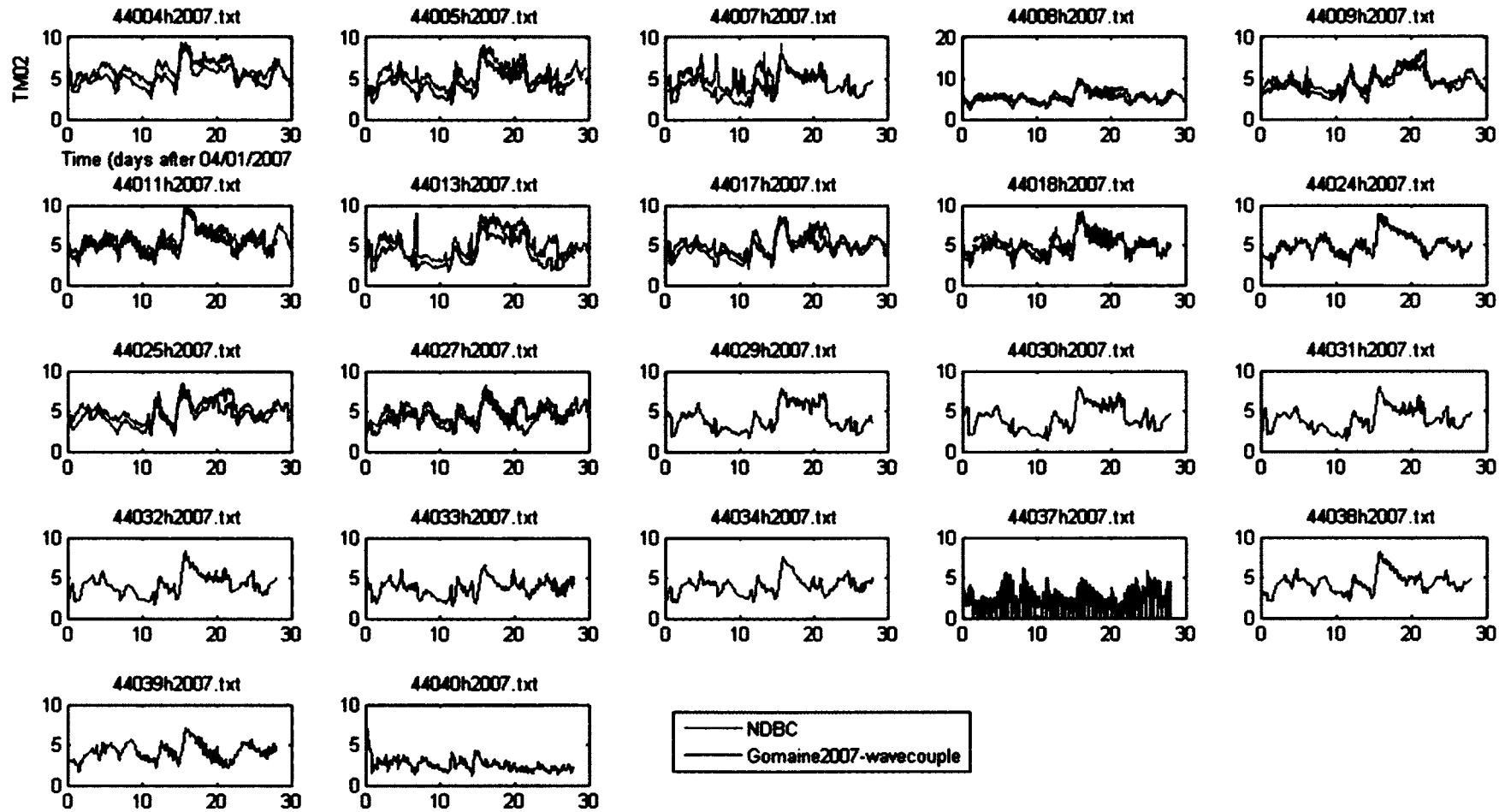
(a)



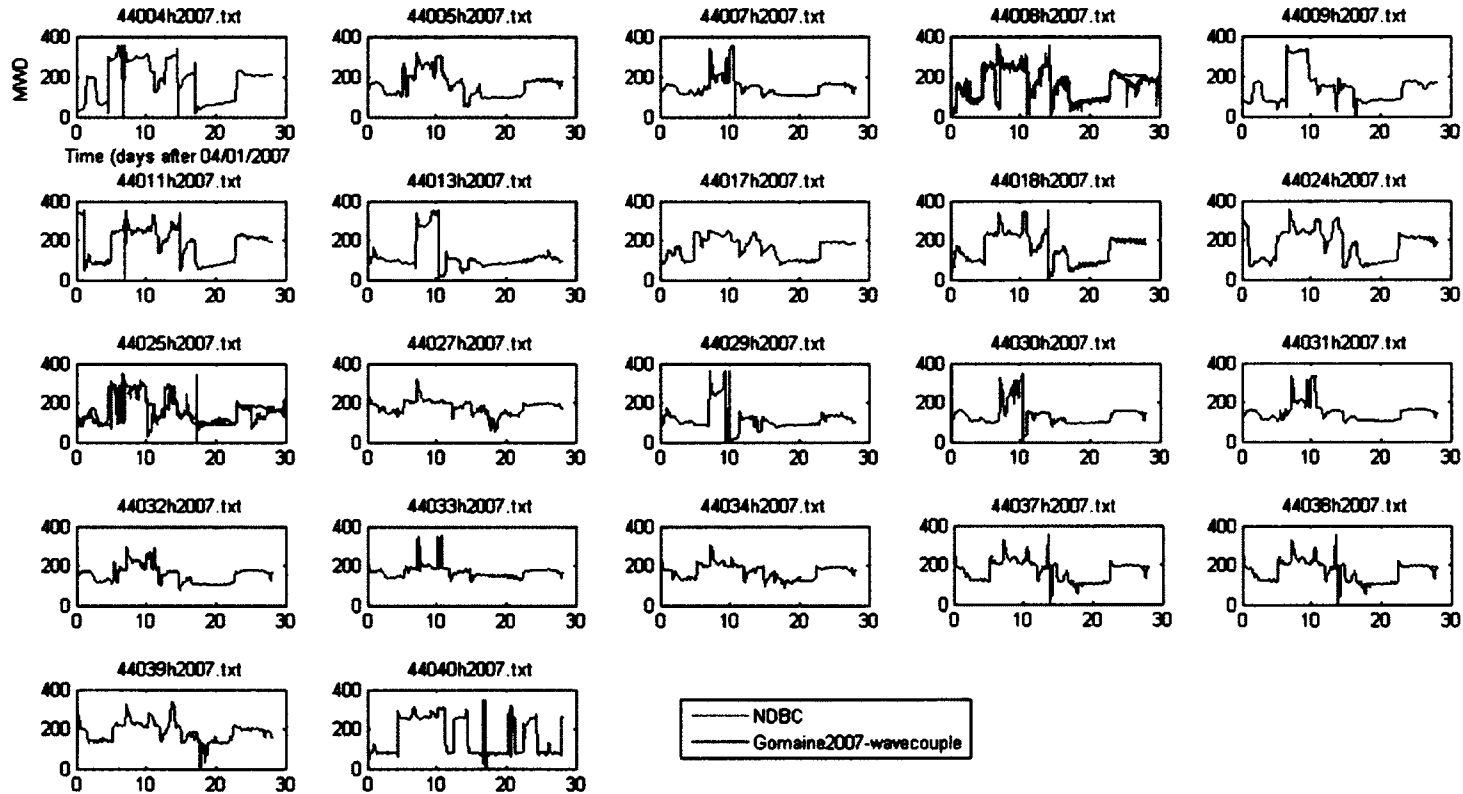




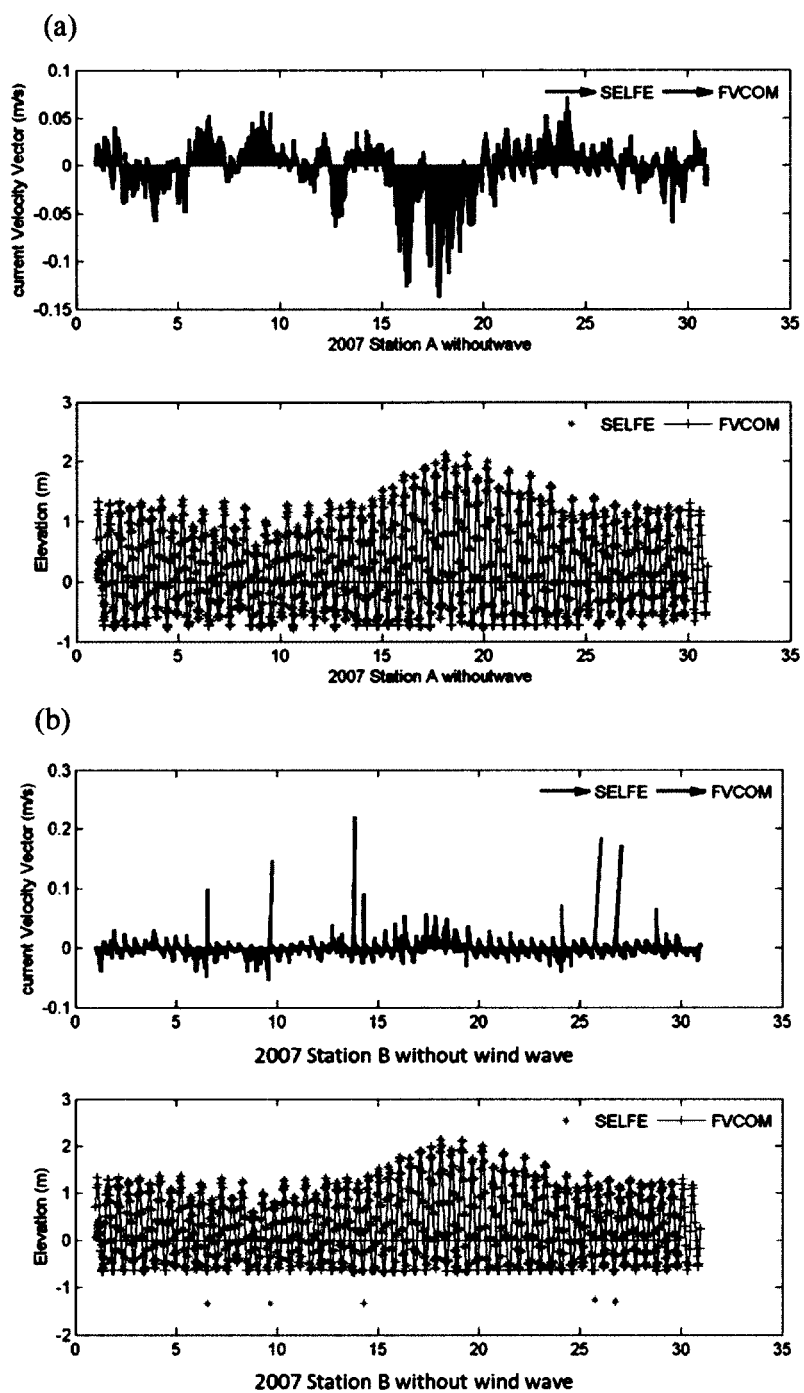
(c)

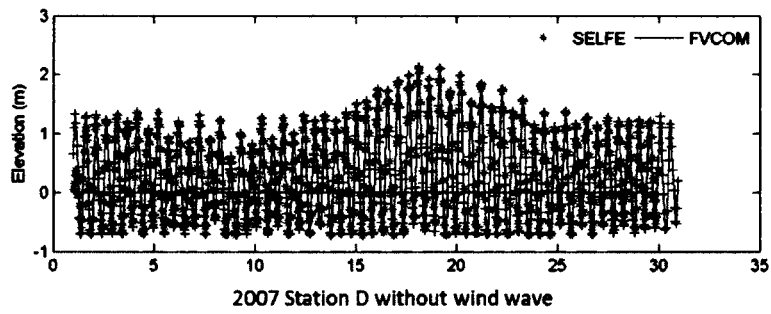
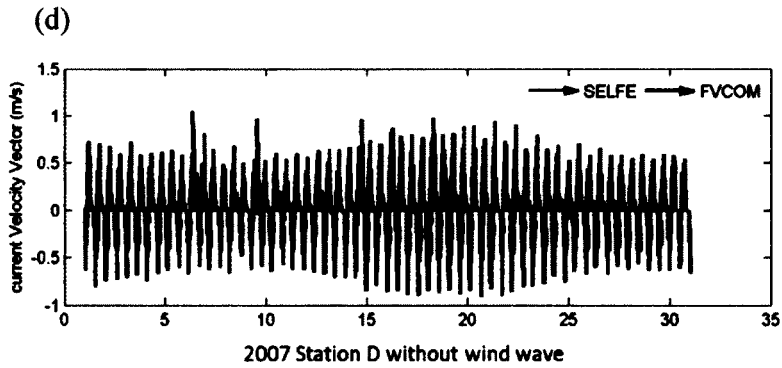
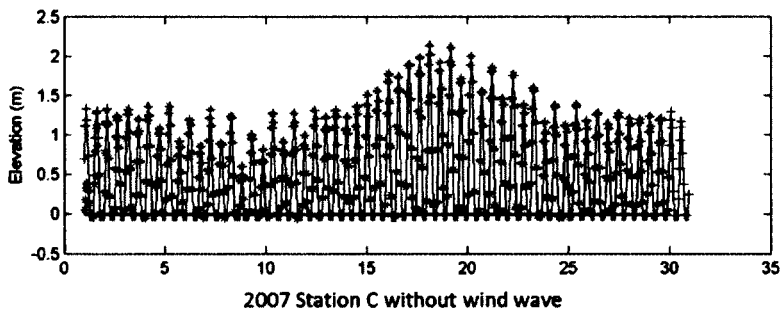
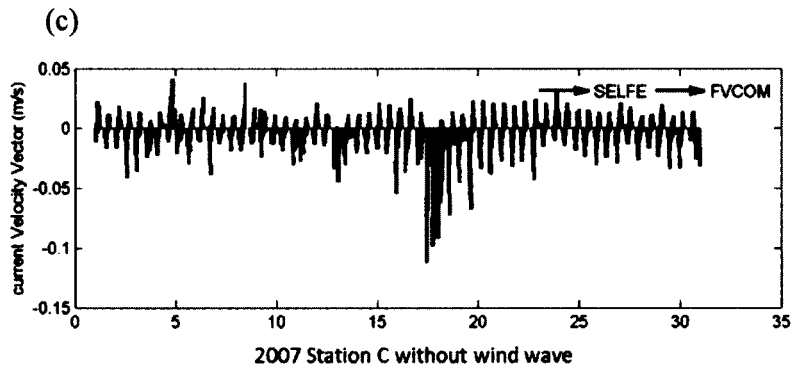


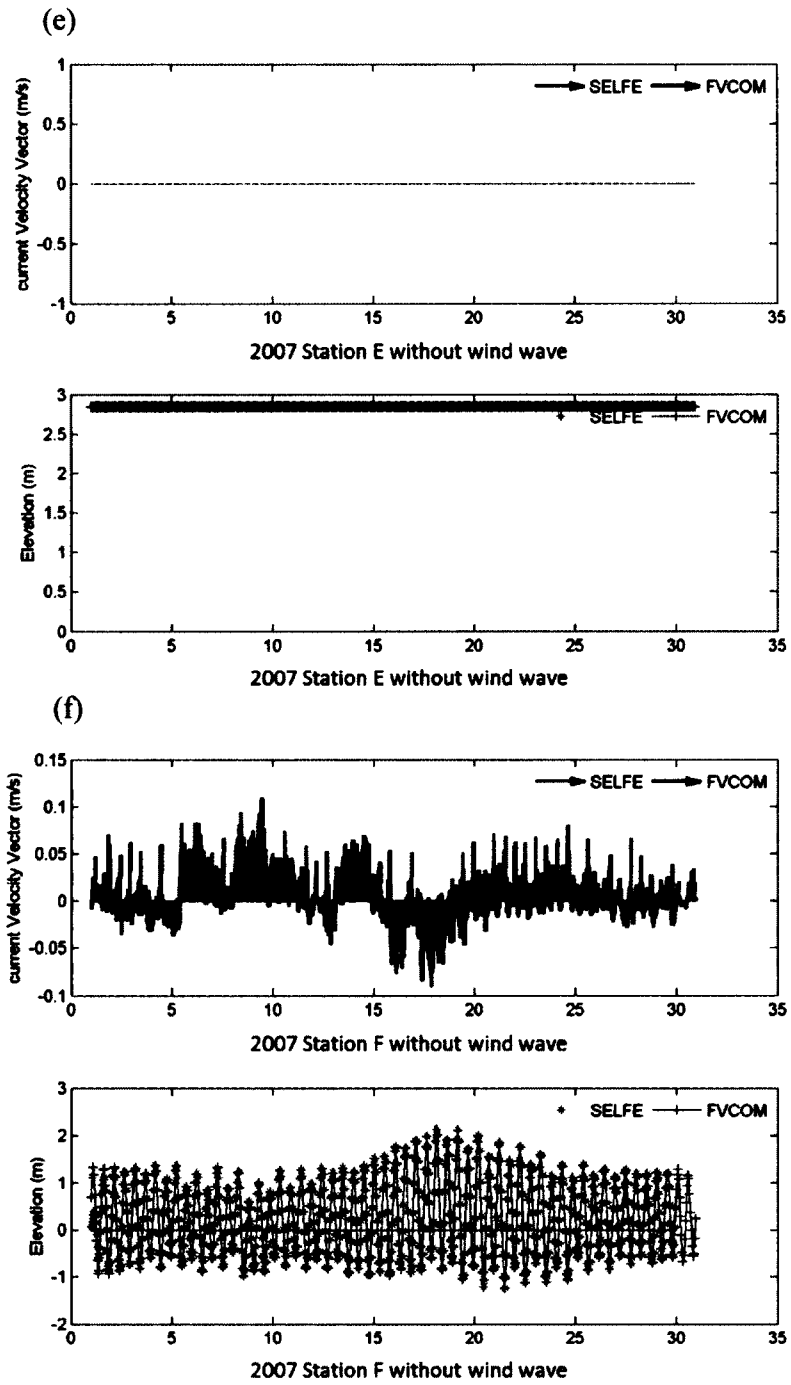
(d)

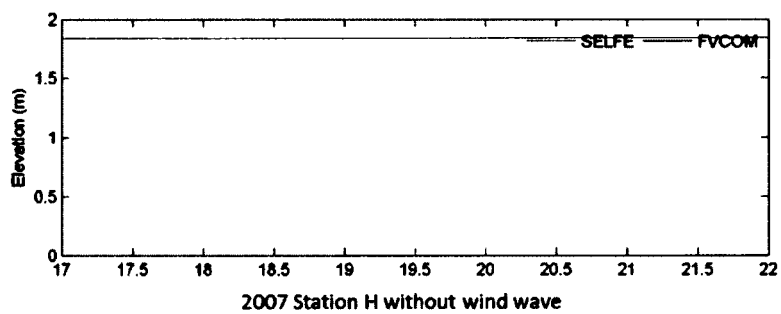
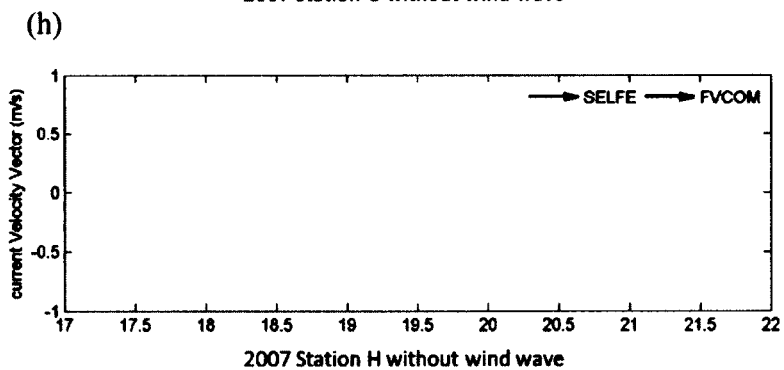
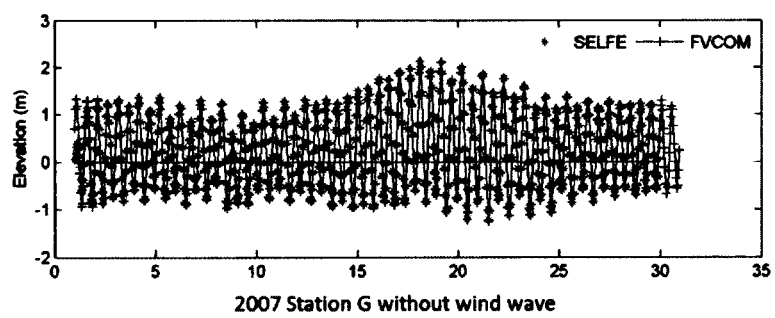
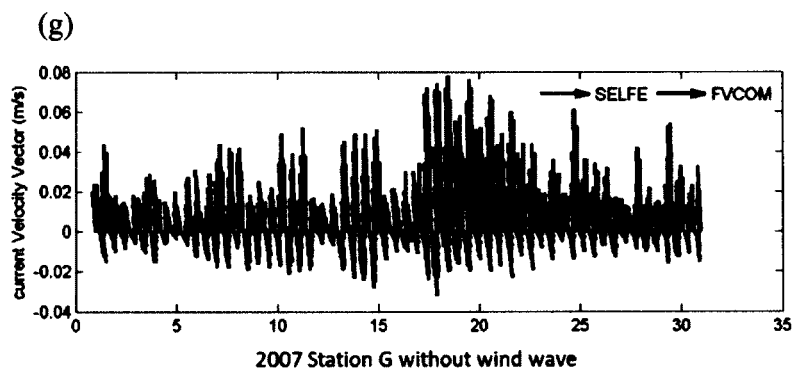


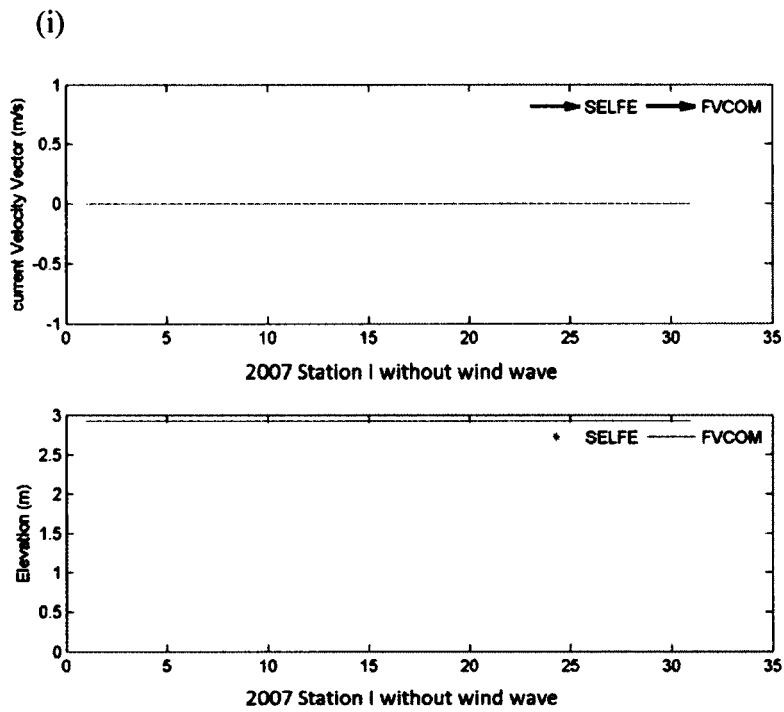
**Figure 5-8** Modeled wave characteristics during April Nor'easter at 22 NDBC buoys. (a) Significant wave height (m); (b) peak wave period (sec); (c) mean wave period (sec); (d) peak wave direction.





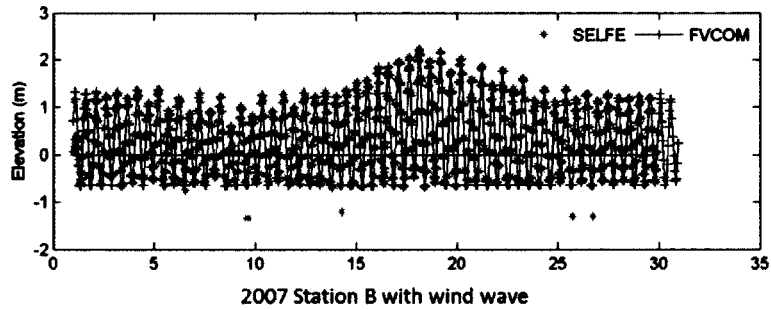
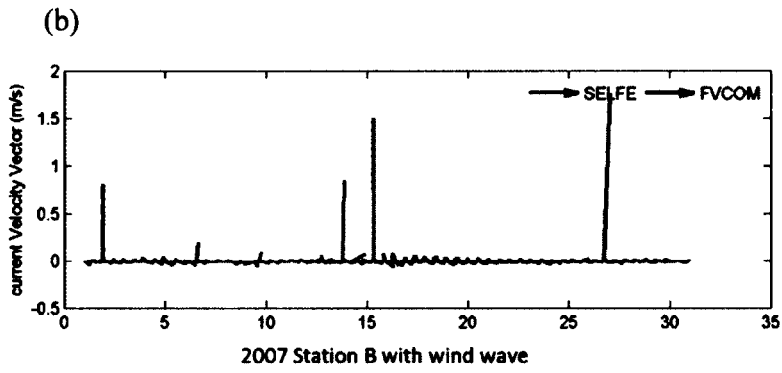
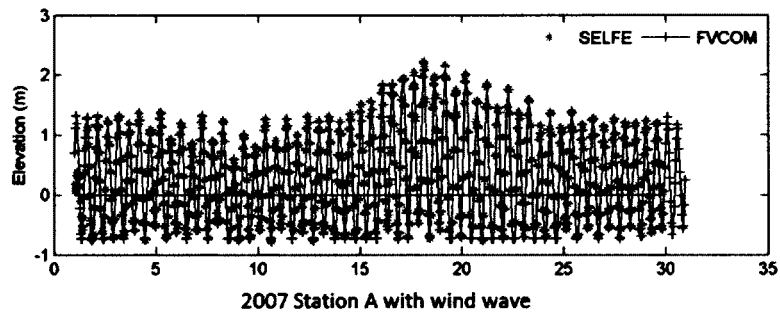
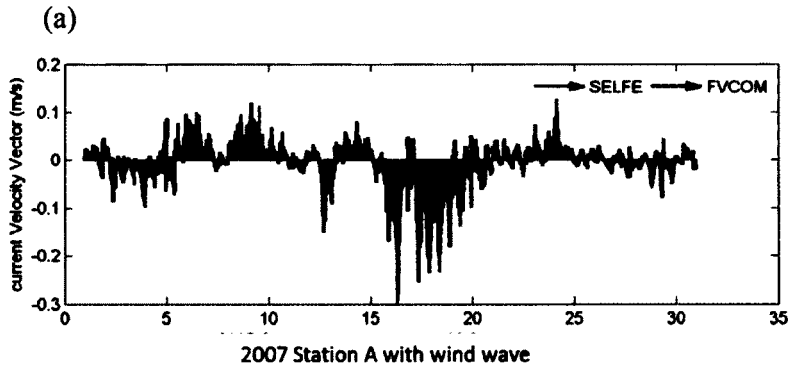


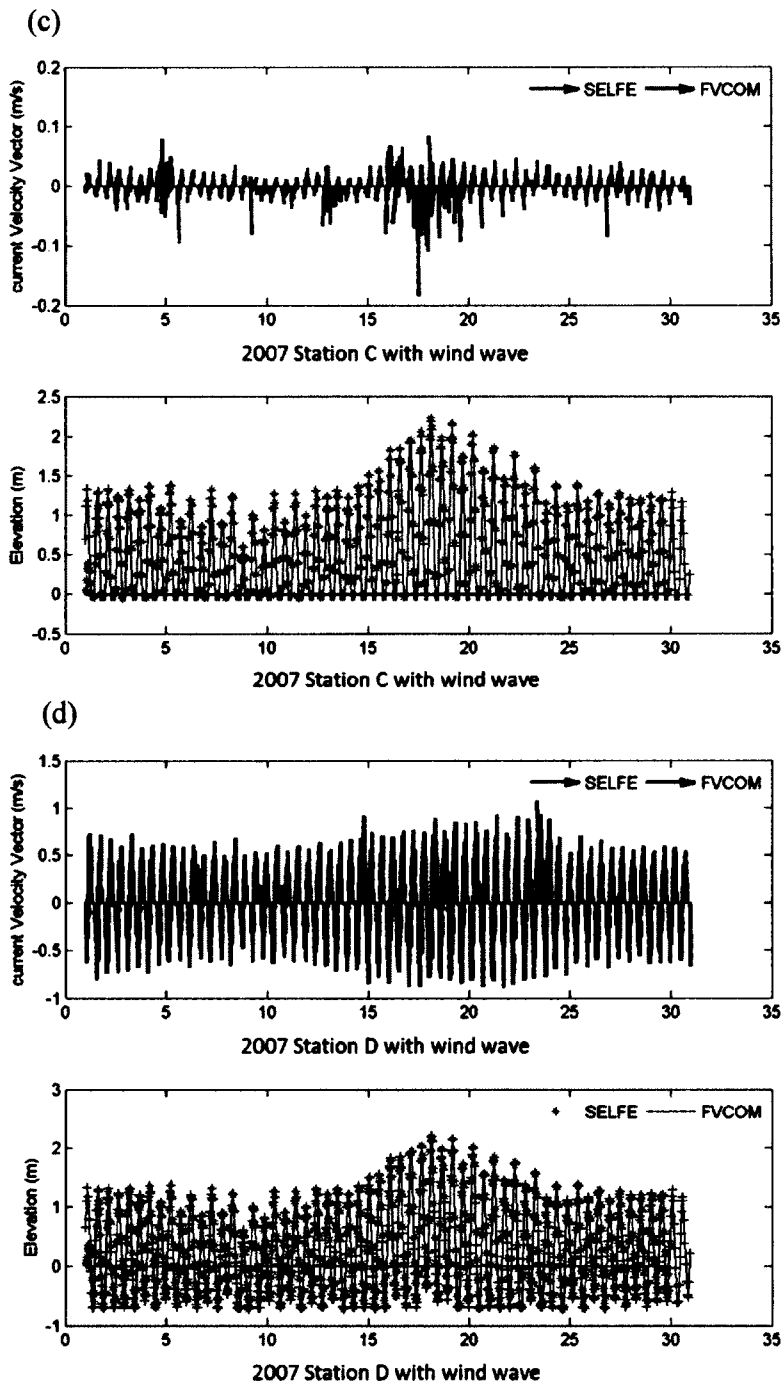


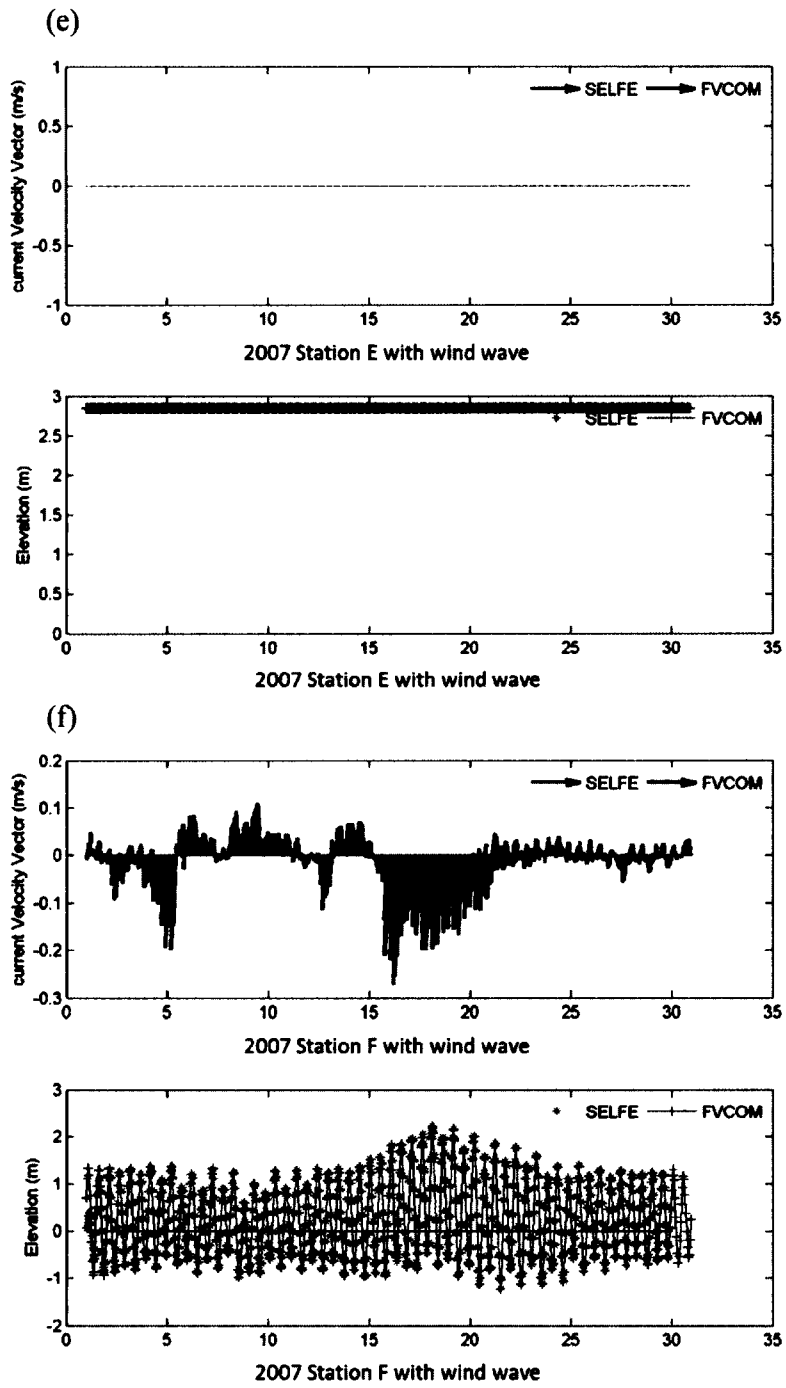


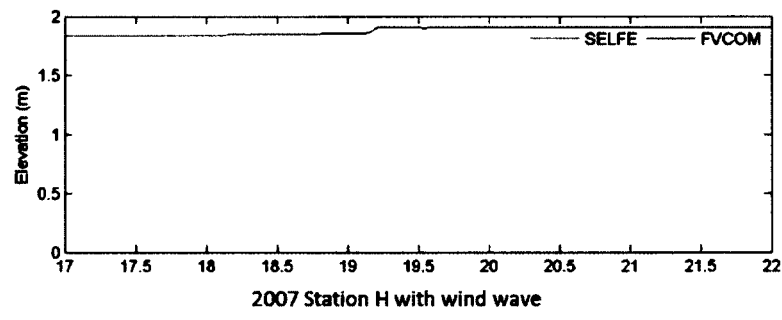
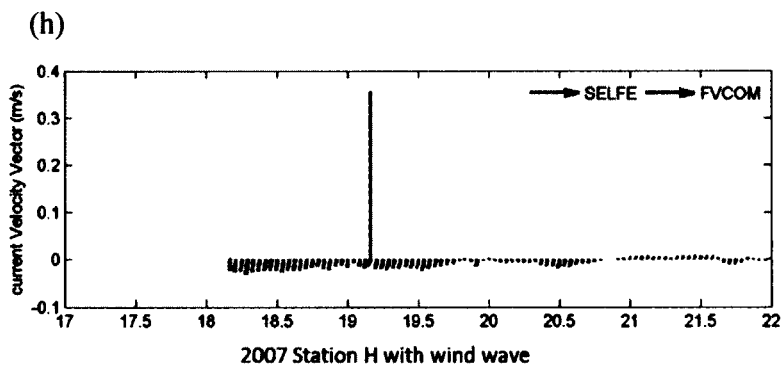
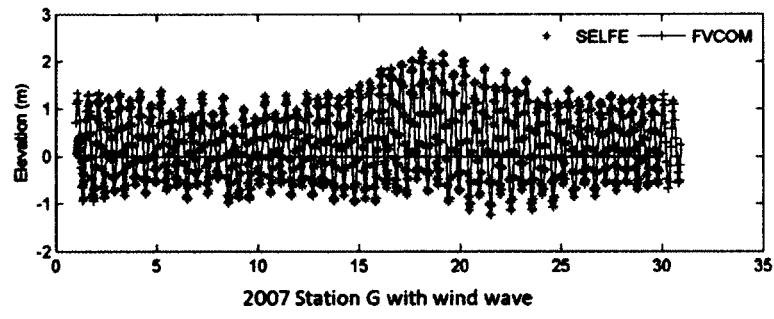
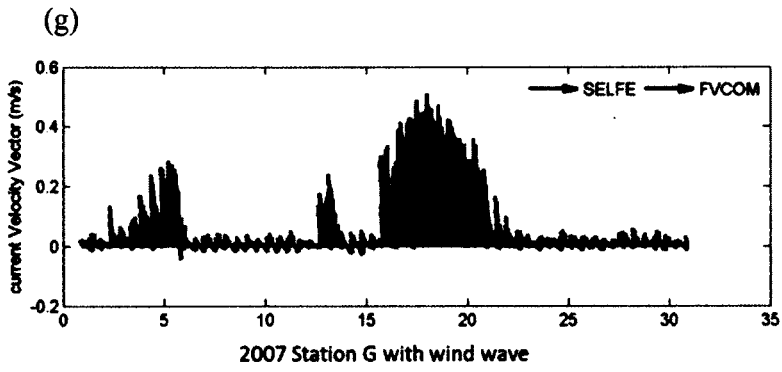
**Figure 5-9** Time series of surface water level and depth-averaged velocity at nine locations inside Scituate Harbor (Fig. 5-6). Red color and blue color represent simulated results without wind wave effect from SELFE and FVCOM, respectively.











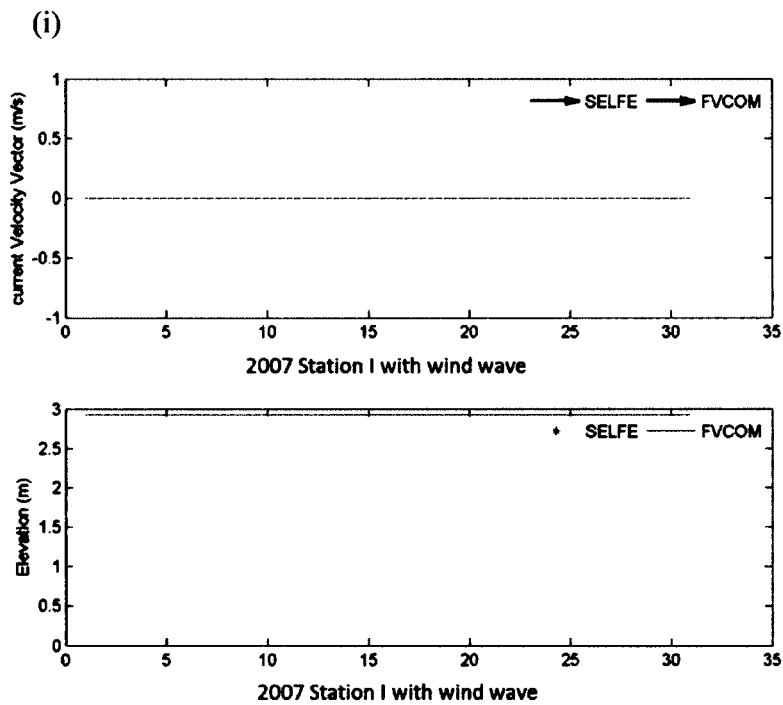


**Figure 5-10** Time series of surface water level and depth-averaged velocity at nine locations inside Scituate Harbor (Fig. 5-6). Red color and blue color represent simulated results with wind wave effect from SELFE and FVCOM, respectively.

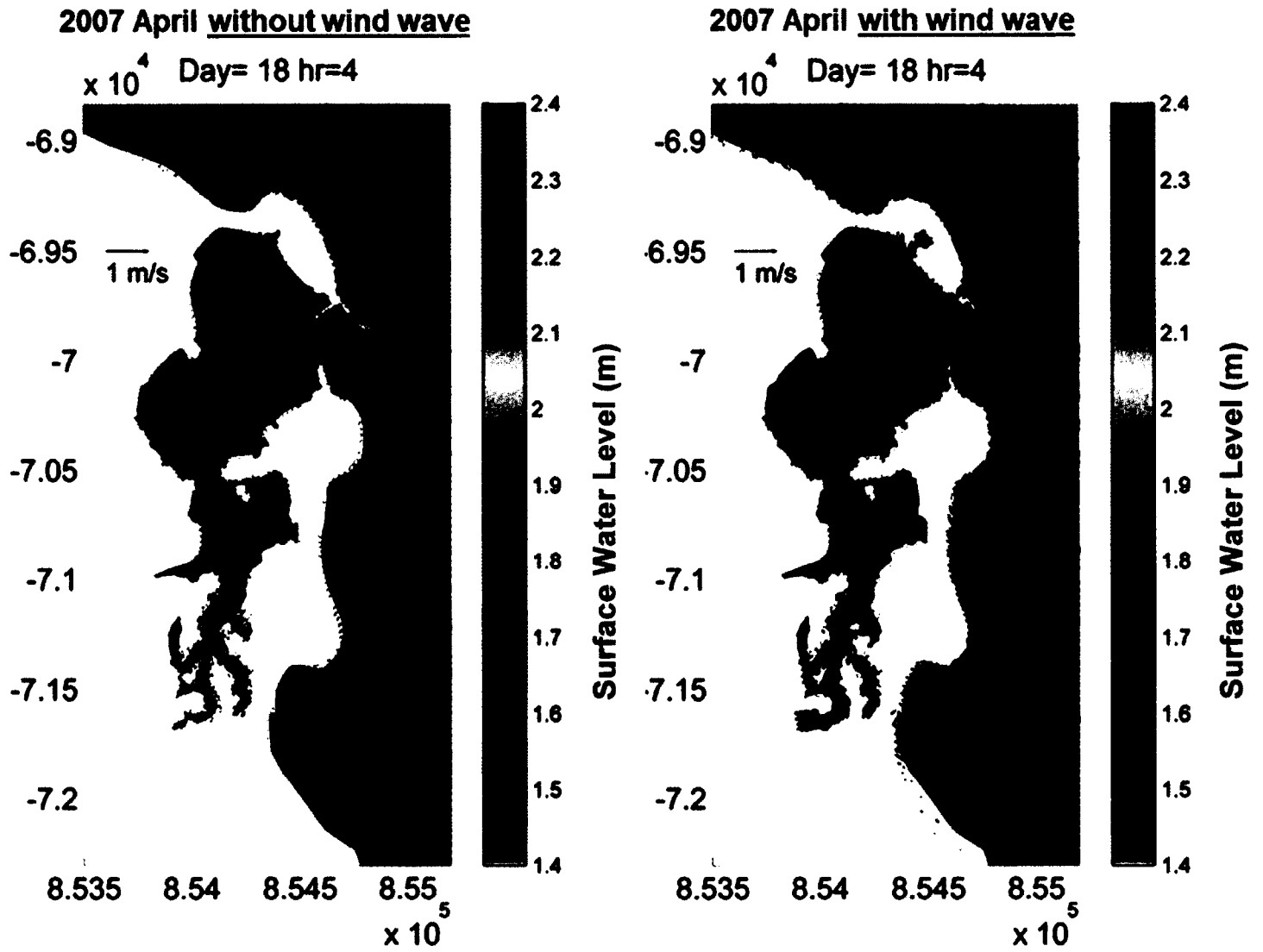


**Figure 5-11** Computed water level and depth-averaged current field (left: without wave effect; right: with wave effect) at 04:00 UTC 4/18/2007.

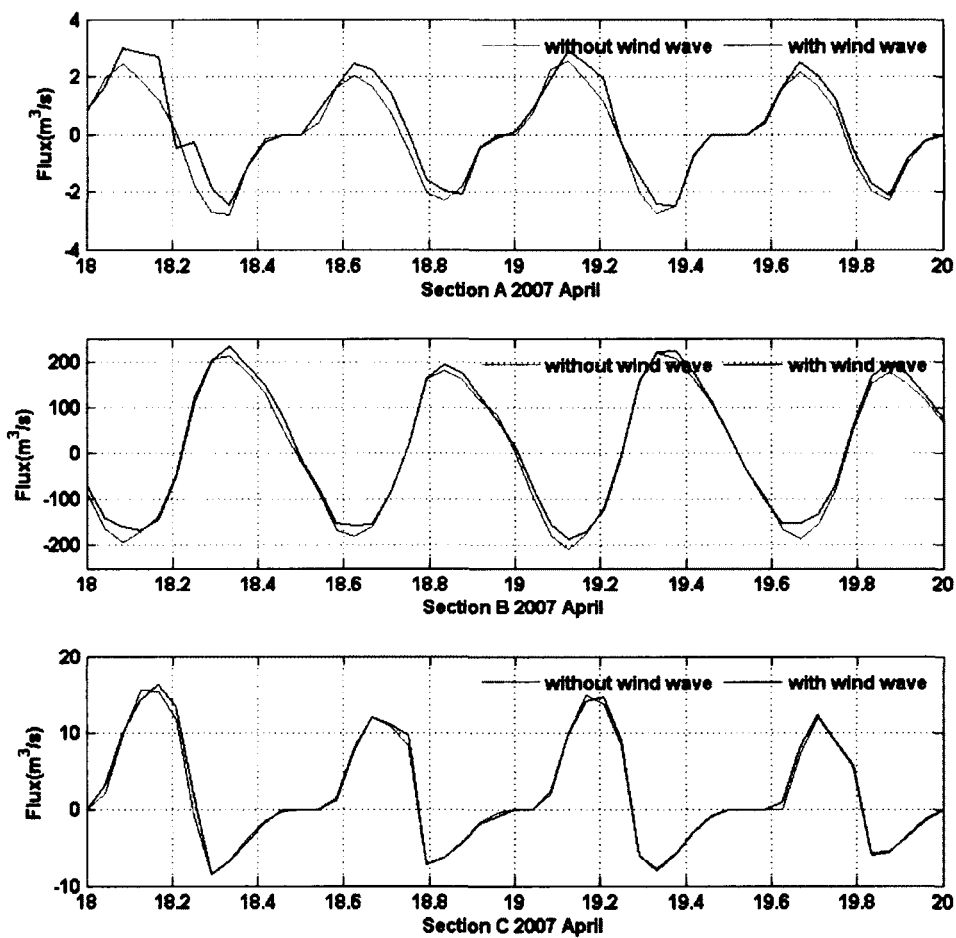


**Figure 5-12** Time series of water transport at transect A, B, and C (Fig. 5-6). Red line and blue line represent calculated results without and with the wind wave effect, respectively.

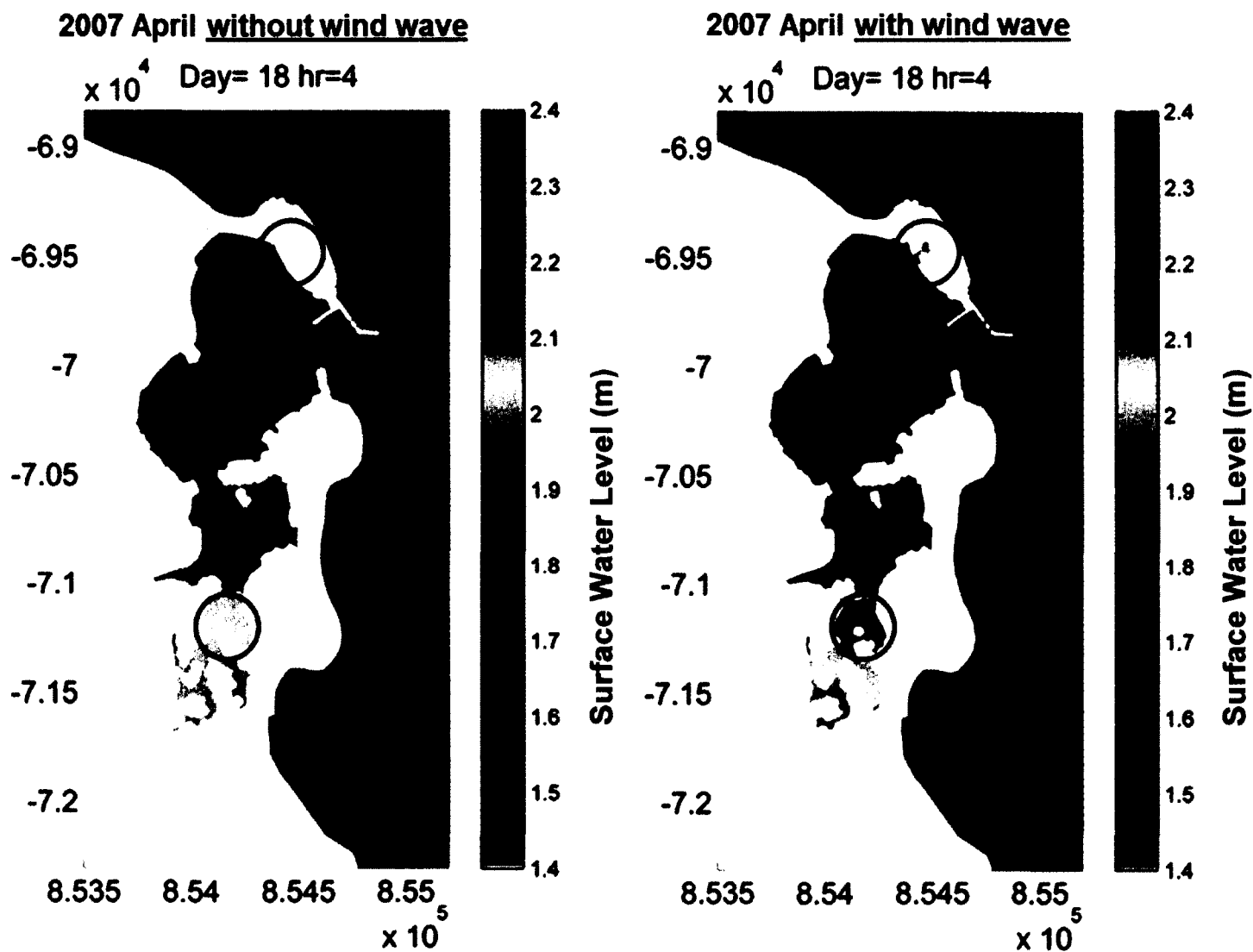


**Figure 5-13** Computed water level (a) without wave effect, and (b) with wave effect on 04:00 UTC 4/18/2007. Black and blue circles represent the inundated areas that are influenced by wave-current interaction.



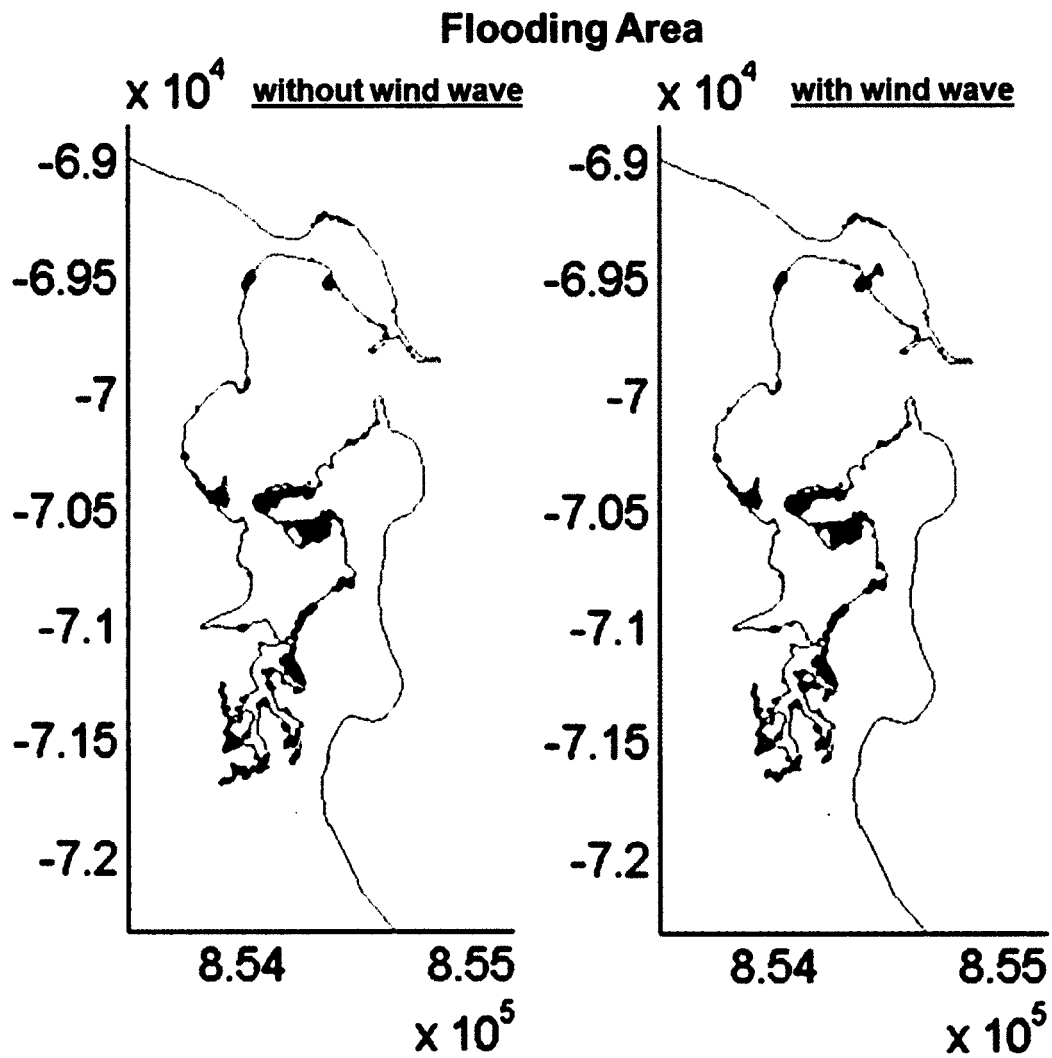


**Figure 5-14** Simulated flooding areas inside Scituate Harbor (with and without the wind wave effect) on 04:00 UTC 4/18/2007. The blue shade represents the flooding areas and the red shade represents the drying areas.

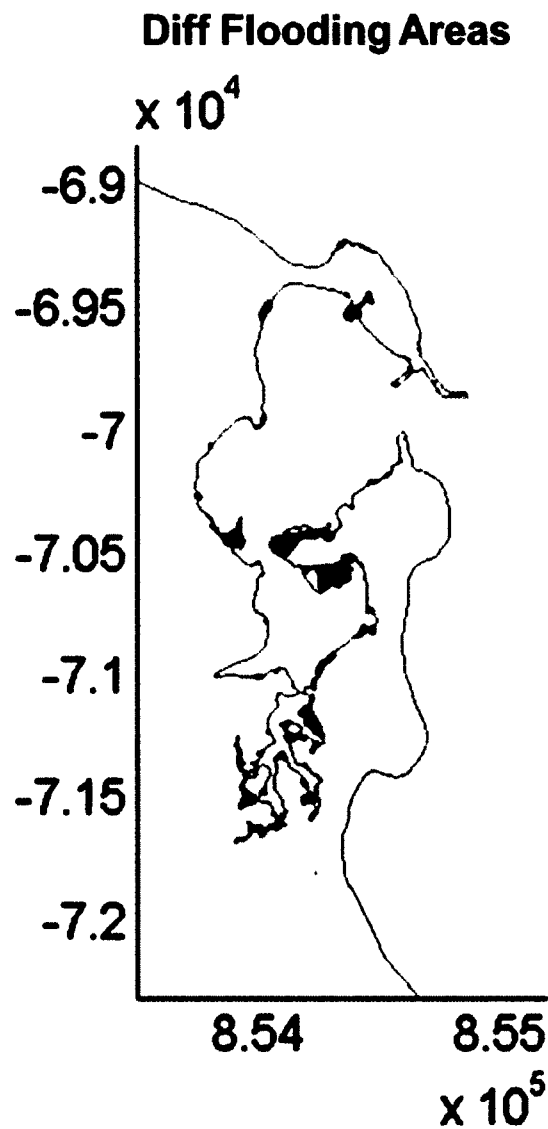


**Figure 5-15** The difference of flooding areas between with wave and without wave effects on 04:00 UTC 4/18/2007. The blue shade represents the areas that are flooded in both cases; the red shade represents the drying areas in both cases; the black shade represents increased flooding and gray shade represents reduced flooding due to the wave effects.

## CHAPTER VI. Summary and Conclusion

A fully coupled wave-current interaction model based on a 3D hydrodynamic model (SELFE) and the spectral wave model (WWM II) has been developed in this study. Both models were implemented on unstructured grids with parallel computing capability, which makes the coupled model effective in multi-scale applications without grid nesting.

The two models are tightly coupled with the same domain decomposition but with different time-stepping schemes to ensure maximum efficiency and flexibility. Three major effects of wave-current interaction are considered in the coupled model: (1) wave-induced radiation stress; (2) wave-enhanced surface stress as well as mixing due to the surface wave-breaking; and (3) wave-enhanced bottom shear stress. The wave-current coupled model has been demonstrated to be accurate, robust, and also efficient through a series of stringent tests consisting of two analytical solutions, three laboratory experiments, and several river-to-ocean scale field tests. The inclusion of the wave-current interaction mechanism enables the storm surge model to function more accurately and thus to predict surface water responses including the coastal flooding more realistically during tropical and extra-tropical storm events.

Hurricane Ike made landfall in the Gulf of Mexico in 2008 and caused devastating damages around the Galveston Bay. A large forerunner contributed significantly to the total

water level during the ensuing primary surge when the hurricane approached the coastline. Numerical model results indicate that the forerunner occurs as a result of Ekman set-up along the broad continental shelf by the shore-parallel wind field. Moreover, it was found that the cross-shore Ekman set-up is highly sensitive to the selection of the bottom drag coefficient.

Most storm surge simulation studies focus on the effects of surface wind stress. However, it has been found that, in the inner shelf regions, the conditions of the BBL also have significant changes during storm events and should not be neglected. Given the fact that the Gulf of Mexico is known to be rich in fluid mud, and near-bed flows generally are weak under fair-weather conditions, the suspended sediment-induced density stratification is likely to be ubiquitously present at the BBL during storm events. A sediment-transport model and wave-current BBL sub-model including the sediment-induced stratification effect were developed and coupled to the unstructured grid wave-current model for simulating the forerunner during Hurricane Ike. The model results demonstrate that BBL dynamics have significant effects on the cross-shelf Ekman set-up.

Our experiences with the 3D wave-current coupled model in the Chesapeake Bay and the Gulf of Mexico highlighted the need of the post-analysis on the model results in order to understand the complicated coupling mechanisms since the end results are not always easy to interpret. Consistent physical formulations for the wave-current interactions, such as those in Arduin et al. (2008), should be adopted in the coupled model, which can provide a more systematic investigation to the effects of wave-current interaction on storm surge and inundation simulation.

In this dissertation, the effects of wave-current interaction on inundation simulation in the small coastal basin were also conducted in the Scituate domain. The results indicated that wave-current interaction effects should be taken into account not only for storm surge prediction, but also, very importantly, for inundation simulation.

The major findings and conclusions of this dissertation can be summarized as follows:

1. A 3D unstructured storm surge and inundation modeling system, coupling the unstructured grid current model SELFE and the wave model WWM II, has been developed and successfully applied for storm surge and inundation simulations in the Chesapeake Bay, the Gulf of Mexico, and Scituate Harbor in the Gulf of Maine.
2. It was demonstrated that the storm surge caused by Hurricane Ike can be separated into two stages: (a) forerunner surge induced by the Ekman set-up under geostrophic balance; and (b) primary surge induced by the local on-shore winds.
3. The comparison of predictions from the Ekman dynamics-induced forerunner simulation with measured data is good; however, the model tends to underpredict the magnitude of the Hurricane Ike forerunner by 40% unless the bottom friction is reduced by one order of magnitude.
4. In order to study the effects of BBL dynamics on forerunner surge, we further built a sediment-transport model and coupled this model with the wave-current model. A stability function was introduced to the bottom friction to consider the effects of sediment-induced stratification on the BBL. It was shown that including both wave-current interaction and sediment-induced stratification can increase the magnitude of

alongshore current as well as the cross-shelf Ekman set-up by 30% and, hence, yield better results for forerunner simulation.

5. A practical approach was adopted in the 3D wave-current coupled model based on the relationship between normalized orbital velocity and sediment-induced stratification. By implementing the simple practical approach over the inner-LATEX area, the predictions of total water level were generally reasonable compared with measured data and results from the fully 3D wave-current-sediment-transport coupled model.
6. Including wave-current interaction in the models substantially strengthens and changes the direction of the velocity field in the Scituate Harbor and surrounding areas. The effect of wave-induced radiation stress generates additional flux into Scituate Harbor and enhanced small scale velocity features within the Harbor. While these do not translate to large differences in surface water level inside the Scituate Harbor, they do influence the inundation simulations of areas in the southern and northern basins.

The wave-current coupled model developed in this study showed great potential and capability to be established as a real-time forecast system in the future. Given the complexity of the processes and tasks at hands, there are, however, still many challenges that lie ahead. First, even though the coupled model has generated satisfying wave, storm surge, and inundations for several multi-scales field tests, more tests should be conducted to validate the capability of the coupled model. Second, a “self-consistent” framework for various physical formulations of wave-current interactions should be implemented in our coupled model to further investigate and improve our 3D model results. Thirdly, the effects of wave-enhanced

surface and bottom stresses should be considered for further improvements of inundation prediction in the future. Last but not least, the effect of sediment-induced stratification on the BBL in the Gulf of Mexico needs to be further investigated for better storm surge prediction. Moreover, the effect of morphological changes should also be considered in the future study.

## APPENDICES

## Appendix A Definition of statistical measures for error analysis

The following statistical measures have been calculated to evaluate the skill of the SELFE-WWM II model in tide, storm surge simulation in this study.

Here,  $x$  represents the time series data,  $\bar{x}$  is its time mean, while subscripts “*mod*” and “*obs*” denote the model results and observations, respectively.

1. The root-mean-square error is defined as

$$RMSE = \left\{ \frac{1}{N} \sum_{i=1}^N (x_{mod} - x_{obs})^2 \right\}^{1/2}$$

2. The mean absolute relative error (ARE) is defined as

$$ARE = \frac{1}{N} \sum_{i=1}^N \left( \left| \frac{x_{mod} - x_{obs}}{x_{mod}} \right| \right) * 100(\%)$$

3. The correlation coefficient ( $r$ ) is defined as

$$r = \frac{\sum_{i=1}^N (x_{mod} - \bar{x}_{mod})(x_{obs} - \bar{x}_{obs})}{\left[ \sum_{i=1}^N (x_{mod} - \bar{x}_{mod})^2 \sum_{i=1}^N (x_{obs} - \bar{x}_{obs})^2 \right]^{1/2}}$$



## Appendix B Definition of wave characteristics used for model-data comparison

1. Significant wave height,  $H_{m0}$ : Significant wave height,  $H_{m0}$ , can be estimated from the variance of a wave elevation record assuming that the non-directional spectrum is narrow. The variance can be calculated directly from the record or by integration of the spectrum as a function of frequency. Using the latter approach,  $H_{m0}$  is given by

$$H_{m0} = 4(m_0)^{1/2}$$

where  $m_0$  is the zero moment of non-directional spectrum and defined as

$$m_r = \sum_{n=1}^{N_b} (f_n)^r C_{11}(f_n) \Delta f_n, \quad r = 0$$

where  $\Delta f_n$  is the spectrum frequency band width,  $f_n$  is frequency,  $C_{11}$  is non-directional-spectral density, and  $N_b$  is the number of frequency bands in the spectrum.

During analysis, pressure spectra are converted to equivalent sea surface (elevation) spectra so that these calculations can be made. Due to the narrow spectrum assumption,  $H_{m0}$  is usually slightly larger than significant wave height,  $H_{1/3}$ , calculated by zero-crossing analysis.

2. Zero-crossing wave period: Zero-crossing wave period is the average of the wave periods that occur in a wave height time-series record where a wave period is defined as the time interval between consecutive crossings in the same direction of mean sea level during a wave measurement time period. It is also statistically the same as dividing the measurement time period by the number of waves. An estimate of zero-crossing wave period can be computed from a non-directional spectrum. This

estimate is statically the same as averaging all wave periods that occurred in the wave record. NDBC calculates zero-crossing wave period from the following equation:

$$T_{zero} = \left(\frac{m_0}{m_2}\right)^{\frac{1}{2}}$$

3. Peak wave period: peak, or dominant, wave period is the wave period corresponding to the center frequency of the frequency band with the maximum non-directional spectral density. Peak wave period is also called the period of maximum wave energy.

## LITERATURE CITED

- Abgrall, R. (2006): "Residual distribution schemes: Current status and future trends". *Computers & Fluids*, 35(7), 641-669.
- Abramowitz, M., and I. A. Stegun (1972): "Handbook of Mathematical Functions". Dover, New York, 1045 pp.
- Adams, C. E., Jr., and G. L. Weatherly (1981): "Some Effects of Suspended Sediment Stratification on an Oceanic Bottom Boundary Layer". *J. Geophys. Res.*, 86(C5), 4161-4172.
- Allison, M.A., T. S. Bianchi, B. A. McKee, and T. P. Sampere (2007): "Carbon burial on river-dominated continental shelves: impact of historical changes in sediment loading adjacent to the Mississippi River". *Geophysical Research Letter*, 34 (L01606), doi:10.1029/2006GL028362.
- Andrews, D. G., and M. E. McIntyre (1978a): "On wave-action and its relatives". *J. Fluid Mech.*, 89, 647-664. Corrigendum Vol 95, pp. 796; also Vol. 106, pp.331.
- Andrews, D. G., and M.E. McIntyre (1978b): "An exact theory of nonlinear waves on a Lagrangian-mean flow". *J. Fluid Mech.*, 89, 609-646.
- Ardhuin, F., and A. D. Jenkins (2006): "On the Interaction of Surface Waves and Upper Ocean Turbulence". *J. Phys. Oceanography*, 36, 551-557.

- Ardhuin, F., N. Rascle, and K. A. Belibassakis (2008): "Explicit wave-averaged primitive equations using a generalized Lagrangian mean". *Ocean Modelling*, 20(1), 35-60.
- Ardhuin, F., L. Marié, N. Rascle, P. Forget, and A. Roland (2009): "Observation and Estimation of Lagrangian, Stokes, and Eulerian Currents Induced by Wind and Waves at the Sea Surface". *Journal of Physical Oceanography*, 39(11), 2820-2838.
- Ardhuin, F., E. Rogers, A. V. Babanin, J.F. Filipot, R. Magne, A. Roland, A.V. Westhuysen, P. Queffelec, J. M. Lefevre, L. Aouf, and F. Collard (2010): "Semiempirical Dissipation Source Functions for Ocean Waves. Part I: Definition, Calibration, and Validation". *Journal of Physical Oceanography*, 40(9), 1917-1941.
- Ardhuin, F., et al. (2012): "Semi-empirical dissipation source functions for ocean waves: Part II, evaluation in conditions with strong currents, and general validation of wave models in currents". Submitted to *Journal of Physical Oceanography*.
- Ardhuin, F. and A. Roland (2012): "Coastal wave reflection, directional spread, and seismo-acoustic noise sources". Submitted to *J. Geophys. Res* (this issue).
- Ariathurai, C.R., and K. Arulanandan (1978): "Erosion rates of cohesive soils". *Journal of Hydraulics Division*, 104 (2), 279-282.
- Azevedo, A., A. Oliveira, A. B. Fortunato, and X. Bertin (2009): "Application of an Eulerian-Lagrangian oil spill modeling system to the Prestige accident: trajectory analysis". *J. Coastal Res.*, SI 56, 777-781.

- Babanin, A. (2011): "Breaking and dissipation of ocean surface waves". Cambridge University Press., 463 pp.
- Battjes, J. A. (1972): "Radiation stresses in short-crested gravity waves". *J. Mar. Res.*, 30, 56-64.
- Battjes, J. A. (1974): "Computation of Set-Up, Longshore Currents, Run-Up, and Overtopping Due to Wind-Generated Waves". Report 74-2, Committee on Hydraulics, Department of Civil Engineering, Delft University of Technology, The Netherlands.
- Battjes, J. A., and J. Janssen (1978): "Energy loss and set-up due to breaking of random waves". Paper presented at Proceedings of the 16th international conference on coastal engineering.
- Beardsley, R., C. Chen, Q. Xu, J. Qi, and H. Lin (2011): "Extratropical Storm-Induced Coastal Inundation: Scituate, MA. Inundation TestBed Workshop". North Carolina University, March 7-8, 2011.
- Bennis, A. C., and F. Ardhuin (2011): "Comments on "The Depth-Dependent Current and Wave Interaction Equations: A Revision". *Journal of Physical Oceanography*, 41(10), 2008-2012.
- Bennis, A. C., F. Ardhuin, and F. Dumas (2011): "On the coupling of wave and three-dimensional circulation models: Choice of theoretical framework, practical implementation and adiabatic tests". *Ocean Modelling*, 40(3-4), 260-272.
- Bernier, N. B., and K. R. Thompson (2006): "Predicting the frequency of storm surges and extreme sea levels in the northwest Atlantic". *J. Geophys. Res.*, 111(C10), C10009.

- Bertin, X., A. Oliveira, and A. B. Fortunato (2009): "Simulating morphodynamics with unstructured grids: Description and validation of a modeling system for coastal applications". *Ocean Modelling*, 28(1-3), 75-87.
- Bertin, X., N. Bruneau, J. F. Breilh, A. B. Fortunato, and M. Karpytchev (2012): "Importance of wave age and resonance in storm surges: The case Xynthia, Bay of Biscay". *Ocean Modelling*, 42(0), 16-30.
- Bhagat, R. (2009): "Cold Wakes of Hurricanes in the Gulf of Mexico". Research report written under the supervision of Professor Robert Leben, Niwot High School, 18 pp.
- Bidlot, J.R., J. H. Damian, A. W. Paul, L. Roop, and S.C. Hsuan (2002): "Intercomparison of the Performance of Operational Ocean Wave Forecasting Systems with Buoy Data". *Wea. Forecasting*, 17, 287-310.
- Blain, C. A., J. J. Westerink, and R. A. Luettich, Jr. (1994): "The influence of domain size on the response characteristics of a hurricane storm surge model". *J. Geophys. Res.*, 99(C9), 18467-18479.
- Blumberg, A. F., and G. L. Mellor (1987): "A description of a three-dimensional coastal ocean circulation model". In N. Heaps (ed.), *Three-Dimensional Coastal Ocean Circulation Models*, American Geophysical Union, Washington, D.C., 4:1-16.

- Boers, M. (1996): "Simulation of a surf zone with a barred beach; Report 1: wave heights and wave breaking, Communications on hydraulic and geotechnical engineering". Delft University of Technology, ISSN 0169-6548.
- Booij, N., R. C. Ris, and L. H. Holthuijsen (1999): "A third-generation wave model for coastal regions 1. Model description and validation". *J. Geophys. Res.*, 104(C4), 7649-7666.
- Bretherton, F. P., and C. J. R. Garrett (1969): "Wavetrains in Inhomogeneous Moving Media". Proceedings of the Royal Society of London. Series A, *Mathematical and Physical Sciences*, 302(1471), 529-554.
- Brovchenko I., V. Maderich, and K . Terletska (2011): "Numerical simulations of 3D structure of currents in the region of deep canyons on the east coast of the Black Sea". *International Journal for Computational Civil and Structural Engineering*, 7 (2): 47-53.
- Bruneau, N., A. B. Fortunato, G. Dodet, P. Freire, A. Oliveira, and X. Bertin (2011): "Future evolution of a tidal inlet due to changes in wave climate, Sea level and lagoon morphology (Óbidos lagoon, Portugal)". *Continental Shelf Research*, 31(18), 1915-1930.
- Bunpamong, M., R. O. Reid, and R.E. Whitaker (1985): "an investigation of hurricane-induced forerunner surge in the Gulf of Mexico". Rep. CERC-85-5, 201 pp., Coastal Eng. Res. Cent., Vicksburg, Miss.

- Bunya, S., J. C. Dietrich, J. J. Westerink, B. A. Ebersole, J. M. Smith, J. H. Atkinson, R. Jensen, D. T. Resio, R. A. Luettich, C. Dawson, V. J. Cardone, A. T. Cox, M.D. Powell, and H. J. Westerink (2010): "A High-Resolution Coupled Riverine Flow, Tide, Wind, Wind Wave, and Storm Surge Model for Southern Louisiana and Mississippi. Part I: Model Development and Validation". *Monthly Weather Review*, 138(2), 345-377.
- Burla, M., A. M. Baptista, Y. Zhang, and S. Frolov (2010): "Seasonal and interannual variability of the Columbia River plume: A perspective enabled by multiyear simulation databases". *J. Geophys. Res.*, 115, C00B16.
- Byun, D.S. and X. H. Wang (2005): "The effect of sediment stratification on tidal dynamics and sediment transport patterns". *J Geophysical Res.* 110:C03011.
- Cacchione, D. A., D. E. Drake, R. W. Kayen, R. W. Sternberg, G. C. Kineke, and G. B. Tate (1995): "Measurements in the bottom boundary layer on the Amazon subaqueous delta". *Marine Geology*, 125(3-4), 235-257.
- Canuto, V.M., A. Howard, Y. Cheng, and M.S. Dubovikov (2001): "Ocean turbulence I: one-point closure model. Momentum and heat vertical diffusivities". *Journal of Physical Oceanography*, 31, 1413-1426.
- Carter, H.H., and D.W. Pritchard (1988): "Oceanography of Chesapeake Bay". In: Kjerfve, B. (Ed.), *Hydrodynamics of Estuaries: Dynamics of Partially Mixed Estuaries*, vol. 1. CRC Press, Boca Raton, FL, pp. 1-16.



- Casulli, V., and R.V. Walters (2000): “An unstructured grid, three-dimensional model based on the shallow water equations. *International Journal for Numerical Methods in Fluids*, 32, 331-348.
- Cheng, R. T., C.-H. Ling, J. W. Gartner, and P. F. Wang (1999): “Estimates of bottom roughness length and bottom shear stress in South San Francisco Bay”. California, *J. Geophys. Res.*, 104(C4), 7715-7728.
- Cho, K. (2009): “A numerical modeling study on barotropic and baroclinic responses of the Chesapeake Bay to hurricane events”. PhD Dissertation, Virginia Institute of Marine Science, College of William and Mary.
- Cho, K.-H., H. V. Wang, J. Shen, A. V. Levinson, and Y.-C. Teng (2012): “a modeling study on the response of Chesapeake Bay to hurricane events of Floyd and Isabel”. *Ocean Modelling*, 49-50, 22-46.
- Comblen, R., S. Legrand, E. Deleersnijder, and V. Legat (2009): “A finite element method for solving the shallow water equations on the sphere”. *Ocean Modelling*, 28(1–3), 12-23.
- Conley, D. C., S. Falchetti, I. P. Lohmann, and M. Brocchini (2008): “The effects of flow stratification by non-cohesive sediment on transport in high-energy wave-driven flows”. *Journal of Fluid Mechanics*, 610, 43-67.

Cox, A. T., J. A. Greenwood, V. J. Cardone, and V. R. Swail (1995): "An interactive objective kinematic analysis system". Proc. Fourth Int. Workshop on Wave Hindcasting and Forecasting, Banff, AB, Canada, Atmospheric Environment Service, 109–118.

Craig, P. D., and M. L. Banner (1994): "Modeling Wave-Enhanced Turbulence in the Ocean Surface Layer". *Journal of Physical Oceanography*, 24(12), 2546-2559.

Craik, A. D. D., and S. Leibovich (1976): "A rational model for Langmuir circulations". *Journal of Fluid Mech.*, 73:401-426.

Curray, J.R., (1960): "Sediments and history of the Holocene transgression Continental Shelf, Northwest Gulf of Mexico". Recent Sediments Northwest Gulf of Mexico, American Association of Petroleum Geologists Bulletin, Tulsa, OK, pp. 221–226.

Dietrich, J. C., S. Bunya, J. J. Westerink, B. A. Edersole, J. M. Smith, J. H. Atkinson, R. Jensen, D. T. Resio, R. A. Luettich, C. Dawson, V. J. Cardone, A. T. Cox, M. D. Powell, H. J. Westerink, and H. J. Roberts (2010): "A High-Resolution Coupled Riverine Flow, Tide, Wind, Wind Wave, and Storm Surge Model for Southern Louisiana and Mississippi. Part II: Synoptic Description and Analysis of Hurricanes Katrina and Rita". *Monthly Weather Review*, 138(2), 378-404.

Dietrich, J. C., M. Zijlema, J. J. Westerink, L. H. Holthuijsen, C. Dawson, R. A. Luettich Jr, R. E. Jensen, J. M. Smith, G. S. Stelling, and G. W. Stone (2011a): "Modeling hurricane waves and storm surge using integrally-coupled, scalable computations". *Coastal Engineering*, 58(1), 45-65.

- Dietrich, J. C., J. J. Westerink, A. B. Kennedy, J. M. Smith, R. E. Jensen, M. Zijlema, L. H. Holthuijsen, C. Dawson, R. A. Luettich Jr., M. D. Powell, V. J. Cardone, A. T. Cox, G. W. Stone, H. Pourtaheri, M. E. Hope, S. Tanaka, L. G. Westerink, H. J. Westerink, and Z. Cobell (2011b): "Hurricane Gustav (2008): "Waves and Storm Surge: Hindcast, Synoptic Analysis, and Validation in Southern Louisiana". *Monthly Weather Review*, 139(8), 2488-2522.
- Dingemans, M. W. (1987): "Verification of numerical wave propagation models with laboratory measurements; HISWA verification in the directional wave basin". Delft Hydraulics, Report H228, 400 pp.
- Dingemans, M. W. (1998): "A review of the physical formulations in SWAN". Delft Hydraulics, Report No. H3306..
- Donelan, M. A., F. W. Dobson, S. D. Smith, and R. J. Anderson (1993): "On the dependence of sea-surface roughness on wave development". *J. Phys. Oceanogr.*, 23, 2143 – 2149, doi:10.1175/1520-0485(1993)023 <2143:OTDOSS>2.0.CO;2
- Draut, A. E., G. C. Kineke, D. W. Velasco, M. A. Allison, and R. J. Prime (2005): "Influence of the Atchafalaya River on recent evolution of the chenier-plain inner continental shelf, northern Gulf of Mexico". *Continental Shelf Research*, 25(1), 91-112.
- Dyer, K. R. (1986): "Coastal and Estuarine Sediment dynamics". *Chichester: John Wiley*, 342 pp.

- Dyer, K. R., M. C. Christie, and A. J. Manning (2004): "The effects of suspended sediment on turbulence within an estuarine turbidity maximum". *Estuarine, Coastal and Shelf Science*, 59(2), 237-248.
- Eldeberky, Y. (1996): "Nonlinear Transformation of Wave Spectra in the Nearshore Zone".  
Ph.D. Thesis, TU-Delft, The Netherlands.
- Ekman, V. W. (1905): "On the influence of the earth's rotation on ocean currents".  
*Arch. Math. Astron. Phys.*, 2, 1-52.
- Emanuel, K., R. Sundararajan, and J. Williams (2008): "Hurricanes and Global Warming: Results from Downscaling IPCC AR4 Simulations". *Bulletin of the American Meteorological Society*, 89(3), 347-367.
- Ferrarin, C., G. Umgiesser, A. Cucco, T.-W. Hsu, A. Roland, and C. L. Amos (2008): "Development and validation of a finite element morphological model for shallow water basins". *Coastal Engineering*, 55(9), 716-731.
- Filipot, J.-F., F. Ardhuin, and A. V. Babanin (2010): "A unified deep-to-shallow water wave-breaking probability parameterization". *J. Geophys. Res.*, 115(C4), C04022.
- Flather, R.A., R. Proctor, and J. Wolf (1991): "Oceanographic forecast models". *Computer Modeling in the Environmental Sciences*, D.G. Famer and M.J. Rycroft (Eds.), Oxford. U.K., 15-30.

Freeman, J. C., L. Baer, and C. H. Hung (1957): "The bathystrophic storm tide", *J. Mar. Res.*, 16, 12–23.

Friedrichs, C. T., L. D. Wright, D. A. Hepworth, and S. C. Kim (2000): "Bottom-boundary-layer processes associated with fine sediment accumulation in coastal seas and bays". *Continental Shelf Research*, 20(7), 807-841.

Fringer, O.B., M. Gerritsen, and R. L. Street (2006): "An unstructured-grid, finite-volume, nonhydrostatic, parallel coastal ocean simulator". *Ocean Modelling*, 139, 173.

Funakoshi, Y., S. C. Hagen, and P. Bacopoulos (2008): "Coupling of Hydrodynamic and Wave Models: Case Study for Hurricane Floyd (1999) Hindcast". *Journal of Waterway, Port, Coastal, and Ocean Engineering*, 134(6), 321-335.

Galperin, B., L.H. Kantha, S. Hassid, and A. Rosati (1988): "A quasi-equilibrium turbulent energy model for geophysical flows". *Journal of Atmospheric Science*, 45, 55-62.

Ganju, N. K., and C. R. Sherwood (2010): "Effect of roughness formulation on the performance of a coupled wave, hydrodynamic, and sediment transport model". *Ocean Modelling*, 33(3–4), 299-313.

Gao, J. (2011): "A Numerical Modeling Study of Storm Surge and Inundation in the Chesapeake Bay during the November 2009 Nor'easter". MS Thesis, Virginia Institute of Marine Science, College of William and Mary.

- Garrett, C., (1976): "Generation of Langmuir circulations by surface waves – A feedback mechanism". *J. Mar. Res.*, 34, 116-130.
- Geyer, W. R., P. S. Hill, and G. C. Kineke (2004): "The transport, transformation and dispersal of sediment by buoyant coastal flows". *Continental Shelf Research*, 24(7–8), 927-949.
- Glahn, B., A. Taylor, N. Kurkowski, and W. Shaffer (2009): "The role of the SLOSH model in national weather service storm surge forecasting". *National Weather Digest*, 33(1), 3-14.
- Glenn, S. M., and W. D. Grant (1987): "A Suspended Sediment Stratification Correction for Combined Wave and Current Flows". *J. Geophys. Res.*, 92(C8), 8244-8264.
- Gong, W., J. Shen, and W. G. Reay (2007): "The hydrodynamic response of the York River estuary to Tropical Cyclone Isabel, 2003". *Estuarine, Coastal and Shelf Science*, 73(3–4), 695-710.
- Gong, W., J. Shen, K. H. Cho, and H. V. Wang (2009): "A numerical model study of barotropic subtidal water exchange between estuary and subestuaries (tributaries) in the Chesapeake Bay during northeaster events". *Ocean Modelling*, 26(3–4), 170-189.
- Gottlieb, S., and C.-W. Shu (1998): "Total Variation Diminishing Runge-Kutta Schemes". *Mathematics of Computation*, 67, 73-85.
- Grant, W. D., and O. S. Madsen (1979): "Combined Wave and Current Interaction With a Rough Bottom". *J. Geophys. Res.*, 84(C4), 1797-1808.

- Grant, W. D., and O. S. Madsen (1986): "THE CONTINENTAL-SHELF BOTTOM BOUNDARY-LAYER", *Annual Review of Fluid Mechanics*, 18, 265-305.
- Grant, W. D., A. J. Williams, and S. M. Glenn (1984): "Bottom Stress Estimates and their Prediction on the Northern California Continental Shelf during CODE-1: The Importance of Wave-Current Interaction". *Journal of Physical Oceanography*, 14(3), 506-527.
- Group, T. W. (1988): "The WAM Model—A Third Generation Ocean Wave Prediction Model". *Journal of Physical Oceanography*, 18(12), 1775-1810.
- Guo, X., and A. Valle-Levinson (2007): "Tidal effects on estuarine circulation in Chesapeake Bay". *Continental Shelf Research* 27, 20–42.
- Hagy, J. D., J. C. Lehrter, and M. C. Murrell (2006): "Effects of Hurricane Ivan on water quality in Pensacola Bay, Florida". *Estuaries Coasts* 29, 919-925.
- Harris, D. L. (1963): "Characteristics of the Hurricane storm surge". Technical Paper No. 48, U.S. Weather Bureau.
- Hasselmann, K., T. P. Barnett, E. Bouws, D. E. Carlson, and P. Hasselmann (1973): "Measurements of wind-wave growth and swell decay during the Joint North Sea Wave Project (JONSWAP)". *Deutsche Hydrographische Zeitschrift*, 8(12).
- Hasselmann, K. (1962): "On the non-linear energy transfer in a gravity-wave spectrum Part 1. General theory". *Journal of Fluid Mechanics*, 12(04), 481-500.

Hasselmann, S., and K. Hasselmann (1985): "Computations and Parameterizations of the Nonlinear Energy Transfer in a Gravity-Wave Spectrum. Part I: A New Method for Efficient Computations of the Exact Nonlinear Transfer Integral". *Journal of Physical Oceanography*, 15(11), 1369-1377.

Hasselmann, S., K. Hasselmann, J. H. Allender, and T. P. Barnett (1985): "Computations and Parameterizations of the Nonlinear Energy Transfer in a Gravity-Wave Spectrum. Part II: Parameterizations of the Nonlinear Energy Transfer for Application in Wave Models". *Journal of Physical Oceanography*, 15(11), 1378-1391.

Hersbach, H., and P. A. E. M. Janssen (1999): "Improvement of the Short-Fetch Behavior in the Wave Ocean Model (WAM)". *Journal of Atmospheric and Oceanic Technology*, 16(7), 884-892.

Hicks, S.D. (1964): "Tidal wave characteristics of Chesapeake Bay". *Chesapeake Science*, 5, 103-113.

Holthuijsen, L. H., A. Herman, and N. Booij (2003): "Phase-decoupled refraction-diffraction for spectral wave models". *Coastal Engineering*, 49(4), 291-305.

Hsu, T.-W., S.-H. Ou, and J.-M. Liao (2005): "Hindcasting nearshore wind waves using a FEM code for SWAN". *Coastal Engineering*, 52(2), 177-195.

Janssen, P. (1989): "Wave-Induced Stress and the Drag of Air Flow over Sea Waves". *Journal of Physical Oceanography*, 19(6), 745-754.



Janssen, P. (1991): "Quasi-linear Theory of Wind-Wave Generation Applied to Wave Forecasting".

*Journal of Physical Oceanography*, 21(11), 1631-1642.

Janssen, P. A. E. M. (2001): "Reply". *Journal of Physical Oceanography*, 31(8), 2537

Janssen, P. (2004): "The interaction of ocean waves and wind". Cambridge University Press,  
Cambridge, 300 pp.

Janssen, P.A.E.M. (2010): "Ocean wave effects on the daily cycle in STT", ECMWF, Technical  
Memorandum.

Janssen, P.A.E.M. (2011): "Ocean wave effects on the daily cycle in STT". Technical  
Memoranda, ECMWF, No.: 634.

Jelesnianski, C.P., J. Chen, and W.A. Shaffer (1992): "SLOSH: sea, lake, and overland surges from  
hurricane". National Weather Service, Silver Springs, MD.

Johnson, H. K., J. Højstrup, H. J. Vested, and S. E. Larsen (1998): "On the Dependence of Sea  
Surface Roughness on Wind Waves". *Journal of Physical Oceanography*, 28(9), 1702-  
1716.

Jonsson, I. G. (1993): "Wave current interactions, in The Sea". Ocean Eng. Sci.Ser., vol. 9, part A,  
edited by B. Le Mehaute and D. M. Hanes, pp.65-70, John Wiley, New York.

Kantha, L.H., and C.A. Clayson (1994): "An improved mixed layer model for geophysical  
applications". *Journal of Geophysical Research*, 99(25), 235-266.

- Keller, J. B. (1958): "Surface waves on water of non-uniform depth". *Journal of Fluid Mechanics*, 4(06), 607-614.
- Kennedy, A. B., U. Gravois, B. C. Zachry, J. J. Westerink, M. E. Hope, J. C. Dietrich, M. D. Powell, A. T. Cox, R. A. Luettich, Jr., and R. G. Dean (2011): "Origin of the Hurricane Ike forerunner surge". *Geophys. Res. Lett.*, 38(8), L08608.
- Kineke, G. C., E.E. Higgins, K. Hart, and D. Velasco (2006): "Fine-sediment transport associated with cold-front passages on the shallow shelf". Gulf of Mexico, *Continental Shelf Research*, 26, 2073-2091.
- Kim, K. O., T. Yamashita, and B. H. Choi (2008): "Coupled process-based cyclone surge simulation for the Bay of Bengal". *Ocean Modelling*, 25(3-4), 132-143.
- King, B., and E. Wolanski (1996): "Bottom friction reduction in turbid estuaries, in Mixing in Estuaries and Coastal Seas". *Coastal Estuarine Stud.*, vol.50, edited by C. Pattiaratchi, pp. 325-337, AGU, Washington, D.C.
- Kirby, R., and W. R. Parker (1977): "The physical characteristics and environmental significance fine sediment suspensions in estuaries". *Estuaries, geophysics and the environment*, National Research Council, National Academy Press, Washington, D.C., 110-120.
- Kohut, J. T., S. M. Glenn, and J. D. Paduan (2006): "Inner shelf response to Tropical Storm Floyd". *J. Geophys. Res.*, 111(C9), C09S91.

- Komen, G. J., L. Cavaleri, M. Donelan, K. Hasselmann, S. Hasselmann, and P. A. E. M. Janssen (1994): "Dynamics and Modelling of Ocean Waves". Cambridge Univ. Press, New York, 532 pp.
- Kumar, N., G. Voulgaris, and J. C. Warner (2011): "Implementation and modification of a three-dimensional radiation stress formulation for surf zone and rip-current applications". *Coastal Engineering*, 58(12), 1097-1117.
- Lai, R. J., S. R. Long, and N. E. Huang (1989): "Laboratory Studies of Wave-Current Interaction: Kinematics of the Strong Interaction". *J. Geophys. Res.*, 94(C11), 16201-16214.
- Lane, E. M., J. M. Restrepo, and J. C. McWilliams (2007): "Wave-current interaction: A comparison of radiation-stress and vortex force representation". *J. Phys. Oceanography*, 37, 1122-1141.
- Lavrenov, I.V. (2004): "Weak turbulent fluxes estimation in surface water wave spectrum". 8th International Workshop on Wave Hindcasting and Forecasting, North Shore, Oahu, Hawaii.
- Le Provost, C., F. Lyard, J. M. Molines, M. L. Genco, and F. Rabilloud (1998): "A hydrodynamic ocean tide model improved by assimilating a satellite altimeter-derived data set". *J. Geophys. Res.*, 103(C3), 5513-5529.
- Le Roux, D. Y., C. A. Lin, and A. Staniforth (1997): "An accurate interpolating scheme for semi-Lagrangian advection on an unstructured mesh for ocean modeling". *Tellus A*, 49(1), 119-138.

- Leonard, B. P. (1991): "The ultimate conservative difference scheme applied to unsteady one-dimensional advection". *Computer Methods in Applied Mechanics and Engineering*, 88(1), 17-74.
- Lewis, D. M., and S. E. Belcher (2004): "Time-dependent, coupled, Ekman boundary layer solutions incorporating Stokes drift". *Dynamics of atmospheres and oceans*, 37, 313-351.
- Li, M., L. Zhong, W. C. Boicourt, S. Zhang, and D.-L. Zhang (2006): "Hurricane-induced storm surges, currents and destratification in a semi-enclosed bay". *Geophys. Res. Lett.*, 33(2), L02604.
- Liau, J.-M., A. Roland, T.-W. Hsu, S.-H. Ou, and Y.-T. Li (2011): "Wave refraction-diffraction effect in the wind wave model WWM". *Coastal Engineering*, 58(5), 429-443.
- Liu, W.-C., W.-B. Chen, J.-T. Kuo, and C. Wu (2008): "Numerical determination of residence time and age in a partially mixed estuary using three-dimensional hydrodynamic model". *Continental Shelf Research*, 28(8), 1068-1088.
- Longuet-Higgins, M. S., and R. W. Stewart (1962): "Radiation stress and mass transport in gravity waves, with application to "surf beats"". *Journal of Fluid Mechanics*, 13(04), 481-504.
- Longuet-Higgins, M. S., and R. W. Stewart (1964): "Radiation stresses in water waves; a physical discussion, with applications". *Deep Sea Research and Oceanographic Abstracts*, 11(4), 529-562.

Luettich, R. A., J. C. Muccino, and M. G. G. Foreman (2002): "Considerations in the Calculation of Vertical Velocity in Three-Dimensional Circulation Models". *Journal of Atmospheric and Oceanic Technology*, 19(12), 2063-2076.

Madsen, O.S. (1994): "Spectral wave-current bottom boundary layer flows". In: Coastal Engineering 1994. Proceedings of the 24th International Conference on Coastal Engineering Research Council, Kobe, Japan, pp. 384-398.

Mastenbroek, C., G. Burgers, and P. Janssen (1993): "The dynamical coupling of a wave model and a storm surge model through the atmospheric boundary layer". *J. Phys. Oceanogr.* 23, 1856-1867.

Mathisen, P. P., and O. S. Madsen (1996): "Waves and currents over a fixed rippled bed 2. Bottom and apparent roughness experienced by currents in the presence of waves". *J. Geophys. Res.*, 101(C7), 16543-16550.

Mathisen, P. P., and O. S. Madsen (1999): "Waves and currents over a fixed rippled bed 3. Bottom and apparent roughness for spectral waves and currents". *J. Geophys. Res.*, 104(C8), 18447-18461.

McWilliams, J. C., J. M. Restrepo, and E. M. Lane (2004). "An asymptotic theory for the interaction of waves and currents in coastal waters". *Journal of Fluid Mechanics*, 511, 135-178.

- McWilliams, J. C., and Y. Uchiyama (2008): "The effects of surface Gravity Waves on Coastal Currents: Implementation, Phenomenological Exploration, and Realistic Simulation with ROSS". ONR report, 12 pp.
- Mellor, G.L., and T. Yamada, (1982): "Development of a turbulence closure model for geophysical fluid problems". *Reviews in Geophysics*, 20, 851-875.
- Mellor, G. (2003): "The Three-Dimensional Current and Surface Wave Equations". *J. Phys. Oceanography*, 33(9), 1978-1989.
- Mellor, G. (2005): "Some consequences of the three-dimensional current and surface wave equations". *J. Phys. Oceanography*, 35,2291-2298
- Mellor, G. L. (2008): "The Depth-Dependent Current and Wave Interaction Equations: A Revision". *Journal of Physical Oceanography*, 38(11), 2587-2596.
- Mellor, G. (2011a): "Reply". *Journal of Physical Oceanography*, 41(10), 2013-2015.
- Mellor, G. (2011b): "Wave radiation stress". *Ocean Dynamics*, 61(5), 563-568.
- Mingxiao, X. (2011): "Establishment, validation and discussions of a three dimensional wave-induced current model". *Ocean Modelling*, 38(3-4), 230-243.
- Morey, S. L., S. Baig, M. A. Bourassa, D. S. Dukhovskoy, and J. J. O'Brien (2006): "Remote forcing contribution to storm-induced sea level rise during Hurricane Dennis". *Geophys. Res. Lett.*, 33(19), L19603.

- Mukai, A., J. J. Westerink, R. Luettich, and D. Mark (2002): "East coast 2001: A tidal constituent database for the Western North Atlantic, Gulf of Mexico, and Caribbean Sea". Tech. Rep. ERDC/CHL TR-02-24, U.S. Army Corps of Engineers, 201 pp.
- National Hurricane Center, National Weather Service (2009).  
<http://www.nhc.noaa.gov/aboutgloss.shtml>
- Nicholson, J., I. Broker, J. A. Roelvink, D. Price, J. M. Tanguy, and L. Moreno (1997):  
"Intercomparison of coastal area morphodynamic models". *Coastal Engineering*, 31(1-4), 97-123.
- NTHMP (2011): "NTHMP MMS Tsunami Inundation Model Validation Workshop". Galveston, April 2011. NOAA internal report (in press).
- Pawlowicz, R., B. Beardsley, and S. Lentz (2002): "Classical tidal harmonic analysis including error estimates in MATLAB using T\_TIDE". *Computers Geosciences*, 28, 929-937.
- Peregrine, D. H., and I. G. Jonsson (1983): "Interaction of waves and currents". US army corps of engineers miscellaneous reports, MR83-6.
- Phillips, O. M. (1977): "The Dynamics of the Upper Ocean". Cambridge Univ. Press, New York, 336 pp.
- Pond, S., and G.L. Pickard (1998): "Introductory Dynamical Oceanography". Butterworth-Heinemann, 349 pp.

- Pore, N. A. (1960): "Chesapeake Bay hurricane surges". *Chesapeake Science*, 1, 178–186.
- Pore, N. A. (1965): "Chesapeake Bay extratropical storm surges". *Chesapeake Science*, 6, 172–182.
- Powell, M. D., S. H. Houston, and T. A. Reinhold (1996): "Hurricane Andrew's landfall in South Florida Part {I}: Standardizing measurements for documentation of surface wind fields". *Weather and Forecasting*, 11, 304-328.
- Powell, M. D., S. H. Houston, L. Amat, and N. Morrisseau-Leroy (1998): "The HRD real-time hurricane wind analysis system". *J. Wind Eng. Ind. Aerodyn.*, 77–78, 53–64..
- Powell, M. D. (2006): "Drag coefficient distribution and wind speed dependence in tropical cyclones". Final report to the NOAA Joint Hurricane Testbed (JHT) Program, 26 pp.
- Qi, J., C. Chen, R. Beardsley, W. Perrie, G. Cowles, and Z. Lai (2009): "An Unstructured-Grid Finite-Volume Surface Wave Model ({FVCOM-SWAVE}): Implementation, Validations and Applications". *Ocean Modelling*, 28, 153-166.
- Qin, Q. (2011): "Personal communication". Graduate student, Virginia Institute of Marine Science, Gloucester Pt., VA. 2011-2012.
- Reid, R. O. (1990): "Water level changes". Handbook of Coastal and Ocean Engineering. Gulf Publishing, Houston, TX.
- Rego, J. L., and C. Li (2010b): "Nonlinear terms in storm surge predictions: Effect of tide and shelf geometry with case study from Hurricane Rita", *J. Geophys. Res.*, 115(C6), C06020.



- Ris, R., L.H. Holthuijsen, J. M. Smith, N. Booij, and A.R. van Dongeren (2002): "The ONR test bed for Coastal and Oceanic Wave Models, 28<sup>th</sup> Int. Conf. Coastal Eng., ASCE, Cardiff:380-391.
- Rodi, W. (1984): "Turbulence models and their applications in hydraulics: a state of the art review". Delft, The Netherlands, International Association for Hydraulics Research..
- Rodrigues, M., A. Oliveira, H. Queiroga, A.B. Fortunato, Y.-L. Zhang (2009): "Three-dimensional modeling of the lower trophic levels in the Ria de Aveiro (Portugal)". *Ecological Modelling*, 220(9-10),1274-1290.
- Roe, P. L. (1982): "Numerical modelling of shockwaves and other discontinuities". In Numerical Methods in Aeronautical Fluid Dynamics, ed. P. L. Roe, pp. 21 1-43. London: Academic.
- Roland, A. (2009): "Development of WWM II - Spectral wave modeling on unstructured meshes". PhD Thesis, Darmstadt University of Technology, Institute for Hydraulic Engineering and Water Resources Management, Darmstadt, Germany.
- Roland, A., A. Cucco, C. Ferrarin, T.-W. Hsu, J.-M. Liau, S.-H. Ou, G. Umgiesser, and U. Zanke (2009): "On the development and verification of a 2-D coupled wave-current model on unstructured meshes". *Journal of Marine Systems*, 78, Supplement(0), S244-S254.
- Roland, A., Y. Zhang, H. V. Wang, Y. Meng, Y.-C. Teng, V. Maderich, I. Brovchenko, M. Dutour, and U. Zanke (2012): "A fully coupled 3D wave-current interaction model on unstructured grids (submitted)".

- Safak, I., A. Sheremet, M. A. Allison, and T.-J. Hsu (2010): "Bottom turbulence on the muddy Atchafalaya Shelf, Louisiana". USA, *J. Geophys. Res.*, 115(C12), C12019.
- Sallenger, A. H., H. F. Stockdon, L. Fauver, M. Hansen, D. Thompson, C. W. Wright, and J. Lillycrop (2006): "Hurricane 2004: An overview of their characteristics and coastal change". *Estuaries Coasts*, 29, 880–888.
- Shapiro, R. (1970): "Smoothing, filtering, and boundary effects". *Rev. Geophys.*, 8(2), 359-387.
- Shen, J., and W. Gong (2009): "Influence of model domain size, wind directions and Ekman transport on storm surge development inside the Chesapeake Bay: A case study of extratropical cyclone Ernesto, 2006". *Journal of Marine Systems*, 75(1–2), 198-215.
- Shen, J., W. Gong, and H. V. Wang (2006a): "Water level response to 1999 Hurricane Floyd in the Chesapeake Bay". *Continental Shelf Research*, 26(19), 2484-2502.
- Shen, J., H. Wang, M. Sisson, and W. Gong (2006b), Storm tide simulation in the Chesapeake Bay using an unstructured grid model, *Estuarine, Coastal and Shelf Science*, 68(1–2), 1-16.
- Shen, T. (2009): "Development of a Storm Surge Model Using a High-Resolution Unstructured Grid". MS Thesis, Virginia Institute of Marine Science, College of William and Mary.
- Sheng, Y. P., and T. Liu (2011): "Three-dimensional simulation of wave-induced circulation: Comparison of three radiation stress formulations". *J. Geophys. Res.*, 116(C5), C05021.

- Sheng, Y. P., V. Alymov, and V. A. Paramygin (2010): "Simulation of storm surge, wave, currents, and inundation in the Outer Banks and Chesapeake Bay during Hurricane Isabel in 2003: The importance of waves", *J. Geophys. Res.*, 115(C4), C04008.
- Sheremet, A., and G.W. Stone (2003): "Observations of nearshore wave dissipation over muddy sea beds". *J. Geophys. Res.*, 108(C11), 3357, doi:10.1029/2003JC001885.
- Sheremet, A., A. J. Mehta, B. Liu, and G. W. Stone (2005): "Wave-sediment interaction on a muddy inner shelf during Hurricane Claudette". *Estuarine, Coastal and Shelf Science*, 63(1-2), 225-233.
- Sherwood, C. R., J. R. Lacy, and G. Voulgaris (2006): "Shear velocity estimates on the inner shelf off Grays Harbor, Washington, USA". *Continental Shelf Research*, 26(17-18), 1995-2018.
- Shyu, J.-H., and O. M. Phillips (1990): "The blockage of gravity and capillary waves by longer waves and currents". *Journal of Fluid Mechanics*, 217, 115-141.
- Smith, J. D. and S. R. McLean (1977a): "Spatially averaged flow over a wave surface". *Journal of Geophysical Research*, 82, 1735-46.
- Smith, J. D. and S. R. McLean (1977b): "Boundary layer adjustments to bottom topography and suspended sediment". In *Bottom Turbulence*, ed. J. C. J. Nihoul, pp. 123-51. New York: Elsevier.
- Smith, S. D. (1980): "Wind stress and heat flux over the ocean in gale force winds". *Journal of Physical Oceanography*, 10, 709-726.

- Soulsby, R. L., and B. L. S. A. Wainwright (1987): "The bottom boundary layer of shelf seas, in *Physical Oceanography of Coastal and Shelf Seas*". *Oceanogr. Ser.*, vol. 35, edited by B. Johns, pp. 189-266, Elsevier, New York.
- Stewart, S. R. (2005): "Tropical Cyclone Report, Hurricane Ivan 2-24 September 2004". National Oceanic and Atmospheric Administration, National Hurricane Center, Tropical Prediction Center, Miami, Florida.
- Styles, R., and S. M. Glenn (2000): "Modeling stratified wave and current bottom boundary layers on the continental shelf". *J. Geophys. Res.*, 105(C10), 24119-24139.
- SURA Test bed (2011), <http://testbed.sura.org/>.
- Taylor, J. R., and S. Sarkar (2008): "Stratification effects in a bottom Ekman layer". *J. Phys. Oceanography*, 38, 2535–2555.
- Teng, Y. C., H.W. Wang, and Z. Wang (2012): "The development of an Unstructured Grid, three dimensional Integrated Model (SELFE-WQM) for the water quality and Plankton Dynamics in the Maryland Coastal Bay". *In prep.*.
- Titov, V.V., and C. E. Synolakis (1995): "Modeling of breaking and non-breaking long-wave evolution and runup using VTCS-2". *J. Waterway, Ports, Coastal and Ocean Engin.* 121(6), 308–316.

- Toledo, Y., T.-W. Hsu, and A. Roland (2012): "Extended time dependent mild-slope and wave-action equations for wave bottom and wave-current interactions". *Proc. Roy. Soc. Lond.A*, 468, 184–205, doi:10.1098/rspa.2011.037.
- Tolman, H. L. (1992): "Effects of Numerics on the Physics in a Third-Generation Wind-Wave Model". *Journal of Physical Oceanography*, 22(10), 1095-1111.
- Tolman, H. L. (1999), User manual and system documentation of WAVEWATCH-III version 1.18, OMB Tech. Note 167, Natl. Cent. for Environ.Predict., Washington, D. C.
- Uchiyama, Y., J. C. McWilliams, and A. F. Shchepetkin (2010): "Wave-current interaction in an oceanic circulation model with a vortex-force formalism: Application to the surf zone". *Ocean Modelling*, 34(1–2), 16-35.
- UMass Dartmouth/WHOI group (2012): "Inter-model comparison experiments for 2005 and 2007 extratropical storm events in Scituate, Massachusetts". Plan to be submitted to JGR.
- Umgiesser, G., D. M. Canu, A. Cucco, and C. Solidoro (2004): "A finite element model for the Venice Lagoon. Development, set up, calibration and validation". *Journal of Marine Systems*, 51(1–4), 123-145.
- Umlauf, L., and H. Burchard (2003): "A generic length-scale equation for geophysical turbulence models". *Journal of Marine Research*, 61, 235-265.
- Umlauf, L., and H. Burchard (2005): "Second-order turbulence closure models for geophysical boundary layers. A review of recent work". *Continental Shelf Research*, 25, 795-827.

- United States Congress (2006): “A failure of initiative: final report of the select bipartisan committee to investigate the preparation for and response to Hurricane Katrina”. *Government Printing Office*, Washington, DC.
- Valle-Levinson, A., K.-C. Wong, and K. T. Bosley (2002): “Response of the lower Chesapeake Bay to forcing from Hurricane Floyd”. *Continental Shelf Research*, 22(11–13), 1715-1729.
- Van Vledder, G.Ph. (2006). The WRT method for the computation of non-linear four-wave interactions in discrete spectral wave models. *Coastal Engineering*, 53, 223-242.
- The Wamdi Group (1988): “The WAM model—A third generation ocean wave prediction model”. *J. Phys. Oceanography*, 18, 1775– 1810.
- Wang, D. W., D. A. Mitchell, W. J. Teague, E. Jarosz, and M. S. Hulbert (2005): “Extreme waves under hurricane Ivan”. *Science*, 309, 896.
- Wang, X. H. (2002): “Tide-induced sediment resuspension and the bottom boundary layer in an idealized estuary with a muddy bed”. *J. Phys. Oceanography*, 32(11), 3113–3131.
- Warner, J. C., B. Armstrong, R. He, and J. B. Zambon (2010): “Development of a Coupled Ocean–Atmosphere–Wave–Sediment Transport (COAWST) Modeling System”. *Ocean Modelling*, 35(3), 230-244.
- Warner, J. C., C. R. Sherwood, R. P. Signell, C. K. Harris, and H. G. Arango (2008): “Development of a three-dimensional, regional, coupled wave, current, and sediment-transport model”. *Computers & Geosciences*, 34(10), 1284-1306.

- Weisberg, R., and L. Zheng (2006): "Hurricane storm surge simulations for Tampa Bay". *Estuaries and Coasts*, 29(6), 899-913.
- Weisberg, R. H., and L. Zheng (2008): "Hurricane storm surge simulations comparing three-dimensional with two-dimensional formulations based on an Ivan-like storm over the Tampa Bay". Florida region, *J. Geophys. Res.*, 113(C12), C12001.
- Westerink, J.J., R.A. Luettich, and J. Muccino (1994): "Modeling tides in the western North Atlantic using unstructured graded grids". *Tellus*, 46A, 178-199.
- Wilcox, D.C. (1998): "Reassessment of scale determining equation for advance turbulence models". *ALAA Journal*, 26, 1299-1310.
- Wolf, J. (2009): "Coastal flooding: impacts of coupled wave-surge-tide models". *Nat. Hazards*, 49, 241-260.
- Wright, L. D., C. R. Sherwood, and R. W. Sternberg (1997): "Field measurements of fairweather bottom boundary layer processes and sediment suspension on the Louisiana inner continental shelf". *Marine Geology*, 140(3-4), 329-345.
- Xia, H., Z. Xia, and L. Zhu (2004): "Vertical variation in radiation stress and wave-induced current". *Coastal Engineering*, 51(4), 309-321.
- Xie, L., K. Wu, L. Pietrafesa, and C. Zhang (2001): "A numerical study of wave-current interaction through surface and bottom stresses: Wind-driven circulation in the SouthAtlantic Bight under uniform winds". *J. Geophys. Res.*, 106(C8), 16841-16855.

- Xie, L., H. Liu, and M. Peng (2008): "The effect of wave–current interactions on the storm surge and inundation in Charleston Harbor during Hurricane Hugo 1989". *Ocean Modelling*, 20(3), 252-269.
- Xu, H., K. Zhang, J. Shen, and Y. Li (2010): "Storm surge simulation along the U.S. East and Gulf Coasts using a multi-scale numerical model approach". *Ocean Dynamics*, 60(6), 1597-1619.
- Xu, K., C. K. Harris, R. D. Hetland, and J. M. Kaihatu (2011): "Dispersal of Mississippi and Atchafalaya sediment on the Texas–Louisiana shelf: Model estimates for the year 1993". *Continental Shelf Research*, 31(15), 1558-1575.
- Yanenko, N. N. (1971), *The method of fractional steps*. Springer-Verlag.
- Zeng, X., M. Zhao, and R. E. Dickinson (1998): "Intercomparison of Bulk Aerodynamic Algorithms for the Computation of Sea Surface Fluxes Using TOGA COARE and TAO Data". *Journal of Climate*, 11(10), 2628-2644.
- Zhang, H., O. S. Madsen, S. A. Sannasiraj, and E. Soon Chan (2004): "Hydrodynamic model with wave–current interaction in coastal regions". *Estuarine, Coastal and Shelf Science*, 61(2), 317-324.
- Zhang, K., C. Xiao, and J. Shen (2008): "Comparison of the CEST and SLOSH Models for Storm Surge Flooding". *Journal of Coastal Research*, 489-499.
- Zhang, Y., and A. M. Baptista (2008a): "SELFE: A semi-implicit Eulerian–Lagrangian finite-element model for cross-scale ocean circulation". *Ocean Modelling*, 21(3–4), 71-96.



- Zhang, Y., and A. M. Baptista (2008b): “An efficient and robust tsunami model on unstructured grids. Part I: Inundation benchmarks”. *Pure Appl. Geophys.* 165, 2229-2248.
- Zhang, Y., A. M. Baptista, and E. P. Myers (2004): “A cross-scale model for 3D baroclinic circulation in estuary–plume–shelf systems: I. Formulation and skill assessment”. *Continental Shelf Research*, 24(18), 2187-2214.
- Zhang, Y. J., R. C. Witter, and G. R. Priest (2011): “Tsunami–tide interaction in 1964 Prince William Sound tsunami”. *Ocean Modelling*, 40(3–4), 246-259.
- Zhong, L., and M. Li (2006): “Tidal energy fluxes and dissipation in the Chesapeake Bay”. *Continental Shelf Research*, 26, 752–770.
- Zhong, L., M. Li, and D.-L. Zhang (2010): “How do uncertainties in hurricane model forecasts affect storm surge predictions in a semi-enclosed bay?”. *Estuarine, Coastal and Shelf Science*, 90(2), 61-72.
- Zijlema, M. (2010): “Computation of wind-wave spectra in coastal waters with SWAN on unstructured grids”. *Coastal Engineering*, 57(3), 267-277.

**VITA****Yi-Cheng Teng**

**Born in Taipei, Republic of China (Taiwan), on the 20th of December 1981. Received B.S. in Civil Engineering from National Taiwan Ocean University in 2004. Earned M.S. in Hydrological and Oceanic Sciences from National Central University in 2006. Entered Ph.D. program of the College of William and Mary, School of Marine Science in Fall of 2008.**